# Saharan dust transport studied by airborne Doppler wind lidar and numerical models

**Fernando Germán Chouza Keil**


München 2016

# Saharan dust transport studied by airborne Doppler wind lidar and numerical models

**Fernando Germán Chouza Keil**

Dissertation
an der Fakultät für Physik
der Ludwig–Maximilians–Universität
München

vorgelegt von
Fernando Germán Chouza Keil
aus Buenos Aires, Argentina

München, den 25. Oktober 2016

Erstgutachter: Prof. Dr. Bernadett Weinzierl
Zweitgutachter: Prof. Dr. Markus Rapp
Tag der mündlichen Prüfung: 21. Dezember 2016

# Contents

# Zusammenfassung

Jedes Jahr wird eine große Menge an Staub über den Nordatlantik von Nordafrika in die Karibik transportiert. Trotz der Fortschritte, die in den vergangenen Jahrzehnten im Verständnis und der Modellierung dieses Prozesses erzielt wurden, bleiben noch viele Unsicherheiten. In dieser kumulativen Dissertation werden die bei der SALTRACE - Kampagne (Juni - Juli 2013) durchgeführten flugzeuggetragenen Doppler Wind Lidar (DWL) Messungen, Large Eddy Simulationen und das globale Modell MACC verwendet, um verschiedene Aspekte des Staubtransportprozesses zu untersuchen und die aktuellen Modellierungsmöglichkeiten zu bewerten.

Als Teil dieser Dissertation wird ein neuartiger Kalibrierungsalgorithmus für die Bestimmung von quantitativen Aerosolrückstreuungs- und -extinktionskoeffizienten aus DWL-Messungen eingeführt. Diese Methode beruht auf der gleichzeitigen Messung des atmosphärischen Volumens durch das flugzeuggetragene DWL und ein bodengebundenes Aerosol Lidar. Diese Methode wird mit dem satellitengetragenen Lidar CALIOP und bodengebundenen Lidarmessungen validiert. Zusätzlich wird eine Reihe von Verbesserungen bei vertikalen Windauswertealgorithmen diskutiert und deren Auswirkung auf die Retrievalgenauigkeit mittels zweier verschiedener Verfahren abgeschätzt.

Basierend auf diesem erweiterten DWL-Datensatz, der simultane Rückstreuungs- und Windmessungen umfasst, werden verschiedene Prozesse des Staubtransports aus der Sahara untersucht. Die Messungen in der Nähe der Kap Verden Inselgruppe und Barbados zeigen die Anwesenheit von Schwerewellen hervorgerufen durch die Orographie der Inseln. Diese Messungen werden zusammen mit der in-situ Wind und Partikelanzahldichte, den Large Eddy Simulationen und der Wavelet-Analyse verwendet, um die Hauptcharakteristiken der beobachteten Schwerwellen und deren Wechselwirkung mit der Sahara-Luftschicht zu bestimmen. Schließlich wird versucht, unter Nutzung der gewonnenen DWL- und CALIOP-Messungen den Sahara-Staub Transportprozess während der SALTRACE Kampagne im globalen MACC-Aerosolmodell zu reproduzieren, um dessen Vorhersagequalität zu bewerten. Ein Vergleich und eine Analyse der gemessenen und simulierten mittleren Wind- und Staubverteilungen in den westafrikanischen und karibischen Regionen wird vorgestellt. Drei Fallstudien, die verschiedene charakteristische Merkmale behandeln, wie der African Easterly Jet und die Staubtransportmodulation durch die African Easterly Waves, werden im Hinblick auf zukünftige Kampagnen und die Assimilierung der Datenprodukte für die zukünftigen ESA-Satellitenmission Aeolus und EarthCARE diskutiert.

# Abstract

Every year a large amount of dust is transported over the north Atlantic ocean from North Africa into the Caribbean region. Despite the progress made during the last decades in the understanding and modeling of this process, many uncertainties still remain. In this cumulative thesis, the airborne Doppler wind lidar (DWL) measurements performed during the SALTRACE campaign (June-July 2013), large eddy simulations and the global atmospheric composition model MACC are used to study different aspects of the dust transport process and evaluate the current modeling capabilities.

As part of this work, a novel calibration algorithm for the retrieval of quantitative aerosol backscatter and extinction coefficients from the DWL measurements is introduced. This calibration procedure relies on the simultaneous measurement of the same atmospheric volume by the airborne DWL and an aerosol ground-based lidar. This method is then validated with satellite lidar CALIOP and ground-based lidar measurements. Additionally, improvements in vertical wind retrieval algorithms are discussed and their impact on the retrieval accuracy estimated by means of two different methods.

Based on this extended airborne DWL dataset, which includes simultaneous backscatter and wind measurements, different processes associated with the Saharan dust transport are investigated. Measurements carried out in the Cabo Verde and Barbados regions revealed the presence of island-induced gravity waves. These measurements are used in combination with in-situ wind and particle number density retrievals, large eddy simulations, and wavelet analysis to determine the main characteristics of the observed waves and their interaction with the Saharan Air Layer. Finally, DWL and CALIOP measurements are used to evaluate the capabilities of the MACC global aerosol model to reproduce the Saharan dust long-range transport process during SALTRACE. A comparison and analysis of the measured and simulated average wind and dust distributions in the West African and Caribbean regions is presented. Three case studies covering different characteristic features, like the African Easterly Jet and the dust transport modulation by the African Easterly Waves, are discussed with an outlook to future campaigns and the assimilation of the data products for the ESA's future satellite missions Aeolus and EarthCARE.

# Chapter 1

# Introduction

Climate change has gained increasing relevance during the last decades, becoming one of the main focus areas of research in the field of atmospheric sciences. According to fifth Intergovernmental Panel on Climate Change (IPCC) assesment report (AR5) (IPCC, 2013), the global surface temperature increased by $0.85 \pm 0.2$ °C during the period comprehended between 1880 and 2012. This change is very likely driven by an unbalance in the Earths radiative budget product of the strong increase in the concentration of greenhouse gases in the atmosphere during the last century. Despite the progress made during the last decades in our understanding and quantification of the Earths radiative budget, big uncertainties associated with the radiative forcing of aerosols, clouds and their interaction still remain. As can be seen in Fig. 1.1, the IPCC estimations presented in the AR5 exhibit the largest uncertainties on the aerosol and precursors section, with values above $\pm 50$ % for the mineral dust and aerosol-cloud interaction contributions.

Along with its role in the Earth's radiative budget, aerosols can also strongly affect the air quality (Kulmala et al., 2011), visibility (Weinzierl et al., 2012) and ecosystems (Baker et al., 2003). Despite the different nature of the processes involved in these fields, their understanding and modeling require an accurate characterization of the aerosols microphysical properties (e.g. size, shape, chemical composition) and spatial distribution, which in turn, is strongly coupled to the atmospheric circulation and dynamic processes.

Atmospheric aerosols are solid or liquid particles suspended in the atmosphere with diameters ranging between tens of nanometers and hundreds of micrometers. While the sources can be classified as anthropogenic and natural, the generation process is cataloged as primary or secondary depending on whether the aerosol was emitted as a particle or resulted from combination of gaseous precursors. The aerosol microphysical properties are widely variable and strongly related with the emission source, which in turn leads to a strong variability in the optical properties, radiative forcing effect and impact in human health. Different aerosol classification schemes based on different sets of properties can be found in the literature. The classification introduced by the AR5 defines five main aerosol types: inorganic species (sulphate, nitrate, ammonia and sea salt), organic species, black carbon (carbonaceous material formed from the incomplete combustion of fossil and biomass fuels), primary biological particles and mineral species (mainly dust).

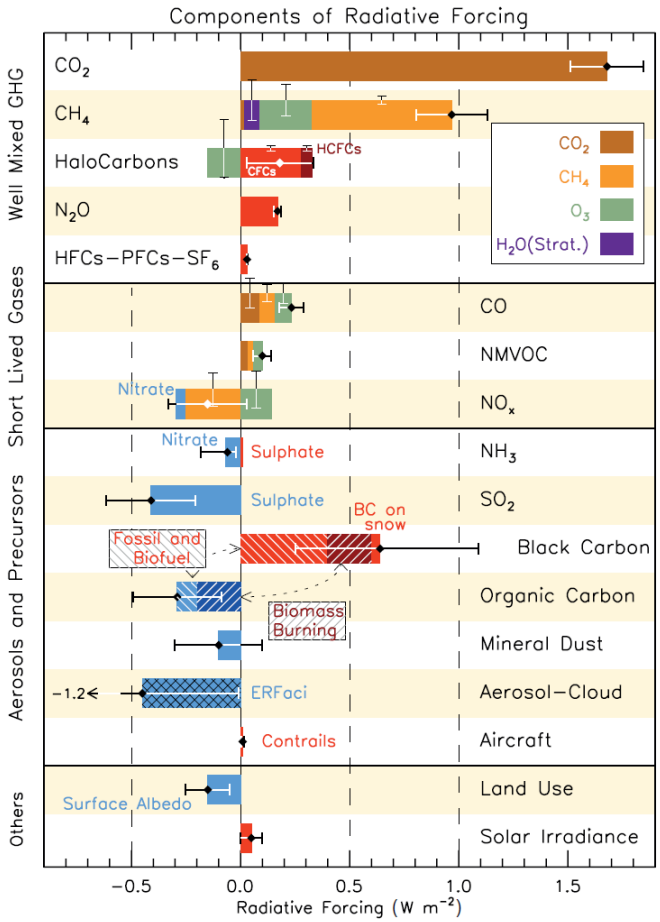


Figure 1.1: Radiative forcing for the period 1750-2011 corresponding to each atmospheric component and associated uncertainties. NMVOC are non-methane volatile organic compounds. ERFaci is ERF due to aerosol-cloud interaction. Reproduced from (IPCC, 2013).

In contrast to greenhouse gases, which introduce a net warming effect, aerosols can either warm or cool the atmosphere and Earth‘s surface depending on their type, vertical and horizontal distribution (Fig. 1.1). In the same way, the impact of aerosols on air quality or visibility is strongly variable and dependent on their composition and concentration. Although some of these factors can be studied separately, for example, by analyzing the aerosol chemical composition of in-situ samples or transport patters by means satellite observations, there is an increasing need to quantify the the effect of feedback processes between atmospheric dynamics, aerosol concentration and microphysical properties.

While large particles with a diameter larger than 20 $\mu$m are expected to settle within a few hours due to the effect of the gravitational force, sub-micron particles can reside in the troposphere for weeks and therefore be subject to long-range transport (Seinfeld and Pandis, 1998). This different vertical speed experienced by aerosols of different sizes and

shapes introduces a link between the transport speed of an air mass and the size distribution of the advected aerosols. Additionally, recent studies indicate that other dynamical processes like convective mixing (Gasteiger et al., 2016) and gravity waves (Chane Ming et al., 2016) can enhance the turbulent mixing, partially counteracting the effects of the size selective deposition. As a result, an accurate estimation of the aerosol mass transported between two regions requires not only the knowledge of the concentration of aerosols in the source and the horizontal wind field between the source and the sink regions, but also a accurate characterization of other dynamical processes (e.g. gravity waves, convection, turbulent mixing). In a similar way, as the advected aerosols interact with the atmosphere, they can undergo a series of physical and chemical transformations known as aging. Aged aerosols can exhibit changes in their optical properties (Groß et al., 2015) and efficiency as cloud condensation nuclei (CCN), adding more complexity to the process. Although simplified, these examples illustrate the need for a comprehensive approach to accurately characterize aerosol processes, and thus provide the base to improve our understanding and modeling capabilities.

## 1.1 Saharan dust

Among aerosols, mineral dust plays a distinctive role. Mineral dust are soil particles suspended in the atmosphere which are typically composed of a mixture of oxides and carbonates. Approximately 30 % of the atmospheric optical depth (AOD) corresponds to airborne dust (Tegen et al., 1997). Most of the Earths dust sources are located in the Northern Hemisphere within what Prospero et al. (2002) named global dust belt, which extends during summer from the West coast of Africa into Central Asia. In the Southern Hemisphere, some relatively week and sparse sources can be identified in Australia and the south of Argentina. Dust emissions can have natural or anthropogenic origin. The relevance of agricultural land use, changes in the surface water and industrial processes (e.g. cement production) in the dust global emissions is still under debate. While some early studies (Tegen and Fung, 1995) indicated that up to half of the total emissions originate from anthropogenically modified soils, some later studies showed a large discrepancy depending on the applied model (Tegen et al., 2004; Mahowald et al., 2004), with values ranging from 10 % to 50 %. These differences in the estimations are likely to arise from the limited accuracy of the available emission data sets (Mahowald et al., 2002).

The Saharan desert, with an area of about 9 million $km^2$, is the largest dust source by surface and emitted mass. While sporadic reports about the influence of the Saharan desert close to the West African coast can be found since the mid $19^{th}$ century (Darwin, 1846), first systematic observations of the Saharan dust long-range transport across the Atlantic date from the late fifties and sixties (e.g. Junge, 1956; Delany et al., 1967; Prospero, 1968). Based on the Barbados Oceanographic and Meteorological Experiment (BOMEX) observations in 1969, Carlson and Prospero (1972) presented a first conceptual model of the Saharan Air Layer (SAL) structure and its relation with the African easterly waves (AEWs). With the Global Atmospheric Research Program Atlantic Tropical Experiment (GATE), new know-

ledge about the radiative characteristics of the SAL was gained (Carlson and Caverly, 1977). GATE observations provided also the opportunity to develop a new three dimensional conceptual model (Karyampudi, 1979) able to combine the different features involved in the long-range transport process. A scheme of this conceptual model is presented in Fig. 1.2, while its main characteristics are discussed in the following paragraphs. On this basis, many validation and additional studies were conducted, including the African Monsoon Multidisciplinary Analyses (AMMA) and Lidar In-space Technology Experiment (LITE), where different aspects of this conceptual model were validated (Karyampudi et al., 1999).

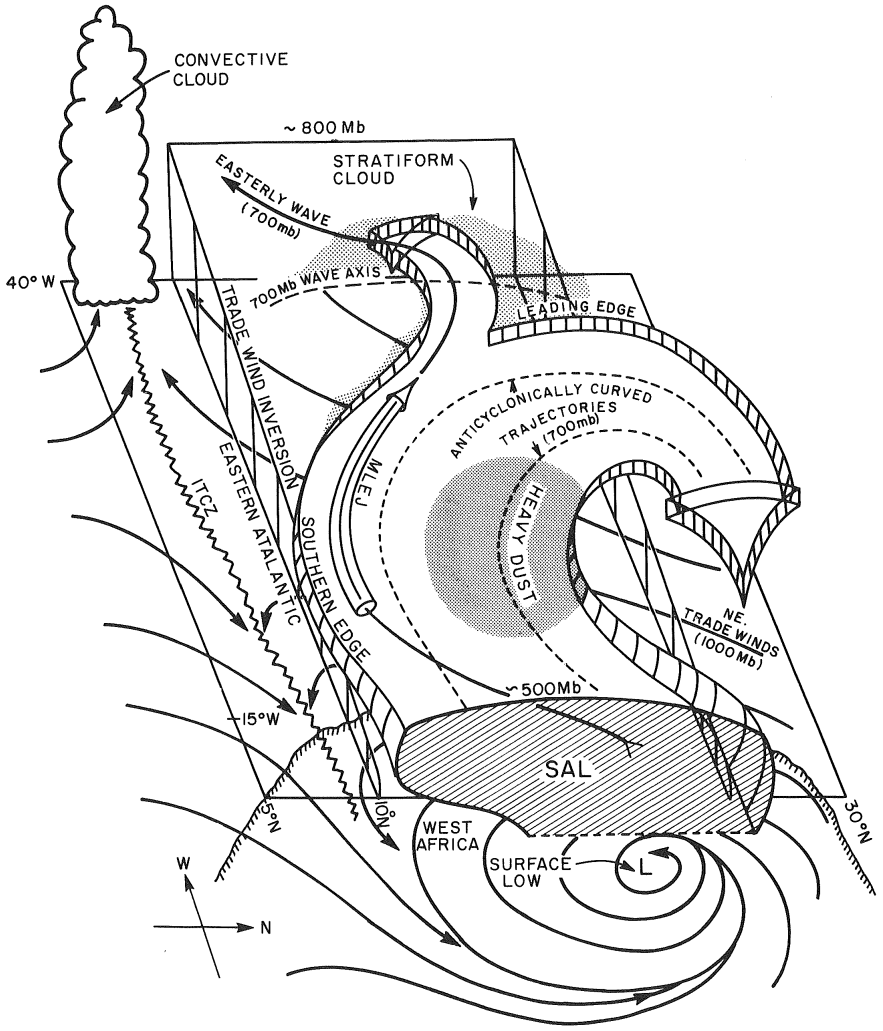


Figure 1.2: Saharan Air Layer conceptual model during summer. Reproduced from Karyampudi (1979).

According to Mahowald et al. (2005), between 50 % and 70 % of the global dust emissions are originated in the Saharan desert, while global model studies situate its annual emissions between 200 Tg and 3000 Tg (Huneeus et al., 2011). The emissions, although

highly variable from day to day, follow a pronounced seasonal pattern linked to the oscillation of the Intertropical Convergence Zone (ITCZ) and African Easterly Jet (AEJ) positions (e.g. Tsamalis et al., 2013). During boreal winter, when the ITCZ and AEJ are in their most southerly position, dust sources located in the southern Sahara and the Sahel region are especially active. The dry northeasterly trade winds, known as Harmattan winds, transport the dust into the Gulf of Guinea, where it meets the biomass burning aerosols coming from equatorial Africa. The dust is then further transported into South America by trade winds in a shallow layer below 1.5-3 km (Schepanski et al., 2009) topped by biomass burning aerosols. As the ITCZ and AEJ move northward during the summer months (Fig. 1.2), the increasement of vegetation and soil humidity limits the emission potential of the Sahel and southern sources at the same time that higher insolation and convective activity enhance the upward mixing of dust in the northern Sahara, reaching altitudes of up to 6 km (Messager et al., 2010). When this dry and warm dust laden air mass is advected towards west and leaves the African continent it is undercut by the moist and relatively cooler trade winds, which leads to the formation of an elevated dust layer lower bounded by a strong inversion at approximately 850 hPa. The SAL is characterized by a quasi-constant potential temperature and water vapor mixing ratio. Close to the African continent, the SAL is topped by a second inversion at approximately 550 hPa (Prospero and Carlson, 1981; Nalli et al., 2005). This inversion results from the higher temperatures exhibited by the SAL compared to the surrounding tropical atmosphere.

The strong moisture and temperature gradient between the Gulf of Guinea and the Saharan Desert leads to the generation of a strong geostrophic wind called AEJ (Cook, 1999). Long term observations of the AEJ (Burpee, 1972) situate the AEJ at latitudes between 5° N and 10° N at an altitude of approximately 3 km. Recorded wind speeds range between 10 and 25 $ms^{-1}$. The AEJ plays a prominent role in the West African and tropical Atlantic weather systems as well as in the Saharan dust long-range transport. Convective activity and barotropic and baroclinic instabilities in the AEJ are usually identified as the main cause for the formation of AEWs (e.g. Wu et al., 2012). These west-propagating disturbances, characterized by a period of between 3-6 days, have been recognized as precursor for the generation of tropical storms (Thorncroft and Hodges, 2001) and as key components in the modulation of the mesoscale convective tropical activity (Janiga and Thorncroft, 2016).

Although there is an ongoing discussion about the nature of the interaction between the AEWs and the Saharan dust, most studies (e.g. Jones et al., 2003; Knippertz and Todd, 2010) indicate a correlation between these waves and the variability observed in the amount of generated and transported dust over North Africa. On the other hand, contradictory results can be found regarding the radiative effect of the Saharan dust on the dynamics and strength of these disturbances. While some studies indicate that the dust strengthens the AEWs (e.g. Jones et al., 2004), others show the opposite effect (e.g. Jury and Santiago, 2010) or an effect dependent on the spatial relationship between the waves and the dust plume (Hosseinpour and Wilcox, 2014).

The interaction of the AEJ with the south edge of the SAL, leads to the advection of dust westwards. As the dust is further transported west, the SAL becomes thinner and its

altitude decreases (Tsamalis et al., 2013). During the long-range transport across the Atlantic, the dust is subject to dry and wet deposition processes which lead to a reduction in the SAL dust concentration. The relative importance of this deposition mechanisms is still under debate and varies according to the location (Prospero et al., 2010; Huneeus et al., 2011), being the wet deposition dominant in the regions close to the ITCZ. Additionally, and according to Maring et al. (2003), the observed change in the Saharan dust size distribution after long-range transport cannot be explained by assuming a Stokes gravitational settling model. Instead, a lower settling velocity has to be assumed, which is compatible with turbulent mixing processes occurring during the transport(Gasteiger et al., 2016; Denjean et al., 2016). Since deposition and mixing processes typically occur in scales not captured by global modes, measurements and high-resolution models are required in order to understand this processes and thus improve their parameterization.

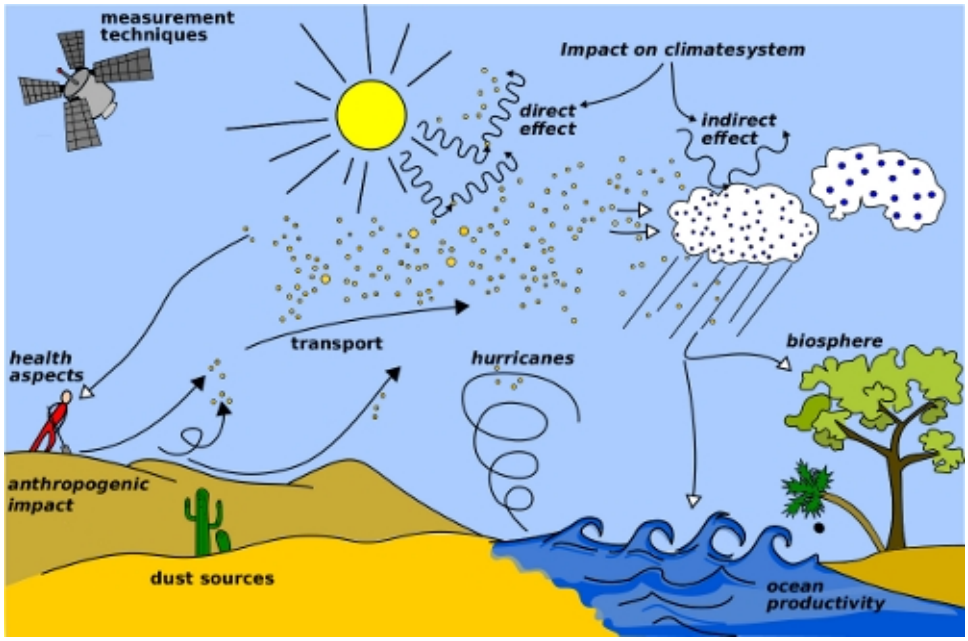


Figure 1.3: Overview of the different dust processes and impacts. Source: World Meteorological Organization - Sand and Dust Storm Warning Advisory and Assessment System

The environmental influence of the dust is not only limited to radiative effects (Fig. 1.3). According to recent estimations (Yu et al., 2015), approximately $28 \pm 20$ Tg of Saharan dust is deposited every year in the Amazon basin. An important part of these emissions originate in the Bodélé depression, located in Chad. This source, a former lake bed, is rich in phosphorus. The deposited dust serves then as source of phosphorus for the rainforest, which is vital for the tree growth process. Along its long range transport, part of the Saharan dust is deposited into the Atlantic Ocean. Recent studies (e.g. Jickells et al., 2005) indicate that the deposited mineral dust, rich in iron, phosphorus and nitrogen, serve as source of nutrients for the development of plankton blooms. Plankton works not only as food for marine life, but also as regulator of the carbon dioxide exchange equilibrium

between atmosphere and oceans.

The impact of the SAL in the tropical cyclogenesis is a long lasting and controversial topic. While first hypothesis (Karyampudi and Carlson, 1988) indicated a positive impact of the SAL in the growth of AEWs into tropical storms, recent studies (e.g. Evan et al., 2006; Lau and Kim, 2007) report more complex interactions between the Saharan dust and the development of tropical storms, with a series of different mechanisms of negative and positive influence. For example, Lau and Kim (2007) argue that the attenuation of the incoming solar radiation reaching the North Atlantic surface in 2006 by an increased dust presence compared to 2005 generated a rapid cooling of the ocean. This situation led to unfavorable conditions for the development of the hurricanes during 2006. Simulation studies presented in Zhang et al. (2009) indicate a complex role of the Saharan dust as CCN in the tropical cyclone evolution. Dust can either weaken or strength the tropical cyclone evolution depending on the age of the hurricane.

Although the interest on the effects of the Saharan dust emissions on the human health and air quality increased during the last decades, our knowledge is still relatively low. Because the dust can be subject of long-range transport, dust affects not only the source region, in West Africa, but also the Mediterranean and the Caribbean regions. Currently available studies, although limited in number and mostly far from the dust source (e.g., Europe and America), indicate a relation between the dust events and an increment in the number of diseases and mortality (Longueville et al., 2012). The mechanisms in which dust affects human health can be catalogued as direct and indirect. Direct effects include respiratory and cardiovascular diseases associated with the inhalation of fine mineral dust. These effects are highly dependent on the particles concentration, size and chemical composition. On the other hand, dust can affect humans indirectly, acting as transport mechanism for pathogens like bacteria, fungus and viruses (Griffin, 2007).

## 1.2 SALTRACE

The Saharan Aerosol Long-range Transport and Aerosol-Cloud-Interaction Experiment (SALTRACE) aircraft field experiment (`http://www.pa.op.dlr.de/saltrace`) conducted between 10 June and 15 July 2013 (Weinzierl et al., in press). It was designed as a closure experiment to address open scientific questions related to the Saharan dust-long range transport. The experiment combined ground-based, airborne, and satellite observations together with models and long-term observations in order to provide new insights into the long-range transport mechanisms, the aging processes that affects the dust in its travel across the Atlantic and its interaction with clouds. SALTRACE was a German initiative, with the participation of institutions and scientist from different countries, including Germany, Spain, France, Cape Verde, Barbados, Puerto Rico and the USA. This international effort is framed in the context of previous studies conducted during the first Saharan Mineral Dust Experiment (SAMUM-1) in 2006 (Heintzenberg, 2009) and second Saharan Mineral Dust Experiment (SAMUM-2) in 2008 (Ansmann et al., 2011) campaigns, which focused on the characterization of the Saharan dust in the African West coast, close to the

emission source. Shortly before SALTRACE, during the period comprehended between 29 April and 23 May 2013, a 1-month transatlantic cruise was carried out by the Meteor research vessel. The cruise started at 60° W and ended at 20°W, close to the west coast of Africa. During this travel, the SAL dust vertical distribution was measured by a combination of instruments, including a shipborne lidar (Kanitz et al., 2014). Between 15 February and 8 March 2014 (SALTRACE-2), ground-based lidar measurements were conducted in order to characterize the optical properties and vertical distribution of the dust-smoke mixture arriving Barbados during winter time. Then, between 19 June and 12 July 2014 (SALTRACE-3), measurements under conditions similar to those corresponding to SALTRACE were carried out in order to investigate the inter-annual variability of the dust properties and distribution.

The main SALTRACE ground-based observation site was located in Barbados. Since Barbados is the easternmost island in the Caribbean, the long-range transported dust can be studied before being affected by other natural or anthropocentric emissions. Additionally, the availability of a 50-year Saharan dust long-term record (Prospero et al., 2014) allows to situate the SALTRACE measurement period in the context of the year to year dust variability. Measurements at Barbados were performed in two different locations. At the campus of the Caribbean Institute of Meteorology and Hydrology (CIMH) (13.14° N, 59.62° W), the ground-based aerosol Portable Lidar System (POLIS) (Groß et al., 2015; Freudenthaler et al., 2015) and backscatter extinction lidar-ratio temperature humidity profiling apparatus (BERTHA) (Haarig et al., 2015) were deployed together with sun-photometers. On the east coast of Barbados, at Ragged Point Station (13.16° N, 59.44° W), a sun-photometer and several instruments for in-situ measurements were installed in order to characterize the dust microphysical and optical properties after the long-range transport process and before being influenced by the Barbados island emissions. Additional measurements where conducted in Cabo Verde, close to the dust source, and Puerto Rico.

Together with the ground-based observations, airborne measurements were performed by the Deutsches Zentrum für Luft- und Raumfahrt (DLR) Falcon 20 research aircraft. The aircraft was equipped with a coherent Doppler wind lidar (DWL), a dropsonde launcher and a set of in-situ instruments for the retrieval of microphysical and optical properties, as well as samplers to conduct further on-ground particle analysis. A list of SALTRACE instruments and datasets used in this study is presented in Appendix A.

During the campaign, a total of 31 research flights where performed, with most of them conducted close to the West coast of Africa and in the Caribbean region. An overview of the SALTRACE flight patterns and ground-based observation sites is presented in Fig. 1.4. During the observation period comprehended between 10 June and 15 July five dust outbreaks and the passage of the tropical storm Chantal were observed. The DWL deployed on-board the Falcon carried out 75 hours of measurements, providing first-time simultaneous extinction and wind measurements corresponding to different features associated with the West African climate system and the Saharan dust long-range transport process.

The wind observations corresponding to flights conducted close to the west Africa coast will allow a better characterization of the AEJ, the AEWs and their interaction. Since

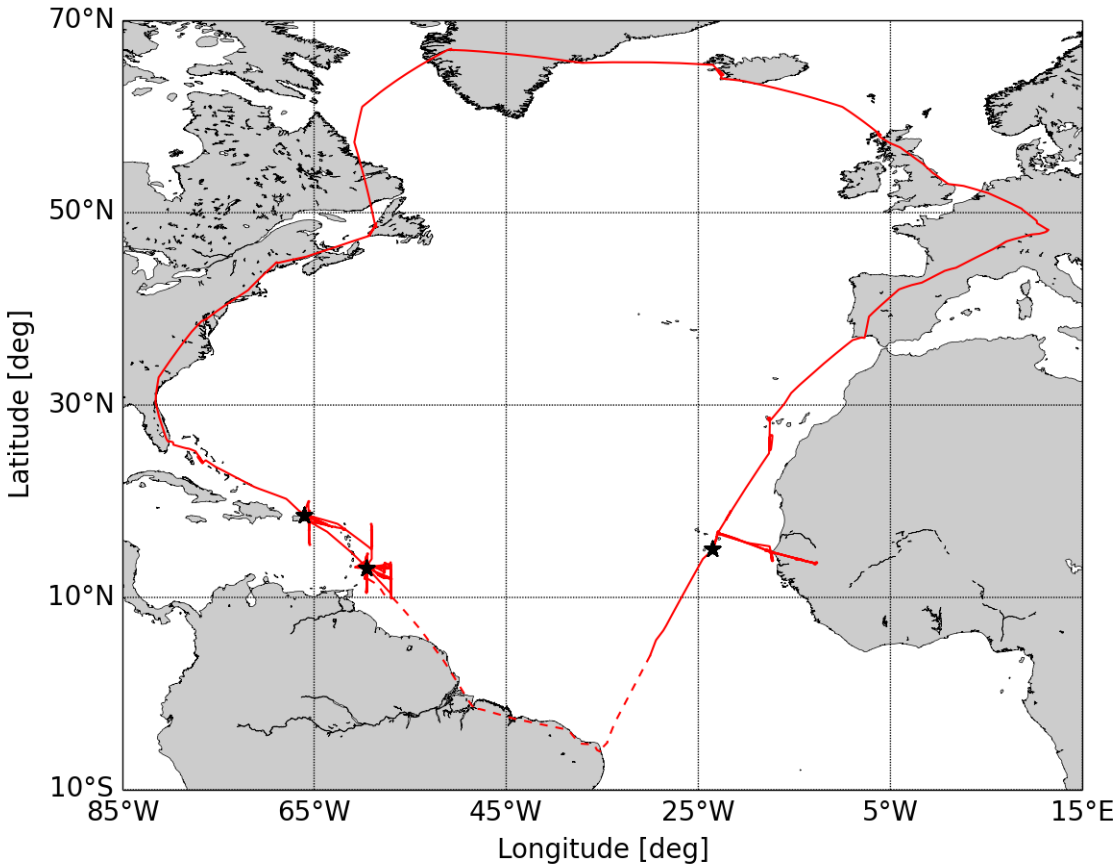


Figure 1.4: SALTRACE flight tracks (red) and ground based observation sites (black stars). No data is available in the flight sections indicated with a dashed line.

simultaneous wind and extinction coefficient measurements are rare, the measurements retrieved from the DWL during SALTRACE provide valuable information for the analysis of wind-dust interactions as well as for the evaluation of regional and global aerosol models. The airborne vertical wind measurements conducted in the Cabo Verde region and on the lee side of Barbados will allow to continue the island effect investigations started during SAMUM-2 (Engelmann et al., 2011). High resolution vertical wind measurements are used in this study, in combination with Large Eddy Simulations (LES), to analyze the possibility of island-induced enhanced dust deposition and the generation of gravity waves.

Along with the presented DWL measurements, a whole set of in-situ meteorological and aerosol measurements were carried out by the Falcon during SALTRACE. In-situ wind measurements, although not spatially coincident with the DWL measurements and only limited to one dimension, allow an independent verification of the vertical wind retrievals from the lidar. On the other hand, in-situ aerosol sampling of the SAL close to Africa and

in the Caribbean are used, in the frame of a Lagrangian experiment, to investigate the aging process that affects the dust during the transport process.

## 1.3 State of the art and objectives

During the last two decades, the number of scientific articles on Saharan dust showed an exponential growth (Knippertz and Stuut, 2014). This growth rate, way above the duplication per decade observed as average, can be explained by the concurrence of different factors. As mentioned before, the largest uncertainties in our estimation of the Earth radiative forcing corresponds to atmospheric aerosols and their interaction with clouds. Given the increasing relevance of climate change, it is then expected to see an increasing interest in aerosols in general and mineral dust in particular. On the other hand, the development of remote sensing techniques and instruments during last decades, including several spaceborne instruments, allowed to collect data over dust source and transport regions on which in-situ measurements are difficult. Finally, a third factor which can contribute to explain the increasing interest in Saharan dust is the rapid development of atmospheric models, mainly driven by an increasing available computing power.

The comparison of the model results with long and short term measurement campaigns is then of vital importance to evaluate the existing models. The Aerosol Comparison between Observations and Models (AeroCom) (`http://aerocom.met.no/`) initiative is an international effort oriented to investigate the current global aerosol modelling capabilities by means of comparison between models and also between models and different datasets (e.g. satellite, sun-photometers). The results of AeroCom Phase I (Textor et al., 2006; Huneeus et al., 2011), indicate that although models were able to reproduce general transatlantic dust transport patterns, strong discrepancies in dust emission, vertical distribution and particle size distribution were observed. As part of the AeroCom Phase II, the Saharan dust transatlantic transport simulated by five different models was compared with a set of satellite and ground based instruments, including AOD measurements from the Moderate Resolution Imaging Spectroradiometer (MODIS) and the Aerosol Robotic Network (AERONET), and aerosol vertical distribution retrieved by the Cloud-Aerosol Lidar and Infrared Pathfinder Satellite Observations (CALIPSO) (Kim et al., 2014). The comparison of the AOD results shows differences between models and measurements ranging from an underestimation of 400 % to an overestimation of 200 % (Fig. 1.5). Dust optical depth (DOD) gradients indicate a model overestimation of the dust removal along the long-range transport. The shape of the modeled dust vertical profiles over Africa decrease with altitude much faster than the corresponding Cloud-Aerosol Lidar with Orthogonal Polarization (CALIOP) profiles, while over the western Atlantic, the modeled aerosol plume show a higher vertical dispersion than the measured one.

In spite of the progress made during last years in our understanding of the Saharan dust life cycle, many questions remain open. While models are able to reproduce general transport patterns, the modeled amount of emissions, deposition and transported dust, the vertical distribution and the dust optical and micro-physical properties is not adequately

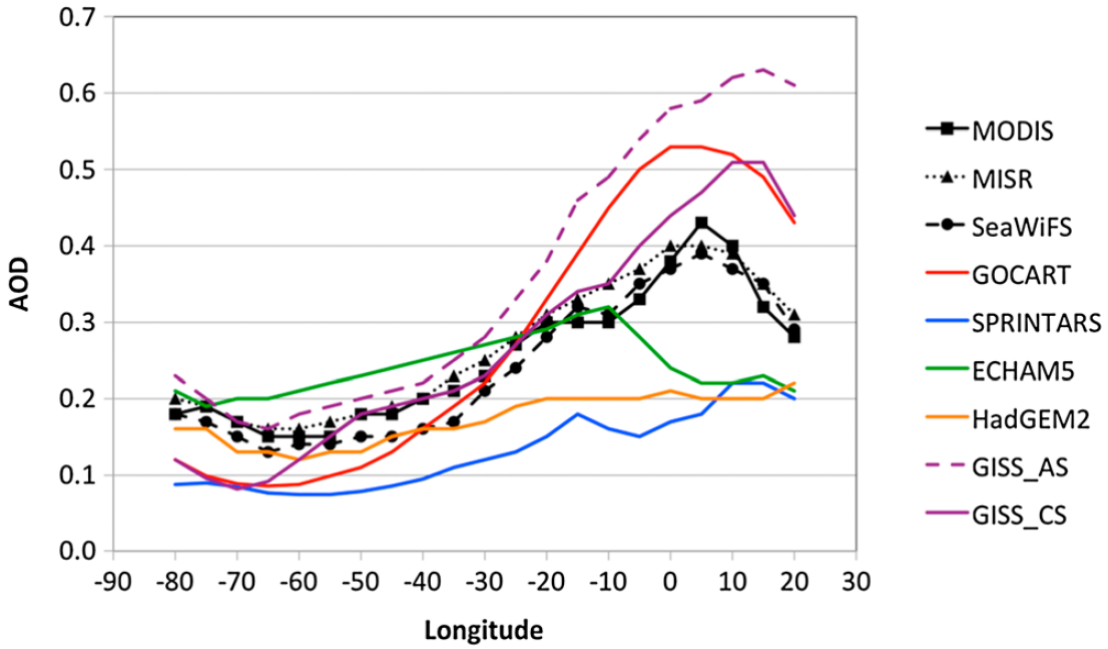


Figure 1.5: Mean AOD from satellites (black) and models averaged in 5° longitude intervals between 0° and 35° N. Reproduced with permission from John Wiley & Sons (Kim et al., 2014).

captured. This limitations result in large uncertainties associated with the Saharan dust radiative forcing and its impact in air quality (Huneeus et al., 2016) and ecosystems (Schulz et al., 2012). The improvement of current models require not only a better characterization of the Saharan dust microphysical and its associated radiative effects, but also a more accurate understanding and quantification of the dynamical processes affecting it along the long-range transport process.

Although satellite remote sensing measurements greatly contributed to our understanding of the dust transport and its properties, measurement campaigns are required to fill gaps in our knowledge and reduce the uncertainties of properties derived from satellite measurements, usually higher than those corresponding to in-situ retrievals. In this work, DWL measurements carried out during SALTRACE are used to investigate different aspects and scales of Saharan dust transport and evaluate the capabilities of state of the art numerical models to reproduce them. Novel methods to extend the actual capabilities of the DWL are also discussed in the frame of this investigations. Among others, this work will address the following scientific questions:

- Is it possible to retrieve backscatter and extinction coefficients from DWL measurements?
- What methods can be applied to reduce the systematic errors associated with the retrieval of vertical winds from an airborne DWL?

- How do island induced gravity waves and turbulence interact with the SAL? Are LESs including passive tracers (e.g. All-Scale Atmospheric Model (ASAM)) able to reproduce these features and interactions?
- What are the current capabilities of the global models (e.g. Monitoring Atmospheric Composition and Climate (MACC)) to reproduce the Saharan dust long-range transport and its associated features?

This cumulative thesis is organized as follows. In Chapter 2, an overview of the newly developed and validated methods during this thesis is presented. This includes a brief resume of the DLR DWL characteristics and limitations, as well as a description of the LES and global aerosol models. Chapter 3 presents the abstracts of the publications included in this cumulative thesis and a description of the contribution of each author to each publication. Finally, Chapter 4 presents a summary of the results obtained in this study together with ideas for future work and system improvements.

# Chapter 2

# Methods

First studies of the Saharan dust long-range transport were conducted based on measurements from a ground-based two-stage cascade impactor located in Florida (Junge, 1956). Subsequent airborne measurements, like the ones performed during BOMEX in 1968, revealed valuable information about the dust transport and the SAL vertical structure based on the combination of in-situ dust sampling, Radon-222 measurements, and meteorological soundings. With the rapid evolution of satellite remote sensing and modeling techniques during the last decades, a whole new set of observations and model results became available to the scientific community. This relatively new techniques, characterized by their large spatial and temporal coverage, provide a context to campaign observations, usually limited in space and time. On the other hand, campaigns provide extensive data sets which are then used to validate satellite measurements and model results. This synergistic approach, applied during many campaigns in recent years, helped to improve our understanding of the processes behind the Saharan dust transport as well as our ability to model and predict them.

SALTRACE was based on this multi-methodical approach. Ground-based and airborne measurements were used, in combination with satellite observations and models, to provide further insights into the Saharan dust transport, deposition and its interaction with clouds. Although this study focuses on the measurements preformed by the DLR DWL and the modeling results provided by the ASAM and the MACC model, additional measurements from the MODIS and CALIPSO satellites, ground-based lidars, sun photometers and in-situ aerosol measurements were also part of this study.

## 2.1 Doppler wind lidar

A few years after the invention of the laser, first lidar (light detection and ranging) measurements were reported (Fiocco and Smullin, 1963). Since then, driven by the rapid evolution of lasers and detectors, lidars have gained relevance in atmospheric studies. Currently, lidars are regularly used to observe many different atmospheric parameters, including but not limited to, aerosol optical properties, trace gases and water vapor mixing ratio, tem-

perature and wind speed, being aerosol lidars the most common type.

First wind observations based on lidar technique were reported by Huffaker (1970). The system, constructed around a 10.6 $\mu$m $CO_2$ laser, relied on the Doppler effect and the heterodyne detection technique to measure the corresponding frequency change. Two years later, Benedetti-Michelangeli et al. (1972) developed the fundamentals of the direct-detection technique. While heterodyne detection is based on the frequency mixing products of the backscattered photons and a reference oscillator, the direct-detection technique typically uses an interferometer to determine the induced frequency change in the backscattered laser radiation by the Doppler effect. Although other measurement techniques based on aerosol lidars and correlation techniques were reported (e.g. Mayor et al., 2016), Doppler-based wind lidars are by far the most usual ones.

The development of the DWL technique started at DLR in the 1980s, being the first DWL constructed based on a 10.6 $\mu$m $CO_2$ continuous-wave (CW) laser and the coherent technique for boundary layer studies (Köpp et al., 1984). One decade later, first airborne DWL measurements were conducted at DLR (Rahm, 1995). As in the previous case, the systems operated based on a CW laser, which limited the vertical resolution of the system. This early research laid the groundwork for the French-German project Wind Infrared Doppler Lidar (WIND), the first airborne DWL able to retrieve wind profiles from ground up to the flying altitude (Werner et al., 2001; Reitebuch et al., 2001). After the successful experience of WIND and supported by the rapid development of solid-state and fiber laser sources, a second generation of DWLs were developed at DLR. These new systems, much more compact and working at wavelengths between 1.6 $\mu$m and 2 $\mu$m, are equipped with a double-wedge scanner. This type of scanners allow the generation of arbitrary pointing patterns, including regular conical scans for horizontal wind retrieval, nadir pointing for vertical wind measurements and linear scans for wake-vortices analysis (Köpp et al., 2004).

Since the study of dust transport would ideally require the knowledge of the aerosol distribution and optical properties as well as the three-dimensional wind fields, it is worth to study the possibility of simultaneous retrieval of these two quantities based on DWL measurements. Nevertheless, because the DWL system involved in the SALTRACE campaign was not originally designed for this propose, a series of issues had to be addressed. While aerosol lidars usually operate at wavelengths below 1 $\mu$m, coherent DWL operate at wavelengths above 1.5 $\mu$m in order to be eye-safe, minimize the impact of the background solar radiation and the broadband molecular backscatter. As side effect, the operation at wavelengths above 1.5 $\mu$m limit the possibility of using the molecular backscatter as reference for the system calibration as is regularly done with aerosol lidars. Additionally, since the retrieval of wind speed does not require quantitative information about the received or transmitted laser power, no direct measurement of the transmitted laser pulse energy is performed by the system and the receiving amplifier and detector system does not have a flat gain as a function of the heterodyne signal frequency, which leads to a change in the measured signal intensity as a function of the measured wind speed. Furthermore, because only one polarization component is measured by the system, the backscatter corresponding to different aerosols will suffer different levels of attenuation depending on the aerosol optical properties. This lack of quantitative aerosol measurements from the DWL was

already noted during the Eyjafjalla volcanic ash flights in 2010 (Schumann et al., 2011).

As part of SALTRACE, two aerosol lidars and four sun-photometers were deployed at Barbados. Based on overflights performed by the DLR Falcon over these ground-based systems and a novel calibration procedure presented in this work, quantitative aerosol backscatter and extinction coefficients were retrived from the DLR 2 $\mu$m DWL. This retrievals are then used, in combination with simulations and simultaneous vertical and horizontal wind retrievals, to study different dust transport processes ranging from small scale island-induced gravity wave disturbances to large scale transport patterns. In the case of small scale features like the gravity waves observed during SALTRACE, the vertical wind measurements retrieved from the DWL operating in scanning mode were not able to capture them since their resolution is comparable to the wavelength of the observed waves. For this reason, a set of measurements with the lidar operating in nadir-pointing mode were carried out. This measurement mode allow to retrieve high spatial resolution profiles of vertical wind speed. Nevertheless, since the vertical wind speeds are relatively low compared to the aircraft speed and the horizontal wind speed, careful corrections have to be implemented in order to minimize the retrieval systematic errors. A series of improvements introduced in the vertical wind retrieval scheme are discussed as part of this study.

## 2.2 Global aerosol models

Global aerosol models are a key component for the study of the weather and climate, and their ability to reproduce our observations, an indicator of our actual understanding of the aerosols lifecycle. Atmospheric composition models can be used for long-term climate forecasting, near real-time analysis and forecasting, as well as for the generation of reanalysis datasets. Long-term forecasts are a very valuable tool for the study of climate change and the associated modifications in the aerosol emissions and spatial distribution. Nevertheless, due to the inherent lack of evaluation datasets, the models used for long-term climate predictions have to be first tested based on short term and reanalysis studies. On the other hand, near real-time aerosol forecasts can profit from current data assimilation systems to generate short-term forecasts, which allow to take appropriate measures to reduce the impact of aerosol events in human health, air quality and visibility. Finally, data assimilation techniques are used in combination with atmospheric models to generate consistent reanalysis of the climate system, which describe the recent history of the atmosphere, land surface, and oceans. This reanalysis can be then used for climate change investigations and model evaluation studies.

A broad set of modeling activities, including the development of atmospheric composition models, are currently being conducted at DLR (Hendricks et al., 2012). A special emphasis is given to the perturbations induced by the transport sector, including their influence in the clouds lifecycle, radiation and climate. As part of this study, the SALTRACE dataset is used to evaluate the MACC model (Morcrette et al., 2009). The MACC model is the result of an international effort conducted in the frame of the Global Monitoring

for Environment and Security (GMES) initiative (now Copernicus) and developed at the European Centre for Medium-Range Weather Forecasts (ECMWF). This initiative, oriented to improve our understanding of the environment and climate change, includes the development of a global atmospheric composition model able to provide global distributions of greenhouse gases, reactive gases and aerosols through assimilations of satellite and in-situ observations (Benedetti et al., 2009). While model intercomparison studies like the ones conducted in the frame of AeroCom provide a first guess of the model capabilities, measurements campaigns and comparisons with long-term observations allow a much more accurate estimation of the model skills. Recent comparison studies conducted over Europe (Mangold et al., 2011) and the North Africa and Middle East Regions (Cuevas et al., 2015) provided a first insight into model strengths and weaknesses. A general good reproduction of the dust seasonality and horizontal distribution was observed, while the vertical aerosol distribution showed higher differences. This is expected due to the assimilation of the MODIS AOD observations, which only constrains the total vertically integrated aerosol quantity. Current efforts are being conducted in order to assimilate CALIPSO attenuated backscatter profiles, nevertheless this is not yet operational (MACC-III, 2016).

Systematic observations of the SAL vertical structure on the West coast of Africa and the north Atlantic Ocean are only available from the CALIPSO satellite. On the other hand, regular wind measurements are limited to commercial aircraft corridors. The SALTRACE dataset, although constrained to a relative short time period, provides a unique opportunity to evaluate the ability of models to reproduce the Saharan dust long-range transport process. The simultaneous measurement of aerosol backscatter and wind vector vertical profiles carried out by the DLR airborne DWL opens the possibility to study the vertical dust distribution and winds not only separately, but in combination with their interactions.

## 2.3 Large eddy simulations

Due to limitations in current computing power, global models rely on parameterizations to represent the influence of sub-grid processes like clouds formation and turbulent fluxes. The development of accurate parameterizations is a though task, which require systematic measurements and, in many cases, the use of numerical models with fine grid scales able to reproduce the influence of turbulent movement. Since atmospheric turbulence spans over scales going from millimeters to kilometers, its resolution by means of Direct Numerical Simulations (DNSs) is beyond our current computing capabilities. The LES technique is a compromise between DNS and turbulence parameterization. In LESs, only large eddies are numerically resolved, while the smaller ones are treated by means of subgrid scale (SGS) modeling. This treatment is justified by the fact that large scale eddies contain most of the energy and are more dependent on the source of instability than the smaller ones. Which part of the inertial turbulence sub-range is resolved numerically and which modeled is determined by the LES low-pass filter cut-off, which in turn depends on the model spatial grid.

The ASAM (`http://asam.tropos.de/`) is a numerical simulation tool developed by the Leibniz Institute for Tropospheric Research (TROPOS). Originally developed as computational fluid dynamics (CFD) simulation around buildings, the ASAM evolved into an atmospheric model able to perform simulations ranging from micro-scale effects in urban environment to island effects in trade wind regimes. Obstacles and island orography can be included in the model by a cut cell approach (Jähn et al., 2015). As part of SAMUM-2, a variant of the ASAM model designed to run on Graphical Processing Units (GPUs), the ASAMgpu, was used to investigate the heat island effect in the Cabo Verde region and analyze its impact in the dust downward mixing. Although the simulations were conducted without taking into account the island orography, the comparisons with a ground-based DWL deployed on Santiago island showed a good agreement (Engelmann et al., 2011).

As part of SALTRACE, an ASAM simulation of the Barbados island was setup and run in order to investigate the modification of the boundary layer structure, the development of cloud street and the vertical mixing of Saharan dust (Jähn et al., 2016), as well as the generation of gravity waves. Additionally, high spatial resolution vertical wind measurements derived from the DLR DWL were used to validate the model results and investigate the relation between the island induced gravity waves and the Saharan dust.

# Chapter 3

# Results

This thesis consist of three first-author publications and two co-authored publications. The abstracts of these publications are presented in this chapter. The full reprint of the papers I to IV are presented in Appendix B. Due to copyright constraints, a reprint of Paper V is not included. Its abstract, DOI and URL is provided in Section 3.5.

## 3.1 Paper I: Chouza et al. (2015) - Retrieval of aerosol backscatter and extinction from airborne coherent Doppler wind lidar measurements

F. Chouza[1], O. Reitebuch[1], S. Groß[1], S. Rahm[1], V. Freudenthaler[2], C. Toledano[3], and B. Weinzierl[1,2]

1. Deutsches Zentrum für Luft- und Raumfahrt (DLR), Institut für Physik der Atmosphäre, Oberpfaffenhofen, Germany
2. Ludwig-Maximilians-Universität Mnchen (LMU), Meteorologisches Institut, München, Germany
3. University of Valladolid, Atmospheric Optics Group, Valladolid, Spain

A novel method for calibration and quantitative aerosol optical property retrieval from Doppler wind lidars (DWLs) is presented in this work. Due to the strong wavelength dependence of the atmospheric molecular backscatter and the low sensitivity of the coherent DWLs to spectrally broad signals, calibration methods for aerosol lidars cannot be applied to coherent DWLs usually operating at wavelengths between 1.5 and 2 $\mu$m. Instead, concurrent measurements of an airborne DWL at 2 $\mu$m and the POLIS ground-based aerosol lidar at 532 nm are used in this work, in combination with sun photometer measurements, for the calibration and retrieval of aerosol backscatter and extinction profiles at 532 nm.

The proposed method was applied to measurements from the SALTRACE experiment in June-July 2013, which aimed at quantifying the aerosol transport and change in aerosol

properties from the Sahara desert to the Caribbean. The retrieved backscatter and extinction coefficient profiles from the airborne DWL are within 20 % of POLIS aerosol lidar and CALIPSO satellite measurements. Thus the proposed method extends the capabilities of coherent DWLs to measure profiles of the horizontal and vertical wind towards aerosol backscatter and extinction profiles, which is of high benefit for aerosol transport studies.

## 3.2 Paper II: Chouza et al. (2016a) - Vertical wind retrieved by airborne lidar and analysis of island induced gravity waves in combination with numerical models and in situ particle measurements

F. Chouza[1], O. Reitebuch[1], M. Jähn[2], S. Rahm[1], and B. Weinzierl[1,3]

1. Deutsches Zentrum für Luft- und Raumfahrt (DLR), Institut für Physik der Atmosphäre, Oberpfaffenhofen, Germany

2. Leibniz Institute for Tropospheric Research, Leipzig, Germany

3. University of Vienna, Faculty of Physics, Boltzmanngasse 5, 1090 Wien, Austria

This study presents the analysis of island induced gravity waves observed by an airborne Doppler wind lidar (DWL) during SALTRACE. First, the instrumental corrections required for the retrieval of high spatial resolution vertical wind measurements from an airborne DWL are presented and the measurement accuracy estimated by means of two different methods. The estimated systematic error is below 0.05 m $s^{-1}$ for the selected case of study, while the random error lies between 0.1 and 0.16 m $s^{-1}$ depending on the estimation method.

Then, the presented method is applied to two measurement flights during which the presence of island induced gravity waves was detected. The first case corresponds to a research flight conducted on 17 June 2013 in the Cabo Verde islands region, while the second case corresponds to a measurement flight on 26 June 2013 in the Barbados region. The presence of trapped lee waves predicted by the calculated Scorer parameter profiles was confirmed by the lidar and in situ observations. The DWL measurements are used in combination with in situ wind and particle number density measurements, large-eddy simulations (LES), and wavelet analysis to determine the main characteristics of the observed island induced trapped waves.

## 3.3 Paper III: Chouza et al. (2016b) - Saharan dust long-range transport across the Atlantic studied by an airborne Doppler lidar and the MACC model

F. Chouza[1], O. Reitebuch[1], A. Benedetti[2], and B. Weinzierl[3]

1. Deutsches Zentrum für Luft- und Raumfahrt (DLR), Institut für Physik der Atmosphäre, Oberpfaffenhofen, Germany

2. European Centre for Medium-Range Weather Forecasts, Reading, UK

3. University of Vienna, Faculty of Physics, Boltzmanngasse 5, 1090 Wien, Austria

A huge amount of dust is transported every year from North Africa into the Caribbean region. This paper presents an investigation of this long-range transport process based on measurements conducted during the SALTRACE campaign (June-July 2013), as well as an evaluation of the ability of the MACC global aerosol model to reproduce it and its associated features. First, the horizontal wind speed measurements obtained by the DLR airborne Doppler wind lidar (DWL) during the SALTRACE experiment are validated by means of a comparison with collocated dropsondes. The comparison indicates a systematic speed difference of 0.08 m $s^{-1}$ and a standard deviation of 0.92 m $s^{-1}$, while wind direction show a mean difference of 0.5° and a standard deviation between 5° and 10° depending on measurement conditions. Modelled winds in West Africa and Caribbean regions are compared to those measured by the DWL. Although a general good agreement between measurements and model is observed, some differences, particularly in the African Easterly Jet (AEJ) intensity, were noted. The observed differences between modelled and measured wind jet speeds are between 5 and 10 m $s^{-1}$. The MACC model aerosol vertical distribution is compared with the CALIOP satellite extinction profiles corresponding to the campaign period. While the modelled Saharan dust plume shape shows a good agreement with the measurements, a systematic underestimation of the marine boundary layer extinction is observed.

Additionally, three selected case studies covering different aspects of the Saharan dust long-range transport along the West African coast, over the North Atlantic Ocean and the Caribbean are presented. For first time, DWL measurements are used to investigate the Saharan dust long-range transport. Simultaneous wind and backscatter measurements from the DWL are used, in combination with the MACC model, to analyse different features associated with the long-range transport, including an African Easterly Wave trough, the African Easterly Jet and the Intertropical Convergence Zone.

## 3.4 Paper IV: Jähn et al. (2016) - Investigations of boundary layer structure, cloud characteristics and vertical mixing of aerosols at Barbados with large eddy simulations

M. Jähn[1], D. Muñoz-Esparza[2], F. Chouza[3], O. Reitebuch[3], O. Knoth[1], M. Haarig[1], and A. Ansmann[1]

1. Leibniz Institute for Tropospheric Research, Leipzig, Germany
2. Earth and Environmental Sciences Division (EES-16), Los Alamos National Laboratory, P.O. Box 1663, Los Alamos, New Mexico 87545, USA
3. Deutsches Zentrum für Luft- und Raumfahrt (DLR), Institut für Physik der Atmosphäre, Oberpfaffenhofen, Germany

Large eddy simulations (LESs) are performed for the area of the Caribbean island Barbados to investigate island effects on boundary layer modification, cloud generation and vertical mixing of aerosols. Due to the presence of a topographically structured island surface in the domain center, the model setup has to be designed with open lateral boundaries. In order to generate inflow turbulence consistent with the upstream marine boundary layer forcing, we use the cell perturbation method based on finite amplitude potential temperature perturbations. In this work, this method is for the first time tested and validated for moist boundary layer simulations with open lateral boundary conditions. Observational data obtained from the SALTRACE field campaign is used for both model initialization and a comparison with Doppler wind and Raman lidar data. Several numerical sensitivity tests are carried out to demonstrate the problems related to "gray zone modeling" when using coarser spatial grid spacings beyond the inertial subrange of three-dimensional turbulence or when the turbulent marine boundary layer flow is replaced by laminar winds. Especially cloud properties in the downwind area west of Barbados are markedly affected in these kinds of simulations. Results of an additional simulation with a strong trade-wind inversion reveal its effect on cloud layer depth and location. Saharan dust layers that reach Barbados via long-range transport over the North Atlantic are included as passive tracers in the model. Effects of layer thinning, subsidence and turbulent downward transport near the layer bottom at $z \approx 1800$ m become apparent. The exact position of these layers and strength of downward mixing is found to be mainly controlled atmospheric stability (especially inversion strength) and wind shear. Comparisons of LES model output with wind lidar data show similarities in the downwind vertical wind structure. Additionally, the model results accurately reproduce the development of the daytime convective boundary layer measured by the Raman lidar.

## 3.5 Paper V: Weinzierl et al. (in press) - The Saharan Aerosol Long-range TRansport and Aerosol-Cloud-Interaction Experiment (SALTRACE): overview and selected highlights

B. Weinzierl[1,2], A. Ansmann[3], J. M. Prospero[4], D. Althausen[3], N. Benker[7], F. Chouza[1], M. Dollner[2,5], D. Farrell[6], W. K. Fomba[3], V. Freudenthaler[5], J. Gasteiger[2,5], S. Groß[1], M. Haarig[3], B. Heinold[3], K. Kandler[7], T. B. Kristensen[3], O. L. Mayol-Bracero[8], T. Müller[3], O. Reitebuch[1], D. Sauer[1], A. Schäfler[1], K. Schepanski[3], A. Spanu[2,1], I. Tegen[3], C. Toledano[9], A. Walser[5,1]

1. Deutsches Zentrum für Luft- und Raumfahrt (DLR), Institut für Physik der Atmosphäre, Oberpfaffenhofen, Germany
2. University of Vienna, Aerosol Physics and Environmental Physics, Wien, Austria
3. Leibniz Institute for Tropospheric Research, Leipzig, Germany
4. University of Miami, Miami, USA
5. Meteorologisches Institut (MIM), Ludwig-Maximilians-Universität, München, Germany
6. Caribbean Institute for Meteorology and Hydrology (CIMH), Bridgetown, Barbados
7. Technische Universität Darmstadt, Institut für Angewandte Geowissenschaften, Darmstadt, Germany
8. University of Puerto Rico, Department of Environmental Science, San Juan, USA
9. Universidad de Valladolid, Grupo de Óptica Atmosférica, Valladolid, Spain

North Africa is the world's largest source of dust, a large part of which is transported across the Atlantic to the Caribbean and beyond where it can impact radiation and clouds. Many aspects of this transport and its climate effects remain speculative. The Saharan Aerosol Long-range Transport and Aerosol-Cloud-Interaction Experiment (SALTRACE: http://www.pa.op.dlr.de/saltrace) linked ground-based and airborne measurements with remote-sensing and modeling techniques to address these issues in a program that took place in 2013-2014. Specific objectives were: to (1) characterize the chemical, microphysical and optical properties of aged dust in the Caribbean, (2) quantify the impact of physical and chemical changes ("aging") on the radiation budget and cloud-microphysical processes, (3) investigate the meteorological context of trans-Atlantic dust transport, and (4) assess the roles of removal processes during transport.

SALTRACE was a German-led initiative involving scientists from Europe, Cabo Verde, the Caribbean and the US. The Falcon research aircraft of the Deutsches Zentrum für Luft- und Raumfahrt (DLR), equipped with a comprehensive aerosol and wind-lidar payload, played a central role. Several major dust outbreaks were studied with 86 hours of flight time

under different conditions making it by far the most extensive investigation on long-range transported dust ever made.

This article presents an overview of SALTRACE and highlight selected results including data from trans-Atlantic flights in coherent air masses separated by more than 4,000 km distance that enabled measurements of transport effects on dust properties.

SALTRACE will improve our knowledge on the role of mineral dust in the climate system and provide data for studies on dust interactions with clouds, radiation and health.

The full text of this publication can be found at:
`http://journals.ametsoc.org/doi/abs/10.1175/BAMS-D-15-00142.1`

## 3.6 Contribution of the author

The publications presented in this cumulative thesis (Chouza et al., 2015, 2016a,b) were written by myself with specific contributions and comments from the co-authors. All figures included in these publications were prepared by myself.

In Chouza et al. (2015), I developed, implemented and evaluated the instrumental corrections and the method to retrieve calibrated backscatter from the DWL based on the datasets provided by Dr. Rahm and ideas from Dr. Reitebuch and Dr. Weinzierl. The additional datasets used for the calibration procedure from the POLIS aerosol ground-based lidar were provided by Dr. Groß and Dr. Freudenthaler. The sun-photometer dataset was provided by Dr. Toledano.

In Chouza et al. (2016a), I developed, implemented and evaluated improvements to the vertical wind retrieval method based on datasets provided by Dr. Rahm and ideas from Dr. Reitebuch. The analysis of the gravity waves was done by myself based on the LES results provided by Dr. Jähn and the in-situ datasets from Dr. Weinzierl.

In Chouza et al. (2016b), I developed the algorithms to compare the DWL measurements retrieved based on the methods presented in Chouza et al. (2015) with the MACC model results provided by Dr. Benedetti. The evaluation of the comaprison results was done by myself with contributions from Dr. Reitebuch, Dr. Weinzierl and Dr. Benedetti.

In Jähn et al. (2016), I contributed with a comparison of the LES results with the DWL measurements, including a sub-section (Sec. 4.1) and the corresponding figures.

In Weinzierl et al. (in press), I contributed with the retrieval of backscatter profiles from the DWL measurements and the corresponding plots in Fig. 7.

# Chapter 4

# Conclusions and outlook

This cumulative dissertation present a set of novel DWL retrieval methods to investigate different aspects of the Saharan dust transport and the ability of different numerical models to simulate them. These studies, carried out with the SALTRACE dataset, range from island-induced gravity waves with a wavelength shorter than 10 km to synoptic-scale AEWs.

Based on a novel calibration method, backscatter and extinction coefficient measurements are retrieved from the airborne DWL deployed onboard the DLR Falcon during SALTRACE. This method, which rely on the simultaneous measurements of the DWL, a ground-based aerosol lidar and optical properties derived from sun-photometers, extend the capabilities of the DWL and allow the simultaneous retrieval of aerosol optical properties and winds. The calibration constants, derived on one calibration flight, were applied to several other measurement flights conducted in the Caribbean region as well as near the west coast of Africa. The results, validated with ground-based aerosol lidar measurements and CALIPSO retrievals, indicate that the lidar is stable enough to provide meaningful results without need for periodic recalculation of the calibration constants. The backscatter and extinction coefficient profiles retrieved from the airborne DWL are within $\pm 20$ % of POLIS aerosol lidar and CALIPSO satellite measurements. Since the system is only sensitive to the non-depolarized component of the atmospheric signal, the method require additional information about the aerosol type and its spatial distribution in order to provide accurate retrievals. This limitation could be overcome by measuring both polarization components of the return signal. Implementing this polarization detection channel would allow the DWL to operate as a stand-alone system, without need of additional information sources for the retrieval.

A set of improvements to the retrieval process of vertical winds from the DWL were presented. In order to reduce the systematic error associated with the mounting angle of the DWL on the aircraft, an automatic retrieval method based on the measurements of ground and sea relative speed and distance was developed. The inclusion of distance measurements on the lidar mounting angle retrieval proved to improve the angles estimations, specially in the case of the mounting angle perpendicular to the flight direction. Since no active control of the pointing direction was implemented during SALTRACE, a correction of

the horizontal wind speed projection was applied based on horizontal wind speed profiles derived form dropsondes and previous DWL measurements. The estimated systematic error showed to be lower than $0.05 ms^{-1}$, while the random error is between 0.1 and $0.16 ms^{-1}$ depending on the method used for its estimation. The results obtained during SALTRACE indicate that the system orientation with respect to the aircraft IRS change according to the flight conditions (e.g. altitude, speed). This change in the relative position of the lidar and the aircraft IRS is likely to be due to small aircraft deformations. In order to reduce this effect, the operator could perform regular scanning measurements during the flight which allow a recalculation of the lidar mounting angles during the different operation conditions and thus a reduction of the impact of this changes.

The simultaneous retrieval of calibrated backscatter and vertical winds were used to characterize island-induced gravity waves observed in the Cabo Verde and Barbados region during SALTRACE. The measurements, quite unique due to the excellent coverage conditions provided by the high amount of Saharan dust, provided a very good opportunity to test the capabilities of the ASAM model to reproduce them. The results show a good agreement in the wavelength and spatial extension of the waves, although the amplitude was underestimated by the model. Additionally, the interaction of the waves and the SAL was investigated based on the simultaneous measurements of backscatter and vertical wind from the lidar on one side, and the in-situ particle number and vertical wind measurements on the other side. The wave-dust interaction, particularly visible in regions with a high gradient in the dust concentration, exhibit a consistent 90 degrees phase shift which resulted in a zero net dust flux.

While the vertical wind measurements conducted during SALTRACE provided a very high resolution picture of the island induced gravity waves, only vertical wind measurements do not provide all the information required for a complete characterization of the waves and associated quantities, like momentum flux. For this reason, new measurements schemes should be implemented in order to provide a more comprehensive set of measurements for gravity waves characterization. Currently, measurement patterns based on the technique developed by Vincent and Reid (1983) for gravity waves momentum flux estimation are being implemented in the DLR DWL.

The synchronous measurements of backscatter and high resolution vertical wind opens the possibility to perform eddy flux studies. Although vertical wind measurements from a DWL were used in the past in combination with other lidars to perform water vapor and aerosol eddy flux studies, the use of only one instrument for the calculation of mass flux would reduce the complexity of the retrievals by providing consistent temporal and spatial resolutions and reduce the uncertainties arising from the bias in the measurement position proper from measurement setups involving to lidars. The main issue associated with the lidar measurement of aerosol eddy flux is the hygroscopic growth that aerosol particles experience when they are transported from a relative dry environment to a high humidity atmospheric layer. This water uptake would lead to a higher backscatter coefficient and thus to an overestimation of the aerosol mass flux. An adequate characterization of the aerosol hygroscopicity and the atmospheric humidity profile is then required in order to reduce the impact of this effect.

For the fist time, a DWL was deployed over the main Saharan dust transport path across the Atlantic ocean. The results, presented in this dissertation, include backscatter and horizontal wind observations corresponding to different features associated with the dust long-range transport (e.g. AEJ, AEW). These retrievals allowed to evaluate the current capabilities of the MACC global aerosol model, with a view to the assimilation of the data products of the future missions Aeolus and EarthCARE. While a general good agreement was observed between the measurements and the modeled winds, a general underestimation of the AEJ by up to 10 $ms^{-1}$ was observed. Future studies will be conducted in order to investigate the impact of the dust forcing effect in the jet intensity. In the case of the modeled aerosol distributions larger differences were observed, specially above and below the SAL. Below the SAL, in the boundary layer, the aerosol concentration was consistently underestimated by the model. On the other hand, a thin aerosol layer was observed in the model extending from the top of the SAL up to almost 10 km. This feature, not observed by the lidars, is likely to be an artifact introduced by the model in order to compensate the lack of aerosols in the boundary layer and thus match the assimilated AOD.

The methods and lessons resulting from this work could help to extend the results form future measurement campaigns. The upcoming A-LIFE campaign, to be conducted in April/May 2017, would provide the opportunity to test the range of applicability of the retrieval methods presented in this dissertation as well as a whole new set of data which will help us to extend our knowledge on the field of aerosols and their transport.

# Appendix A

# SALTRACE datasets

| Dataset | Description |
|---|---|
| **Airborne Doppler wind lidar (DWL) profiles** | Horizontal wind vector (≈ 6 km horizontal resolution), vertical wind speed (≈ 200 m horizontal resolution), equivalent backscatter and extinction coefficient at 532 nm (≈ 200 m horizontal resolution); vertical resolution: 100 m. |
| **Falcon standard instrumentation** | Position, temperature, pressure humidity, horizontal and vertical wind velocity. |
| **Dropsondes profiles** | Vaisala RD93 dropsondes. Provide vertical profiles of temperature, pressure, humidity and horizontal wind vector. |
| **Multi-channel condensation particle counter (CPC) (2 unheated, 2 heated channels)** | Integral number concentration of ultrafine particles (0.004 $\mu$m <Dp <2.5 $\mu$m) and non-volatile particle fraction. |
| **Ground-based lidar POLIS profiles** | Backscatter coefficient, extinction coefficient, depolarization ratio and lidar ratio at 355 nm and 532 nm. Raw range resolution: 3.5 m (a moving average of 191 m was applied to the profiles presented in this work). Temporal resolution: 5-10 s (depending on atmospheric conditions). |
| **AERONET sun-photometers** | Aerosol optical depth at 8 wavelengths (340 nm - 1640 nm) |
| **CALIPSO profiles** | Backscatter coefficient, extinction coefficient and depolarization ratio at 532 nm and 1064 nm. Vertical resolution: 30-60 m. Horizontal resolution: 5 km. |
| **ASAM** | Large-Eddy Simulations in the Barbados region. Temperature, humidity, 3D-wind velocity and passive tracers concentration with an horizontal resolution of 200 m and a vertical resolution of 50 m. Time step: 4 s. |
| **MACC** | Global aerosol model. Temperature, humidity, 3D-wind velocity and five aerosol types: sea-salt, dust, organic and black carbon, and sulphate aerosols. Horizontal resolution: 78 x 78 km. Vertical resolution: 60 levels. Time step: 3 h. |

Table A.1: List of instruments and datasets used for the studies included in this thesis. A complete list of SALTRACE instruments can be found in (Weinzierl et al., in press)

# Appendix B

# Enclosed papers

Atmos. Meas. Tech., 8, 2909–2926, 2015
www.atmos-meas-tech.net/8/2909/2015/
doi:10.5194/amt-8-2909-2015


Atmospheric Measurement Techniques
Open Access

# Retrieval of aerosol backscatter and extinction from airborne coherent Doppler wind lidar measurements

**F. Chouza[1], O. Reitebuch[1], S. Groß[1], S. Rahm[1], V. Freudenthaler[2], C. Toledano[3], and B. Weinzierl[1,2]**

[1]Deutsches Zentrum für Luft- und Raumfahrt (DLR), Institut für Physik der Atmosphäre, Oberpfaffenhofen, Germany
[2]Ludwig-Maximilians-Universität München (LMU), Meteorologisches Institut, München, Germany
[3]University of Valladolid, Atmospheric Optics Group, Valladolid, Spain

*Correspondence to:* F. Chouza (fernando.chouza@dlr.de)

Received: 29 January 2015 – Published in Atmos. Meas. Tech. Discuss.: 18 February 2015
Revised: 9 June 2015 – Accepted: 16 June 2015 – Published: 21 July 2015

**Abstract.** A novel method for calibration and quantitative aerosol optical property retrieval from Doppler wind lidars (DWLs) is presented in this work. Due to the strong wavelength dependence of the atmospheric molecular backscatter and the low sensitivity of the coherent DWLs to spectrally broad signals, calibration methods for aerosol lidars cannot be applied to coherent DWLs usually operating at wavelengths between 1.5 and 2 µm. Instead, concurrent measurements of an airborne DWL at 2 µm and the POLIS ground-based aerosol lidar at 532 nm are used in this work, in combination with sun photometer measurements, for the calibration and retrieval of aerosol backscatter and extinction profiles at 532 nm.

The proposed method was applied to measurements from the SALTRACE experiment in June–July 2013, which aimed at quantifying the aerosol transport and change in aerosol properties from the Sahara desert to the Caribbean. The retrieved backscatter and extinction coefficient profiles from the airborne DWL are within 20 % of POLIS aerosol lidar and CALIPSO satellite measurements. Thus the proposed method extends the capabilities of coherent DWLs to measure profiles of the horizontal and vertical wind towards aerosol backscatter and extinction profiles, which is of high benefit for aerosol transport studies.

## 1 Introduction

Mineral dust plays a key role in the climate system. About half of the annually emitted aerosol mass is mineral dust (e.g., Hinds 1999) which disturbs the radiation budget, acts as cloud and ice nuclei and is observed to modify the cloud glaciation process (e.g., Seifert et al., 2010).

The Saharan desert has been identified as the world's largest source of mineral dust (e.g., Mahowald et al., 2005). Saharan dust is regularly transported westwards across the Atlantic Ocean (e.g., Prospero, 1999), covering huge areas of the Atlantic Ocean with the dust-containing Saharan Air Layer (SAL). Despite the progress made during the last years, many key questions about the transport, deposition mechanisms and transformation of the Saharan dust remain unanswered (Ansmann et al., 2011).

To study the aging and modification of Saharan mineral dust during long-range transport from the Sahara across the Atlantic Ocean into the Caribbean and investigate the impact of aged mineral dust on the radiation budget and cloud evolution processes, the Saharan Aerosol Long-range Transport and Aerosol-Cloud-Interaction Experiment (SALTRACE: http://www.pa.op.dlr.de/saltrace) was performed in June/July 2013. SALTRACE was designed as a closure experiment combining a set of ground-based lidar, in situ and sun photometer instruments deployed on Barbados (main SALTRACE supersite), Cape Verde and Puerto Rico with airborne aerosol and wind measurements of the DLR (Deutsches Zentrum für Luft- und Raumfahrt) research aircraft Falcon, satellite observations and model simulations. Altogether 31 research flights were conducted between 10 June and 15 July 2013. For the first time, an airborne 2 µm Doppler wind lidar (DWL) was deployed to study the dust transport across the Atlantic Ocean. While airborne DWLs were mainly used in the past for atmospheric dynamical studies providing the horizontal wind vector and turbulence mea-

surements (Reitebuch, 2012; Weissmann et al., 2005; Smalikho, 2003; Reitebuch et al., 2001), they were also used to obtain qualitative aerosol data (Bou Karam et al., 2008; Schumann et al., 2011; Weinzierl et al., 2012). Quantitative aerosol optical properties derived from airborne coherent DWLs, like backscatter and extinction coefficient, are rarely reported (Menzies and Tratt, 1994).

The calibration of aerosol lidars is usually performed using the Rayleigh molecular backscatter from the stratosphere or the high troposphere (Fernald et al., 1984; Klett, 1985; Böckmann et al., 2004). However, this method is not applicable to a coherent DWL operating at a wavelength of 2 µm. The main reason for that are the low intensity of the molecular backscatter, caused by the strong dependence of the Rayleigh backscatter intensity on the lidar operation wavelength ($P \propto \lambda^{-4}$), and the low sensitivity of the coherent DWLs to spectrally broad signals (Henderson et al., 2005). The latter is a consequence of the DWL's design to match the spectrally narrow aerosol return signal to increase the signal-to-noise ratio.

Up to now, different approaches were used to retrieve calibrated atmospheric parameters from coherent lidars which are not suitable to be calibrated using molecular background as a reference. Most of these techniques rely on the use of the return signals from targets with known optical properties, including ground-based hard targets (Menzies and Tratt, 1994), sea surface (Bufton et al., 1983) and ground return (Cutten et al., 2002).

The main problems associated with the calibration of a coherent DWL at ground using calibrated targets (Menzies and Tratt, 1994) are the variability in the optical transmission of the boundary layer, the effect of the turbulence in the heterodyning efficiency, the limitations of the calibration range due to target size restrictions and the necessity of a well-characterized system heterodyne efficiency. This last problem is related to practical limitations in the distance at which the target can be placed. For usual distances (< 1 km) the lidar is not operating in far field regime and a correction has to be applied taking into account the heterodyne efficiency function. However, the use of different hard targets such as flame-sprayed aluminium or sandpaper allows the characterization of the system depolarization effects and, through the use of moving targets, of the system response to return signal frequency shifts.

The use of sea and ground returns for the calibration of airborne lidars (Bufton et al., 1983; Cutten et al., 2002) avoids some of the previously described problems at the cost of losing some of the advantages of ground-based targets. The refractive turbulence effects are lower because the path-integrated turbulence is smaller and the heterodyne efficiency function is not essential for the calibration procedure because the ground or sea surface is normally in the region of far field regime. The use of ground return allows also us to perform a continuous calibration, with the instrument operating in normal measuring conditions. Nevertheless, the optical properties of the ground and sea returns have a higher uncertainty and are highly variable between different locations. In the case of the sea surface, they are affected by the wind and the consequent generation of waves and whitecaps (Li et al., 2010), while in the case of the ground return relatively constant optical properties are limited to specific regions.

A third method, developed to calibrate cloud lidars (O'Connor et al., 2004), consists in scaling the backscatter signal to match the derived lidar ratio with the theoretical lidar ratio corresponding to stratocumulus clouds. This requires the presence of homogeneous and well-characterized stratocumulus clouds.

The aim of this paper is to provide an alternative calibration method for coherent DWLs. As the combination of ground-based and airborne lidars is a usual approach for large field campaigns aiming at the characterization of aerosols and its transport (Heintzenberg, 2009; Ansmann et al., 2011), the availability of simultaneous airborne and ground-based measurements opens the possibility to a new DWL calibration method. The proposed method relies on the measurement of the same atmospheric volume by two different lidars: a reference aerosol lidar to which the Klett–Fernald method can be applied and the coherent DWL to be calibrated. Based on simultaneous measurements, calibration constants corresponding to different aerosol types are calculated. Those constants can be then applied to retrieve calibrated backscatter and extinction coefficient profiles from the coherent DWL measurements during other flight periods. With the proposed method, not only can information on horizontal and vertical wind vector and transport of the aerosol layers be derived from the (airborne) DWL but synchronous aerosol backscatter and extinction coefficients can also be retrieved.

The paper is organized as follows. Section 2 provides a brief description of the coherent DWL mounted on the Falcon research aircraft of DLR during SALTRACE and an outline of the acquired signal processing. Section 3 describes the instrumental corrections, calibration and retrieval method. Section 4 gives a description of the measurement sets used for the calibration and validation of the method. Section 5 shows the results of the method applied to parts of the SALTRACE measurement set. Finally, a summary and relevant conclusions are presented in Sect. 6.

## 2 Coherent DWL instrument

### 2.1 Instrument description

The airborne coherent DWL used during SALTRACE is based on an instrument from CLR Photonics (Henderson et al., 1993), today Lockheed Martin Coherent Technologies (LMCT), together with a scanning and acquisition system developed by DLR (Köpp et al., 2004) which provides airborne wind measurement capabilities. The lidar operates at a wavelength of 2.02254 µm, with a pulse full width at half

maximum of 400 ns, a pulse energy of 1–2 mJ and a repetition frequency of 500 Hz. The key system specifications are summarized in Table 1.

The system is composed of three units: first, a transceiver head holding the diode pumped solid-state Tm:LuAG laser, the 10.8 cm diameter afocal transceiver telescope, the receiver optics and detectors and a double wedge scanner; second, a rack with the laser power supply and the cooling unit; third, another rack that contains the data acquisition and control electronics.

The system is deployed in the DLR Falcon 20 research aircraft in order to provide horizontal and vertical wind profiles as well as backscatter measurements. The transceiver head is mounted above the aircraft optical window pointing downwards to allow the measurement of vertical profiles (Fig. 1). The aircraft window consists of a 400 mm diameter and 35 mm thick INFRASIL-302 fused silica window with an antireflection coating which was optimized for an angle of incidence of 10°.

While single wedge scanners are only able to perform conical scans with a fixed off-nadir angle, the double wedge scanner used in this system (Käsler et al., 2010) allows us to perform arbitrary scanning patterns. Typically, for airborne measurements the lidar is operated in two modes: step-stare scanning and nadir pointing. The step-stare scanning mode consists of 24 lines of sight (LOS) $\boldsymbol{I}$ in a conical distribution with an off-nadir angle of 20°and a staring duration of 1 s per LOS direction. This configuration allows the measurement of horizontal wind speeds with a horizontal resolution of approximately 6 km, depending on aircraft ground speed. However, when the system is operated in nadir pointing mode, the system LOS is kept fixed downwards pointing, while the accumulation period of 1 s remains the same as for the scanning mode. The nadir pointing mode allows the system to retrieve vertical wind profiles with a horizontal resolution of 200 m. In order to minimize the horizontal wind projection over $\boldsymbol{I}$ when the system is operating in nadir pointing mode, the transceiver head was mounted with a pitch angle $\theta_\mathrm{m}$ of $-2°$. Together with a variable deflection provided by the scanner $\theta_\mathrm{s}$ (which can be set by the operator during flight), the system can compensate the aircraft pitch angle $\theta_\mathrm{p}$ and provide nadir pointing measurements $\boldsymbol{I} = \boldsymbol{n}$.

**Table 1.** Key parameters of the DWL.

| | | |
|---|---|---|
| Laser | Laser type | Solid-state Tm:LuAG |
| | Operation wavelength | 2.02254 µm |
| | Laser energy | 1–2 mJ |
| | Repetition rate | 500 Hz |
| | Pulse length (full width at half maximum) | 400 ns |
| | Frequency offset ($f_\mathrm{IF}$) | 102 MHz |
| Transceiver | Telescope type | Off-axis |
| | Telescope diameter | 10.8 cm |
| | Focal length | Afocal |
| | Beam diameter ($1/e^2$) | 8 cm |
| | Transmitted polarization | Circular |
| | Detected polarization | Co-polarized |
| Scanner | Type | Double wedge |
| | Material | Fused silica |
| Aircraft window | Material | INFRASIL-302 |
| | Coating | Anti-reflection (10°) |
| | Diameter/thickness | 400/35 mm |
| Data acquisition | Sampling rate | 500 MHz |
| | Resolution | 8 bits |
| | Mode | Single shot acquisition |

## 2.2 Coherent lidar signal equation

The following subsection discusses the properties and the analysis steps applied to the signal measured by the DWL in order to obtain a magnitude proportional to the atmospheric backscattered power.

The coherent DWL operation relies on the heterodyning technique. The frequency of the light scattered in the atmosphere, $f_\mathrm{s} = f_0 + f_\mathrm{D}$, is affected by the Doppler effect, which introduces a frequency shift $f_\mathrm{D}$ to the laser pulse frequency $f_0$ proportional to the projection of the relative speed $\mathrm{v_{LOS}}$ between the laser source and the backscattering aerosols on the laser pulse direction, with $f_\mathrm{D} = 2\mathrm{v_{LOS}} f_0 \mathrm{c}^{-1}$. A positive frequency shift $f_\mathrm{D}$ indicates a positive relative speed $\mathrm{v_{LOS}}$, which, in turn, indicates that the scattering aerosols are moving towards the lidar. For the case of an airborne downward pointing lidar, this sign convention leads to positive relative speeds for upward winds and negative relative speeds for downward winds. The atmospheric backscattered fraction of the outgoing pulse is mixed with a frequency shifted $f_m = f_0 + f_\mathrm{IF}$ sample of the same local oscillator (LO) used for seeding the outgoing pulse. As a result, the mixed signal contains one spectral component with a frequency equal to the sum of the atmospheric backscatter frequency and the shifted LO frequency $f_\mathrm{s} + f_m$ and another component with a frequency equal to the difference of both frequencies $\Delta \mathrm{f} = f_\mathrm{s} - f_m = f_\mathrm{D} + f_\mathrm{IF}$. Due to the limited detector bandwidth, only the component with frequency $\Delta f$ can be detected. Knowing the frequency of the LO and the shift applied to the LO ($f_\mathrm{IF}$), it is possible to calculate the shift on the backscatter due to the Doppler effect.

Several authors (e.g., Sonnenschein and Horrigan, 1971; Frehlich and Kavaya, 1991) describe the coherent DWL in different levels of generality. In this work, we will focus on the received power for the specific case of a monostatic pulsed coherent lidar. For a detector with uniform response, the signal photocurrent generated by the atmospheric backscatter can be written as (Henderson et al., 2005)

$$i_\mathrm{h}(t) = 2\frac{\eta_\mathrm{q} e}{h f_0}\sqrt{\eta_\mathrm{LO} P_\mathrm{LO} \eta_\mathrm{h}(t)\, P_{\mathrm{sd},\boldsymbol{I}}(t)}\cos\left(2\pi \Delta f t + \Delta\theta(t)\right), \quad (1)$$

where $i_\mathrm{h}$ is the output current from the detector, $t$ the elapsed time since the laser trigger, $\eta_\mathrm{q}$ the quantum efficiency, $e$ the electron charge, $h$ the Planck constant, $f_0$ the laser frequency, $\eta_\mathrm{h}$ the heterodyne efficiency, $\eta_\mathrm{LO}$ the local oscillator trunca-

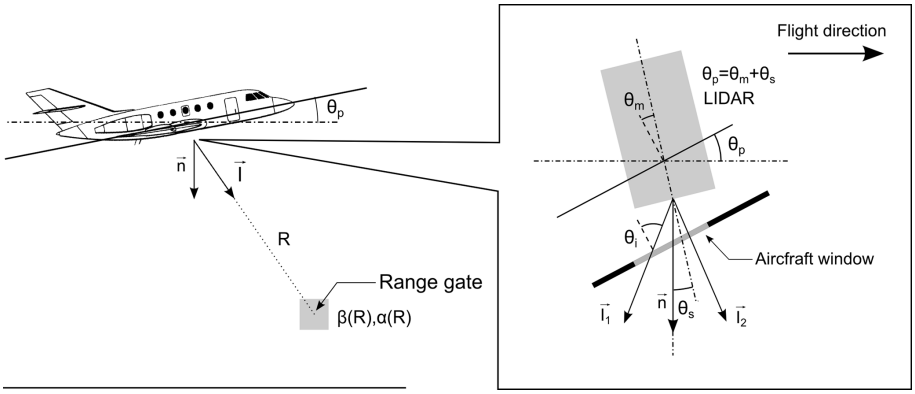


**Figure 1.** Variables used to calculate the backscattered power from a given range gate, where $R$ is the distance between the range gate and the lidar, $\boldsymbol{I}$ is a unit vector that represents the line of sight (LOS) of the lidar, $\boldsymbol{n}$ is the unit nadir pointing vector, $\beta(R)$ is the backscatter coefficient and $\alpha(R)$ is the extinction coefficient of the sampled atmospheric volume. The zoomed area shows a mounting scheme of the lidar transceiver head. $\boldsymbol{I_1}$ and $\boldsymbol{I_2}$ are examples of the LOS vector when the instrument operates in scanning mode, $\theta_\mathrm{p}$ is the aircraft pitch angle, $\theta_\mathrm{m}$ is the lidar mounting angle about the transverse aircraft axis, $\theta_\mathrm{s}$ is the angle between the transceiver head geometric axis and $\boldsymbol{n}$, and $\theta_\mathrm{i}$ is the angle of incidence of the transmitted laser beam on the aircraft window.

tion efficiency, $P_\mathrm{LO}$ the LO power at the detector plane, $P_{\mathrm{sd},\boldsymbol{I}}$ the atmospheric received power at the detector plane, $\Delta f$ the beat signal frequency and $\Delta\theta$ the signal phase. The heterodyning efficiency reflects the phase and amplitude matching between the backscattered signal and the LO, while the LO truncation efficiency represents the fraction of the LO power applied over the detector area.

The detector output is digitalized by an acquisition board with 8 bit resolution, input impedance $R_\mathrm{in}$, gain $G$ and a sampling frequency of 500 MHz ($T_\mathrm{s} = 2$ ns). The digitized signal $u_\mathrm{h}$ (n) can be written as

$$u_\mathrm{h}(n) = i_\mathrm{h}(nT_\mathrm{s})\, R_\mathrm{in} G. \tag{2}$$

Because the system operates in single shot acquisition mode, the digitized signal $u_\mathrm{h}(n)$ for each laser shot is stored during measurement flight. The following processing steps are performed during signal analysis on ground, allowing different instrumental corrections and changes in the temporal and vertical averaging parameters.

In order to obtain range resolved measurements of the backscattered power, the acquired signal is divided in range gates of $N$ samples, with $N = 512$. For a range gate at distance $R$, the power spectra $\hat{P}_\mathrm{S}(R,k)$ can be calculated from the Fast Fourier Transform using the following expression:

$$\hat{P}_\mathrm{S}(R,k) = \frac{1}{N}\left|\sum_{n=N_1}^{N_2} u_\mathrm{h}(n) e^{-j\frac{2\pi kn}{N}}\right|^2, \tag{3}$$

where $N_1 = N_\mathrm{R} - \frac{N}{2}$, $N_2 = N_\mathrm{R} + \frac{N}{2}$ and $N_\mathrm{R}$ is the sample corresponding to the center of the range gate and it is given by the integer part of $N_\mathrm{R} = \left(\frac{2R}{T_\mathrm{s} c}\right)$.

Replacing Eq. (3) with Eqs. (2) and (1) gives

$$\hat{P}_\mathrm{S}(R,k) = \frac{1}{N}\left|\sum_{n=N_1}^{N_2} 2\frac{\eta_\mathrm{q} e}{h f_0} R_\mathrm{in} G \sqrt{\eta_\mathrm{LO} P_\mathrm{LO} \eta_\mathrm{h}(nT_\mathrm{s}) P_{\mathrm{sd},\boldsymbol{I}}(nT_\mathrm{s})}\cos(2\pi\Delta T_\mathrm{s} + \Delta\theta(nT_\mathrm{s})) e^{-j\frac{2\pi kn}{N}}\right|^2. \tag{4}$$

For all the samples belonging to a range gate, the atmospheric return is supposed to be constant: $P_\mathrm{sd}(nT_\mathrm{s}) = P_\mathrm{sd}(R)$. This approximation leads to the following expression:

$$\hat{P}_\mathrm{S}(R,k) = \frac{1}{N}\left(2\frac{\eta_\mathrm{q} e}{h f_0} R_\mathrm{in} G\right)^2 \eta_\mathrm{LO} P_\mathrm{LO} P_{\mathrm{sd},\boldsymbol{I}}(R) \left|\sum_{n=N_1}^{N_2} \sqrt{\eta_h(nT_\mathrm{s})}\cos(2\pi\Delta f n T_\mathrm{s} + \Delta\theta(nT_\mathrm{s})) e^{-j\frac{2\pi kn}{N}}\right|^2. \tag{5}$$

Equation (5) represents the backscatter power spectrum of a given range gate for a single shot. Because the received backscatter power $\hat{P}_\mathrm{S}(R,k)$ is subject to large amplitude variations between different shots due to speckle effect (Fig. 2a), the power spectrums of many shots are averaged in order to reduce its influence

$$\langle \hat{P}_s(R,k)\rangle = \frac{1}{\mathrm{I}}\sum_{i=1}^{\mathrm{I}} \hat{P}_{\mathrm{S},i}(R,k), \tag{6}$$

where $\hat{P}_{\mathrm{S,i}}(R,k)$ is the power spectrum of a range gate at distance $R$ corresponding to the shot $i$ and $I$ is the number of averaged shots, which is typically 500 corresponding to

the temporal average over 1 s. Figure 2b illustrates the exponential probability density distribution corresponding to the received power of a ground return range gate for 500 shots.

Finally, in order to estimate the backscattered power for the averaged range gates, the summation of the power spectra components around the spectral maximum is performed. For the sake of simplicity, the noise affecting the system was omitted from the previous equations. During the processing, the noise floor is subtracted from the averaged power spectra before estimating the backscattered power.

The expected value for the backscatter power corresponding to the averaged range gates is calculated through the integration of the average backscatter power spectrum:

$$\langle P(R)\rangle = \sum_{k=K_1}^{K_2} \langle \hat{P}(R,k)\rangle = \frac{1}{N}\left(2\frac{\eta_{\mathrm{q}} e}{h f_0} R_{\mathrm{in}} G\right)^2 \eta_{\mathrm{LO}} P_{\mathrm{LO}} \eta_{\mathrm{h}}(R)\, P_{\mathrm{sd},\boldsymbol{I}}(R), \quad (7)$$

where $K_1 = k_{\max} - \frac{K}{2}$, $K_2 = k_{\max} + \frac{K}{2}$, $k_{\max}$ is the index corresponding to the maximum of the power spectra and $K$ is the width of the spectral peak corresponding to the backscattered signal. The optimal value for the integration window width $K$ is the one that exactly matches the return pulse spectral width. A shorter integration window will lead to an underestimation of the backscattered power, while a longer integration window increases the estimation error due to the integration of measurement noise. Based on these facts, the integration window width $K$ was set to be 6 (approximately 6 MHz).

Because each power spectra $\langle \hat{P}_s(R,k)\rangle$ is calculated based on the average of 500 shots and the received power for a single shot follows an exponential probability density function, the mean received power $\langle P(R)\rangle$ can be modeled as a gamma function. If 500 shots are averaged, the resulting average received power relative standard deviation is lower than 5 %.

The received atmospheric power $P_{\mathrm{sd}}$, for a given lidar line of sight $\boldsymbol{I}$, can be written as

$$P_{\mathrm{sd},\boldsymbol{I}}(R) = k_{\mathrm{in},\boldsymbol{I}}(R)\, E_{\mathrm{T}} \frac{A_R}{R^2} \frac{\mathrm{c}}{2} \beta(R)\, T^2(R), \quad (8)$$

where $k_{\mathrm{in},\boldsymbol{I}}(R)$ condenses different instrumental constants, $E_{\mathrm{T}}$ is the mean transmitted energy of the averaged laser pulses, $A_{\mathrm{R}}$ is the telescope area, $c$ is the speed of light, $\beta$ is the backscatter coefficient and $T$ the atmospheric transmission.

Combining all constants in one constant $k_d$, replacing Eq. (8) into Eq. (7) and applying a range correction multiplying the backscattered power of each range gate by its squared distance to the lidar, Eq. (7) can be rewritten as

$$\langle P(R)\rangle R^2 = k_d E_{\mathrm{T}} k_{\mathrm{in},\boldsymbol{I}}(R)\, \eta_{\mathrm{h}}(R)\, \beta(R)\, T^2(R), \quad (9)$$

where $k_d = \frac{1}{N}\left(2\frac{\eta_{\mathrm{q}} \mathrm{e}}{\mathrm{h} f_0} R_{\mathrm{in}} G\right)^2 \eta_{\mathrm{LO}} P_{\mathrm{LO}} A_{\mathrm{R}} \frac{\mathrm{c}}{2}$.

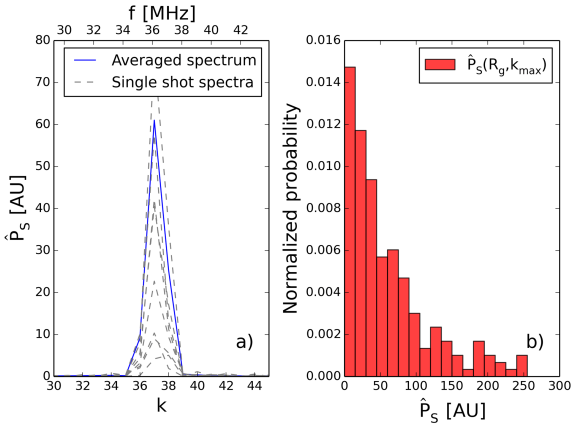


**Figure 2. (a)** Power spectra of single shots (dashed) and the averaged spectrum of 500 shots (solid) for the range gate corresponding to the ground return $R_{\mathrm{g}}$, an acquisition frequency of 500 MHz and an Fast Fourier Transform length of 512 samples. **(b)** Exponential distribution for the maximum of the power spectra $\hat{P}_{\mathrm{S}}(R_{\mathrm{g}}, k_{\max})$ for 500 shots and the range gate $R_{\mathrm{g}}$.

## 3 Calibration and retrieval method

### 3.1 Instrumental corrections

In order to establish the lidar calibration constants (Sect. 3.3), it is necessary to remove the effect of all the instrumental parameters that change during the measurement, i.e., the laser pulse energy $E_{\mathrm{T}}$, the heterodyne efficiency and the instrumental constants summarized by $k_{\mathrm{in},\boldsymbol{I}}(R)$.

To remove the dependency of the measured atmospheric signal power on the fluctuation of the laser energy, the range-corrected signal is divided by the averaged outgoing laser pulse energy $E_{\mathrm{T}}$ corresponding to all the shots averaged to calculate the backscattered power. Although the outgoing pulse energy is not directly measured, a part of each outgoing pulse is mixed with the LO and the resulting beat signal is stored as frequency reference. The time elapsed between the laser Q-switch trigger and the amplitude maximum of the digitized beat signal corresponds to the pulse build-up time. Based on laboratory measurements (LMCT, personal communication) of the outgoing pulse energy as function of the Q-Switch build-up time (Fig. 3), it is possible to estimate the energy $E_{\mathrm{T}}$ of the outgoing pulses during the lidar operation.

The laser pulse energy-corrected signal is obtained from Eq. (9),

$$\frac{\langle P(R)\rangle R^2}{E_{\mathrm{T}}} = k_d k_{\mathrm{in},\boldsymbol{I}}(R)\, \eta_{\mathrm{h}}(R)\, \beta(R)\, T^2(R), \quad (10)$$

where the instrumental constant $k_{\mathrm{in},\boldsymbol{I}}(R)$ can be expressed as follows:

$$k_{\mathrm{in},\boldsymbol{I}}(R) = k_{\mathrm{G}} k_{\mathrm{h}}(\Delta f)\, k_\theta(\boldsymbol{I})\, k_\delta(R), \quad (11)$$

with $k_{\mathrm{G}}$ the acquisition board attenuator, $k_{\mathrm{h}}(\Delta f)$ the system gain as a function of the backscattered signal frequency $\Delta f$,

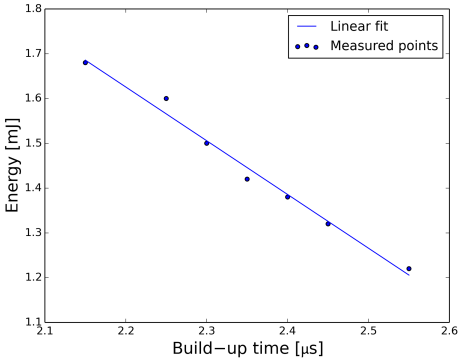


**Figure 3.** Measured and interpolated pulse energy as a function of the build-up time.

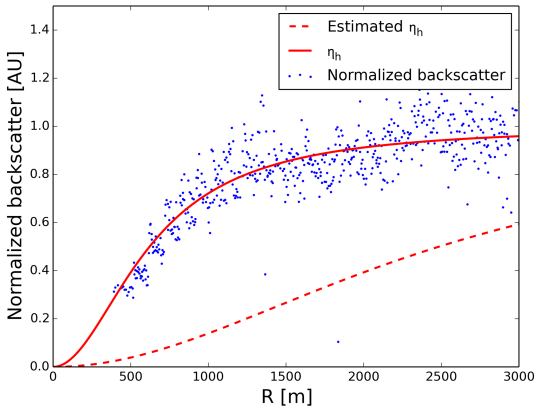


**Figure 4.** Estimated (red, dashed) and derived (red, solid) heterodyne efficiency $\eta_h$ as a function of range $R$. The normalized backscatter data points (blue dots) correspond to the averaged backscatter power corresponding to range gates at altitudes between 4.5 and 5 km for a flight altitude between 5.5 and 8 km during the flights on 22 June and 11 July.

$k_\theta(\boldsymbol{I})$ the change in the received power as a function of the line of sight angle of incidence on the aircraft window $\theta_i$ (Fig. 1) and $k_\delta(R)$ the detector response depending on the depolarization of the backscattered signal.

The effect of the acquisition board attenuator $k_G$ can be calculated based on the values stored by the acquisition software.

To estimate the change in the heterodyne efficiency $\eta_h$ as a function of the range $R$, measurements corresponding to a set of range gates with the same altitude and similar instrumental constants and atmospheric optical properties were used. The measurements, performed during flight periods for which the aircraft was changing its altitude, show the change of the received power as a function of the range gate distance $R$ due to the variation of the heterodyne efficiency in the near field regime (Fig. 4). Due to sampling of the outgoing laser pulse, atmospheric range gates at distances lower than 500 m are not digitized. For this reason, the proposed method is applicable only if the extinction corresponding to those range gates can be considered 0 or can be estimated from other sources.

Nonetheless, neglecting the turbulence effects and assuming a monostatic afocal untruncated Gaussian beam lidar, the heterodyne efficiency change as a function of the range $R$ can be approximated with the following expression (Henderson et al., 2005):

$$\eta_h(R) = \left[1 + \left(\frac{\pi\rho^2}{\lambda R}\right)^2\right]^{-1}, \tag{12}$$

where $\rho$ is the $1/e^2$ irradiance beam radius and $\lambda$ the laser wavelength. Based on the specifications presented in Table 1 and Eq. (12), the expected heterodyne efficiency was calculated and compared with the measured one (Fig. 4). It can be seen that the expected heterodyne efficiency is much lower than the measured one, suggesting that some of the assumptions are not applicable for this case. In order to get a practical correction of the heterodyne efficiency the same function was fit to the measured backscatter power, leaving $\pi\rho^2/\lambda$ as optimization parameter. The resulting correction function is (Fig. 4)

$$\eta_h(R) = \left[1 + \left(\frac{621.5}{R}\right)^2\right]^{-1}. \tag{13}$$

The heterodyne efficiency corrected signal can be obtained from Eqs. (10) and (13):

$$\frac{\langle P(R)\rangle R^2}{E_T\eta_h(R)} = k_d k_{in,\boldsymbol{I}}(R)\,\beta(R)\,T^2(R). \tag{14}$$

According to Eq. (13), for range gates corresponding to ranges $R$ larger than 3500 m, which is the case of the measurements presented in this work (Table 2), the heterodyne efficiency is almost constant (less than 3 % variation) and the system can be considered operating in far field regime with a constant heterodyne efficiency $\eta_h(R) = \eta_h$.

A sample of the received atmospheric backscattered power after applying the energy and attenuator corrections is shown in Fig. 5a. There are also abrupt changes and periodic oscillations present in the atmospheric backscattered power. These steps and oscillations in the received power are due two reasons: the system gain that changes with the backscattered signal frequency $\Delta f$ and the variability of the optical transmission of the transceiver optics (double wedge scanner and aircraft window) with the angle of incidence $\theta_i$.

The system gain as a function of the backscattered signal frequency $k_h(\Delta f)$ was estimated based on the power spectra of the range gates acquired after ground return. These range gates contain only instrumental noise and no atmospheric signal. If the noise that affects the system is constant with the frequency (white noise), the normalized power spectrum of the acquired noise is identical to the frequency response of the system (Fig. 6).

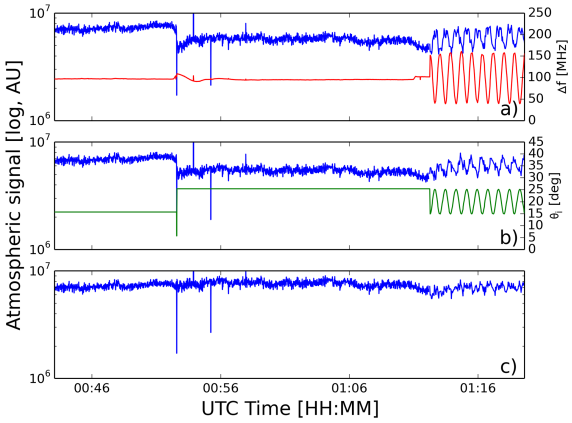


**Figure 5.** Atmospheric signal (blue) from 26 June averaged between 3 and 4 km after correcting for acquisition board gain **(a)**, for system gain as a function of the beat signal frequency **(b)** and additionally for the system gain as a function of the angle of incidence of the laser beam **(c)**. Beat signal frequency (**a**, red). Angle of incidence of the laser beam (**b**, green).

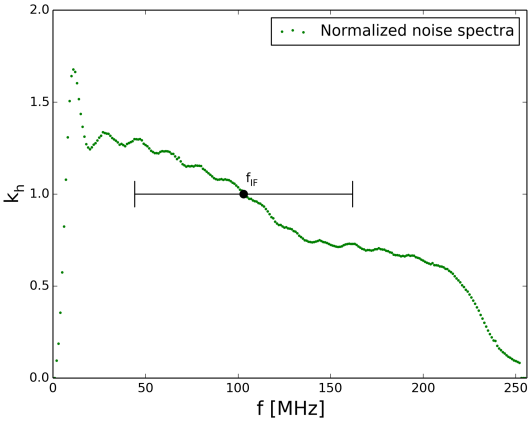


**Figure 6.** Estimated system frequency response $k_h$ based on the digitized noise spectra. The black dot indicates the beat signal frequency ($f_{IF} = 102$ MHz) when the relative speed between the lidar and the measured range gate is zero. The horizontal line indicates the range of variation of the beat signal frequency produced by the projection of the aircraft speed on the lidar LOS, when the system operates in scanning mode.

This correction is applied to the power spectra of each range gate given by Eq. (6) before computing the power of the backscattered signal. An example of the atmospheric backscattered signal after being corrected by the system gain $k_h$ can be seen in Fig. 5b.

The transmission of the transceiver optics as a function of the angle of incidence $k_\theta(\boldsymbol{I})$ can be estimated based on measurements for which all the other atmospheric and instrumental parameters can be considered to be constant. For a range $R_k$ at which the atmosphere can be considered homogenous, a set of measurements with different angles of

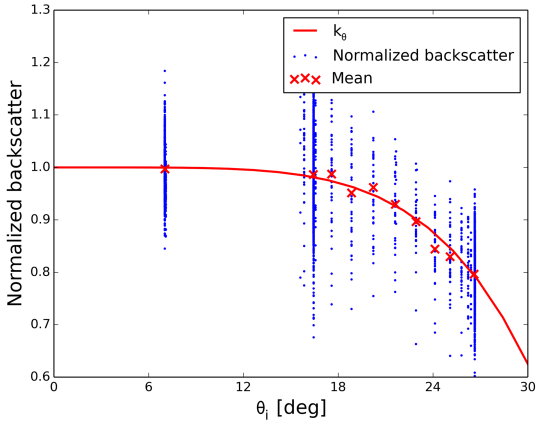


**Figure 7.** Estimated system response $k_\theta$ (red line) as a function of the angle of incidence $\theta_i$ of the laser beam on the aircraft window. The normalized backscatter data points (blue dots) are the averaged measured backscatter power at altitudes between 2 and 3 km for several vertical profiles and different angles of incidence during the flight on 26 June. The mean values for the normalized backscatter (red crosses) are derived from measurements with similar angle of incidence.

incidence (5, 15 and 25° off nadir and scanning mode) was used to estimate $k_\theta(\boldsymbol{I})$ (Fig. 7). The measurements at 5, 15 and 25° used for this estimation were pointing perpendicular to the aircraft flying direction to minimize the effects of the system gain changes with the backscattered signal frequency (described above).

$$\frac{\langle P(R_k)\rangle R_k^2}{E_T \eta_h k_G k_h(R_k, \boldsymbol{I})} = k_\theta(\theta_i(\boldsymbol{I}))\, k_d k_\delta(R_k)\, \beta(R_k)\, T^2(R_k) \quad (15)$$

Several functions were tested to model the relation between the line of sight angle of incidence $\theta_i$ and the received backscattered power. The best agreement was achieved using the following polynomial function (Fig. 7):

$$k_\theta(\theta_i(\boldsymbol{I})) = -12\theta_i^5 + 1. \quad (16)$$

Dividing Eq. (15) by Eq. (16) results in

$$\langle P_c(R)\rangle = \frac{\langle P(R)\rangle R^2}{E_T \eta_h k_G k_h(R, \boldsymbol{I})\, k_\theta(\boldsymbol{I})} = k_d k_\delta(R)\, \beta(R)\, T^2(R), \quad (17)$$

where $\langle P_c(R)\rangle$ represents the backscattered power after being corrected for the previously mentioned instrumental effects (Fig. 5c). It can be seen that the instrumental influence on the atmospheric backscatter signal is strongly removed by comparing Fig. 5a and c.

### 3.2 Limitations of the instrumental corrections

As specified in Table 1, the system emits circular polarization and detects the co-polarized component of the backscattered signal, which is attenuated by atmospheric depolarization. There are other factors that have to be taken into ac-

**Table 2.** List of flights below CALIPSO (12 June 2013) and over POLIS lidar (other dates). The overflights were defined as the time periods during which the DLR Falcon was flying in the region defined by a square cantered at the POLIS position with sides of 3 km. Dates and time are in UTC.

| Date | DWL time period | | Altitude [m] | DWL mode | CALIPSO and POLIS time period | |
|---|---|---|---|---|---|---|
| | Start | Stop | | | Start | Stop |
| 12 Jun 2013 | 14:52:00 | 14:56:00 | 9418 | Nadir pointing | 14:52:00 | 14:56:00 |
| 26 Jun 2013 | 23:56:18 | 23:56:37 | 7773 | Nadir pointing | 23:54:58 | 23:57:02 |
| 27 Jun 2013 | 00:20:34 | 00:20:54 | 7773 | 5° off-nadir | 00:20:08 | 00:22:19 |
| 27 Jun 2013 | 00:46:38 | 00:46:57 | 7773 | 15° off-nadir | 00:45:17 | 00:47:22 |
| 27 Jun 2013 | 01:00:07 | 01:00:26 | 7776 | 25° off-nadir | 00:59:41 | 01:01:50 |
| 27 Jun 2013 | 01:23:37 | 01:23:56 | 7777 | Scan | 01:22:16 | 01:24:21 |
| 27 Jun 2013 | 01:55:31 | 01:55:50 | 7778 | Nadir pointing | 01:54:48 | 01:57:41 |
| 10 Jul 2013 | 15:27:30 | 15:27:47 | 8743 | Nadir pointing | 15:00:00 | 15:26:00 |
| 11 Jul 2013 | 13:16:34 | 13:16:52 | 8726 | Nadir pointing | 13:08:00 | 13:29:00 |

count in the optical path of the LIDAR that cannot be neglected in the calculation of $k_\delta(R)$: the lidar optics, the scanning wedges and the aircraft window. These optical elements can further decrease the signal due to polarization-dependent attenuation. Due to the difficulty to characterize these attenuations, another approximation was used to get a calibrated backscatter and extinction coefficient (Sect. 3.3).

As stated in the Sect. 3.1, the proposed method supposes that the atmospheric extinction corresponding to range gates at distances shorter than 500 m from the DWL is negligible. Otherwise, the extinction correction will be wrongly estimated. At the moment, this condition limits the application of the presented method to airborne measurements for which the aerosol load of this range gates can be considered negligible. The use of this algorithm for ground-based DWLs would require a previous estimation of the extinction corresponding to this range gates based on other sources.


**Figure 8.** Scheme of the atmospheric layers with different aerosol types ($L_\mathrm{n}$), where $S_{532}(L_\mathrm{n})$ is the lidar ratio, $k_\beta^{532\to2022}(L_\mathrm{n})$ and $k_\alpha^{532\to2022}(L_\mathrm{n})$ are the conversion factor of the backscatter and extinction coefficient, respectively, and $k_\delta(L_\mathrm{n})$ the system depolarization response corresponding to the aerosol type. Within each layer, the aerosol properties are assumed to be constant.

### 3.3 Calibration of the DWL signal

Based on the measurements of a ground-based aerosol lidar, an atmospheric model with distinct aerosol layers is derived (Fig. 8). Each layer $L_\mathrm{n}$ of the atmospheric model represents an aerosol type and is defined as a region in which the particle depolarization ratio, the lidar ratio and the wavelength dependency of the extinction coefficient are considered to be constant.

Because the ground-based measurements of the backscatter coefficient $\beta_{532}^{\mathrm{POLIS}}(R)$ and extinction coefficient $\alpha_{532}^{\mathrm{POLIS}}(R)$ are performed at 532 nm by the aerosol lidar POLIS (Sect. 4.2), we have to rewrite Eq. (17) in terms of the atmospheric parameters at this wavelength in order to use ground-based measurements to calculate the DWL calibration constant corresponding to each aerosol type. For a given aerosol type and size distribution, it is possible to estimate the backscatter and extinction coefficient at 2 µm by applying a wavelength conversion factor ($k_\beta^{532\to2022}$ and $k_\alpha^{532\to2022}$).

Rewriting Eq. (17) in terms of $\beta_{532}^{\mathrm{POLIS}}(R)$ and $\alpha_{532}^{\mathrm{POLIS}}(R)$ yields

$$\langle P_{\mathrm{c},2\,\mu\mathrm{m}}(R)\rangle = k_d k_\delta(L_\mathrm{n})\,\beta_{532}^{\mathrm{POLIS}}(R)\,k_\beta^{532\to2022}(L_\mathrm{n}) \exp\left[-2\int_0^R \alpha_{532}^{\mathrm{POLIS}}(r)k_\alpha^{532\to2022}(L_\mathrm{n})\,\mathrm{d}r\right]. \quad (18)$$

All parameters that remain constant for a given layer can be grouped in a single constant $k(L_\mathrm{n})$, resulting in the following equation:

$$\langle P_{\mathrm{c},2\,\mu\mathrm{m}}(R)\rangle = k(L_\mathrm{n})\beta_{532}^{\mathrm{POLIS}}(R)\,T_{2\,\mu\mathrm{m}}^2(R), \quad (19)$$

with $T^2_{2\,\mu m}(R) = \exp\left[-2\int_0^R \alpha^{\mathrm{POLIS}}_{532}(r) k^{532\to2022}_{\alpha}(L_n)\,dr\right]$ and

$$k(L_n) = k_d k_\delta(L_n) k^{532\to2022}_{\beta}(L_n). \quad (20)$$

In order to get a linear relation between the measured and corrected backscattered power $\langle P_{c,2\,\mu m}(R)\rangle$ and the backscatter coefficient $\beta^{\mathrm{POLIS}}_{532}(R)$ measured by the ground-based lidar, it is necessary to remove the effect of the atmospheric attenuation $T^2_{2\,\mu m}$. The atmospheric attenuation at 2 µm can be estimated based on the extinction coefficient measured by the ground-based lidar $\alpha^{\mathrm{POLIS}}_{532}(R)$ and its corresponding conversion factor $k^{532\to2022}_{\alpha}(L_n)$.

In general, if the aerosol size distribution follows the Junge power law or the wavelength difference is small, the conversion factor $k^{532\to2022}_{\alpha}$ can be calculated using the Ångström exponent, which can be obtained from literature references (e.g., Ansmann and Müller, 2005). However, in our case the mentioned requirements are not fulfilled. For this reason, measurements from a collocated sun photometer were used to estimate this dependency (Sect. 4.3).

Finally, the conversion constant $k(L_n)$ corresponding to each layer can be estimated applying a LSF (least squares fit) between the backscatter coefficient $\beta^{\mathrm{POLIS}}_{532}$ measured by the ground-based lidar POLIS and the extinction-corrected signal measured by the DWL from

$$\frac{\langle P_{c,2\,\mu m}(R)\rangle}{T^2_{2\,\mu m}(R)} = k(L_n)\beta^{\mathrm{POLIS}}_{532}(R). \quad (21)$$

The principle of the calibration is shown in Fig. 9 (blue box).

### 3.4 Backscatter and extinction coefficient retrieval

Based on the layer distribution and the conversion coefficients $k(L_n)$ calculated for each layer, it is possible to retrieve the backscatter coefficient at 532 nm based on the 2 µm measurements $\beta^{\mathrm{DWL}}_{532}$ through an iterative process (Fig. 9, purple box).

For the first step it is assumed that $\alpha^{\mathrm{DWL}}_{532}(R) = 0$. This leads to $T^2_{2\,\mu m}(R) = 1$. Based on this approximation, it is possible to calculate a first order approximation of the backscatter $\beta^{\mathrm{DWL}}_{532}(R)$ for each layer of the model using Eq. (22) and the corresponding constant $k(L_n)$

$$\langle P_{c,2\,\mu m}(R)\rangle k^{-1}(L_n) = \beta^{\mathrm{DWL}}_{532}(R) \quad (22)$$

Then, using the estimated backscatter coefficient $\beta^{\mathrm{DWL}}_{532}(R)$ and the lidar ratio $S^{\mathrm{POLIS}}_{532}(L_n)$ provided by the ground-based lidar, a new value for the extinction coefficient $\alpha^{\mathrm{DWL}}_{532}(R)$ can be estimated:

$$\alpha^{\mathrm{DWL}}_{532}(R) = \beta^{\mathrm{DWL}}_{532}(R)\, S^{\mathrm{POLIS}}_{532}(L_n). \quad (23)$$

Based on the extinction coefficient $\alpha^{\mathrm{DWL}}_{532}(R)$ and its conversion factor $k^{532\to2022}_{\alpha}(L_n)$, the new transmission $T^2_{2\,\mu m}(R)$ is calculated:

$$T^2_{2\,\mu m}(R) = \exp\left[-2\int_0^R \alpha^{\mathrm{DWL}}_{532}(r) k^{532\to2022}_{\alpha}(L_n)\,dr\right]. \quad (24)$$

Finally, the calculated transmission is used to retrieve a new approximation for the backscatter coefficient:

$$\frac{\langle P_{c,2\,\mu m}(R)\rangle}{T^2_{2\,\mu m}(R)} k^{-1}(L_n) = \beta^{\mathrm{DWL}}_{532}(R). \quad (25)$$

The procedure can be written in form of an iterative equation (Fig. 9, grey box inside purple box):

$$\beta^{\mathrm{DWL}}_{532,i}(R) = \frac{\langle P_{c,2\,\mu m}(R)\rangle}{T^2_{2\,\mu m,i-1}(R)} \frac{1}{k(L_n),} \quad (26)$$

$$\alpha^{\mathrm{DWL}}_{532,i}(R) = \beta^{\mathrm{DWL}}_{532,i}(R)\, S^{\mathrm{POLIS}}_{532}(L_n), \quad (27)$$

with the iteration number $i$ and $T^2_{2\,\mu m,0}(R) = 1$ as starting value.

## 4 Description of the data sets

### 4.1 2 µm DWL data set

During SALTRACE, the DLR Falcon research aircraft performed 31 research flights. The 2 µm DWL was operational during all flights, totalizing 75 h of measurements. For this work, we will focus on the research flights conducted in the Barbados region where the Falcon overflew the ground-based lidar POLIS (see Table 2) and on an overpass of the CALIPSO lidar satellite in the Dakar region during the flight on 12 June 2013.

During the flight on 26 June, planned as calibration flight, eight overflights (Fig. 10) were conducted with the system operating in different modes and altitudes with relatively constant atmospheric conditions. It is for this reason that the correction of the different instrumental effects (Sect. 3.1) and the calibration constants (Sect. 3.3) where calculated based on the measurements obtained from this flight.

Because the calibration method proposed in the previous section supposes that the extinction is 0 for range gates at distances shorter than 500 m, only the overflights performed above the aerosol layers were used for the calculation of the calibration constants. For these cases, the SAL top was at around 4000 m.

In order to validate the method and verify the stability of the instrumental corrections and derived calibrations constants, the constants were applied to the measurements of other three flights and compared, during the overflights, with the profiles measured by the POLIS ground-based lidar and CALIPSO satellite. For this propose the flights on 12 June and 10 and 11 July were used.

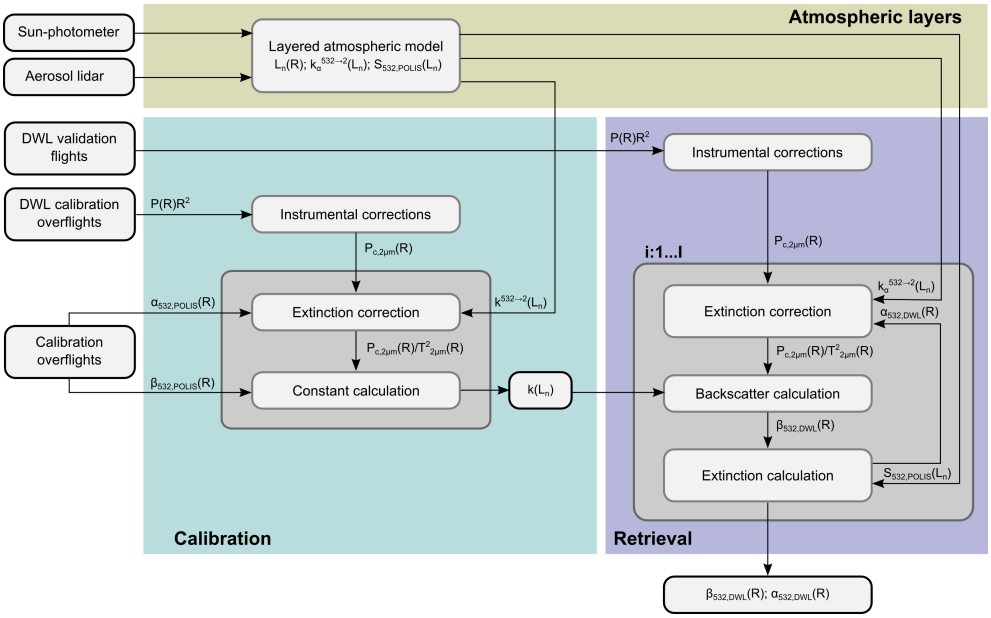


**Figure 9.** Overview of the calibration and retrieval procedure.

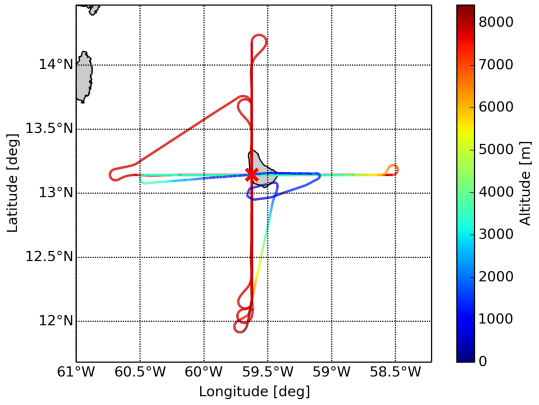


**Figure 10.** Track for the calibration flight on 26 June. The red cross indicates the position of the ground-based lidar POLIS.

### 4.2 Ground-based lidar POLIS data set

POLIS is a small portable six-channel lidar system measuring the $N_2$-Raman shifted backscatter at 387 and 607 nm (nighttime measurements) and the elastic backscatter (cross and parallel polarized) at 355 and 532 nm (day- and nighttime measurements). The full overlap of POLIS was about 200 to 250 m depending on system settings. The system was developed by the Meteorological Institute of the Ludwig-Maximilians-Universität München (Freudenthaler et al., 2009, 2015) and was extended to the six channels mentioned above in the meantime. The measurements site was located in the southwestern part of Barbados at the Caribbean Institute for Meteorology and Hydrology (CIMH) (13°08′55″ N, 59° 37′30″ W, 110 m a.s.l.). For nighttime the Raman methodology (Ansmann et al., 1992) was applied to derive independent profiles of the particle extinction coefficient $\alpha_{532}^{\mathrm{POLIS}}(R)$, the particle backscatter coefficient $\beta_{532}^{\mathrm{POLIS}}(R)$ and thus of the extinction-to-backscatter ratio $S_{532}^{\mathrm{POLIS}}(R)$ (lidar ratio). A possible wavelength dependence between the Raman-shifted wavelengths and the elastically backscattered wavelengths is considered in this methodology, but as both the Saharan dust aerosols as well as marine aerosols are large compared to the lidar wavelength, the wavelength dependency can be neglected in this study. As the signal-to-noise ratio of the Raman signals is comparably low, temporal averages of 1 to 2 hours were used, taking care of the temporal stability of the atmospheric layering. The lidar ratio was then used to analyze the elastic backscattered signals (from both day- and nighttime measurements) with the Klett–Fernald (Fernald, 1984) inversion algorithm to achieve better temporal and vertical resolution.

### 4.3 AERONET sun photometer data set

A CIMEL sun photometer from the AERONET network was operating in Barbados during SALTRACE, performing AOD (aerosol optical depth) measurements at eight different wavelengths. The system was deployed in the facilities of the CIMH collocated with the aerosol lidar POLIS. The site name in the AERONET database is “Barbados_SALTRACE”.

The calibration algorithm presented in the previous section requires the extinction coefficient conversion factor $k_\alpha^{532\rightarrow2022}$ corresponding to each aerosol type as input. In this particular case, where the POLIS lidar operates at 532 nm and the DWL operates at 2.022 µm, the relation between the

extinction coefficients at these two wavelengths, for each aerosol type, has to be determined.

The wavelength dependency of the AOD is characterized by the Ångström exponent, which is usually defined as the slope on the logarithm of the AOD vs. the logarithm of the wavelength. Nevertheless, for this case, the conventional linear fit performed to estimate the Ångström exponent will not provide a good approximation (Fig. 11). For this reason, a second-order fit (King and Byrne, 1976; Eck, et al. 1999) was used to model the logarithm of the AOD as a function of the logarithm of the wavelength. Based on the estimated function, the extinction coefficient conversion factor from 532 nm to 2 µm $k_\alpha^{532\rightarrow2022}$ was calculated.

The sun-photometer-measured AOD is equal to the column-integrated atmospheric extinction coefficient. If different aerosol types are present, the AOD wavelength dependency will depend on the wavelength dependency of the extinction coefficient of each aerosol type and the relative contribution of each one to the total AOD. In order to determine the wavelength dependency of the extinction coefficient corresponding to the different aerosol types identified by the POLIS lidar, a specific set of sun photometer measurements was used.

The marine aerosol extinction coefficient behavior as a function of the wavelength can be estimated by analyzing the AOD as a function of the wavelength for those measurement periods during which no dust or other aerosol types were present. An example of this situation occurred on 7 July. As can be seen in the Fig. 11c, the fitted function has a positive curvature, which is compatible with an aerosol size distribution dominated by intermediate-sized coarse mode particles (O'Neill et al., 2008) as expected for the marine boundary layer.

For the case of the aerosol mixture layer, a different approach was applied. Because there is no day during which only a layer of aerosol mixture was present, only a coarse estimation of the AOD as a function of the wavelength can be achieved. During 6 July, only two aerosol layers were present, the lower one corresponding to marine aerosol and the upper one corresponding to a mixture of aerosols. The contribution of the marine aerosol to the measured total AOD is lower than the contribution of the mixed layer. Based on this fact, the wavelength dependency of the measured AOD can be considered, taking into account the limitations, as representative of the mixed aerosol type extinction coefficient wavelength behavior. Due to its mixed nature, the spectral dependency of this layer is expected to be intermediate with respect to the marine layer and the Saharan layer. The fitted function (Fig. 11b) shows a positive but lower curvature, which is coincident with the expected behavior.

For the case of the Saharan dust present on the uppermost aerosol layer during the flights on 26 June and 10 and 11 July 2013, a similar approach to the one used for the case of the aerosol mixture was applied. Nevertheless, because the contribution of the dust layer to the total AOD is much larger than the contribution of the other two layers, the approximation is much more accurate than in the previous case. In this case, the fitted function shows a negative curvature, which is consistent with the results obtained during SAMUM-2 (Toledano et al., 2011).

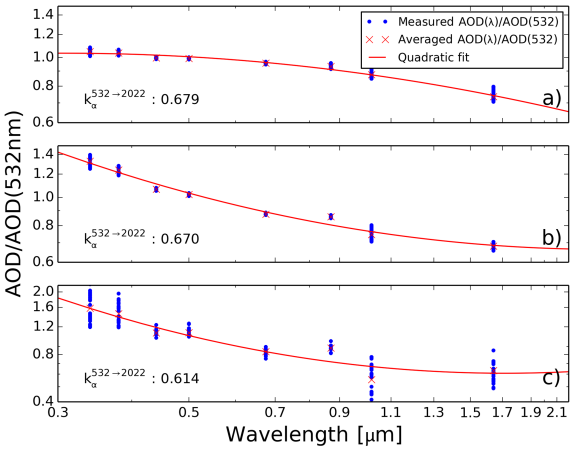


**Figure 11.** Estimated extinction coefficient conversion factor $k_\alpha^{532\rightarrow2022}$ based on sun photometer AOD measurements for three different aerosol types. **(a)** Dust: the wavelength dependency was calculated based on 103 AOD measurements (blue dots) on 26 June (between 12:07 and 21:05 UTC), 10 July (between 10:33 and 21:20 UTC) and 11 July (between 13:16 and 20:09 UTC). **(b)** Mixed aerosol: for this case, 33 AOD measurements taken on the 6 July, between 15:48 and 21:26 UTC, were used for the estimation. **(c)** Marine aerosol: 31 AOD measurements from 7 July, between 12:30 and 19:58 UTC, were used.

The calculated conversion factors for each aerosol type are presented in Table 3.

## 5 Results and discussion

### 5.1 Calibration

As stated in Sect. 3.3, the calculation of the calibration constants $k(L_n)$ starts with the classification of different aerosol layers based on the POLIS measurements taken for each DLR Falcon overflight on 26 June 2013 (Fig. 12). This classification is based on measurements of the lidar intensive properties, the lidar ratio and the particle linear depolarization ratio. The classification scheme is described by Groß et al. (2013). The layer altitudes and properties derived from the overflights were supposed to remain constant for the rest of the flight.

Then, using the extinction coefficient measured by POLIS during each overflight and the extinction coefficient conversion factor calculated from the sun photometer measurements, the backscattered power profiles measured by the DWL during the overflights were corrected by extinction as stated in the Eq. (21). The backscattered DWL profiles cor-

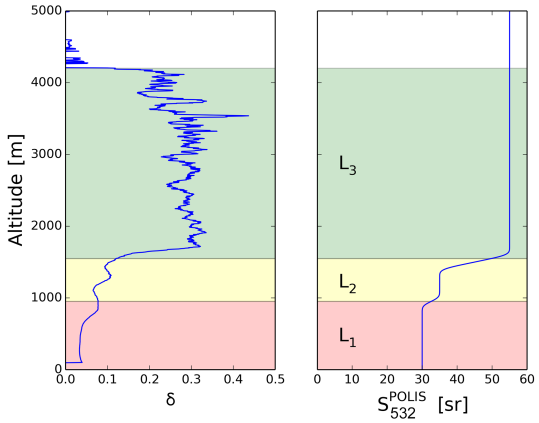


**Figure 12.** Measured particle linear depolarization ratio $\delta$ and the derived lidar ratio $S_{532}^{POLIS}$ for the first calibration overflight (23:56:18–23:56:37 UTC) on 26 June obtained by the ground-based lidar POLIS and the aerosol layers with boundary layer $L_1$ (red, 0 to 1000 m), mixed layer $L_2$ (yellow, 1000 to 1500 m) and SAL $L_3$ (green, 1500 to 4200 m).

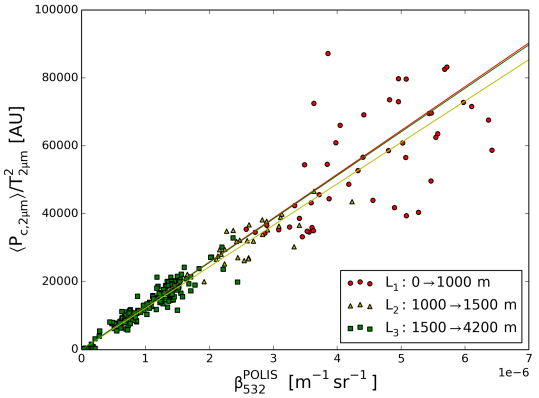


**Figure 13.** Correlation between the extinction-corrected backscattered power of the DWL and the POLIS measured backscatter coefficient for the six calibration overflights on the 26 June and the three different aerosol layers: boundary layer (red dots), mixed layer (yellow triangles) and SAL (green squares).

responding to each overflight result from the average of the vertical profiles acquired during the time periods defined in Table 2. Each averaged measured profile is filtered using a fixed manually adjusted threshold ($\beta_{532}^{DWL} < 10\,Mm^{-1}\,sr^{-1}$) in order to remove clouds.

Finally, the calibration constants $k(L_n)$ corresponding to each layer were estimated using the backscatter coefficient measured by POLIS for the six overflights by a linear LSF (Fig. 13). The estimated inverse of the constants $k^{-1}(L_n)$ and its standard deviation $\sigma_{k^{-1}(L_n)}$ obtained from the LSF are resumed in Table 3.

The data in Fig. 13 show a higher spread in the measurements corresponding to the boundary layer ($L_1$), which is explained by the higher horizontal inhomogeneity of that layer and the accumulated error in the retrieval of the upper layers. In contrast, the measurements corresponding to the mixed layer ($L_2$) and SAL ($L_3$) show a lower spread compatible with their higher homogeneity.

Although the calculated calibration constants $k$ for each aerosol type are very similar, this result seems to be just casual. Each calibration constant (Eq. 20) includes depolarization effects $k_\delta$ and the wavelength dependency of the backscatter coefficient $k_\beta^{532\to2022}$ which are strongly dependent of the aerosol type. The retrieval of extinction-corrected backscatter coefficients profiles still requires the definition of aerosol layers with different lidar ratios to perform the extinction correction. For these reasons, and even though the retrieved calibration constants are similar in this case, the use of different layers is still required.

### 5.2 Backscatter and extinction coefficient retrieval for the flight on 26 June

Using the constants calculated in the previous step and applying the iterative Eqs. (26) and (27) for each measured vertical profile, the backscatter and extinction coefficients for the whole flight were calculated (Fig. 14). The calculation was conducted using five iterations for each profile. The retrieved vertical profiles of the backscatter coefficient from the DWL and POLIS corresponding to the overflights are shown for comparison in Fig. 15.

As can be seen in Figs. 13 and 14, the SAL upper and lower boundaries have a constant altitude of 1.5 and 4 km, respectively, for the whole flight, which corresponds to a square area with sides of 200 km and centered in Barbados. It can also be noted that the SAL has an internal two layer structure with a boundary at around 2.5–3 km. While both sublayers are horizontally homogeneous, the lower sub-layer is characterized by a higher backscatter coefficient $\beta_{532}^{DWL}$ ($\sim 1.5\,Mm^{-1}\,sr^{-1}$) than the upper one ($\sim 0.7\,Mm^{-1}\,sr^{-1}$).

For the measurements corresponding to the time period between 00:05 and 00:20 UTC, a perturbation of the internal structure of the SAL can be observed in coincidence with the presence of clouds on the top of the mixed layer. The vertical wind speed, also available from the DWL, shows a relatively constant upward wind flow with a mean speed of $0.3\,m\,s^{-1}$ above the cloud layer, which is likely to be associated with convection processes.

The non-averaged DWL retrievals presented in Fig. 15 (black dots) illustrate the higher variability of the boundary layer observed during the calibration constant retrieval. Most of the aerosol load is located in the lower 500 m of the boundary layer, with backscatter coefficients $\beta_{532}^{DWL}$ up to $6\,Mm^{-1}\,sr^{-1}$.

**Table 3.** Extinction coefficient conversion factor $k_{\alpha}^{532\rightarrow2022}$, inverse of the calibration constants $k^{-1}$ and its corresponding standard deviation $\sigma_{k^{-1}}$ retrieved for each layer. The mean $\mu$[Mm sr$^{-1}$] and the standard deviation $\sigma$[Mm sr$^{-1}$] of the difference between the retrieved backscatter coefficient from the DWL and POLIS are also shown together with the relative standard deviation ($\sigma/\mu_{\mathrm{POLIS}}$).

| Layer | Calibration | | | Error analysis | | |
|---|---|---|---|---|---|---|
| | $k_{\alpha}^{532\rightarrow2022}$ | $k^{-1}$ | $\sigma_{k^{-1}}$ | μ | $\sigma$ | RSD |
| Boundary layer ($L_1$) | 0.614 | $7.75\times10^{-11}$ | $2.26\times10^{-12}$ | −0.185 | 0.572 | 0.162 |
| Mixed layer ($L_2$) | 0.670 | $8.20\times10^{-11}$ | $1.80\times10^{-12}$ | 0.126 | 0.352 | 0.111 |
| Saharan Air Layer ($L_3$) | 0.679 | $7.80\times10^{-11}$ | $7.85\times10^{-13}$ | −0.068 | 0.217 | 0.165 |

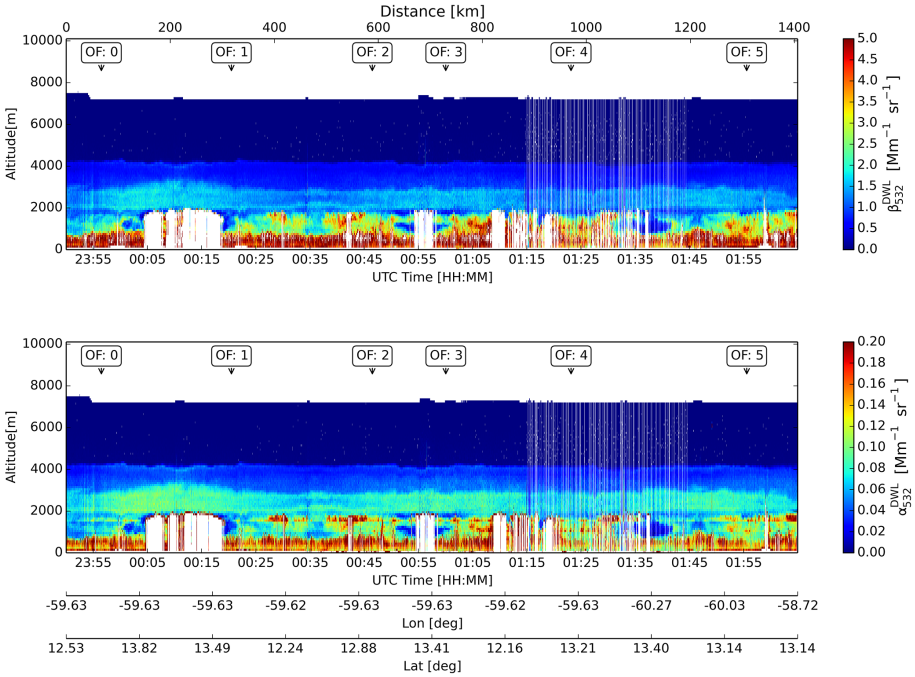


**Figure 14.** Overview of the retrieved backscatter and extinction coefficient for the flight on 26 June. The label "OF" indicates the time of the overflight over POLIS lidar. The white color indicates regions where no atmospheric signal is available (e.g., below clouds, low laser energy).

### 5.3 Validation of the calculated calibration constants

The calibration constants calculated from the measurements taken on 26 June 2013 and the layer model derived from the POLIS measurements on 10 and 11 July 2013 were used to retrieve the backscatter and extinction coefficient for the flights on 10 and 11 July. In this case, only the backscatter coefficient is shown (Fig. 16). The results were compared to the POLIS lidar measurements during the Falcon overflights (Fig. 17).

Similar to the previous case, the retrieved backscatter coefficient profiles for 10 and 11 July show a constant SAL upper boundary at 5 and 4.5 km, respectively. The SAL exhibit for both days the same two sub-layer structure as found on 26 June, with a higher backscatter coefficient in the lower layer than in the upper one.

The comparisons with the POLIS ground-based lidar show good agreement for the retrieved backscatter coefficient corresponding to the SAL. The overall shapes of the vertical profiles as well as the altitudes of the maximums and minimums correspond to each other.

### 5.4 Uncertainty estimation

For each overflight belonging to the calibration flight and validation flights, the retrieved averaged vertical backscatter coefficient profile calculated for each iteration was compared to the measured POLIS vertical profile (Figs. 14 and 16) in order to analyze the root-mean-square difference as a function of the iteration number (Fig. 18). It can be seen that the algorithm converges after two or three iterations. For this case, five iterations were performed for all other retrievals.

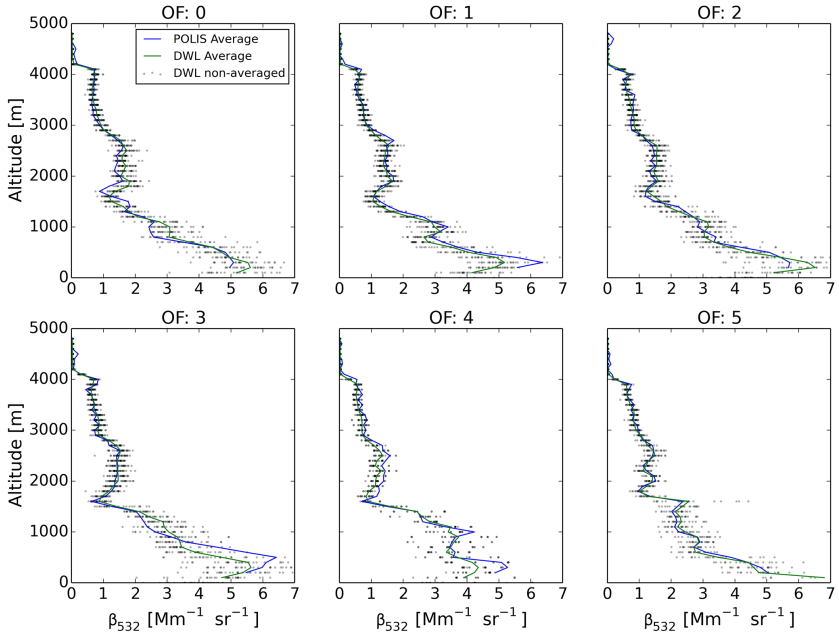


**Figure 15.** Comparison of the non-averaged (grey dots) and averaged (green) backscatter coefficient profiles corresponding to the retrieved data for the flight on the 26 June and the averaged profiles measured by POLIS (blue) during the Falcon overflights (OF).

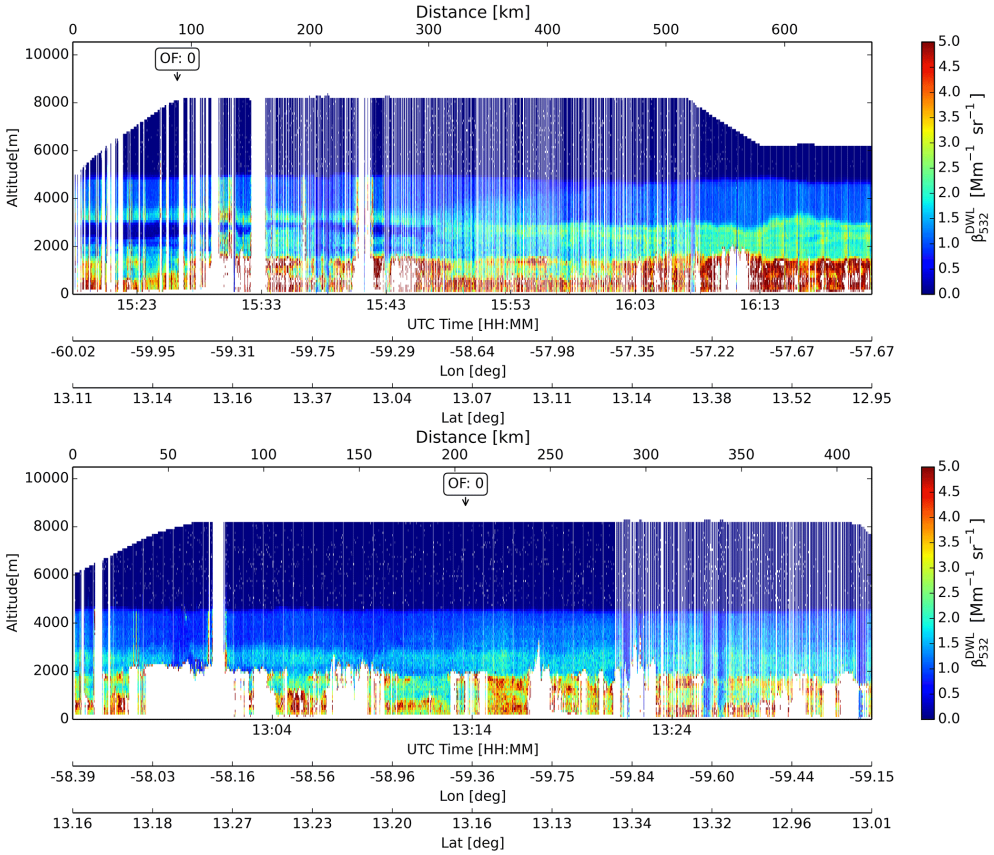


**Figure 16.** Overview of the retrieved backscatter coefficient for the flights on the 10 July (upper panel) and 11 July (lower panel). The label "OF" indicates the approximated time of the overflight over POLIS lidar. The white color indicates regions were no atmospheric signal is available (e.g., below clouds, low laser energy).

**Table 4.** Mean error $\mu$[Mm sr$^{-1}$] and standard deviation $\sigma$[Mm sr$^{-1}$] as function of the aerosol layer and extinction coefficient conversion factor.

| Layer | $k_\alpha^{532\to2022}$ | | $k_\alpha^{532\to2022}$ 20 % higher | | $k_\alpha^{532\to2022}$ 20 % lower | |
|---|---|---|---|---|---|---|
| | $\mu$ | $\sigma$ | $\mu$ | $\sigma$ | $\mu$ | $\sigma$ |
| Boundary layer ($L_1$) | −0.185 | 0.572 | −0.362 | 0.577 | −0.309 | 0.538 |
| Mixed layer ($L_2$) | 0.126 | 0.352 | 0.027 | 0.348 | 0.029 | 0.342 |
| Saharan Air layer ($L_3$) | −0.068 | 0.217 | −0.085 | 0.217 | −0.077 | 0.232 |

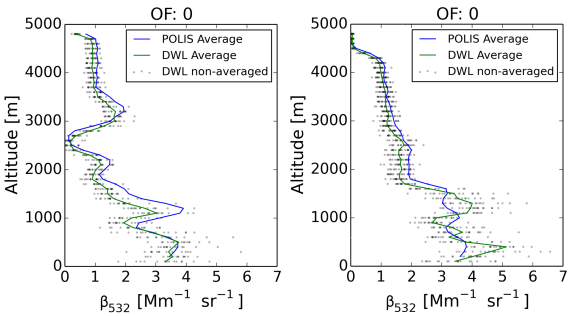


**Figure 17.** Comparison of the non-averaged (grey dots) and averaged (green) backscatter coefficient profiles corresponding to the retrieved data for the flights on 10 July (left) and 11 July (right), and the averaged profiles measured by POLIS (blue) during the Falcon overflights (OF).

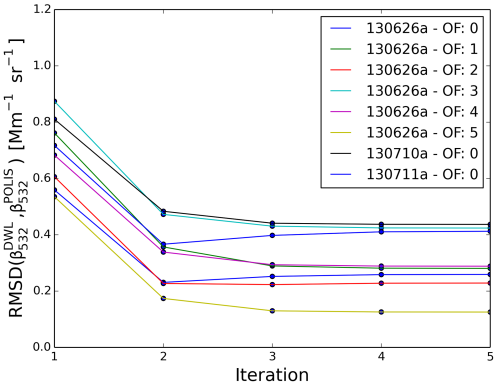


**Figure 18.** Root-mean-square difference (RMSD) between the backscatter coefficients derived from the DWL and POLIS, calculated for each iteration and overflight. The backscatter coefficients of the three layers are used for the calculation.

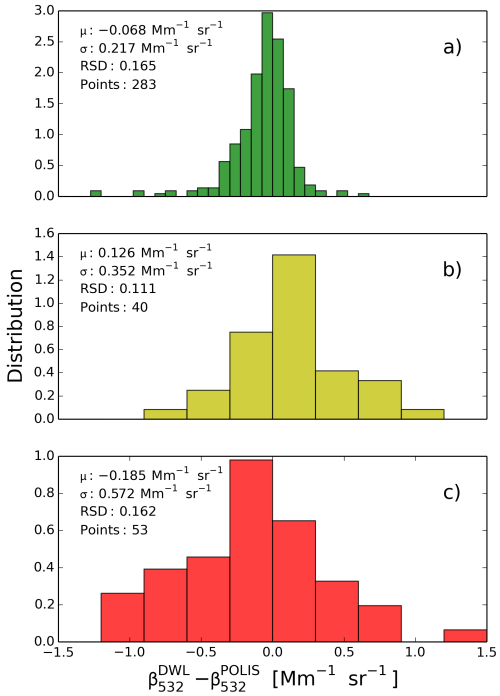


**Figure 19.** Distribution of the difference between the averaged retrieved DWL backscatter coefficient profiles and the averaged POLIS profiles for each overflight and layer on 26 June, 10 July and 11 July: the upper dust layer **(a)**, the mixed aerosol layer **(b)** and the lower marine aerosol layer **(c)**. Mean difference μ, standard deviation of the difference $\sigma$, relative standard deviation (RSD) of the difference with respect to the mean of backscatter coefficient measured by POLIS and number of data points are given for each layer.

In order to characterize the uncertainties of the DWL backscatter coefficient retrieval, the difference between the averaged DWL backscatter profiles and the POLIS measurements is shown as a histogram for each layer (Fig. 19) with their corresponding mean difference and the standard deviation of the differences.

Figure 19 shows a change in the standard deviation as a function of the measured layer. The largest standard deviation is found in the boundary layer. This can be explained by two reasons: the representativeness error caused by the higher variability of the boundary layer and a larger extinction estimation uncertainty caused by the accumulated error in the previous two layers. As was explained in Sect. 4.3, the extinction coefficient conversion factor of the mixed layer was probably overestimated due to the impossibility to separate the effect of the marine aerosol layer and the mixed layer. This can be an explanation for the higher bias observed in the boundary layer measurements.

In order to investigate the effect of the uncertainty of the conversion factor on the retrieved values, the backscatter coefficients, the extinction coefficients and the error distribu-

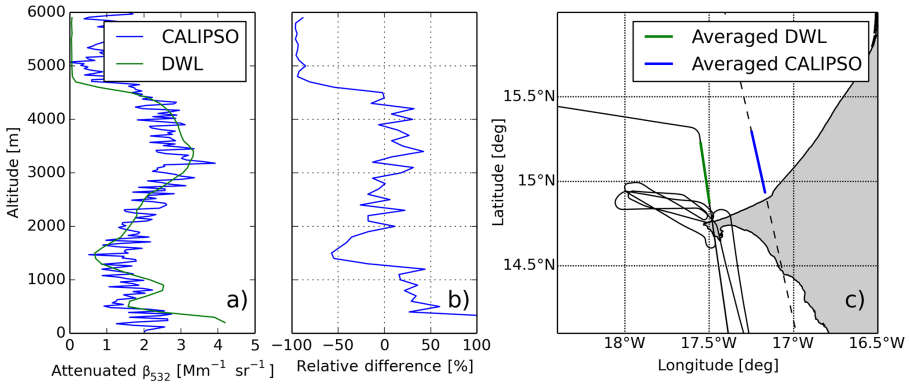


**Figure 20. (a)** Comparison of the averaged attenuated backscatter profiles retrieved from the DWL (green) and the corresponding averaged profile measured by CALIPSO (blue) during its overpass over Dakar region on 12 June. **(b)** Relative difference between the backscatter profiles retrieved from the DWL and the corresponding profile measured by CALIPSO as function of the altitude. **(c)** DLR Falcon (black, solid) and CALIPSO (black, dashed) tracks, together with the averaged sections (green for the DWL and blue for CALIPSO).

tions were recalculated using conversion factors 20 % higher and 20 % lower than the values estimated in Sect. 4.3 (Table 4).

It can be seen from Table 4 that the estimated conversion factors are of the right magnitude considering that a change of ±20 % generally increases the error of the retrieved backscatter coefficient.

### 5.5 Validation with CALIPSO

In order to perform an independent validation, the proposed method was applied to retrieve the attenuated backscatter coefficients (Eq. 20) for the flight on 12 June (Fig. 20a). During that flight, the DLR Falcon and the CALIPSO satellite performed simultaneous measurements on similar tracks (Fig. 20c). The aerosol layer used in this case consisted of one layer corresponding to Saharan dust and the corresponding calibration constant (Table 3) was used. The retrieved attenuated backscatter coefficient profile was compared with the corresponding CALIPSO attenuated backscatter profile (Level 1 data product).

As the measurements were performed during day, the attenuated backscatter profile retrieved from CALIPSO presents high levels of noise. Nevertheless, the comparison shows a good quantitative agreement between the CALIPSO and the DWL profiles (Fig. 20b) for altitudes between 500 and 4500 m. The discrepancy observed in the boundary layer can be explained, as was mentioned before, by its higher variability. However, the difference observed for altitudes higher than 4500 m can be explained by the lack of DWL signal due to the very low aerosol concentrations.

## 6 Summary and conclusions

A new technique for the calibration of coherent DWL intensity to obtain backscatter and extinction coefficient was presented and the derived results were validated with ground-based and satellite lidar measurements. The comparisons show good agreement between the coherent DWL operating at 2 µm and the ground-based aerosol lidar working at 532 nm, with a discrepancy lower than 20 % in most of the cases.

The presented method can be applied to other lidar systems for which the molecular return intensity is too low to be used as reference for calibration. Although in the case of airborne systems the extinction corresponding to the first 500 m can be normally neglected, for ground-based systems it has to be determined and its influence corrected before the method can be applied.

The requirement of a ground-based aerosol lidar does not represent a serious limitation in the method's range of application considering that they are usually deployed during aerosol characterization campaigns.

In further studies, the use of the sea surface return intensity measured with the airborne DWL will be tested as complementary calibration and monitoring of the stability of the calibration constants.

Auxiliary lidar measurements and modeling of aerosol optical properties based on airborne in situ measurements (Gasteiger et al., 2011) can be used instead of sun photometer measurements to determine the extinction coefficient conversion factor corresponding to each aerosol layer with a higher accuracy and better aerosol type discrimination.

*Acknowledgements.* This work was funded by the Helmholtz Association under grant number VH-NG-606 (Helmholtz-Hochschul-Nachwuchsforschergruppe AerCARE). The SALTRACE campaign was mainly funded by the Helmholtz Association, DLR, LMU and TROPOS. The SALTRACE test flights and the local flights on Cape Verde were funded through the DLR internal project VolcATS (Volcanic ash impact on the Air Transport System). CALIOP/CALIPSO data sets were obtained through the EOSDIS

website (https://earthdata.nasa.gov/). The sun photometer work leading to these results has received funding from the European Union Seventh Framework Programme (FP7/2007-2013) under grant agreement nr. 262254 [ACTRIS]. We thank the AERONET teams at GSFC, LOA and UVA for their support.

The article processing charges for this open-access publication were covered by a Research Centre of the Helmholtz Association.

Edited by: U. Wandinger

## References

Ansmann, A. and Müller, D.: Lidar and Atmospheric Aerosol Particles, in: Lidar, edited by: Weitkamp, C., Springer, New York, 105–141, 2005.

Ansmann, A., Wandinger, U., Riebesell, M., Weitkamp, C., and Michaelis, W.: Independent measurement of extinction and backscatter profiles in cirrus clouds by using a combined Raman elastic-backscatter lidar, Appl. Optics, 31, 7113–7113, 1992.

Ansmann, A., Petzold, A., Kandler, K., Tegen, I., Wendisch, M., Müller, D., Weinzierl, B., Müller, T., and Heintzenberg, J.: Saharan Mineral Dust Experiments SAMUM-1 and SAMUM-2: What have we learned?, Tellus B, 63, 403–429, 2011.

Böckmann, C., Wandinger, U., Ansmann, A., Bösenberg, J., Amiridis, V., Boselli, A., Delaval, A., De Tomasi, F., Frioud, M., Grigorov, I., Hågård, A., Horvat, M., Iarlori, M., Komguem, L., Kreipl, S., Larchevêque, G., Matthias, V., Papayannis, A., Pappalardo, G., Rocadenbosch, F., Rodrigues, J., Schneider, J., Shcherbakov, V., and Wiegner, M.: Aerosol lidar inter- comparison in the framework of the EARLINET project: Part II – Aerosol backscatter algo- rithms, Appl. Optics, 43, 977–989, 2004.

Bou Karam, D., Flamant, C., Knippertz, P., Reitebuch, O., Pelon, J., Chong, M., and Dabas, A.: Dust emissions over the Sahel associated with the West African monsoon intertropical discontinuity region: A representative case-study, Q. J. Roy. Meteor. Soc., 134, 621–634, 2008.

Bufton, J. L., Hoge, F. E., and Swift, R. N.: Airborne measurements of laser backscatter from the ocean surface, Appl. Optics, 22, 2603–2618, 1983.

Cutten, D. R., Rothermel, J., Jarzembski, M. A., Hardesty, R. M., Howell, J. N., Tratt, D. M., and Srivastava, V.: Radiometric calibration of an airborne $CO_2$ pulsed Doppler lidar with a natural earth surface, Appl. Optics, 41, 3530–3537, 2002.

Eck, T. F., Holben, B. N., Reid, J. S., Dubovik, O., Smirnov, A., O'Neill, N. T., and Slutsker, I.: Wavelength dependence of the optical depth of biomass burning, urban, and desert dust aerosols, J. Geophys. Res., 104, 31333–31349, 1999.

Fernald, F. G.: Analysis of atmospheric lidar observations: some comments, Appl. Optics, 23, 652–653, 1984.

Frehlich, R. G. and Kavaya, M. J.: Coherent laser radar performance for general atmospheric refractive turbulence, Appl. Optics, 30, 5325–5352, 1991.

Freudenthaler, V., Esselborn, M., Wiegner, M., Heese, B., Tesche, M., Ansmann, A., Müller, D., Althause, D., Wirth, M., Fix, A., Ehret, G., Knippertz, P., Toledano, C., Gasteiger, J., Garhammer, M., and Seefeldner, M.: Depolarization ratio profiing at several wavelengths in pure Saharan dust during SAMUM 2006, Tellus B, 61, 165–179, 2009.

Freudenthaler, V., Seefeldner, M., Groß, S., and Wandinger, U.: Accuracy of linear depolarisation ratios in clean air ranges measured with POLIS-6 at 355 and 532 nm, Proceeding of 27. International Laser Radar Conference, 5–10 July 2015, New York, 2015.

Gasteiger, J., Wiegner, M., Groß, S., Freudenthaler, V., Toledano, C., Tesche, M., and Kandler, K.: Modelling lidar-relevant optical properties of complex mineral dust aerosols, Tellus B, 63, 725–741, 2011.

Groß, S., Esselborn, M., Weinzierl, B., Wirth, M., Fix, A., and Petzold, A.: Aerosol classification by airborne high spectral resolution lidar observations, Atmos. Chem. Phys., 13, 2487–2505, doi:10.5194/acp-13-2487-2013, 2013.

Heintzenberg, J.: The SAMUM-1 experiment over Southern Morocco: Overview and introduction, Tellus Series B, 61, 2–11, 2009.

Henderson, S. W., Suni, P. J. M., Hale, C. P., Hannon, S. M., Magee, J. R., Bruns, D. L., and Yuen, E. H.: Coherent laser radar at 2 µm using solid-state lasers, IEEE T. Geosci. Remote, 31.1, 4–15, doi:10.1109/36.210439, 1993.

Henderson, S. W., Gatt, P., Rees, D., and Huffaker, R. M.: Wind Lidar, in: Laser Remote Sensing, edited by: Fujii, T. and Fukuchi, T., CRC Press, Boca Raton, 469–722, 2005.

Hinds, W. C.: Aerosol Technology: Properties, Behaviour and Measurement of Airborne Particles, John Wiley & Sons, Inc., New York, 304–305, 1999.

Käsler, Y., Rahm, S., Simmet, R., and Kühn, M.: Wake measurements of a multi-MW wind turbine with coherent long-range pulsed doppler wind lidar, J. Atmos. Ocean. Tech., 27, 1529–1532, 2010.

King, M. D. and Byrne, D. M.: A Method for Inferring Total Ozone Content from the Spectral Variation of Total Optical Depth Obtained with a Solar Radiometer, J. Atmos. Sci., 33, 2242–2251, 1976.

Klett, J. D.: Lidar inversion with variable backscatter/extinction ratios, Appl. Optics, 24, 1638–1643, 1985.

Köpp, F., Rahm, S., and Smalikho, I.: Characterization of Aircraft Wake Vortices by 2-µm Pulsed Doppler Lidar, J. Atmos. Ocean. Tech., 21, 194–206, 2004.

Li, Z., Lemmerz, C., Paffrath, U., Reitebuch, O., and Witschas, B.: Airborne Doppler Lidar Investigation of Sea Surface Reflectance at a 355-nm Ultraviolet Wavelength, J. Atmos. Ocean. Tech., 27, 693–704, 2010.

Mahowald, N. M., Baker, A. R., Bergametti, G., Brooks, N., Duce, R. A., Jickells, T. D., Kubilay, N., Prospero, J. M., and Tegen, I.: Atmospheric global dust cycle and iron inputs to the ocean, Global Biogeochem. Cy., 19, 1–15, 2005.

Menzies, R. T. and Tratt, D. M.: Airborne $CO_2$ coherent lidar for measurements of atmospheric aerosol and cloud backscatter, Appl. Optics, 33, 5698–5711, 1994.

O'Connor, E. J., Illingworth, A. J., and Hogan, R. J.: A technique for autocalibration of cloud lidar, J. Atmos. Ocean. Tech., 21, 777–786, 2004.

O'Neill, N. T., Eck, T. F., Reid, J. S., Smirnov, A., and Pancrati, O.: Coarse mode optical information retrievable using ultraviolet to short-wave infrared Sun photometry: Application to United Arab Emirates Unified Aerosol Experiment data, J. Geophys. Res., 113, D05212, doi:10.1029/2007JD009052, 2008.

Prospero, J. M.: Long-range transport of mineral dust in the global atmosphere: Impact of African dust on the environment of the southeastern United States, P. Natl. Acad. Sci. USA., 96, 3396–3403, 1999.

Reitebuch, O.: Wind Lidar for Atmospheric Research, in: Atmospheric Physics, edited by: Schumann, U., Springer, Berlin Heidelberg, 487–507, 2012.

Reitebuch, O., Werner, C., Leike, I., Delville, P., Flamant, P. H., Cress, A., and Engelbart, D.: Experimental validation of wind profiling performed by the airbone 10- µm heterodyne Doppler Lidar WIND, J. Atmos. Ocean. Tech., 18, 1331–1344, 2001.

Schumann, U., Weinzierl, B., Reitebuch, O., Schlager, H., Minikin, A., Forster, C., Baumann, R., Sailer, T., Graf, K., Mannstein, H., Voigt, C., Rahm, S., Simmet, R., Scheibe, M., Lichtenstern, M., Stock, P., Rüba, H., Schäuble, D., Tafferner, A., Rautenhaus, M., Gerz, T., Ziereis, H., Krautstrunk, M., Mallaun, C., Gayet, J.-F., Lieke, K., Kandler, K., Ebert, M., Weinbruch, S., Stohl, A., Gasteiger, J., Groß, S., Freudenthaler, V., Wiegner, M., Ansmann, A., Tesche, M., Olafsson, H., and Sturm, K.: Airborne observations of the Eyjafjalla volcano ash cloud over Europe during air space closure in April and May 2010, Atmos. Chem. Phys., 11, 2245–2279, doi:10.5194/acp-11-2245-2011, 2011.

Seifert, P., Ansmann, A., Mattis, I., Wandinger, U., Tesche, M., Engelmann, R., Müller, D., Pérez, C., and Haustein, K.: Saharan dust and heterogeneous ice formation: Eleven years of cloud observations at a central European EARLINET site, J. Geophys. Res., 115, D20201, doi:10.1029/2009JD013222, 2010.

Smalikho, I.: Techniques of wind vector estimation from data measured with a scanning coherent Doppler Lidar, J. Atmos. Ocean. Tech., 20, 276–291, 2003.

Sonnenschein, C. M. and Horrigan, F. A.: Signal-to-Noise Relationships for Coaxial Systems that Heterodyne Backscatter from the Atmosphere, Appl. Optics, 10, 1600–1604, 1971.

Toledano, C., Wiegner, M., Groß, S., Freudenthaler, V., Gasteiger, J., Müller, D., Müller, T., Schladitz, A., Weinzierl, B., Torres, B., and O'Neill, N. T.: Optical properties of aerosol mixtures derived from sun-sky radiometry during SAMUM-2, Tellus Series B, 63, 635–648, 2011.

Weinzierl, B., Sauer, D., Minikin, A., Reitebuch, O., Dahlkötter, F., Mayer, B., Emde, C., Tegen, I., Gasteiger, J., Petzold, A., Veira, A., Kueppers, U., and Schumann, U.: On the visibility of airborne volcanic ash and mineral dust from the pilot's perspective in flight, J. Phys. Chem. Earth, 45, 87–102, 2012.

Weissmann, M., Busen, R., Dörnbrack, A., Rahm, S., and Reitebuch, O.: Targeted observations with an airborne wind lidar, J. Atmos. Ocean. Tech., 22, 1706–1719, 2005.

Atmos. Chem. Phys., 16, 4675–4692, 2016
www.atmos-chem-phys.net/16/4675/2016/
doi:10.5194/acp-16-4675-2016


Atmospheric Chemistry and Physics Open Access EGU

# Vertical wind retrieved by airborne lidar and analysis of island induced gravity waves in combination with numerical models and in situ particle measurements

**Fernando Chouza[1], Oliver Reitebuch[1], Michael Jähn[2], Stephan Rahm[1], and Bernadett Weinzierl[1,3]**

[1]Deutsches Zentrum für Luft- und Raumfahrt (DLR), Institut für Physik der Atmosphäre, Oberpfaffenhofen, Germany
[2]Leibniz Institute for Tropospheric Research, Leipzig, Germany
[3]University of Vienna, Faculty of Physics, Boltzmanngasse 5, 1090 Wien, Austria

*Correspondence to:* Fernando Chouza (fernando.chouza@dlr.de)

Received: 14 December 2015 – Published in Atmos. Chem. Phys. Discuss.: 19 January 2016
Revised: 29 March 2016 – Accepted: 29 March 2016 – Published: 14 April 2016

**Abstract.** This study presents the analysis of island induced gravity waves observed by an airborne Doppler wind lidar (DWL) during SALTRACE. First, the instrumental corrections required for the retrieval of high spatial resolution vertical wind measurements from an airborne DWL are presented and the measurement accuracy estimated by means of two different methods. The estimated systematic error is below $-0.05\,\mathrm{m\,s^{-1}}$ for the selected case of study, while the random error lies between 0.1 and $0.16\,\mathrm{m\,s^{-1}}$ depending on the estimation method.

Then, the presented method is applied to two measurement flights during which the presence of island induced gravity waves was detected. The first case corresponds to a research flight conducted on 17 June 2013 in the Cabo Verde islands region, while the second case corresponds to a measurement flight on 26 June 2013 in the Barbados region. The presence of trapped lee waves predicted by the calculated Scorer parameter profiles was confirmed by the lidar and in situ observations. The DWL measurements are used in combination with in situ wind and particle number density measurements, large-eddy simulations (LES), and wavelet analysis to determine the main characteristics of the observed island induced trapped waves.

## 1 Introduction

Large amounts of Saharan dust are transported every year across the Atlantic into the Caribbean region (e.g. Prospero, 1999; Prospero and Mayol-Bracero, 2013). The Cabo Verde and Barbados islands, located along the main Saharan dust transport path, interact with the dust advective flow through different mechanisms, including island induced gravity waves. This interaction can give place to changes in the dust sedimentation rates, the vertical mixing, and clouds formation among other effects (e.g. Engelmann et al., 2011; Savijärvi and , 2004; Cui et al., 2012).

In order to provide new insights into the different processes that affect the Saharan mineral dust during the long-range transport from the Sahara into the Caribbean, the Saharan Aerosol Long-range Transport and Aerosol-Cloud-Interaction Experiment (SALTRACE: http://www.pa.op.dlr.de/saltrace) took place in June and July 2013. In the framework of SALTRACE, 31 research flights were conducted between 10 June and 15 July 2013 by the DLR (Deutsches Zentrum für Luft- und Raumfahrt) research aircraft Falcon, including several flights in the Cabo Verde islands region and Barbados. The payload deployed on board the Falcon included a DWL (Doppler wind lidar), aerosol, temperature, humidity and wind speed in situ sensors, and dropsondes. The measurement data set generated during the SALTRACE campaign provides a good opportunity to study the generation of gravity waves by the Cabo Verde islands and Barbados and their interaction with the Saharan dust during its transport.

**Published by Copernicus Publications on behalf of the European Geosciences Union.**

Although it is well known that gravity waves can be generated by orography (Smith, 1980; Alexander and Grimsdell, 2013) and thermal effects (e.g. Baik, 1992; Savijärvi and Matthews, 2004), the relative impact of these two mechanisms depend on the specific island topography, location and atmospheric conditions. During the SAMUM-2 campaign, a large-eddy simulation (LES) study was performed in the Cabo Verde region (Engelmann et al., 2011). This study showed that a flat island with the characteristics of the Santiago Island (Cabo Verde) can induce the generation of gravity waves and enhance the aerosol downward mixing, only through its heat island effect, without taking into account its orography. Another recent LES study (Jähn et al., 2016) conducted in the Barbados area also revealed the presence of island induced gravity waves on the lee side of the island and provided further insight into the dust turbulent downward mixing, cloud generation and boundary layer modification in the lee side of the island. In contrast with the previous case, the heating effect and the orography were taken into account in this case.

Although several different measurement techniques were used to analyse gravity waves (e.g. Kirkwood, et al., 2010; Kühnlein et al., 2013; Ehard et al., 2015), including, but not limited to, ground-based lidars and radars, airborne lidars and in situ sensors, balloons and satellites, the use of airborne Doppler wind lidars is unusual (Bluman and Hart, 1988). While horizontal wind measurements retrieved by airborne DWLs are frequently found in the literature (Reitebuch et al., 2001, 2003; Weissmann et al., 2005; De Wekker et al., 2012; Kavaya et al., 2014), only a few high-resolution measurements of vertical winds are reported (Kiemle et al., 2007, 2011; Emmit and Godwin, 2014). Usually, DWLs provide measurements of the relative wind speed between the instrument and the sensed atmospheric volume every second. Using a conically arranged measurement pattern and the velocity-azimuth display (VAD) technique (Reitebuch et al., 2001), three-dimensional measurements of the wind field can be retrieved based on a few tens of measurements, which corresponds to a spatial resolution on the order of a few kilometres for airborne platforms. Although this is enough to resolve the main features of the horizontal wind field, a higher spatial resolution in the vertical wind component is required to perform turbulence, eddy flux and short-wavelength gravity wave studies.

In order to increase the spatial resolution of the vertical wind retrieval, fixed downward (nadir) pointing measurements can be performed instead of the previously mentioned conical scanning pattern. This allows the retrieval of one measurement every second, which is equivalent to a spatial resolution of around 50 to 200 m, depending on the aircraft type and speed. Nevertheless, there are some problems associated with this technique which have to be addressed to allow an accurate vertical wind retrieval.

The paper is organised as follows. Section 2 provides a brief description of the coherent DWL mounted on the Falcon research aircraft of DLR during SALTRACE and an overview of the method applied to retrieve high spatial resolution vertical wind measurements. Then, in Sect. 3, the resulting data set is used in combination with in situ observations and large-eddy simulations to analyse the generation, evolution and interaction with aerosols of island induced gravity waves. Two different cases were analysed: one in the Cabo Verde region and the other in the Barbados Island. The measurements corresponding to both cases and simulation results from the second case are compared in order to determine the similarities and differences between the two cases, as well as the ability of the simulation to reproduce the observed waves and provide a context to the in situ and lidar measurements. Finally, Sect. 4 provides a summary and concluding remarks.

**Table 1.** Key parameters of the DWL.

| Laser | Laser type | Solid-state Tm:LuAG |
|---|---|---|
| | Operation wavelength | 2.02254 µm |
| | Laser energy | 1–2 mJ |
| | Repetition rate | 500 Hz |
| | Pulse length (FWHM) | 400 ns |
| Transceiver | Telescope type | Off-axis |
| | Telescope diameter | 10.8 cm |
| | Transmitted polarization | Circular |
| | Detected polarization | Co-polarised |
| Scanner | Type | Double wedge |
| | Material | Fused silica |
| Data acquisition | Sampling rate | 500 MHz |
| | Resolution | 8 bits |
| | Mode | Single shot acquisition |

## 2 Coherent DWL instrument

### 2.1 Instrument description

During SALTRACE an airborne coherent DWL was deployed on board the DLR Falcon 20 research aircraft. The system, based on an instrument developed by CLR Photonics (Henderson et al., 1993), today Lockheed Martin Coherent Technologies (LMCT), was modified by DLR (Köpp et al., 2004) to provide airborne measurement capabilities. The transceiver head, holding the diode pumped solid-state Tm:LuAG laser, the 10.8 cm diameter afocal transceiver telescope, the receiver optics and detectors, and a double wedge scanner is mounted on the front part of the passenger cabin (Fig. 1), while the laser power supply, the cooling unit, the data acquisition and control electronics are mounted in two separated racks.

The lidar operates at a wavelength of 2.02254 µm, with a pulse full width at half maximum (FWHM) of 400 ns, a pulse energy of 1–2 mJ, and a repetition frequency of 500 Hz. The key system specifications are presented in Table 1.

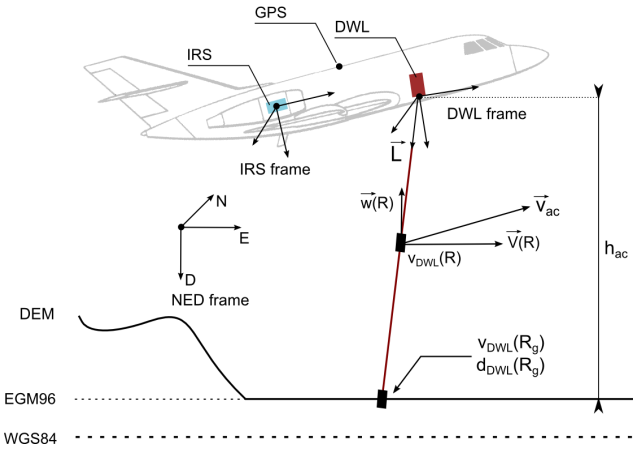


**Figure 1.** Scheme with the different reference frames and magnitudes involved in the vertical wind retrieval calculations. The DWL frame is a reference frame fixed to the DWL transceiver head, the IRS frame is a reference frame fixed to aircraft inertial reference system (IRS) and the NED (North-East-Down) frame is an Earth reference frame for which the $x$ axis is pointing northwards, the $y$ axis is pointing eastwards and the $z$ axis completes the right-handed reference system pointing downwards, parallel to the norm of a plane tangential to the Earth reference ellipsoid. $\boldsymbol{L}$ is a unit vector that represents the DWL line of sight (LOS), $\boldsymbol{v}_{\mathrm{ac}}$ is the aircraft speed, $\boldsymbol{V}$ and $\boldsymbol{w}$ are the horizontal and vertical wind speed respectively in a range R from the lidar, $v_{\mathrm{DWL}}$ is the relative speed measured by the DWL, $h_{\mathrm{ac}}$ is the aircraft altitude about ground level and $R_{\mathrm{g}}$ is the range between the lidar and the ground. WGS84 is the World Geodetic System 1984 standard used by the GPS system, while EGM96 is the Earth Gravitational Model 1996 used for correction. DEM is digital elevation model.

Based on the heterodyne technique, DWLs are able to measure the projection of the relative velocity between the lidar and wind along the laser pulse propagation direction. The backscattered atmospheric signal frequency, which was affected by the Doppler effect, is measured by mixing the backscatter signal with the laser source used to seed the outgoing sensing pulse. Because the outgoing pulse is frequency shifted by 100 MHz with respect to the seeding laser by an acousto-optical modulator (AOM), the DWL is able to resolve the magnitude and sign of the Doppler induced frequency shift. Finally, applying the Doppler equation, the measured frequency difference can be converted to a relative speed.

As mentioned before, the DWL has a dual wedge scanner system mounted in front of the transceiver telescope. While single wedge scanners allow fixed line of sight (LOS) and conical scan patterns with a fixed off-nadir angle, dual wedge scanning systems allow the generation of arbitrary scanning patterns (Rahm et al., 2007; Käsler et al., 2010). In the case of the DLR DWL, the dual wedge scanner system consists of two independently rotating silicon wedges, with a wedge angle of 6° and their flat sides arranged in parallel. Based on the vector form of the Snell's law and the angular measurements $\theta_1$ and $\theta_2$ provided by the rotary encoders attached to each wedge, the DWL pointing direction $\boldsymbol{L}_{\mathrm{DWL}}(\theta_1, \theta_2)$ can be calculated (Amirault et al., 1985).

Particularly in the case of airborne measurements, two operation modes are used: the conical step and stare and the nadir pointing mode. The step and stare mode retrieves horizontal wind speed and direction based on the previously mentioned VAD technique (Reitebuch, 2012; Weissmann et al., 2005; Reitebuch et al., 2001). The measurement pattern consists of a set of up to 24 regularly spaced pointing directions $\boldsymbol{L}_{\mathrm{DWL}}$ distributed in a conical geometry with an accumulation time of 1 or 2 s for each position. On the other side, for the retrieval of vertical wind speed, the LOS vector $\boldsymbol{L}_{\mathrm{DWL}}$ is set pointing approximately in nadir direction, and the measurements are performed with an accumulation time of 1 s. Corrections to the LOS speed resulting from a non-zero nadir angle are discussed in Sect. 2.3.

While horizontal wind speeds are about 1 order of magnitude lower than the aircraft speed (approx. 180 m s$^{-1}$), vertical winds are usually 2 orders of magnitude lower. Because the DWLs measure relative speed between the instrument and the sensed atmospheric volume, the retrieval of the wind speed requires knowing the aircraft speed component of the measurement. This calculation requires especially accurate measurements of the aircraft speed, orientation, and DWL relative position with respect to the aircraft. A second problem associated with this measurement scheme is the projection of the horizontal wind speed. A deviation of the DWL LOS from the nadir direction introduces a projection of the horizontal wind speed in the vertical wind measurement that can be only partially corrected.

Although the vertical wind retrieval would require a constant nadir pointing LOS in order to avoid the projection of the horizontal wind speed, the system configuration during SALTRACE did not perform an automatic correction of the LOS. However, a manual adjustment of the LOS was performed during flight to partially correct the pitch angle of the aircraft. The $\boldsymbol{L}_{\mathrm{DWL}}$ vector was set with an offset angle between $-2$ and $-2.5°$ around the $y$ axis to partially compensate, in combination with the DWL mounting angle, the aircraft pitch (normally between 4 and 6°).

### 2.2 Calculation of the LOS pointing direction

Based on the angles read by the scanner encoders, the output beam direction with respect to the DWL frame can be determined. Nevertheless, because the system is mounted on an aircraft which changes its orientation during the flight, additional transformations are required to relate the lidar LOS vector to an Earth-fixed reference frame.

As can be seen in Fig. 1, the DWL transceiver head is mounted on the front part of the DLR Falcon 20 research aircraft, with the transceiver telescope pointing downwards to allow the measurement of vertical profiles. The orien-

tation of the transceiver head with respect to the aircraft frame (IRS frame) can be described by a set of Euler angles $\boldsymbol{\theta}_{\mathrm{DWL}} = [r_{\mathrm{DWL}}, p_{\mathrm{DWL}}, y_{\mathrm{DWL}}]$ which are determined by the mechanical mounting of the lidar, where $r$ is the roll angle, $p$ the pitch angle and $y$ the yaw angle. Although the magnitude of these angles is small (on the order of a few degrees), they have to be taken into account to avoid large systematic errors in the wind retrieval algorithm. A second set of Euler angles $\boldsymbol{\theta}_{\mathrm{IRS}} = [r_{\mathrm{IRS}}, p_{\mathrm{IRS}}, y_{\mathrm{IRS}}]$, measured by the IRS of the aircraft, describes the orientation of the aircraft with respect to a local NED (North-East-Down) Earth reference frame. The Falcon IRS system provides yaw angle measurements at a rate of 20 Hz, and pitch and roll measurements at 50 Hz. These measurements are then averaged for 1 s to match the DWL accumulation time.

The LOS vector $\boldsymbol{L}_{\mathrm{DWL}}$ calculated based on the angles measured by the scanner encoders can be translated to a reference frame fixed to the Earth applying the following equation

$$\boldsymbol{L} = \begin{bmatrix} L_{\mathrm{N}} \\ L_{\mathrm{E}} \\ L_{\mathrm{D}} \end{bmatrix} = \mathbf{C}^{\mathrm{IRS}}_{\mathrm{NED}}(\boldsymbol{\theta}_{\mathrm{IRS}}) \cdot \mathbf{C}^{\mathrm{DWL}}_{\mathrm{IRS}}(\boldsymbol{\theta}_{\mathrm{DWL}}) \cdot \boldsymbol{L}_{\mathrm{DWL}}(\theta_1, \theta_2), \quad (1)$$

where $\boldsymbol{L}$ is the LOS vector $\boldsymbol{L}_{\mathrm{DWL}}$ referred to the Earth reference system for a given aircraft orientation $\boldsymbol{\theta}_{\mathrm{IRS}}$, $\mathbf{C}^{\mathrm{IRS}}_{\mathrm{NED}}(\boldsymbol{\theta}_{\mathrm{IRS}})$ is a coordinate transformation matrix between the IRS and the NED reference frames based on the IRS measurements and the $\mathrm{C}^{\mathrm{DWL}}_{\mathrm{IRS}}(\boldsymbol{\theta}_{\mathrm{DWL}})$ is a coordinate transformation matrix between the DWL reference frame and IRS reference frame, calculated for a set of mounting angles $\boldsymbol{\theta}_{\mathrm{DWL}}$ (Grewal et al., 2007).

### 2.3 Vertical wind retrieval method

For an airborne DWL with a given pointing direction, the retrieved velocity corresponds to the relative speed, projected on the laser beam direction of propagation, between the aircraft and the atmospheric target or ground surface contained by the sensed volume at distance $R$. This relation is summarized by the equation

$$v_{\mathrm{DWL}}(R) = \boldsymbol{L} \cdot \boldsymbol{v}_{\mathrm{ac}} + \boldsymbol{L} \cdot \boldsymbol{V}(R) + \boldsymbol{L} \cdot \boldsymbol{w}(R), \quad (2)$$

where $v_{\mathrm{DWL}}(R)$ is the speed measured by the airborne DWL, $\boldsymbol{L}$ is the beam direction of propagation or LOS, $\boldsymbol{v}_{\mathrm{ac}}$ is the aircraft speed, $\boldsymbol{V}(R) = [u(R), v(R), 0]$ and $\boldsymbol{w}(R) = [0, 0, w(R)]$ are the horizontal and the vertical component of the wind speed respectively. In all cases, the vectors are referred to as an Earth reference frame.

The first step in the wind retrieval process is the removal of the aircraft speed projection on the measured LOS. While accurate measurements of the aircraft speed are obtained from a GPS system mounted on the aircraft, the LOS vector $\boldsymbol{L}$ is determined based on the angle measurements of the scanner encoders, the transceiver mounting orientation and the aircraft orientation measured by the IRS.

As mentioned in the previous section, the exact transceiver head mounting angles can be derived from DWL measurements. The proposed method for the mounting angles $\boldsymbol{\theta}_{\mathrm{DWL}}$ estimation is based on surface returns. Previous studies used the fact that the land is immobile to derive alignment parameters for airborne Doppler radars (Bosart et al., 2002) and lidars (Reitebuch et al., 2001; Kavaya et al., 2014). Although this assumption is valid for the case of land returns, in the case of sea surface returns (which is the case of most surface retrievals during SALTRACE), the wind-induced movement of the surface can introduce non depreciable offsets in the retrievals. On the other side, deviations perpendicular to the flight direction are hard to resolve using only surface speed measurements because this parameter is less sensitive to rotations around the aircraft longitudinal axis (roll angle). The proposed method for the mounting orientation estimation is based on a combination of relative surface speeds and distances.

For the case of a range gate corresponding to land surface return, Eq. (2) is reduced to the following expression:

$$v_{\mathrm{DWL}}(R_{\mathrm{g}}) = \boldsymbol{L} \cdot \boldsymbol{v}_{\mathrm{ac}}. \quad (3)$$

As was mentioned in the previous section, the DWL mounting angles are small. Based on this fact, a small angle approximation can be applied to the rotation matrix $\mathbf{C}^{\mathrm{DWL}}_{\mathrm{IRS}}$ from Eq. (1), resulting in the following matrix:

$$\mathbf{C}^{\mathrm{DWL}}_{\mathrm{IRS}}(\boldsymbol{\theta}_{\mathrm{DWL}}) \approx \begin{pmatrix} 1 & -y_{\mathrm{DWL}} & p_{\mathrm{DWL}} \\ y_{\mathrm{DWL}} & 1 & -r_{\mathrm{DWL}} \\ -p_{\mathrm{DWL}} & r_{\mathrm{DWL}} & 1 \end{pmatrix} \quad (4)$$

Then, substituting Eq. (4) in Eq. (1) and the result in Eq. (3), we can write the following linear equation:

$$v_{\mathrm{DWL}}(R_{\mathrm{g}}) = \mathrm{C}^{\mathrm{IRS}}_{\mathrm{NED}}(\boldsymbol{\theta}_{\mathrm{IRS}}) \cdot \begin{pmatrix} 1 & -y_{\mathrm{DWL}} & p_{\mathrm{DWL}} \\ y_{\mathrm{DWL}} & 1 & -r_{\mathrm{DWL}} \\ -p_{\mathrm{DWL}} & r_{\mathrm{DWL}} & 1 \end{pmatrix} \cdot \boldsymbol{L}_{\mathrm{DWL}}(\theta_1, \theta_2) \cdot \boldsymbol{v}_{\mathrm{ac}}. \quad (5)$$

Using a set of land surface return measurements obtained by the lidar operating in conical scanning mode, an overdetermined set of linear equations can be defined. Its solution gives us an estimation of the DWL mounting orientation $\boldsymbol{\theta}_{\mathrm{DWL}}$.

Although it is possible to estimate the mounting angles based only on land surface speed measurements, the additional use of surface distance measurements reduces the amount of required data points and increases the accuracy of the estimation, especially with respect to rotations of the transceiver head around the aircraft longitudinal axis $r_{\mathrm{DWL}}$.

For a range gate corresponding to sea surface return and neglecting Earth curvature effects, the measured distance by the lidar can be approximated by

$$d_{\mathrm{DWL}}(R_{\mathrm{g}}) = \frac{h_{\mathrm{ac}}}{L_{\mathrm{D}}}, \quad (6)$$

where $d_{\mathrm{DWL}}(R_{\mathrm{g}})$ is the distance measured by the lidar, $h_{\mathrm{ac}}$ is the altitude of the DWL measured by the GPS (World Geodetic System 1984 standard, WGS84) and corrected taking in account the Earth Gravitational Model 1996 (EGM96, http://earth-info.nga.mil/GandG/wgs84/gravitymod/egm96/egm96.html), and $L_{\mathrm{D}}$ is the vertical component of the LOS vector $\boldsymbol{L}$ approximated by Eq. (5). While the use of land surface return is also possible, it requires additional processing and the use of a DEM (Digital Elevation Model). For the particular case of SALTRACE, for which most of the measurements were performed over sea, only the sea surface was used as distance reference for the estimation of the mounting orientation.

In order to characterize the stability of the mounting angles of the DWL, three different analyses were performed. First, an analysis was done based on the observation of the changes in the mounting angle for different flight conditions. For a given flight, the surface returns were grouped according to the flight altitude and the mounting angles retrieved using Eqs. (5) and (6). For altitudes below 5000 m, the mounting angles showed a slight change with respect to those retrieved for higher altitudes. This effect can be attributed to small aircraft deformations, mounting angle variation due to the lidar flexible mounting system and the consequent change in the orientation of the lidar with respect to the aircraft IRS.

Then, a second stability analysis between different flights was performed. For each flight, surface returns (land and sea) corresponding to measurements in scanning operation mode were used to retrieve the mounting angle. Only the retrievals corresponding to flight altitudes higher than 5000 m and with vertical aircraft speeds lower than $0.05\,\mathrm{m\,s^{-1}}$ were included in the calculation. An equation system based on Eq. (5) was defined for the case of points retrieved from land surface, while Eq. (6) was used for the case of sea surface returns. For flights for which more than 50 land and sea surface return measurements were available, the equation system was solved. The results are presented in Table 2, together with the results obtained for the same flights using only one of both return types.

As can be seen in Table 2, the estimated mounting pitch angle $p_{\mathrm{DWL}}$ does not show a big difference between both methods. This result is expected because both the distance and the ground speed measurements are strongly affected by deviations in the pitch angle. On the other hand, for the case of the roll mounting angle $r_{\mathrm{DWL}}$, the use of only one method gives place to different solutions between methods and flights, while the combination of both methods gives more stable results. The yaw angle $y_{\mathrm{DWL}}$ is better resolved by the speed measurements, which is compatible with the expected behaviour. In general, the simultaneous use of both methods gives more stable results between flights.

Finally, because the orientation showed to be stable between different flights, the same method was applied using all sea and ground surface returns which fulfill the altitude, vertical velocity and operation mode previously described, independently of the flight. The coincidence with the flight by flight calculation using distance and velocity equations is better than 0.1° for pitch and yaw angles, and better than 0.2° for the roll angle estimation.

The mounting orientation estimation resulting from the last calculation with all flights $\boldsymbol{\theta}_{\mathrm{DWL}} = [0.98, -2.08, 1.62°]$ was used in the horizontal and vertical wind retrieval process for all SALTRACE flight legs flown above 5000 m. For the case of low-level flight legs (< 5000 m) during which the aircraft deformation was relevant and surface returns are available, two different approaches can be applied to correct this effect. If the surface measurements were obtained by the lidar operating in scanning mode, it is possible to recalculate the DWL mounting orientation based on those observations. On the other hand, if the measurements were performed in nadir pointing mode, the mean difference between the surface return speed measured by the lidar $\mathrm{v}_{\mathrm{DWL}}\left(R_{\mathrm{g}}\right)$ and their estimation $\boldsymbol{L} \times \boldsymbol{v}_{\mathrm{ac}}$ can be subtracted from the retrievals corresponding to atmospheric range gates $v_{\mathrm{DWL}}(R)$ in order to partially compensate this effect.

For the particular case of vertical wind measurements, the LOS vector $\boldsymbol{L}$ has to be pointing downwards during the measurements. The better this condition is fulfilled, the better the retrieved vertical wind measurements will be. Small deviations from vertical pointing, introduces a projection of the horizontal wind speed on the LOS which cannot be distinguished from the vertical wind component. For example, for a horizontal wind speed of $10\,\mathrm{m\,s^{-1}}$ and a direction contrary to the flight direction, a deviation of 0.5° from nadir in the pitch axis will introduce a bias of $0.09\,\mathrm{m\,s^{-1}}$ in the measured LOS speed.

As mentioned in Sect. 2.1, because no mounting orientation characterization was performed before the campaign and no automatic LOS correction was implemented to compensate changes in the aircraft orientation; the vertical wind measurements include the effects of the horizontal wind projection on the LOS $\boldsymbol{L} \times \boldsymbol{V}(\mathrm{R})$. To partially correct this effect, estimations of the horizontal wind speed based on DWL measurements, dropsondes and models from the same flight leg or close were used.

### 2.4 Validation of method and error analysis

In order to test and validate the method presented in the previous section, the measurements corresponding to a flight performed on 20 June 2013 were used. As a first approach, the mounting angles retrieved in the previous section were applied to estimate the surface return speed for the particular case of the leg flown between 10:31 and 10:45 LT at an altitude of 2900 m during which the lidar was operating in nadir pointing mode. The resulting surface speed measurements show a standard deviation of $\sim 0.4\,\mathrm{m\,s^{-1}}$ for sea return points and $\sim 0.1\,\mathrm{m\,s^{-1}}$ for land return points with a systematic difference of around $-0.4\,\mathrm{m\,s^{-1}}$ between the expected and the measured ground speed values. This difference, as explained

**Table 2.** Estimated lidar mounting angles. The first row of each flight corresponds to the retrieved mounting angle using distance and speed measurements, while the second and third rows correspond to the use of only distance or speed respectively.

| Date | Sea surface points (Distance method) | Land surface points (Speed method) | Estimated mounting angle [°] | | |
|---|---|---|---|---|---|
| | | | $r_{\mathrm{DWL}}$ | $p_{\mathrm{DWL}}$ | $y_{\mathrm{DWL}}$ |
| | **58** | **304** | **0.91** | **−2.09** | **1.64** |
| 12.06.13 | 58 | – | 0.82 | −2.14 | 3.23 |
| | – | 304 | 0.66 | −2.10 | 1.61 |
| | **277** | **500** | **1.00** | **−2.07** | **1.63** |
| 18.06.13 | 277 | – | 1.31 | −2.13 | −1.94 |
| | – | 500 | 0.11 | −2.11 | 1.55 |
| | **60** | **136** | **0.99** | **−2.07** | **1.63** |
| 13.07.13 | 60 | – | 1.09 | −2.11 | −0.04 |
| | – | 136 | 0.89 | −2.08 | 1.63 |
| | **269** | **161** | **0.80** | **−2.13** | **1.64** |
| 14.07.13 | 269 | – | 0.20 | −2.33 | 11.52 |
| | – | 161 | 0.66 | −2.14 | 1.64 |
| | **59** | **397** | **0.92** | **−2.07** | **1.69** |
| 14.07.13 | 59 | – | 1.13 | −2.04 | 1.82 |
| | – | 397 | 0.88 | −2.07 | 1.69 |
| | **5403** | **3449** | **0.98** | **−2.08** | **1.62** |
| All flights | 5403 | – | 0.99 | −2.11 | 1.37 |
| | – | 3449 | 1.00 | −2.08 | 1.62 |

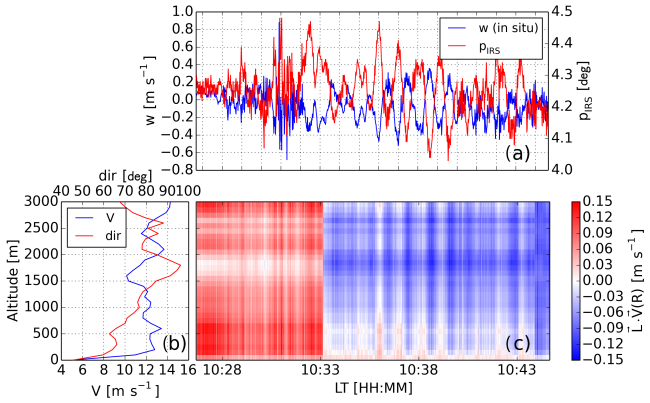


**Figure 2. (a)** Vertical wind speed (blue) measured by the aircraft in situ sensors at 2900 m, together with the aircraft pitch (red). **(b)** Average of the horizontal wind speed (blue) and direction (red) retrieved by the DWL during a previous leg flown along the same track. **(c)** Projection of the horizontal wind speed to the DWL LOS due to changes in the aircraft orientation. At 10:33 LT the DWL LOS was changed by the operator in-flight to reduce the horizontal wind projection.

before, can be attributed to a change in the relative position of the lidar and the aircraft IRS due to aircraft deformations during low level flights. For this case, because measurements using scanning mode were performed during the same flight and under similar speed and altitude conditions, new mounting angles were calculated. The major difference of the recalculated values $\boldsymbol{\theta}_{\mathrm{DWL}} = [0.96, -2.24, 1.68°]$ is in the pitch angle (0.16°), which is consistent with measurements performed to analyse the stability of the mounting orientation during the flight. The recalculated mean difference between the measurements and the estimations obtained based on the new set of mounting angles is 0.036 m s$^{-1}$, while the standard deviation corresponding to land and sea returns remains the same.

From the in situ vertical wind speed measurements of the Falcon nose boom sensors presented in Fig. 2a, it can be seen that the Falcon was flying through gravity waves. These waves induce a change in the aircraft pitch (Fig. 2a), which in turn induce a change in the LOS of the lidar and, therefore, a varying horizontal wind projection with a contribution between ±0.15 m s$^{-1}$ for a horizontal speed of 12 m s$^{-1}$. In order to partially correct this feedback effect, an estimation of the horizontal wind speed and direction obtained from a previous measurement leg (10:00 to 10:15 LT) was used (Fig. 2b). The resulting projection $\boldsymbol{L} \times \boldsymbol{V}(R)$ is shown in Fig. 2c.

Finally, the vertical wind speed can be determined subtracting the aircraft speed and horizontal wind speed projections from the relative speed measured by the DWL. The re-

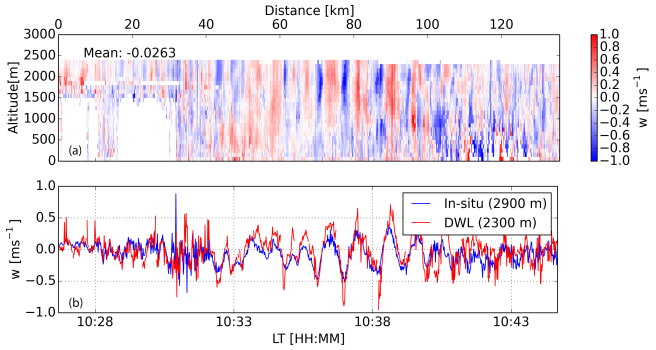


**Figure 3. (a)** DWL vertical wind speed retrieval for a leg flown on 20 June 13 between 10:31 and 10:45 LT. Positive (red) indicates upward winds and negative (blue) indicates downward winds. Between 10:27 and 10:31 LT the DWL coverage is limited due to the presence of clouds (white regions below 1500 m). **(b)** Comparison between the vertical wind retrieved by the Falcon 20 (blue) for an altitude of 2900 m and the DWL retrieval (red) for an altitude of 2300 m.

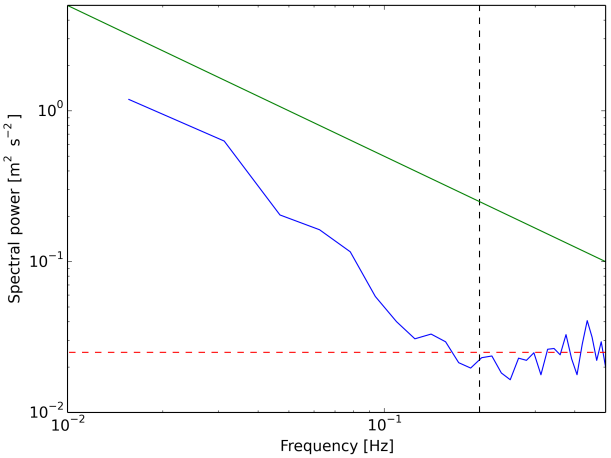


**Figure 4.** Spectral power for the DWL measured vertical wind speed during the flight on 20 June 2013, between 10:31 and 10:45 LT and for an altitude of 2300 m (solid, blue). The expected spectral behaviour according to the Kolmogorov's $-5/3$ law (green line), the noise frequency threshold (black, dotted) and the derived noise floor for the DWL (red, dotted) are shown.

sulting vertical wind speeds are presented in Fig. 3a together with a comparison between the in situ vertical wind speeds measured by the Falcon (Fig. 3b). It has to be noted that the closest DWL measurements are around 500 m below the aircraft, which could explain the difference between the amplitude of the DWL and in situ measurements. Despite this altitude difference, the main features of the vertical wind field (amplitude, oscillation frequency and mean value) are comparable.

In order to estimate the DWL measurement error, two methods were applied. The first method (Frehlich, 2001; O'Connor et al., 2010) is based on the frequency spectrum of the retrieved velocity. For the flight leg presented in Fig. 3, the spectra corresponding to the retrieved vertical wind speed from the DWL measurements at altitude of 2300 m were calculated and averaged. A total of 32 spectra of 64 samples were calculated. A 50 % window overlap factor, a Hanning window and a zero-padding of the missing values was applied to each window for each spectrum calculation (Kiemle et al., 2011). The resulting spectrum, presented in Fig. 4, shows that for frequencies higher than 0.2 Hz the spectrum corresponding to the DWL tends to be a constant value, departing from the Kolmogorov's $-5/3$ law. This high-frequency region represents the spectrum of the random measurement noise. The standard deviation of the measurement is then estimated as the mean of the spectra over its constant region. Based on the presented case, the random measurement error was estimated to be $\sigma_e = 0.16\,\mathrm{m\,s^{-1}}$.

The second method, based on ground return analysis, relies on the fact that the ground surface is not moving. For an ideal system, the difference between the ground return speed measured by the lidar and the aircraft speed projected on the beam direction has to be zero. For a real DWL, the mean of this difference corresponds to the systematic measurement error, while its variations correspond to the lidar random error for high SNR. Based on the land returns, the estimated systematic error is $\mu_e = -0.05\,\mathrm{m\,s^{-1}}$ and random error standard deviation is $\sigma_e = 0.10\,\mathrm{m\,s^{-1}}$.

The errors estimated based on both approaches are on the same order of magnitude. Because the measurement error depends on many different parameters, like SNR, turbulence and flight conditions, relatively small variations in the uncertainty are expected for differing measurement situations.

## 3 Case studies

The vertical wind retrieval method presented in the previous section was applied to the DWL measurements corresponding to two SALTRACE flights during which gravity waves were observed. While the flight corresponding to the first case study took place on 17 June 2013 in the Cabo Verde region (close to the Saharan dust source), the flight analysed in the second case study was conducted in the Barbados region, where the main SALTRACE supersite was located.

### 3.1 Case 1: island induced trapped lee waves in Cabo Verde (17 June 2013)

The synoptic conditions, derived from the ECMWF Era-Interim reanalysis, on the Cabo Verde islands at 12:00 UTC (11:00 LT) on 17 June 2013 are show for 1000 and 700 hPa pressure levels in Fig. 5 (upper panels). Northerly trade winds with a speed on the order of 5–10 $\mathrm{m\,s^{-1}}$ are visible at the 1000 hPa pressure level. For the 700 hPa pressure level the wind changes to easterly direction, which is compatible with the presence of the African Easterly Jet (AEJ).

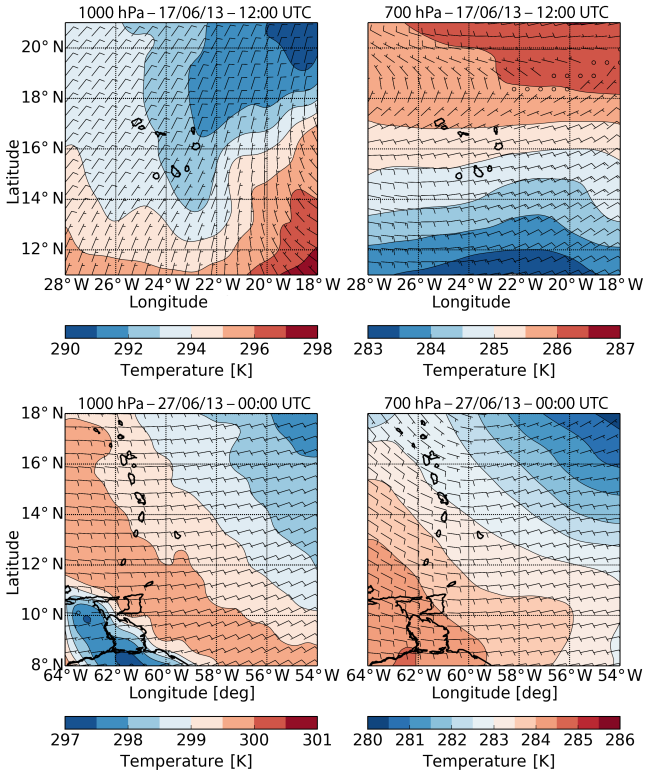


**Figure 5.** Synoptic conditions derived from the ECMWF ERA-Interim reanalysis over the Cabo Verde islands (upper panels) and Barbados (lower panels) for the 17 and 27 June 2013 respectively. Wind vectors (barbs, in m s$^{-1}$) and temperature (in ° K) are shown.

During the morning of 17 June 2013, the Falcon performed a measurement flight in the Cabo Verde islands region, departing from Sal and landing on Praia (Fig. S1 in the Supplement). The flight consisted of three legs between Sal and Praia islands, at altitudes of 4100, 2500 and 900 m respectively. During the ascent phase of the flight, the in situ sensors on board the aircraft recorded vertical profiles of potential temperature, wind speed and direction (Fig. 6a). The horizontal winds retrieved by the DWL during segments of the 1st and 2nd leg (not shown) indicate that the values retrieved by the in situ sensors are representative of the whole flight area and time period. For altitudes below 500 m, a neutrally stratified layer with northerly trade winds can be observed. This layer is capped by a thick strongly stratified trade inversion layer (between 500 and 2000 m) on which the wind direction exhibits a strong shear and a change to north-easterly direction. Above this inversion, the atmosphere shows a weak stratification and relatively constant wind speed and direction. These observations are compatible with the synoptic situation previously described.

According to linear mountain wave theory (e.g. Durran, 1990), the waves that can propagate vertically in the atmosphere can be derived by the use of the Scorer parameter $l^2$

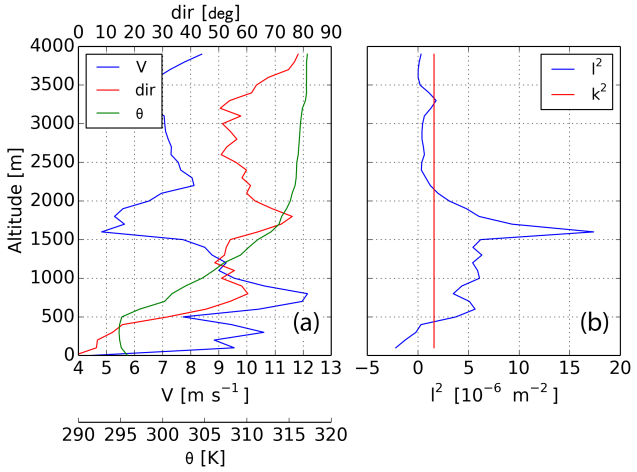


**Figure 6. (a)** Horizontal wind speed (blue), wind direction (red) and potential temperature (green) measured by the Falcon in situ sensors during take-off (10:06 to 10:14 LT). **(b)** Derived Scorer parameter (blue) and approximate wave number corresponding to the observed waves (red).

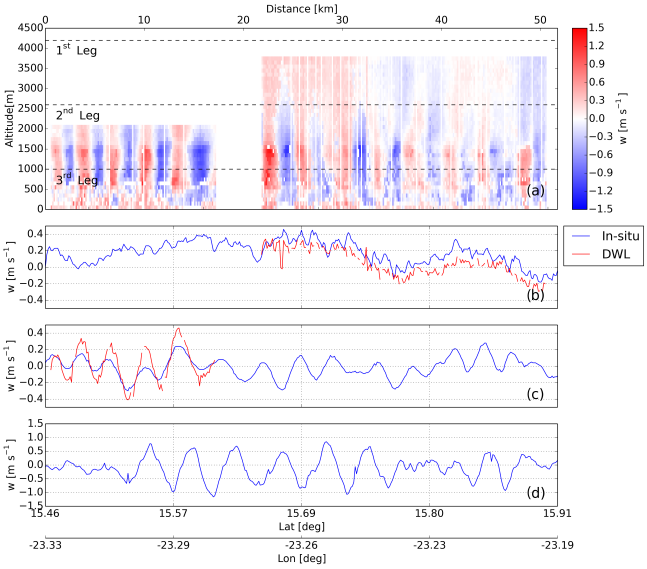


**Figure 7. (a)** Retrieved vertical wind speed by the DWL as a function of the latitude and longitude from legs 1 (10:21 to 10:25 LT) and 2 (10:43 to 10:46 LT), together with the flight levels corresponding to the legs 1, 2 and 3 (11:10 to 11:16 LT) (dashed lines). **(b, c, d)** In situ vertical wind speed corresponding to the legs 1, 2 and 3 (blue line) together with the measured wind corresponding to the uppermost range gate measured on each leg (red line).

(Scorer, 1949), given by

$$l^2 = \frac{N^2}{U^2} - \frac{1}{U}\frac{d^2U}{dz^2}, \quad (7)$$

where $N$ is the Brunt-Väisälä frequency and $U$ is the cross-mountain wind speed. Based on the previously introduced

in situ measurements (Fig. 6a), a profile of the Scorer parameter was calculated (Fig. 6b). Since the difficulty to estimate the second derivate of the wind from real data, an approximated form of the Scorer parameter which neglects the second term (shear term) is used in this study. This simplification is allowed due to the fact that the shear term is dominated by oscillations with wavelengths much smaller than for the waves under analysis (Smith et al., 2002). An additional validation of this approximation was performed based on temperature, humidity and wind speed vertical profiles retrieved from the ECMWF ERA-Interim reanalysis presented in Fig. 5. The Scorer parameter profile calculated based on the model output and including the shear term (not shown) exhibited a similar structure to the approximated profile calculated from the Falcon in situ measurements.

According to the theory, a wave with wavelength $\lambda$ and an associated wave number $k = \frac{2\pi}{\lambda}$ can propagate in the atmosphere if $k^2 < l^2$; otherwise, the wave is evanescent. Trapped lee waves are expected when a layer with high Scorer parameter is bounded by layers with low Scorer parameter. Under such conditions, the energy of the gravity waves is mainly confined in the layer with high Scorer parameter (Durran et al., 2015). As can be seen in Fig. 6b, the conditions for the development of trapped waves are fulfilled for altitudes between 500 and 2000 m, which are coincident with the trade inversion layer lower and upper bound.

Another important parameter to take in account for the study of lee waves is the inverse Froude number, defined as

$$F = \frac{Nh}{U}, \tag{8}$$

where $N$ is the Brunt-Väisälä frequency, $h$ is the island height and $U$ is the cross-mountain wind speed. For an inverse Froude number between 0 and 0.5, the flow behaves as described by the linear theory and waves are expected to form in the lee side of the island (Baines and Hoinka, 1985). For this case study, the Brunt–Väisälä frequency associated with the boundary layer (below 500 m) is approximately $N = 0.01\,\mathrm{s}^{-1}$. This situation leads, together with an inflow speed of $10\,\mathrm{m\,s}^{-1}$ and a maximum island height of 380 m, to a linear flow condition ($F = 0.38$).

The DWL vertical wind measurements presented in Fig. 7a confirm the existence of trapped waves between 500 and 1500 m. At first glance, an apparent wavelength of approximately 5 km and a maximum peak-to-peak amplitude of $1.5\,\mathrm{m\,s}^{-1}$ can be estimated from the measurements presented in Fig. 7a. Unfortunately, although the legs were flown at different altitudes, all were performed along the same track. For this reason, only the apparent wavelength can be estimated from these measurements. This apparent wavelength is always larger than the actual one and related to the angle defined between the flight track and the propagation direction of the waves. Based on the apparent wavelength, the associated apparent wave number was calculated and plotted together with the Scorer parameter profile (Fig. 6b). It can be seen that for the layer on which the trapped waves are observed, the Scorer condition for wave propagation $k^2 < l^2$ is fulfilled, while, for altitudes above 1500 m where evanescent waves are expected ($k^2 > l^2$), the waves exhibit a strong reduction in their amplitude as a function of the altitude ($0.6\,\mathrm{m\,s}^{-1}$ at 2100 m and $0.4\,\mathrm{m\,s}^{-1}$ at 2600 m, Fig. 7c).

Together with the DWL vertical winds, a set of vertical wind speed measurements was retrieved by the Falcon in situ sensors along each measurement leg (Fig. 7b, c and d). Although the vertical wind measurements from the DWL provide a better image of the vertical extension of the wave ducting, the evanescent propagation regime, and the amplitude of the waves than the in situ measurements, the DWL measurements of this case study covers only half of the 1st and one third of the 2nd leg, limiting the spectral range that can be analysed from those measurements. In order to complement the DWL measurements and obtain a more precise picture of the spectral components and extension of the observed waves, the wavelet transform technique using a Morlet wavelet (6th order) was applied (Torrence and Compo, 1998; Woods and Smith, 2010) to the in situ vertical wind measurements of the three measurement legs. Unlike the Fourier transformation, which can only retrieve the frequency of the signal, the wavelet analysis is able to temporally resolve the frequencies of a given signal, similar to the short-time Fourier transformation. For this reason and because the measured waves are restricted to a fraction of the measurement period the wavelet analysis is more adequate than a simple Fourier transformation. The in situ measurements, acquired with a temporal resolution of 1 Hz, were linearly interpolated to a regular spatial grid of 200 m resolution before applying the wavelet transformation to the acquired data sets.

Figure 8 shows the calculated spectral components corresponding to the three legs in situ vertical wind measurements. While the lower leg (Fig. 8, lower panel) exhibits one dominant spectral component with an associated apparent wavelength of 5.2 km, the 2nd leg (Fig. 8, mid panel) shows two spectral peaks with apparent wavelengths of 4.5 and 15.7 km, and the 3rd leg (Fig. 8, upper panel) three peaks with apparent wavelengths of 4.5, 7.53 and 16.5 km. Although some variability in the wavelengths is observed between legs, the modes seem to be in even-harmonic relation. The shorter mode, present in all three legs, shows a strong attenuation in the upper two legs, compatible with the evanescent propagation regime. In contrast, the longer mode, present in the upper two legs, is only slightly attenuated. Previous studies on trapped lee waves (Georgelin and Lott, 2001) showed the presence of upward propagating leaked harmonics above the wave duct. In contrast to that case, the spectral analysis of the lower leg does not show the presence of the harmonics observed in the upper two, which can be attributed to different reasons. On one side, the longer modes have wavelengths comparable to the length of the measurements leg, which limits the confidence of this observation. This limita-

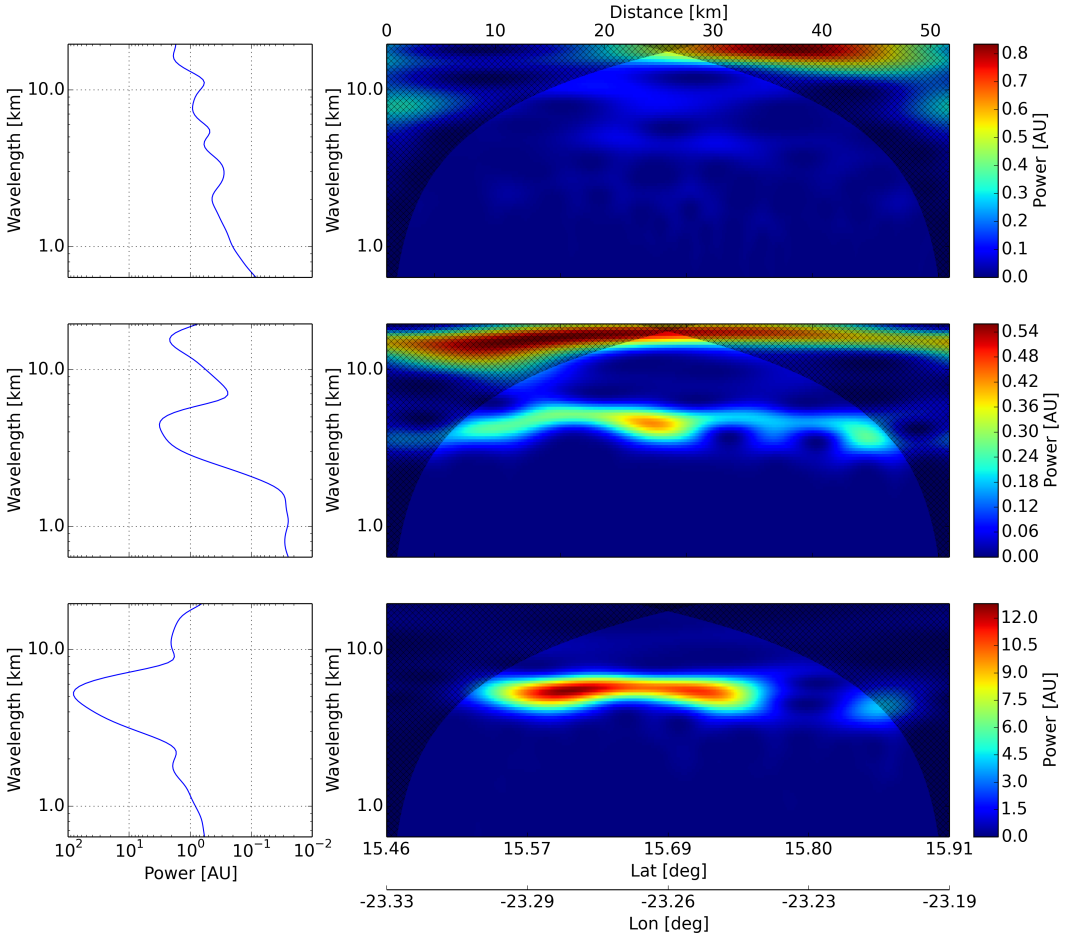


**Figure 8.** In situ vertical wind wavelet analysis corresponding to the three legs flown on 17 June: 1st leg (upper panels), 2nd leg (mid panels) and 3rd leg (lower panels). The hatched areas indicate the cone of influence. The left panels show the average power for each wavelength.

tion is represented by the cone of influence of the wavelet transform, which indicates the region of the wavelet spectra in which edge effects become relevant. On the other side, although the measurement legs were flown within a short time period, changes in the atmospheric conditions could have introduced a modification in the wave propagation and generation conditions. Finally, taking into account that the measurement legs extend along the downwind region of the Boa Vista and Sal islands, an interaction between waves generated by these two islands cannot be discarded.

A second point to be noted from the vertical wind in situ measurements is the change in the position of the wave crests and troughs between the measurements of the 2nd and 3rd leg, which suggest that the waves are not completely stationary.

Together with the vertical wind speed, the DWL measured the backscattered power. Range corrected backscattered power is shown in Fig. 9a together with in situ vertical winds and condensation particle counter (CPC) measurements (Weinzierl et al., 2011) for the three legs (Fig. 9b, c, d). The CPC measurements correspond to the number concentration of particles with a diameter larger than 14 nm. Figure 9a gives a qualitative picture of the aerosol distribution. Below 500 m, a region of high backscatter corresponding to the marine boundary layer can be recognized. The presence of some clouds on top of the marine boundary layer is indicated by high backscatter regions. The interaction between the trapped waves, a thin aerosol layer which extends between 900 and 1300 m, and the bottom of the Saharan Air Layer (SAL) can also be noted. The CPC measurements of the 1st and 2nd legs, corresponding to the legs flown in the SAL, show a relatively homogeneous particle number concentration along the leg, with slightly higher values in the upper one.

As the 3rd measurement leg was flown at an altitude (1000 m) coincident with a strong gradient in the aerosol concentration (Fig. 9a), the CPC measurements show also the effect of the waves in the aerosol distribution, but with a phase difference to the vertical wind speed of 90°. This explains why the waves are only visible in the third leg and not in the upper two, where the aerosol concentration gradient is close to zero. Because the aerosol vertical flux is determined by the

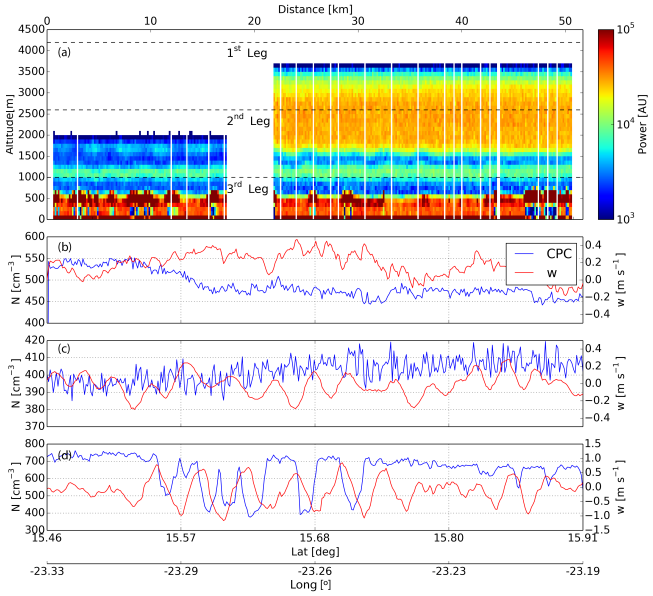


**Figure 9. (a)** Retrieved range corrected backscatter power by the DWL as a function of the latitude and longitude from legs 1 and 2, together with the flight levels corresponding to the legs 1, 2 and 3 (dashed lines). **(b, c, d)** In situ CPC measurements (blue line) corresponding to the legs 1, 2 and 3 together with the in situ measured vertical wind (red line).

integrated product of the vertical wind speed and the variation of the aerosol concentration with respect to the mean along the flight path, a phase difference of 90° between these two quantities results in a zero net flux. The dust loaded air parcels periodically rise and sink without leading to a net downward or upward dust transport.

### 3.2 Case 2: island induced trapped lee waves in Barbados (26 June 2013)

#### 3.2.1 Measurements

During SALTRACE several flights were conducted in the Barbados region. In this study, the measurements corresponding to the flight during the evening of 26 June 2013 are used to study the presence of island induced gravity waves in the lee side of Barbados (Fig. S2). In this case, the flight path had a cross shape centred in Bridgetown city with constant longitude (1st Leg) and latitude (2nd, 3rd and 4th Legs) at an altitude of approximately 7600 m for the first two legs and 3500 and 1200 m for the 3rd and 4th legs respectively.

The synoptic situation at 00:00 UTC (20:00 LT) on 27 June 2013 is show in Fig. 5 (lower panels) for 1000 and 700 hPa pressure levels. Easterly winds with a speed of approximately 10 m s$^{-1}$ can be seen at both pressure levels. Wind speed, direction and potential temperature profiles derived from a dropsonde launched at the end of the second measurement leg (Fig. S2) are presented in Fig. 10a. Below 500 m, an al-

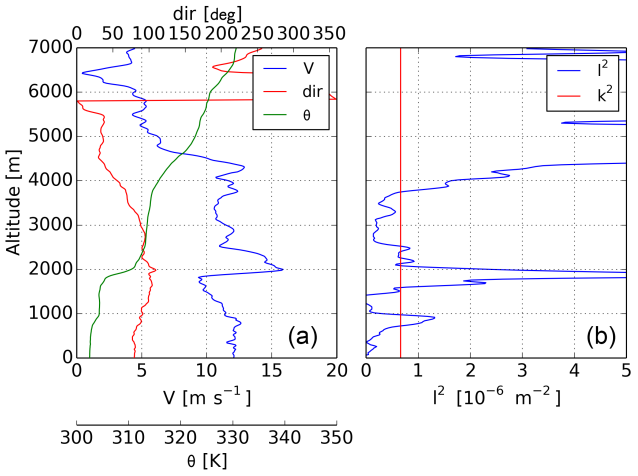


**Figure 10. (a)** Horizontal wind speed (blue), wind direction (red) and potential temperature (green) measured by a dropsonde launched at (26.6.13–22:05 LT). **(b)** Derived Scorer parameter (blue) and approximate wave number corresponding to the observed waves (red).

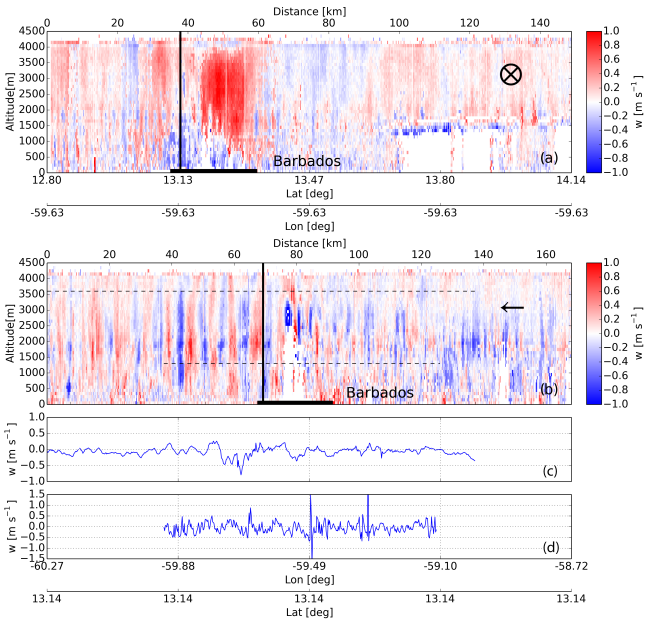


**Figure 11. (a)** Retrieved vertical wind speed by the DWL as a function of the latitude and longitude from leg 1 (19:53 to 20:06 LT), together with the latitude at which legs 2 (21:49 to 22:05 LT), 3 (22:16 to 22:34 LT) and 4 were flown (22:46 to 23:01 LT) (solid line). **(b)** Retrieved vertical wind speed by the DWL as a function of the latitude and longitude from leg 2, the intersection position with the 1st leg (solid line) and the legs 3 and 4 are shown (dashed line). **(c, d, e)** In situ vertical wind speed corresponding to the legs 2, 3 and 4. The average wind inflow direction is indicated on the upper-right corner of panels **(a)** and **(b)**. Barbados indicated in both plots with a horizontal solid black line.

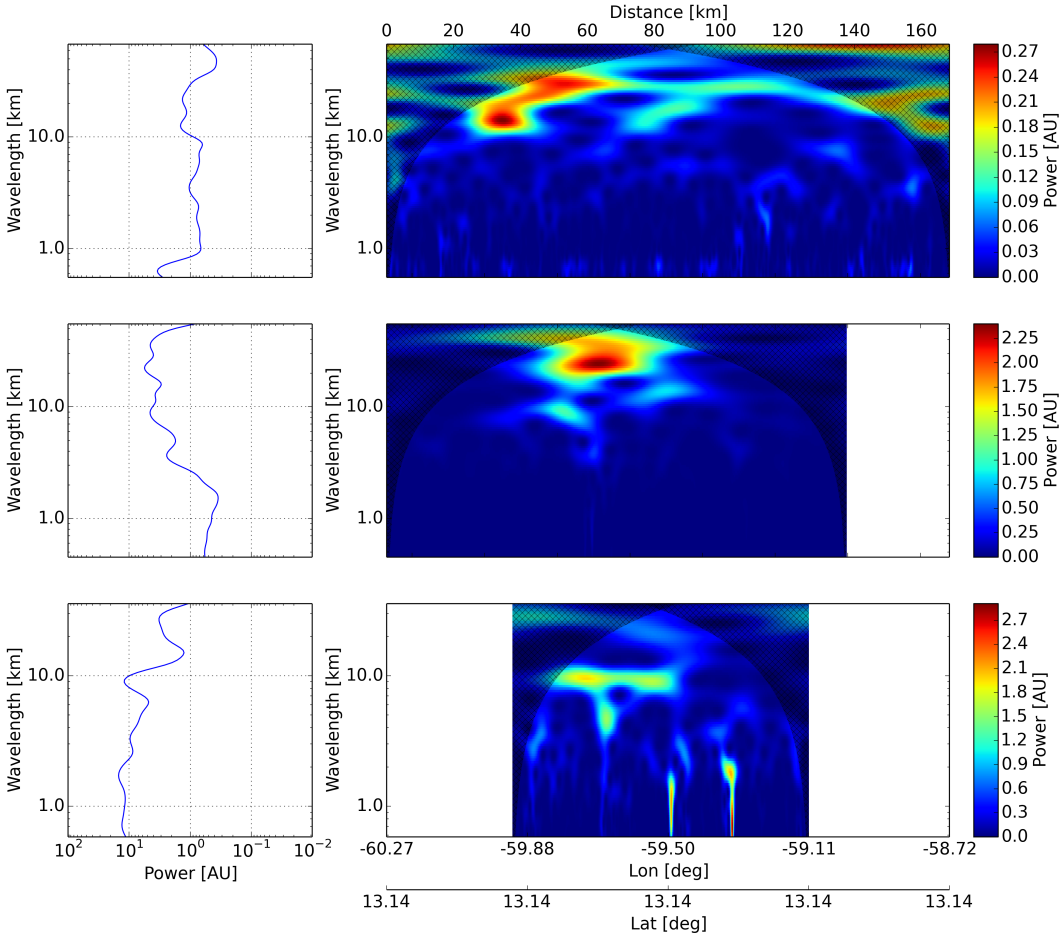


**Figure 12.** In situ vertical wind wavelet analysis corresponding to three legs flown on 26 June: 2nd leg (upper panels), 3rd leg (mid panels) and 4th leg (lower panels). The hatched areas indicate the cone of influence. The left panels show the average power for each wavelength.

most neutrally stratified boundary layer can be recognized, which is topped by a second neutrally stratified layer between 500 and 1800 m. Between 1800 and 2000 m, the sounding measurements show a thin and strong inversion ($\Delta\theta = 6$ K) coincident with the lower bound of the SAL, which extends between 2000 and 4100 m and exhibits a typical weak stratification. Along these three layers, easterly winds with mean wind speed of 10 m s$^{-1}$ are observed, while above the SAL, the stratification increases, the wind speed reduces and the direction reverses. Based on these measurements, the vertical profile of the Scorer parameter in its approximated form (Fig. 10) was calculated. As in the previous case, these measurements were compared to the DWL horizontal wind retrieval and the ECMWF ERA-Interim reanalysis results (not shown) to confirm the representativeness of the measurements.

As expected, the calculated Scorer profile shows a thin layer of high Scorer parameter corresponding to the strong inversion shown at 2000 m, upper bounded by a low Scorer parameter layer which extends up to 3800 m and is associated with the weak stratification of the SAL. Trapped waves at the density discontinuity associated with the inversion at 2000 m are likely to occur in such conditions (Vosper, 2004; Sachsperger et al., 2015). Above the SAL, the Scorer parameter increases due to a decrease in the wind speed and a stronger stability of the atmosphere. The increase in the Scorer parameter can lead to the presence of some wave leakage into the upper layers. Because the boundary layer is very weakly stratified, the inverse Froude number is likely to be very close to zero. Based on the dropsonde observations, the Brunt-Väisälä frequency at the boundary layer was estimated to be $N = 0.0025$ s$^{-1}$ and the cross mountain wind speed approximately 12 m s$^{-1}$, which together with a maximum island height of 340 m gives place to $F = 0.07$, suggesting a linear flow condition.

These expectations were confirmed by the DWL observations, which showed the presence of trapped lee waves on the lee side of Barbados (Fig. 11). The vertical winds measured by the DWL during the first leg (Fig. 11a) show a strong updraft with 1.2 m s$^{-1}$ on the north part of Barbados, which is compatible with a measurement along a crest of the trapped waves. The 2nd leg (Fig. 11b) supports this observa-

tion, showing a wave structure on the lee side, with a wavelength of approximately 9 to 10 km and a vertical extension between 500 m and the top of the SAL. Unfortunately, the low aerosol load above the top of the SAL (4100 m) limits the DWL coverage and the possibility to confirm the leakage by direct lidar measurements. The maximum amplitude (up to 3 m s$^{-1}$ peak to peak) of the waves is found at an altitude of around 2000 m, coinciding with high Scorer parameter layer, the temperature inversion and the maxima in the wind shear altitude. Above and below the inversion, the wave amplitude decrease, which is compatible with the evanescent wave regime $k^2 > l^2$ observed in the Scorer parameter plot (Fig. 10b).

Although in this case the DWL measurement leg is long enough to resolve the spectra of the observed waves below the top of the SAL, the low aerosol load limits the DWL coverage in the upper part of the troposphere. For this reason, a wavelet transform was applied to the in situ vertical wind measurements of the 2nd, 3rd and 4th legs in order to determine the spectra of the waves and whether or not there is leakage of the wave into upper layers (Fig. 12). The spectra of the in situ vertical wind measurements at 7745 m, corresponding to the 2nd leg (Figs. 11c and 12, upper panel), does not show signs of a spectral component with a wavelength around 9 km, suggesting that this propagation mode does not leak into upper layers and that the wave dissipation is dominated by the boundary layer absorption and dispersion (Durran et al., 2015). This finding is compatible with the relatively short wavelength of the observed wave, which leads to a strong vertical decay in the evanescent wave regime regions.

The spectral analysis corresponding to the 3rd and 4th legs (Fig. 12, mid and lower panel) indicate the presence of a spectral component of the same wavelength than the observed by the lidar during the 2nd leg (9.5 km), but with much lower amplitude. Although this change is unexpected due to the short time difference between the 2nd leg (21:49 to 22:05 LT) and the 3rd leg (22:16 to 22:34 LT), relatively small changes in the atmospheric stability conditions could have occurred in the time interval between both measurements, leading to a change in the waves propagation condition.

Together with vertical wind measurements, calibrated backscatter coefficient profiles (Fig. 13a and b) were retrieved from the DWL measurements (Chouza et al., 2015) for the 1st and 2nd leg. A three-layer structure can be recognized in this case, with the marine boundary layer below 500 m, a mixed layer between 500 and 2000 m, and the SAL between 2000 and 4100 m. On the 2nd leg, a wave structure can be identified in the boundary between the SAL and the mixed layer at an altitude of 2000 m on the lee side of Barbados (Fig. 13b). Because the 3rd and 4th legs were flown at altitudes where the gradient in the aerosol concentration was very low, no signature of waves is observed in this case (Fig. 13c and d).

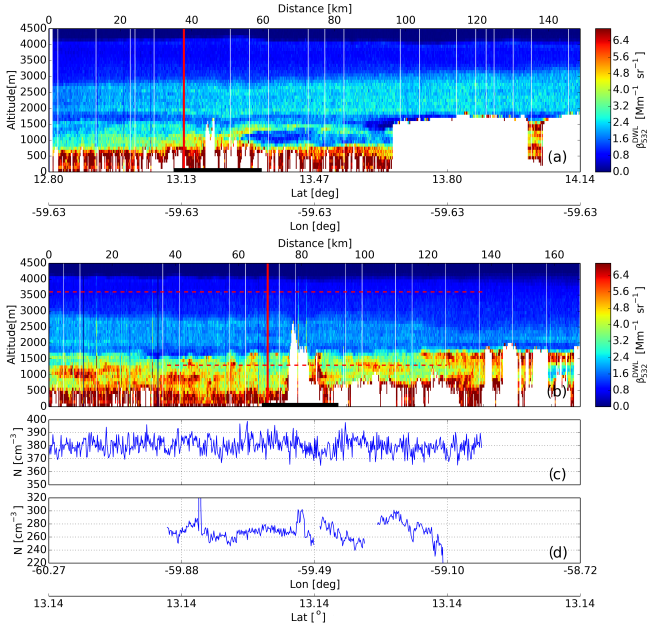


**Figure 13. (a)** Retrieved backscatter coefficient by the DWL as a function of the latitude and longitude from leg 1, together with the latitude at which legs 2, 3 and 4 were flown (solid line, red). **(b)** Retrieved backscatter coefficient by the DWL as a function of the latitude and longitude from leg 2, the intersection position with the 1st leg (solid line, red) and the legs 3 and 4 are shown (dashed line., red). **(c, d)** In situ CPC measurements corresponding to the legs 3 and 4. The white colour indicates regions where no atmospheric signal is available (e.g., below clouds, unseeded laser operation). Barbados indicated in both plots with a horizontal solid black line.

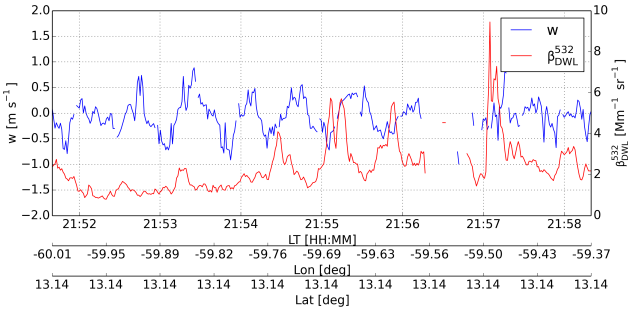


**Figure 14.** Retrieved backscatter coefficient (red) and vertical wind speed (blue) on the lee side of Barbados during the flight of the 2nd leg at an altitude of 1600 m. Due to the presence of clouds, data between 21:56 and 21:57 LT are missing.

The backscatter coefficient and vertical wind corresponding to the boundary where the waves were observed are displayed in Fig. 14. As for the previous case, a phase difference of 90° is observed between both quantities, which is compatible with a no net flux condition. Although in this particular case this feature was already observed by in situ measurements in the previous case study, the shown mea-

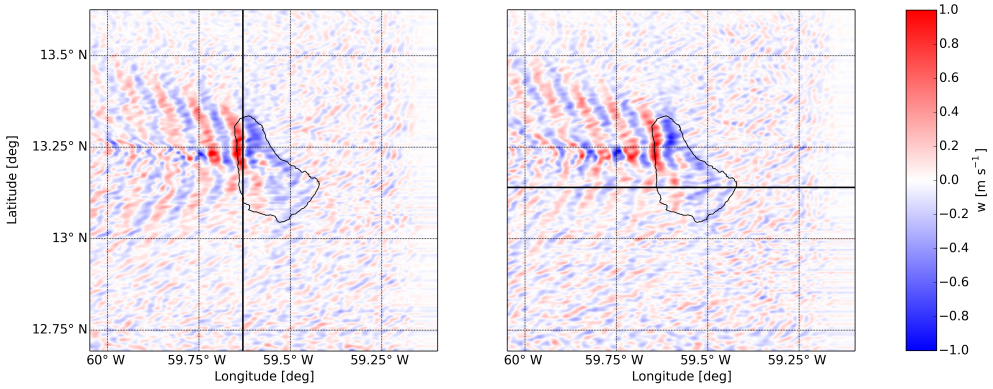


**Figure 15.** Vertical wind speed at 1975 m derived from the LES corresponding to 26 June at 20:00 LT (left panel) and 22:00 LT (right panel). The flight tracks corresponding to leg 1 (left) and 2 (right) are also indicated (solid, black).

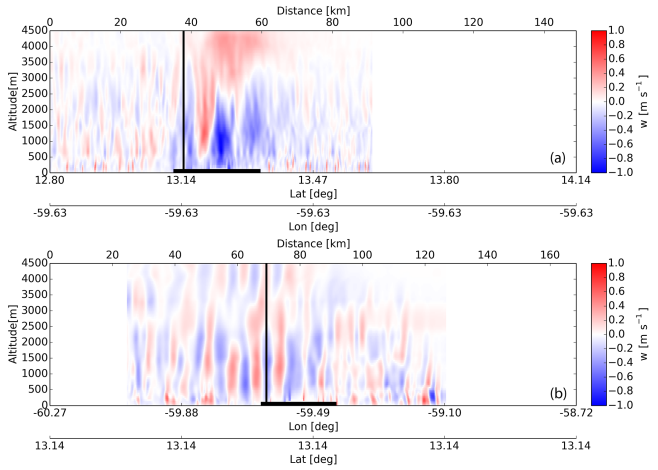


**Figure 16.** Vertical wind speed from the LES for 26 June at 20:00 LT for leg 1 (upper panel) and 22:00 LT for leg 2 (lower panel). The location of Barbados is indicated as a horizontal black segment, while the intersection between legs 1 and 2 is indicated with a vertical line.

surements provide an example of the possibilities opened up by the simultaneous retrieval of vertical wind and calibrated backscatter coefficient from a single instrument along a whole vertical transect. Based on the technique proposed by Engelmann et al. (2008), the simultaneous retrieval of backscatter coefficient and vertical wind can be used, under low humidity conditions, to retrieve aerosol vertical flux profiles. Dry atmospheric conditions are required in order to avoid the hygroscopic growth of aerosol particles, which otherwise would lead to a wrong flux estimation. The exact relative humidity threshold under which hygroscopic growth can be neglected varies according to the aerosol type. For the case of sea salt and desert dust, hygroscopic growth can be safely neglected for a relative humidity below 50 % (e.g. Engelmann et al., 2008; Kaaden et al., 2008).

### 3.2.2 Large-eddy simulations

Large-eddy simulations are performed with the All Scale Atmospheric Model (ASAM, Jähn et al., 2015) for the Barbados area. The model setup is described in Jähn et al. (2016), where the focus of the analysis lies on island effects on boundary layer modification, cloud generation and vertical mixing of aerosols. In this study, the simulation results along the measurement tracks are first compared with the DWL observations in order to provide further validation of the model and setup. Then the whole simulation results are used to provide a broader perspective of the context within which the measurements took place.

For the simulations, a model domain with a spatial extent of $102.4 \times 102.4$ km is chosen with Barbados located at the domain centre. The model top is at 5 km altitude. Grid spacings of 200 m (horizontally) and 50 m (vertically) are used and topographical data are obtained from the Consortium for Spatial Information (CGIAR-CSI) Shuttle Radar Topography Mission (SRTM) data set (http://srtm.csi.cgiar.org) at 200 m resolution. The highest elevation of Barbados is Mount Hillaby, 340 m above sea level. Due to the presence of a topographically structured island surface in the domain centre, the simulations are performed with open lateral boundaries.

In order to generate inflow turbulence consistent with the upstream marine boundary layer forcing, the newly developed turbulence generation method is applied. The model runs are initialised with nighttime radiosonde data of the considered day and are integrated from 02:00 to 22:00 LT. Further details on the setup and comparison with the DWL can be found in Jähn et al. (2016).

In order to allow a qualitative comparison of the results from the LES with the measurements from the DWL, plots of the simulated vertical wind speed on time periods similar to those corresponding to the measurements are presented in Figs. 15 and 16. Figure 15 shows two horizontal cuts of the vertical wind speed at 20:00 and 22:00 LT together with the

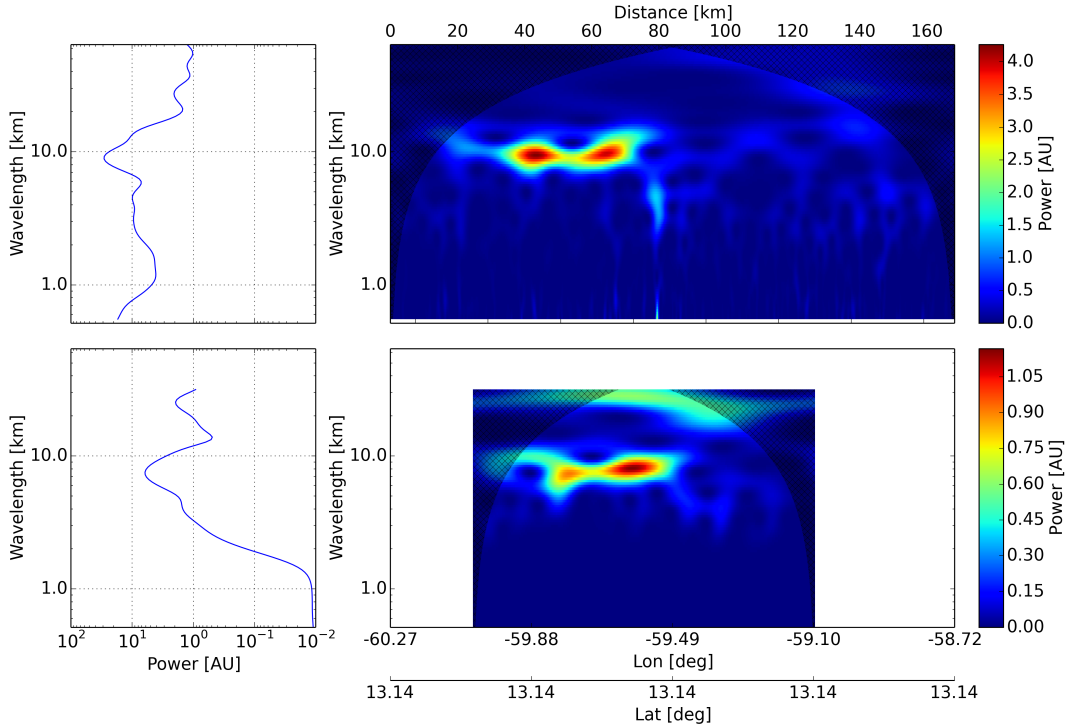


**Figure 17.** Wavelet analysis of the vertical wind corresponding to the 2nd leg for the flight on 26 June derived from the DWL measurements (Fig. 11b) at 2000 m (upper panels) and derived from the LES (Fig. 16b) at 2000 m (lower panels). The hatched areas indicate the cone of influence. The left panels show the average power for each wavelength.

flight track of the Falcon corresponding to legs 1 and 2. The horizontal plane is located at an altitude of 1975 m, coinciding with the temperature inversion observed by the in situ measurements and the maximum in the horizontal wind shear observed by the DWL, in situ and dropsonde measurements. Figure 16 displays the simulated vertical winds corresponding to the 1st and 2nd legs flown by the Falcon (indicated in Fig. 15). The horizontal scales of the plots were adjusted to simplify the comparison with the measurements presented in Fig. 11.

### 3.2.3 Comparison of LES and DWL

As can be seen in Figs. 15 and 16, the LES is able to reproduce the observations from the DWL. A limited coverage over Barbados due to the presence of convective clouds is compatible with the convective plumes observed in the simulations. Trapped waves with a wavelength and extension similar to the lidar observations can be recognized on the lee side of Barbados. The vertical cut presented in Fig. 16a shows an updraft above Barbados similar to the one shown in Figs. 11a, and 15a shows that the vertical cut is located along a wave crest. This simulation result provides support to the hypothesis presented in Sect. 4.1 to explain the strong updraft observed above Barbados during the first measurement leg.

A wavelet transform was applied to the measured and simulated vertical wind speed in order to provide a quantitative wavelength, amplitude and extension comparison of the simulated and measured trapped waves. The measured data were interpolated in the same way as described in Sect. 3, matching for this case, the spatial resolution of the LES (200 m). The results of the wavelet transforms are presented in Fig. 17.

According to the wavelet analysis, the wavelength of the measured waves is approximately 9 km, while for the case of the LES the wavelength is approximately 7.5 km. The difference can be attributed to different reasons such as small differences in the propagation direction of the waves. As mentioned before, the LES is initialised with a constant wind speed direction equal to 90°. This approximation can induce differences in the direction of propagation of the waves, which in turn induce differences in the apparent wavelength of the measurements for the same flight track.

While the amplitude of the simulated waves is quite similar at different altitudes, the DWL measurements show a maximum in the amplitude at approximately 2000 m. This difference is evident from the results of the wavelet analysis, calculated at the altitude of this maximum in both cases. As explained in the previous section, the horizontal wind speed used for the initialization of the LES is assumed constant between 0.7 and 3 km. Because this approximation neglects the strong shear measured at 2000 m, a difference between the

simulated and the measured vertical wind speed is expected at this altitude.

## 4 Summary and conclusions

In the first section of this work, a series of instrumental corrections required for the retrieval of vertical winds from airborne DWL measurements were presented. The difference of almost 2 orders of magnitude between the platform speed and the measured vertical wind speed, together with the varying aircraft orientation during the flight, transforms the retrieval of vertical winds in a challenging problem. Although no control of the lidar pointing direction was active during the vertical wind measurements, the use of horizontal wind from dropsondes and in situ measurements proved to be useful to partially compensate the effects of the horizontal wind component projection. The use of conical scanning pattern measurements and the recalculation of the lidar mounting angle based on the ground return speed and distance previous to the vertical wind measurements proved to be useful to reduce the systematic error, especially after a change in the flight altitude. The measurement uncertainties were estimated based on two different techniques. The estimated systematic error, based one measurement case, was -0.05 $\mathrm{m\,s^{-1}}$, while the random error was between 0.1 and 0.16 $\mathrm{m\,s^{-1}}$ depending on the technique used for the estimation.

The described methods were applied to retrieve vertical winds corresponding to two SALTRACE research flights, one in the Cabo Verde region and a second one in Barbados. The measurements revealed the presence of island induced gravity waves in both cases. Vertical profiles of temperature, wind and humidity obtained from in situ and dropsonde measurements were used to calculate a Scorer parameter profile for each measurement case. The wavelength and the vertical extension of the trapped waves observed from the DWL measurements in the Cabo Verde case study were in coincidence with the retrieved Scorer parameter profile. The spatial extension, amplitude and wavelength retrieved from the in situ vertical wind measurements provided an independent validation for the DWL observation. A second independent observation of the particle number concentration provided an additional confirmation.

Although for the second case study the in situ measurement did not show the waves observed by the DWL in a previous leg, the results of the ASAM model support the lidar observations. The model was able to reproduce the generation of waves in the lee side of the island and provided a context to the lidar observations, which are limited to two dimensional vertical cuts. The amplitude and wavelength of the simulated waves were lower than the observed ones. This can be explained by the simplifications adopted in the horizontal wind profiles used to initialise the model, which did not reproduce the strong shears observed in the dropsondes and in situ measurements.

**The Supplement related to this article is available online at doi:10.5194/acp-16-4675-2016-supplement.**

*Acknowledgements.* This work was funded by the Helmholtz Association under grant number VH-NG-606 (Helmholtz-Hochschul-Nachwuchsforschergruppe AerCARE). The SALTRACE campaign was mainly funded by the Helmholtz Association, DLR, LMU and TROPOS. The SALTRACE flights on Cabo Verde were funded through the DLR-internal project VolcATS (Volcanic ash impact on the Air Transport System). DLR Falcon aircraft in situ data were processed by the DLR Flight Experiment. The first author thanks the German Academic Exchange Service (DAAD) for the financial support.

The article processing charges for this open-access publication were covered by a Research Centre of the Helmholtz Association.

Edited by: J. Schwarz

## References

Alexander, M. J. and Grimsdell, A. W.: Seasonal cycle of orographic gravity wave occurrence above small islands in the Southern Hemisphere: Implications for effects on the general circulation, J. Geophys. Res.-Atmos., 118, 11589–11599, doi:10.1002/2013JD020526, 2013.

Amirault, C. and DiMarzio C.: Precision pointing using a dual-wedge scanner, Appl. Opt., 24, 1302–1308, 1985.

Baik, J.: Response of a Stably Stratified Atmosphere to Low-Level Heating – An Application to the Heat Island Problem, J. Appl. Meteorol., 31, 291–303, doi:10.1175/1520-0450(1992)031<0291:ROASSA>2.0.CO;2, 1992.

Baines, J. and Hoinka, K. P.: Stratified Flow over Two-Dimensional Topography in Fluid of Infinite Depth: A Laboratory Simulation, J. Atmos. Sci., 42, 1614–1630, doi:10.1175/1520-0469(1985)042<1614:SFOTDT>2.0.CO;2, 1985.

Bluman, W. and Hart, J. E.: Airborne Doppler Lidar Wind Field Measurements of Waves in the Lee of Mount Shasta, J. Atmos. Sci., 45, 1571–1583, doi:10.1175/1520-0469(1988)045<1571:ADLWFM>2.0.CO;2, 1988.

Bosart, B., Lee, W., and Wakimoto, R.: Procedures to Improve the Accuracy of Airborne Doppler Radar Data, J. Atmos. Ocean. Tech., 19, 322–339, doi:10.1175/1520-0426-19.3.322, 2002.

Chouza, F., Reitebuch, O., Groß, S., Rahm, S., Freudenthaler, V., Toledano, C., and Weinzierl, B.: Retrieval of aerosol backscatter and extinction from airborne coherent Doppler wind lidar measurements, Atmos. Meas. Tech., 8, 2909–2926, doi:10.5194/amt-8-2909-2015, 2015.

Cui, Z., Blyth, A. M., Bower, K. N., Crosier, J., and Choularton, T.: Aircraft measurements of wave clouds, Atmos. Chem. Phys., 12, 9881–9892, doi:10.5194/acp-12-9881-2012, 2012.

De Wekker, S. F. J., Godwin, K. S., Emmitt, G. D., and Greco, S.: Airborne Doppler Lidar Measurements of Valley Flows in Complex Coastal Terrain, J. Appl. Meteorol. Clim., 51, 1558–1574, doi:10.1175/JAMC-D-10-05034.1, 2012.

Durran, D. R.: Mountain waves and downslope winds, in: Atmospheric Process over Complex Terrain, edited by: Blumen, W., American Meteorological Society, Boston, 59–81, 1990.

Durran, D. R., Hills, M. O. G., and Blossey, P. N.: The Dissipation of Trapped Lee Waves. Part I: Leakage of Inviscid Waves into the Stratosphere, J. Atmos. Sci., 72, 1569–1584, doi:10.1175/JAS-D-14-0238.1, 2015.

Ehard, B., Kaifler, B., Kaifler, N., and Rapp, M.: Evaluation of methods for gravity wave extraction from middle-atmospheric lidar temperature measurements, Atmos. Meas. Tech., 8, 4645–4655, doi:10.5194/amt-8-4645-2015, 2015.

Emmitt, G. D. and Godwin, K.: Advanced airborne Doppler Wind Lidar signal processing for observations in complex terrain, Proc. SPIE 9246, Lidar Technologies, Techniques, and Measurements for Atmospheric Remote Sensing X, 924609, doi:10.1117/12.2068226, 2014.

Engelmann, R., Wandinger, U., Ansmann, A., Müller, D., Žeromskis, E., Althausen, D., and Wehner, B.: Lidar Observations of the Vertical Aerosol Flux in the Planetary Boundary Layer, J. Atmos. Ocean. Tech., 25, 1296–1306, doi:10.1175/2007JTECHA967.1, 2008.

Engelmann, R., Ansmann, A., Horn, S., Seifert, P., Althausen, D., Tesche, M., Esselborn, M., Fruntke, J., Lieke, K., Freudenthaler, V., and Groß, S.: Doppler lidar studies of heat island effects on vertical mixing of aerosols during SAMUM–2, Tellus B, 63, 448–458. doi:10.1111/j.1600-0889.2011.00552.x, 2011.

Frehlich, R.: Errors for Space-Based Doppler Lidar Wind Measurements: Definition, Performance, and Verification, J. Atmos. Ocean. Tech., 18, 1749–1772, 2001.

Georgelin, M. and Lott, F.: On the Transfer of Momentum by Trapped Lee Waves: Case of the IOP 3 of PYREX, J. Atmos. Sci., 58, 3563–3580, doi:10.1175/1520-0469(2001)058<3563:OTTOMB>2.0.CO;2, 2001.

Grewal, M. S., Weill, L. R., and Andrews, A. P.: Appendix C: Coordinate Transformations, in: Global Positioning Systems, Inertial Navigation, and Integration, Second Edn., John Wiley & Sons, Inc., Hoboken, NJ, USA, 456–501, doi:10.1002/9780470099728.app3, 2007.

Henderson, S. W., Suni, P. J. M., Hale, C. P., Hannon, S. M., Magee, J. R., Bruns, D. L., and Yuen, E. H.: Coherent laser radar at 2 µm using solid-state lasers, IEEE T. Geosci. Remote, 31, 4–15, 1993.

Jähn, M., Knoth, O., König, M., and Vogelsberg, U.: ASAM v2.7: a compressible atmospheric model with a Cartesian cut cell approach, Geosci. Model Dev., 8, 317–340, doi:10.5194/gmd-8-317-2015, 2015.

Jähn, M., Muñoz-Esparza, D., Chouza, F., Reitebuch, O., Knoth, O., Haarig, M., and Ansmann, A.: Investigations of boundary layer structure, cloud characteristics and vertical mixing of aerosols at Barbados with large eddy simulations, Atmos. Chem. Phys., 16, 651–674, doi:10.5194/acp-16-651-2016, 2016.

Kaaden, N., Massling, A., Schladitz, A., Müller, T., Kandler, K., Schütz, L., Weinzierl, B., Petzold, A., Tesche, M., Leinert, S., Deutscher, C., Ebert, E., Weinbruch, S., and Wiedensohler, A.: State of mixing, shape factor, number size distribution, and hygroscopic growth of the Saharan anthropogenic and mineral dust aerosol at Tinfou, Morocco, Tellus, 61, 51–63, doi:10.1111/j.1600-0889.2008.00388.x, 2008.

Kavaya, M. J., Beyon, J. Y., Koch, G. J., Petros, M., Petzar, P. J., Singh, U. N., Trieu, B. C., and Yu, J.: The Doppler Aerosol Wind (DAWN) Airborne, Wind-Profiling Coherent-Detection Lidar System: Overview and Preliminary Flight Results, J. Atmos. Ocean. Tech., 31, 826–842, doi:10.1175/JTECH-D-12-00274.1, 2014.

Käsler, Y., Rahm, S., Simmet, R., and Kühn, M.: Wake measurements of a multi-MW wind turbine with coherent long-range pulsed doppler wind lidar, J. Atmos. Ocean. Tech., 27, 1529–1532, 2010.

Kiemle, C., Ehret, G., Fix, A., Wirth, M., Poberaj, G., Brewer, W. A., Hardesty, R. M., Senff, C., and LeMone, M. A.: Latent Heat Flux Profiles from Collocated Airborne Water Vapor and Wind Lidars during IHOP_2002, J. Atmos. Ocean. Tech., 24, 627–639, doi:10.1175/JTECH1997.1, 2007.

Kiemle, C., Wirth, M., Fix, A., Rahm, S., Corsmeier, U., and Di Girolamo, P.: Latent heat flux measurements over complex terrain by airborne water vapour and wind lidars, Q. J. Roy. Meteor. Soc., 137, 190–203, doi:10.1002/qj.757, 2011.

Kirkwood, S., Mihalikova, M., Rao, T. N., and Satheesan, K.: Turbulence associated with mountain waves over Northern Scandinavia – a case study using the ESRAD VHF radar and the WRF mesoscale model, Atmos. Chem. Phys., 10, 3583–3599, doi:10.5194/acp-10-3583-2010, 2010.

Köpp, F., Rahm, S., and Smalikho, I.: Characterization of Aircraft Wake Vortices by 2-µm Pulsed Doppler Lidar, J. Atmos. Ocean. Tech., 21, 194–206, 2004.

Kühnlein, C., Dörnbrack, A., and Weissmann, M.: High-Resolution Doppler Lidar Observations of Transient Downslope Flows and Rotors, Mon. Weather Rev., 141, 3257–3272, doi:10.1175/MWR-D-12-00260.1, 2013.

O'Connor, E. J., Illingworth, A. J., Brooks, I. M., Westbrook, C. D., Hogan, R. J., Davies, F., and Brooks, B. J.: A Method for Estimating the Turbulent Kinetic Energy Dissipation Rate from a Vertically Pointing Doppler Lidar, and Independent Evaluation from Balloon-Borne In Situ Measurements, J. Atmos. Ocean. Tech., 27, 1652–1664, doi:10.1175/2010JTECHA1455.1, 2010.

Prospero, J. M.: Long-range transport of mineral dust in the global atmosphere: Impact of African dust on the environment of the southeastern United States, P. Natl. Acad. Sci. USA, 96, 3396–3403, 1999.

Prospero, J. M. and Mayol-Bracero, O. L.: Understanding the Transport and Impact of African Dust on the Caribbean Basin, B. Am. Meteorol. Soc., 94, 1329–1337, doi:10.1175/BAMS-D-12-00142.1, 2013.

Rahm, R., Smalikho, I., and Köpp, F.: Characterization of Aircraft Wake Vortices by Airborne Coherent Doppler Lidar, J. Aircraft, 44, 799–805, 2007.

Reitebuch, O.: Wind Lidar for Atmospheric Research, in: Atmospheric Physics, edited by: Schumann, U., Springer, Berlin, Heidelberg, 487–507, 2012.

Reitebuch, O., Werner, C., Leike, I., Delville, P., Flamant, P. H., Cress, A., and Engelbart, D.: Experimental validation of wind profiling performed by the airbone 10-µm heterodyne Doppler Lidar WIND, J. Atmos. Ocean. Tech., 18, 1331–1344, 2001.

Reitebuch, O., Volkert, H., Werner, C., Dabas, A., Delville, P., Drobinski, P., Flamant, P. H., and Richard, E.: Determination of air flow across the Alpine ridge by a combination of airborne Doppler lidar, routine radio-sounding, and numerical simulation, Q. J. Roy. Meteor. Soc., 129, 715–728, 2003.

Sachsperger, J., Serafin, S., and Grubišić, V.: Lee Waves on the Boundary-Layer Inversion and Their Dependence on Free-Atmospheric Stability, Front. Earth Sci., 3, 70, doi:10.3389/feart.2015.00070, 2015.

Savijärvi, H. and Matthews, S.: Flow over Small Heat Islands: A Numerical Sensitivity Study, J. Atmos. Sci., 61, 859–868, doi:10.1175/1520-0469(2004)061<0859:FOSHIA>2.0.CO;2, 2004.

Scorer, R. S.: Theory of waves in the lee of mountains, Q. J. Roy. Meteor. Soc., 75, 41–56, doi:10.1002/qj.49707532308, 1949.

Smith, R. B.: Linear theory of stratified hydrostatic flow past an isolated obstacle, Tellus, 32, 348–364, 1980.

Smith, R. B., Skubis, S., Dolye, J. D., Broad, A., and Volkert, H.: Mountain waves over Mont Blanc: Influence of a stagnant boundary layer, J. Atmos. Sci., 59, 2073–2092, 2002.

Torrence, C. and Compo, G. P.: A practical guide to wavelet analysis, B. Am. Meteorol. Soc., 79, 61–78, 1998.

Vosper, S. B.: Inversion effects on mountain lee waves, Q. J. Roy. Meteor. Soc., 130, 1723–1748, doi:10.1256/qj.03.63, 2004.

Weinzierl, B., Sauer, D., Esselborn, M., Petzold, A., Veira, A., Rose, M., Mund, S., Wirth, M., Ansmann, A., Tesche, M., Groß, S., and Freudenthaler, V.: Microphysical and optical properties of dust and tropical biomass burning aerosol layers in the Cape Verde region – an overview of the airborne in situ and lidar measurements during SAMUM-2, Tellus B, 63, 589–618, doi:10.1111/j.1600-0889.2011.00566.x, 2011.

Weissmann, M., Busen, R., Dörnbrack, A., Rahm, S., and Reitebuch, O.: Targeted observations with an airborne wind lidar, J. Atmos. Ocean. Tech., 22, 1706–1719, 2005.

Woods, B. K. and Smith, R. B.: Energy Flux and Wavelet Diagnostics of Secondary Mountain Waves, J. Atmos. Sci., 67, 3721–3738, doi:10.1175/2009JAS3285.1, 2010.

Supplement of Atmos. Chem. Phys., 16, 4675–4692, 2016
http://www.atmos-chem-phys.net/16/4675/2016/
doi:10.5194/acp-16-4675-2016-supplement


Atmospheric Chemistry and Physics Open Access EGU

*Supplement of*

# Vertical wind retrieved by airborne lidar and analysis of island induced gravity waves in combination with numerical models and in situ particle measurements

**Fernando Chouza et al.**

*Correspondence to:* Fernando Chouza (fernando.chouza@dlr.de)

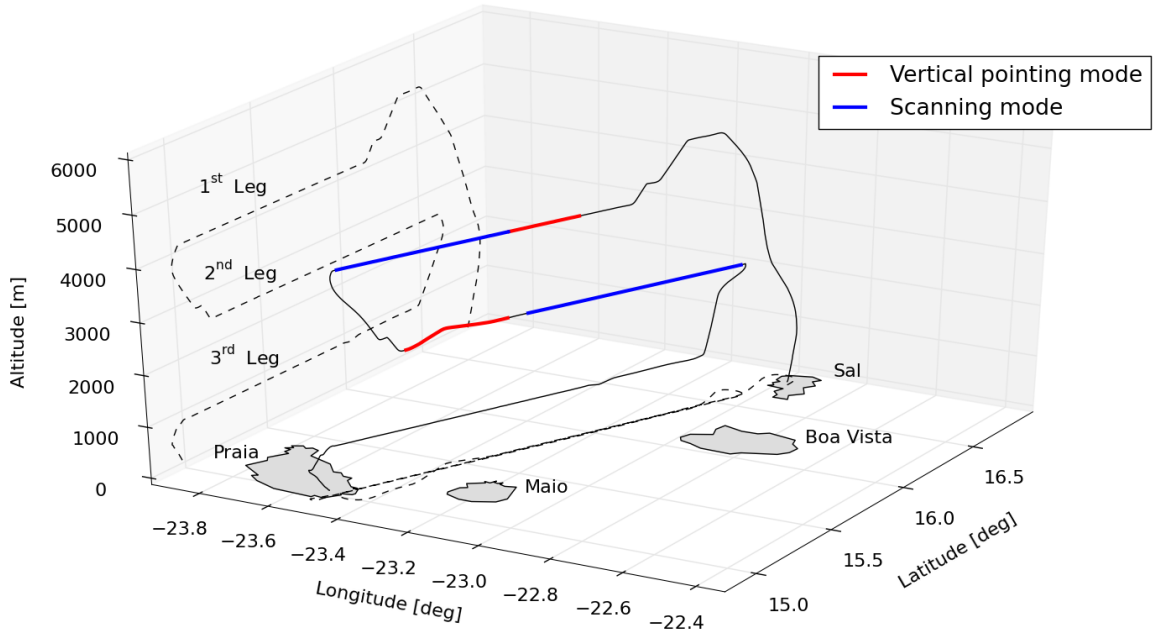


Figure S1. Track corresponding to the flight on 17 June between Sal and Praia, Cape Verde islands. The blue segments represent flight periods during which the DWL was operating in scanning mode (horizontal wind speed), while the red segments correspond to vertical pointing mode (vertical wind).

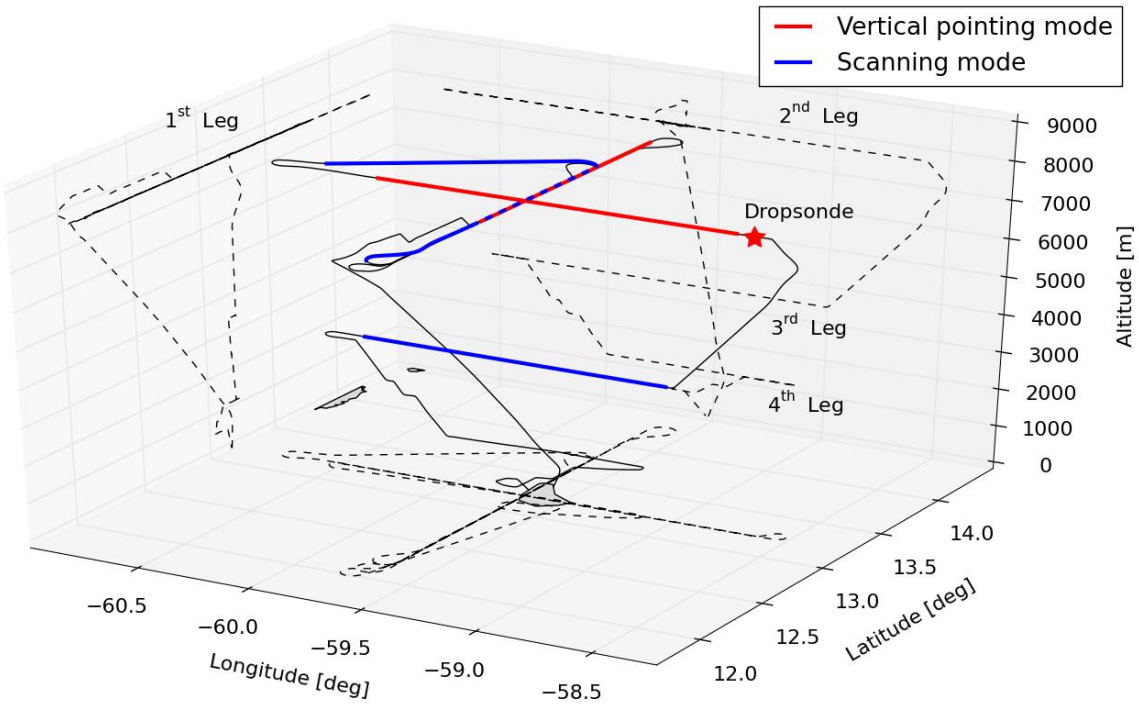


Figure S2. Track corresponding to the flight on 26 June around Barbados. The blue segments represent flight periods during which the DWL was operating in scanning mode (horizontal wind speed), while the red segments correspond to vertical pointing mode (vertical wind). The dropsonde (Fig. 10) launch position is indicated with a red star.

Atmos. Chem. Phys., 16, 11581–11600, 2016
www.atmos-chem-phys.net/16/11581/2016/
doi:10.5194/acp-16-11581-2016


Atmospheric Chemistry and Physics
Open Access
EGU

# Saharan dust long-range transport across the Atlantic studied by an airborne Doppler wind lidar and the MACC model

**Fernando Chouza[1], Oliver Reitebuch[1], Angela Benedetti[2], and Bernadett Weinzierl[3]**

[1]Institut für Physik der Atmosphäre, Deutsches Zentrum für Luft- und Raumfahrt (DLR), Oberpfaffenhofen, Germany
[2]European Centre for Medium-Range Weather Forecasts, Reading, UK
[3]Faculty of Physics, University of Vienna, Boltzmanngasse 5, 1090 Vienna, Austria

*Correspondence to:* Fernando Chouza (fernando.chouza@dlr.de)

Received: 4 May 2016 – Published in Atmos. Chem. Phys. Discuss.: 19 May 2016
Revised: 2 September 2016 – Accepted: 8 September 2016 – Published: 20 September 2016

**Abstract.** A huge amount of dust is transported every year from north Africa into the Caribbean region. This paper presents an investigation of this long-range transport process based on airborne Doppler wind lidar (DWL) measurements conducted during the SALTRACE campaign (June–July 2013), as well as an evaluation of the ability of the MACC (Monitoring Atmospheric Composition and Climate) global aerosol model to reproduce it and its associated features. Although both the modeled winds from MACC and the measurements from the DWL show a generally good agreement, some differences, particularly in the African easterly jet (AEJ) intensity, were noted. The observed differences between modeled and measured wind jet speeds are between 5 and 10 m s$^{-1}$. The vertical aerosol distribution within the Saharan dust plume and the marine boundary layer is investigated during the June–July 2013 period based on the MACC aerosol model results and the CALIOP satellite lidar measurements. While the modeled Saharan dust plume extent shows a good agreement with the measurements, a systematic underestimation of the marine boundary layer extinction is observed.

Additionally, three selected case studies covering different aspects of the Saharan dust long-range transport along the west African coast, over the North Atlantic Ocean and the Caribbean are presented. For the first time, DWL measurements are used to investigate the Saharan dust long-range transport. Simultaneous wind and backscatter measurements from the DWL are used, in combination with the MACC model, to analyze different features associated with the long-range transport, including an African easterly wave trough, the AEJ and the intertropical convergence zone.

## 1 Introduction

Every year, huge amounts of Saharan dust originating from north Africa is transported across the Atlantic into the Caribbean region and the north of South America. The transport, mainly occurring during the summer season, starts with the uplifting of dust by turbulent convection and low-level winds with high speed (Bou Karam et al., 2008), is the amount of emitted dust regulated by different factors like the soil humidity and vegetation. Once lofted, the dust is dispersed into a deep mixed layer, reaching altitudes of up to 6 km during summer (Messager et al., 2010). The dominating easterly winds west advect the dust-laden air masses, which are undercut by the cooler and moister air from the marine boundary layer (MBL) as they reach the west African coast, forming an elevated layer of relatively warm, dry and dust-laden air called Saharan air layer (SAL). As the SAL leaves the African continent, its lower and upper bounds are defined by a strong inversion at approximately 1.5 km and a relatively weaker inversion at around 5 to 6 km, respectively (Prospero and Carlson, 1972; Karyampudi et al., 1999).

Along its life cycle, the airborne dust interacts with the environment in different ways. During its long-range transport phase, the dust modifies the radiative budget, acts as cloud and ice nuclei and is observed to modify the cloud glaciation process (e.g., Seifert et al., 2010). Various mechanisms have been proposed to explain the controversial influence of the SAL on the evolution of African easterly waves (AEWs) into tropical storms (e.g., Dunion et al., 2004; Evan et al., 2006; Lau and Kim, 2007). Regularly mineral dust is impacting aviation, in particular in regions near dust sources,

by inducing poor visibility (Weinzierl et al., 2012). As it deposits, the Saharan dust can affect the air quality (Prospero, 1999) and serves as source of nutrients for plankton and the Amazon basin (Yu et al., 2015).

Several studies were conducted during the last years to provide further insight in the previously mentioned processes, including field campaigns and long-term studies based on models, satellite, airborne and ground-based measurements. Among others, we can mention the African Monsoon Multidisciplinary Analysis (AMMA) and NASA-AMMA (NAMMA) campaigns (Zipser et al., 2009) conducted in 2006, focused on the analysis of the AEW and its evolution into tropical cyclones, and the Saharan Mineral Dust Experiments 1 and 2 (SAMUM-1 and SAMUM-2) (Heintzenberg, 2009; Ansmann et al., 2011) conducted in 2006 and 2008, respectively, which were designed to investigate the Saharan dust size distribution and morphology, and the relation with the optical and radiative properties in the west African region. Additionally, during April–May 2013, a shipborne lidar onboard the research vessel *Meteor* conducted a transatlantic cruise between the Caribbean and the west coast of Africa in order to characterize the mixtures of the Saharan dust with biomass burning aerosols and evaluate the change in its optical properties as result of the long-range transport process (Kanitz et al., 2014). While field campaigns provide an intensive set of observations in relatively small regions and time intervals, satellite observations provide regular observations with a limited set of parameters. On the other hand, global and regional models are frequently used in dust long-range transport studies and forecasting (e.g., Schepanski et al., 2009; Kim et al., 2014; Gläser et al., 2015), as they provide valuable information to interpret the observational data collected by campaigns and satellite measurements. The performance evaluation of these models, like during the intercomparison initiative AeroCom (Aerosol Comparison between Observations and Models) (Kinne et al., 2003), is then not only vital to improve the models but also to know the limits and accuracy of the conclusions extracted based on these models.

The Saharan Aerosol Long-range Transport and Aerosol-Cloud-Interaction Experiment (SALTRACE; Weinzierl et al., 2016) performed in June–July 2013 was framed in this context. SALTRACE was planned as a closure experiment to investigate the Saharan dust long-range transport between Africa and the Caribbean, with a focus on the dust aging and deposition processes and the characterization of its optical properties. The campaign dataset includes a set of measurements from the ground-based aerosol lidars BERTHA (Backscatter Extinction lidar-Ratio Temperature Humidity profiling Apparatus) (Haarig et al., 2015) and POLIS (portable lidar system) (Groß et al., 2015), in situ and sun photometer instruments deployed on Barbados (main SALTRACE super-site), Cabo Verde and Puerto Rico and airborne aerosol and wind measurements from the DLR (Deutsches Zentrum für Luft- und Raumfahrt) research aircraft *Falcon* similar to the measurements done during SAMUM (Weinzierl et al., 2009, 2011). For the first time, an airborne Doppler wind lidar (DWL) was deployed to study the dust transport across the Atlantic Ocean, including its interaction with island-induced gravity waves (Chouza et al., 2016).

In this study, this unique set of DWL wind and extinction measurements along the main dust transport acquired during SALTRACE are used, in combination with dropsondes (DSs) and CALIPSO (Cloud–Aerosol Lidar and Infrared Pathfinder Satellite Observations) satellite measurements, to analyze the Saharan dust long-range transport and to evaluate the performance of the MACC (Monitoring Atmospheric Composition and Climate) aerosol global model to reproduce different associated atmospheric features, like the African easterly jet (AEJ) and its interaction with the SAL, the AEWs and the ITCZ (intertropical convergence zone), among others. Such a comparison provides not only an insight about the current model capabilities, which is of great relevance for model-based studies, but the opportunity to identify the model weaknesses and provide a starting point for future improvements. This type of evaluation has never been performed with a dataset that includes both meteorological fields as well as atmospheric composition fields. Although there is no direct feedback from the atmospheric composition fields onto the meteorological fields (temperature and winds) as the run was not coupled through interactive radiative processes, the aerosols are transported and advected by the winds. Hence, an evaluation of both winds and aerosols in the SAL is a very effective way to understand how well the model represents this natural phenomenon.

The paper is organized as follows. Section 2 presents a brief description of the datasets used for this study, including an evaluation of the DWL accuracy based on collocated dropsonde measurements. Section 3 provides a comparison between the DWL and CALIPSO measurements with the backscatter and winds from the MACC model in the west African and Caribbean regions for the time period of the SALTRACE campaign. Section 4 presents three case studies with relevant features of the Saharan dust long-range transport. Finally, the summary and relevant conclusions are presented in Sect. 5.

## 2 Observations and model data

During the SALTRACE campaign, the DLR *Falcon* research aircraft conducted 31 research flights between 10 June and 15 July 2013, with most of the flights concentrated close to the west African coast and the Caribbean (Fig. 1). The DLR *Falcon* was equipped with a set of instruments for in situ particle measurements, a DWL and dropsondes. Ground-based measurements were conducted in Cabo Verde, Puerto Rico and Barbados. Two aerosol lidars and sun photometers were installed on the west coast of Barba-

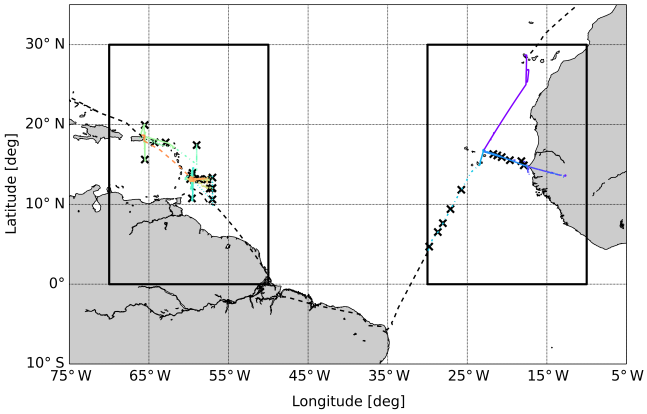


**Figure 1.** DLR *Falcon* flight tracks during SALTRACE. Dropsondes' launch positions are indicated with black crosses. Black boxes indicate the regions which were used in this study (west Africa: 0–30° N; 10–30° W and Caribbean: 0–30° N; 50–70° W). Colored tracks indicate measurement flights included in this study. Black dashed tracks indicate transfer flights which are not used in this work.

dos, at the Caribbean Institute for Meteorology and Hydrology (CIMH) (13°08′55″ N, 59°37′30″ W; 110 m .s.l.), while a sun photometer and a set of ground-based in situ instruments were deployed at Ragged Point, Barbados (Kristensen et al., 2016). A complete list of the instruments involved in the campaign can be found on the SALTRACE website (http://www.pa.op.dlr.de/saltrace/instruments.html) and an overview of SALTRACE is given in Weinzierl et al. (2016). The following subsections describe in detail the characteristics of the datasets used for this study, including the used fields from the MACC model.

### 2.1 Dropsondes

A set of 34 Vaisala RD93 dropsondes, operated in conjunction with the NCAR AVAP system (Busen, 2012), were launched from the *Falcon* during SALTRACE, providing vertical profiles of temperature, relative humidity and wind speed with a vertical resolution of approximately 10 m. According to the manufacturer, the horizontal wind measurements have an accuracy of 0.5 m s$^{-1}$ rms (root mean square) (Vaisala, 2009), where this accuracy definition incorporates both the systematic and the random error of the measurements. Figure 1 indicates the geographical position at which each dropsonde was launched.

### 2.2 Doppler wind lidar

The coherent DWL deployed on the DLR *Falcon* 20 research aircraft during SALTRACE is based on a CLR Photonics instrument (Henderson et al., 1993) combined with a two-wedge scanner and acquisition system developed at DLR (Köpp et al., 2004; Reitebuch, 2012). The system operates at a wavelength of 2.02254 µm, with a pulse duration full width at half maximum (FWHM) of 400 ns, a pulse energy of 1–2 mJ and a repetition frequency of 500 Hz.

When mounted on an aircraft, the system can be operated in two modes: the conical scanning and the nadir pointing mode. The conical scanning mode consists of 24 lines of sight (LOS) in a conical distribution with an off-nadir angle of 20° and a staring duration of 1 s per LOS direction. The inversion algorithm (Smalikho, 2003; Weissmann et al., 2005) is then applied to the 24 LOS measurements from each scan to retrieve horizontal wind speed vector with a horizontal resolution of around 6–10 km (depending on the aircraft speed) and a vertical resolution of 100 m. On the other hand, the nadir pointing mode can be used to retrieve vertical wind measurements with a horizontal resolution of approximately 200 m (Chouza et al., 2016). Both modes allow, by means of an adequate calibration, the retrieval of backscatter and extinction coefficients with a horizontal resolution of approximately 200 m and a vertical resolution of 100 m (Chouza et al., 2015). As in the case of CALIOP, the backscatter and extinction retrievals form the DWL measurements require assuming a lidar ratio for each aerosol type. For the retrievals presented in this study, a lidar ratio of 55 sr was used for the Saharan dust, while 30 and 35 sr were used for the marine boundary layer and the marine-dust mixed layer, respectively. To determine the accuracy of the DWL backscatter and extinction retrieval, the DWL profiles were compared to measurements from the ground-based aerosol lidar POLIS and the CALIPSO satellite, exhibiting a good agreement, with systematic differences lower than 20 % in the backscatter coefficient retrievals.

During SALTRACE, the DWL totalized 75 h of measurements, from which 56 h were performed in scanning mode. The atmospheric conditions present during most of the campaign flights, characterized by a large dust load between the ground and 4 to 6 km, provided excellent backscatter conditions for the DWL.

In order to evaluate the accuracy of the horizontal wind speed and direction measurements performed by the DWL, a set of vertical profiles were compared to those retrieved from collocated dropsonde observations. Only DWL profiles with less than 1 min of difference with respect to the dropsonde launch time were included in the comparison, while the dropsonde measurements were vertically averaged to match the DWL vertical resolution. The results, summarized in Figs. 2 and 3, indicate a systematic difference (bias) of 0.08 ms$^{-1}$ and a standard deviation of 0.92 ms$^{-1}$ for the wind speed difference between the DWL and the dropsondes measurements. The bias and the standard deviation does not exhibit significant dependence with the measurement altitude or measured wind speed, while the amount of points available for comparison as a function of altitude illustrates the average DWL coverage observed during SALTRACE. The mean wind speed measured by the dropsondes and the DWL exhibits a maximum between 4 and 6 km, associated with the

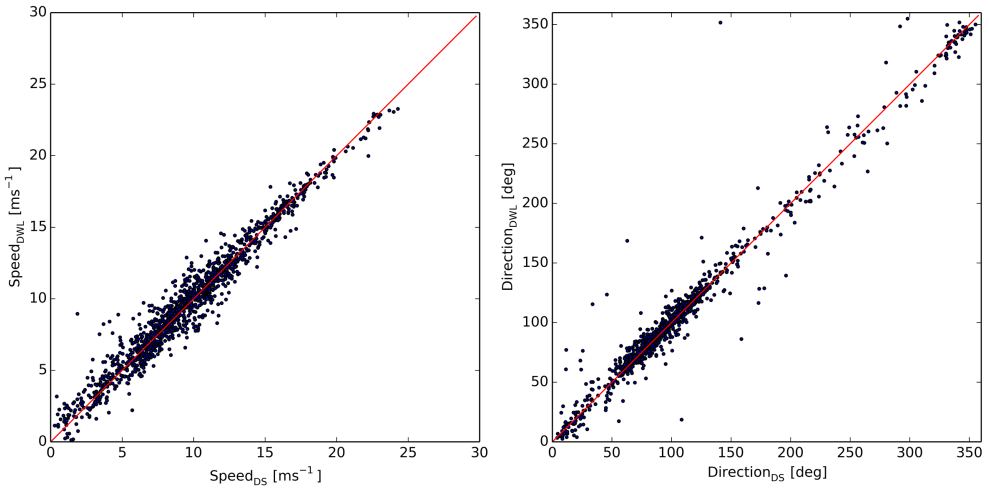


**Figure 2.** Comparison between DSs and DWL horizontal wind vector measurements. A total of 22 DWL/dropsonde profiles are included in this comparison, totaling 1329 speed–direction pairs.

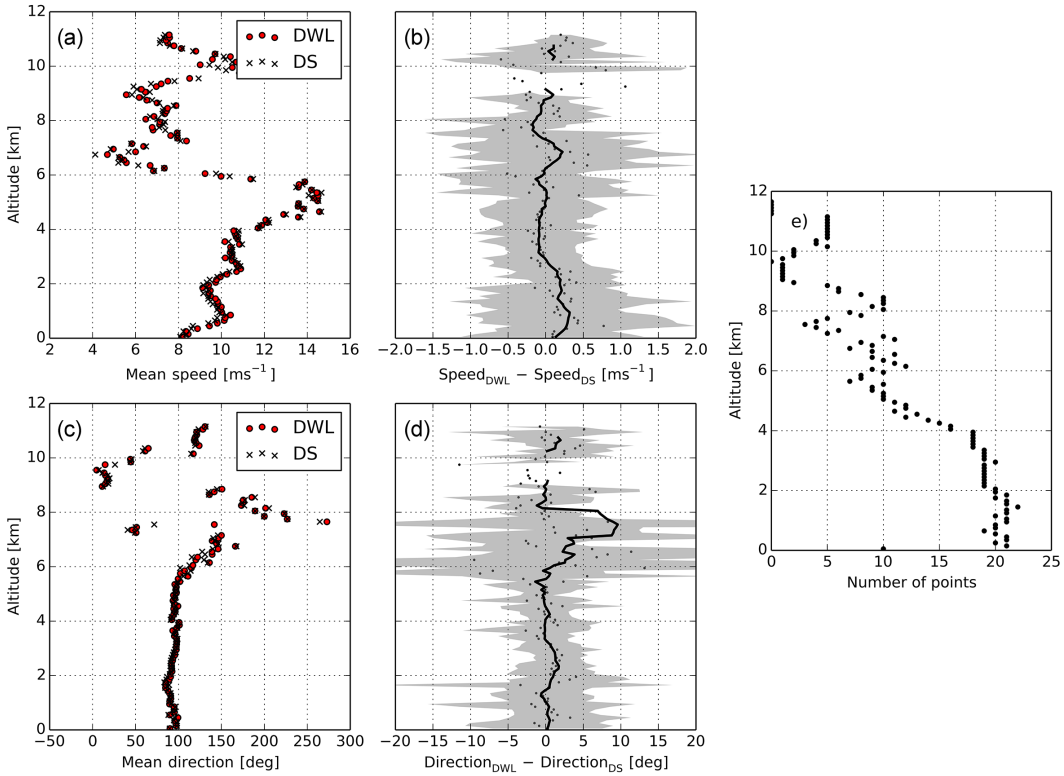


**Figure 3.** Comparison between 22 DSs and the corresponding collocated DWL horizontal wind vector measurements. Panels **(a, c)** show the mean of the DS and DWL wind speed and direction measurements, respectively; **(b, d)** show the difference between the mean DWL and DS wind speed and direction, respectively (dots, black), together with the corresponding 1000 m moving average (solid, black) and the standard deviation of the difference (shaded, grey); **(e)** shows the number of compared measurement points as a function of the altitude.

presence of the AEJ. For the case of the wind direction, the mean difference is 0.5° and the standard deviation is 10°, with values of around 5° between the ground and 6 km, and higher values between 6 and 8 km. The mean direction values between the ground and 6 km are between 90 and 100°, compatible with the easterly dust transport direction. The DWL performance evaluation shows results which are generally consistent with those obtained in the North Atlantic region during the Atlantic THORPEX Regional Campaign (A-TReC) in November 2003 (Weissmann et al., 2005), with

slightly higher standard deviation for the wind direction measurements and smaller differences in the wind speed for the SALTRACE dataset.

### 2.3 CALIOP

The Cloud–Aerosol Lidar with Orthogonal Polarization (CALIOP), the primary instrument of the CALIPSO satellite, is a two-wavelength polarization-sensitive lidar launched in 2006 by NASA (Winker et al., 2009). Based on a three-channel receiver, one for backscatter measurements at 1064 nm and two for the parallel and cross-polarized backscatter at 532 nm, the lidar is able to provide aerosol type classification, aerosol optical depth (AOD) and extinction coefficient vertical profiles. This allows a characterization of the mean Saharan dust vertical distribution close to the source and in the Caribbean region during the SALTRACE campaign, as well as an evaluation of the model to reproduce it. The dust vertical distribution is a key parameter which has a direct influence in the radiative transfer calculations and the atmospheric stability.

For this study, the level 2 (V3.3) dataset was used (https://www-calipso.larc.nasa.gov/search/). This dataset includes aerosol type classification, total column cloud, aerosol and stratospheric optical depth and extinction profiles with a vertical resolution of 60 m and a horizontal resolution of 5 km. In order to include only the most accurate measurements retrieved by CALIOP, a series of masks were applied to the data. First, profiles for which the cloud and stratospheric optical depth was not zero were masked out. A second mask was applied to keep only bins with the "Volume description Bit" equal to 0 ("clean air") or 3 ("aerosols"), cloud–aerosol discrimination (CAD) score is less than −80 and quality control (QC) flag is equal to 0 or 1. Finally, the AOD was derived from the vertical integration of extinction profiles where no data points were missing.

Since the CALIOP extinction coefficient retrieval relies on assumed lidar ratios, any systematic difference in the lidar ratio will directly affect the derived extinction profiles. An estimation of the systematic errors associated with the CALIOP extinction retrieval in the Saharan dust transport region is presented in Tesche et al. (2013). Based on a comparison between a ground-based Raman lidar deployed on the Cabo Verde region during SAMUM-2 and different CALIOP overpasses, this study concluded that CALIOP extinction profile retrievals of the SAL exhibit an average systematic underestimation of around 15 % during the summer season, while in some cases the difference reached 30 %. This systematic underestimation of CALIOP extinction retrievals can be explained by the fact that the CALIOP retrieval scheme assumes a dust lidar ratio of 40 sr, while Raman lidar measurements conducted during SAMUM-2 (Groß et al., 2011) and SALTRACE (Groß et al., 2015) indicate values close to 55 sr.

According to Wandinger et al. (2010), the dust lidar ratio of 40 sr used by the CALIOP algorithms is an effective value which takes into account the effect of multiple scattering and leads to backscatter coefficient profiles which are in good agreement with ground-based lidar measurements. Nevertheless, the use of this effective dust lidar for the calculation of the SAL extinction coefficients leads to their systematic underestimation. Although different techniques to correct this systematic error were proposed (e.g., Wandinger et al., 2010; Amiridis et al., 2013), the CALIOP retrievals shown in this study are presented in their original form. In cases where this effect could alter the derived conclusions, relevant comments are included (Sect. 3.3).

### 2.4 The MACC model

As part of the formerly Global Monitoring for Environment and Security (GMES) initiative (now Copernicus), intended to improve our understanding of the environment and climate change, the European Centre for Medium-Range Weather Forecasts (ECMWF) developed the MACC model, a forecasting and reanalysis system for aerosols, greenhouse gases and reactive gases based on the assimilation of satellite and in situ observations (Hollingsworth et al., 2008). This project extends the capabilities of the operational ECMWF Integrated Forecast System (IFS) by including a new set of forecasted variables. A detailed description of the model and parameterizations is given in Morcrette et al. (2009), while the assimilation process is explained in Benedetti et al. (2009) and a companion paper by Mangold et al. (2011) provides a first validation of the model results. Additional validation of the aerosol MACC products in northern Africa and the Middle East can be found in the work by Cuevas et al. (2015).

The MACC aerosol parameterization is based on the LOA/LMD-Z (Laboratoire d'Optique Atmosphérique/Laboratoire de Météorologie Dynamique-Zoom) model (Boucher et al., 2002; Reddy et al., 2005) and includes five types of tropospheric aerosols: dust, sea salt, organic, black carbon and sulfate. The first two correspond to natural sources and are represented in the model by three size bins for dust (0.03–0.55, 0.55–0.9 and 0.9–20 µm) and other three for sea salt (0.03–0.5, 0.5–5 and 5–20 µm). Currently, stratospheric aerosols are based on the climatology already included in the operational IFS as no prognostic fields are included in the model.

The sea salt emission parameterization is based on the model 10 m winds and a source function based on the works by Guelle et al. (2001) and Schulz et al. (2004). The emission, calculated for a relative humidity of 80 %, is integrated for the three sea salt model bins previously described. Emissions of dust depend on the 10 m wind, soil moisture, the UV-visible component of the surface albedo and the fraction of land covered by vegetation when the surface is snow free, adapted from Ginoux et al. (2001). A correction of the 10 m wind to account for gustiness is also included (Morcrette et al., 2008). The model includes aerosol transport by diffusion,

convection and advection treated with a semi-Lagrangian approach.

A set of different removal processes are included in the model, namely, dry deposition, sedimentation and wet deposition. Wet and dry deposition were directly adapted from the LOA/LMD-Z model, while the sedimentation scheme follows the work from Tompkins (2005a) on ice sedimentation.

One of the distinctive characteristics of the MACC model is the full integration of the aerosol model to the forecasting model. The 4D-Var system regularly employed in the IFS was extended to assimilate AOD observations from the Moderate Resolution Imaging Spectroradiometer (MODIS) on Terra and Aqua satellites at 550 nm, including the total aerosol mixing ratio as an additional control variable (Benedetti et al., 2009). This assimilation process is based on the adjustment of the model control variables (e.g., initial conditions) in order to minimize a cost function. This function depends on the difference between the observations and its model equivalent, and the relative weight assigned to each of them based on the estimated observational and model uncertainties. In the case of the MODIS AOD assimilation, the observations are compared with a model-derived AOD. The AOD observation operator derives the optical depth based on precomputed aerosol optical properties and model relative humidity for the aerosol species included in the model. After assimilation, the model output represents the best statistical compromise between the model background (forecast running without assimilation) and observations.

The MACC reanalysis was not available for 2013, having stopped in 2012, hence the operational run at the time of the campaign (June–August 2013) was used in this study. The model run with a time resolution of 3 h at T255L60, which corresponds to a horizontal resolution of approximately $0.8° \times 0.8°$ (78 km × 78 km) and 60 vertical levels, with the top at 0.1 hPa. The assimilation window is 12 h. Among others, the MACC model provides as output vertically resolved total AOD (natural plus anthropogenic aerosols) corresponding to each of the layers bound by the model levels. Since this study focuses on the comparison of the model with lidar observations, extinction coefficient profiles were calculated dividing the layer AOD by the layer thickness.

## 3 MACC model evaluation

The wind profile is a key parameter which determines the characteristics of the Saharan dust long-range transport. Although many studies were conducted to address the specific role of the trade winds, the AEJ and the AEWs in the dust lifting, transport and deposition, many questions remain still open (Ansmann et al., 2011; Schulz et al., 2012). As the Saharan dust transport path is mainly over the North Atlantic Ocean, the number of assimilated wind observations into a global model is very limited, which in turn affects their accuracy. Since many long-range transport studies use wind information provided by models, the evaluation of the accuracy of these simulations is of great importance. In this context, the wind dataset acquired by the DWL during SALTRACE provides a unique opportunity to evaluate the wind fields by the MACC model which are ultimately responsible for the Saharan dust long-range transport.

The assimilation of AOD from MODIS into the MACC model constrains the total aerosol mass, which is a great advantage considering the large uncertainties associated with the dust emission quantification (Huneeus et al., 2011). Nevertheless, since the assimilated variable is a column-integrated measurement, no independent constraints are introduced for each aerosol type and their vertical distributions. For that reason, the ability of the model to simulate the vertical distribution of each aerosol type still has to be evaluated. While CALIPSO provides regular backscatter and extinction coefficient measurements, which can be used to evaluate the model output and eventually provide data for assimilation, the aerosol detection sensitivity of CALIOP is limited compared to ground-based or airborne lidars. The DWL extinction profiles, simultaneously retrieved with the horizontal wind measurements, allow an independent evaluation of the simulated aerosol vertical distribution as well as the possibility to study the interaction between wind and aerosol distributions.

Since most of the flights were conducted either close to the west coast of Africa or in the Caribbean region, two regions were defined to study the model results with the DWL and CALIOP dataset. The first region is located at the west coast of Africa (0–30° N, 10–30° W), while the second region encloses the flights in the Caribbean (0–30° N, 50–70° W).

### 3.1 Method

Because the MACC model provides an output every 3 h, the horizontal resolution is approximately 80 km (T255) and the vertical levels are not homogeneously distributed as a function of altitude, a re-binning and interpolation process is necessary to compare the model output with the DWL and CALIOP observations. First, the observational data are re-binned to a grid with a horizontal resolution of 80 km and a vertical grid defined according to the 60 model levels for the US Standard Atmosphere, 1976 (http://www.ecmwf.int/en/forecasts/documentation-and-support/60-model-levels). Only bins with more than 50 % of the expected amount of values are used, otherwise, the bin is filled with a missing value flag. Then, the MACC model is linearly interpolated in space and time to match the re-binned observation data grid. Once observations and model data are in a comparable grid, different comparison techniques were applied. In the case of the horizontal winds, the re-gridded DWL measurements and model output corresponding to flights in each region were studied to evaluate the ability of the model to reproduce the main features of the wind in these two regions.

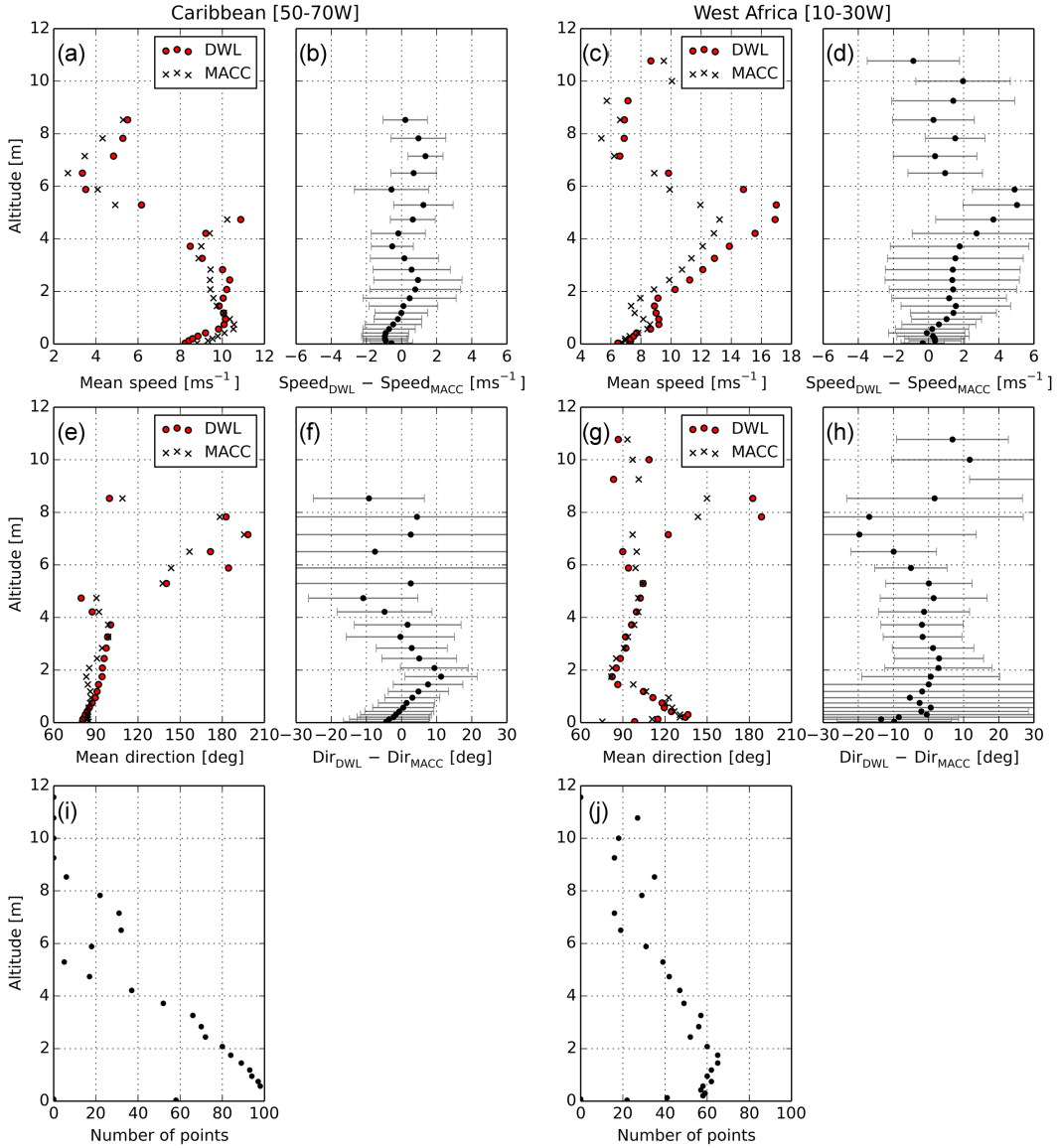


**Figure 4.** Comparison between the DWL and the MACC model horizontal wind measurements for the flights performed in the west African (right) and Caribbean (left) regions. Panels **(a, c)** show the mean of the DWL and MACC wind speed measurements in the Caribbean and west African region, respectively; **(b, d)** show the difference between the mean DWL and MACC wind speed in the Caribbean and west African region, respectively (dots, black), together with the standard deviation of the difference (shaded, grey). Panels **(e, g)** are the same as **(a, c)** but for the wind direction. Panels **(f, h)** are the same as **(b, d)** but for wind direction. Panels **(i, j)** show the distribution of compared points as a function of altitude in the west African (right) and Caribbean (left) regions, respectively.

In the case of the CALIOP extinction retrievals, 2 months of measurements corresponding to June and July 2013 were included in the comparison due to the relatively low amount of AOD and extinction retrievals available after the quality check process (Sect. 2.3). The measurements of CALIOP inside the regions defined in Sect. 3 and the corresponding MACC profiles were then, after re-gridding, zonally averaged in each region to provide a statistically relevant result. Extinction coefficient and AOD are reported by CALIOP and MACC at 532 nm.

### 3.2 Horizontal wind

The spatially averaged DWL wind retrievals were compared with the interpolated MACC winds in the west Africa and Caribbean regions defined in Sect. 3. In the case of the west African region, a total of seven flights conducted between 11 and 17 June 2013 are included in the comparison, which corresponds to 1202 speed–direction pairs. In the Caribbean region, 13 measurement flights conducted between 20 June and 11 July 2013 are compared with a total of 1532 speed–

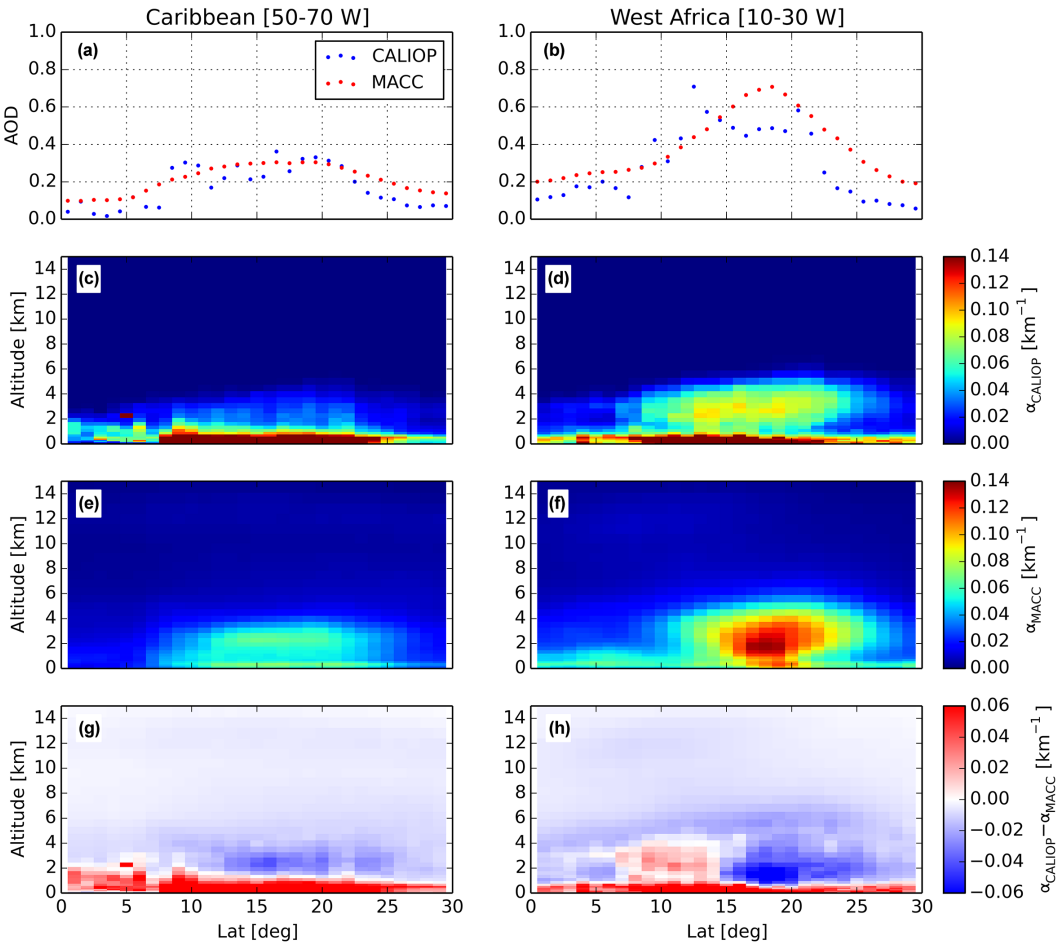


**Figure 5.** Comparison of CALIOP and MACC zonally averaged AOD and extinction coefficient for June–July 2013 in the regions of the study defined in Fig. 1. Panels **(a, b)** indicate CALIOP and MACC AOD zonal mean; **(c, d)** CALIOP extinction coefficient zonal mean; **(e, f)** MACC extinction coefficient zonal mean. Panels **(g, h)** show the difference between the zonally averaged extinction coefficient measured by CALIOP and simulated by MACC.

direction measurement pairs. In order to investigate possible correlations between the altitude and speed and the differences between the lidar and the model, the mean and standard deviation of the difference between the DWL and MACC as a function of the altitude, the number of compared measurements and the mean speed and direction corresponding to the African and Caribbean regions are shown in Fig. 4.

In the case of the west African region, Fig. 4c and g indicate a good agreement in the profile shape between the mean measured and simulated wind speed and direction, respectively, with the altitude of the wind maxima and minima being well reproduced by the model. Regarding the wind speed magnitude, Fig. 4d indicates an underestimation of the wind speed by the model between 0.5 and 6 km, with a maximum difference of 5 m s$^{-1}$ at around 5 km. This is approximately coincident with the altitude of the maximum simulated (13.2 m s$^{-1}$) and measured wind speeds (17 m s$^{-1}$), which corresponds to the presence of the AEJ in the region. The underestimation of the AEJ by the ECMWF model was already reported in previous studies, like the one conducted during the JET2000 campaign in August 2000 (Thorncroft et al., 2003; Tompkins et al., 2005b). The comparison, performed against a set of dropsonde measurements, indicated a similar difference profile, with a maximum difference of around 5 m s$^{-1}$. As in the case of the comparison between the lidar and the dropsondes, the distribution of points included in the comparison (Fig. 4j) is representative of the lidar coverage, which in turn is determined by the aerosol load distribution and cloud coverage. Most of the measurements are available below 6 km, in coincidence with the SAL upper bound.

The left row of Fig. 4 presents the results for the Caribbean region. In contrast to the previous case, some differences in the mean wind speed and direction structures are recognizable in Fig. 4a and e. Both the DWL and the model show a similar behavior below 0.8 km, characterized by an in-

creasing wind speed as a function of altitude, reaching its maximum at 0.8 km. Although the simulated and measured wind gradients are similar, the simulated speeds are around $1\,m\,s^{-1}$ larger than the measured ones. Above the boundary layer, the model shows a decrease in the wind speed and a general underestimation of the wind speed compared to the DWL measurements. As in the previous case, the distribution of compared points as a function of the altitude (Fig. 4i) is correlated with the dust load and cloud coverage. The strong reduction of measurement points above 4 km is related with the general decrease in the altitude of the SAL top boundary as the dust moves westward.

### 3.3 Aerosol extinction coefficient

In order to analyze the accuracy of the MACC model vertical aerosol distribution, the extinction coefficient profiles were compared to those retrieved by CALIOP during the months of June and July 2013 for a wavelength of 532 nm. An overview of the comparison is presented in Fig. 5, where the zonal mean of the simulated and measured AOD and extinction coefficient is presented, together with the difference between the model and measurement, for the west African and Caribbean regions indicated in Fig. 1.

Figure 5a and b show the zonal mean of the AOD for the two regions. The simulated and measured AOD close to the African coast (Fig. 5b) exhibit a similar bell shape, with the model maxima located at 18.5° N and the weighted mean of the CALIOP AOD at 15° N. In the Caribbean region, the model and the CALIOP measurements show a better agreement, with the center of the dust plume located at 16° N in both cases. The change in the AOD between both regions, a reduction by one half due to the transport between the African coast and Barbados, is in relatively good agreement. Nevertheless, the AOD north and south of the dust plume show consistent higher values in the model. This bias is consistent with the study presented in Kim et al. (2013), which showed that MODIS AOD values corresponding to clean marine aerosols approximately double the AOD reported by CALIOP.

While a relatively good agreement of the measured and simulated AOD is expected due to the constraints introduced by the assimilation of MODIS measurements, the vertical distribution of the dust, which plays a crucial role in atmospheric radiative transfer studies (Zhang et al., 2013), has to be evaluated. The zonal averaged extinction coefficient measured by CALIOP in west Africa (Fig. 5d) shows an elevated dust plume between 5 and 30° N, with its lower bound at 1 km and its upper bound at approximately 6 km. Below 1 km, an aerosol-loaded boundary layer is recognizable, with higher extinction coefficients below the SAL, probably due to dust entrainment into the atmospheric boundary layer (ABL). In the Caribbean, the dust plume top sinks to around 4 km, and the extinction decreases to about half of the values measured close to the source region. As in the previous case, the ABL shows higher extinction below the SAL than north or south of it; the characteristic wedge shape as we move from higher to lower latitudes can also be noted.

The modeled aerosols' vertical distribution close to the dust source region is presented, together with the difference with the CALIOP measurements, in Fig. 5f and h, respectively. The modeled dust plume shows relatively good agreement in spatial distribution with respect to the CALIOP measurements, extending between 10 and 30° N. Coincident with the AOD measurements presented in Fig. 5b, the simulated plume is slightly displaced in the north direction and exhibits a higher maximum extinction at around 2 km. This displacement, clearly visible in the difference plot, could lead to a change in the interaction between the SAL and the AEJ, which in turn will promote different dust transport patterns. However, the major difference between CALIOP and MACC is visible in the boundary layer and above the SAL. In the ABL, the model strongly underestimates the extinction coefficient. The model average extinction in the ABL (< 1 km) is $0.045\,km^{-1}$ in the Caribbean region and $0.065\,km^{-1}$ in the west Africa region, while the CALIOP average retrievals are 0.145 and $0.13\,km^{-1}$, respectively. Although the CALIOP retrievals of the ABL extinction are affected by the uncertainty in the lidar ratios and the underestimation of the SAL extinction, these effects cannot explain the large discrepancy observed between the model and the CALIOP retrieval.

The underestimation of the SAL extinction due to an underestimation of the dust lidar ratio would lead to an underestimation of the CALIOP backscatter in the boundary layer, which in turn would lead to an even larger CALIOP retrieval. On the other hand, since the aerosol load found in the ABL below the SAL is dominated by a mixture of marine aerosol and dust, the expected average CALIOP lidar ratio will oscillate between the lidar ratio values corresponding to pure marine (20 sr) and pure dust (40 sr). In the case of the retrievals presented in Fig. 5c and d, the average lidar ratio used by CALIOP for the calculation of the ABL (< 1 km) extinction coefficient was found to be between 33 sr in the west African coast region and 37 sr in the Caribbean region. These values are similar to those presented in Groß et al. (2016), where the average lidar ratio observed in the ABL was $26 \pm 5$ sr, with values ranging from $22 \pm 5$ sr in the case of pure marine aerosol to $35 \pm 3$ sr for the case of a dust-dominated ABL. These results, corresponding to June–July 2013, are in agreement with the CALIOP retrievals presented in Cuevas et al. (2015), where a similar difference in the ABL extinction in the west African region (M'Bour) was also observed during the summer seasons of 2007 and 2008.

The comparison of the CALIOP extinction retrievals and the corresponding model results indicate a relatively small overestimation of the SAL extinction by the model. Even if the CALIOP extinction retrievals of the SAL are multiplied by a correction factor of 1.375 (55 sr/40 sr) to take into account the underestimation of the lidar ratio by CALIOP discussed in Sect. 2.3, most of the MACC results are still

above the CALIOP retrievals (not shown). The SAL AOD derived from MACC is still larger than the SAL AOD derived from CALIOP extinction. Based on SAL lower and upper bounds between 2 and 5 km in the Caribbean and between 1 and 6 km in the African region, the SAL AOD values based on MACC are 50 and 10 % larger than the CALIOP retrievals, respectively. Additionally, although the pure dust lidar ratio used for CALIOP is 40 sr, sometimes the algorithm identifies part of the SAL as polluted dust, with an associated lidar ratio of 55 sr. This leads to an average lidar ratio larger than 40 sr, which in turn leads to a higher extinction and to a smaller systematic bias. If instead of correcting the CALIOP extinction retrievals by using the correction factor suggested by Wandinger et al. (2010) the mean underestimation reported by Tesche et al. (2013) from Table 5 is used ($1/0.858 = 1.165$), the differences are even larger.

Above the SAL, the model indicates the presence of a very thin aerosol layer extending up to 20 km which is not visible in the CALIOP measurements. Since the extinction coefficients predicted by the model above the SAL are in the order of the sensitivity threshold of CALIOP ($\sim 0.01\,\mathrm{km}^{-1}$), a direct validation of these features is not possible only by means of CALIOP measurements. Recent studies (e.g., Rogers et al., 2014) indicate that the lack of detection of weakly backscattering aerosol layers in the free troposphere leads to an underestimation of approximately 0.02 in the CALIOP column AOD. This effect can partially explain the systematically lower CALIOP AOD values observed in Fig. 5a and b. In order to further investigate this feature, a comparison of the model with the DWL measurements performed during the transfer flight between Cabo Verde and South America is presented in the next section.

## 4 Characteristics of the Saharan dust long-range transport

The study presented in the previous section provided a general overview of the performance of the model. In this section, a set of three selected flights form the SALTRACE campaign are used to provide a deeper insight into some characteristic features of the Saharan dust long-range transport mechanism. The first case study, corresponding to a flight between Cabo Verde and Dakar, is included to further investigate the differences observed in the AEJ intensity as well as the ability of the model to reproduce the generation of AEWs. The second case study presents measurements over the North Atlantic Ocean, which provides a second comparison of the AEJ speed and the opportunity to analyze the interaction of the dust with the ITCZ. Finally, the third case presents the measurements of a dust outbreak in the Caribbean region after the long-range transport across the North Atlantic.

In order to facilitate the interpretation of these case studies, the corresponding synoptic situation is presented in Fig. 6. These charts, which include the wind direction and wind speed at 700 hPa and the total AOD, are based on the MACC model results. Additionally, in order to situate the case studies within the context of the SALTRACE campaign, a Hovmöller diagram with the MACC meridional winds and AOD averaged between 0 and 30° N is presented in Fig. 7. This diagram simplifies the visualization of some features associated with the Saharan dust long-range transport, like the dust outbreaks, the AEWs and the passage of the tropical storm Chantal. A period of 3 to 5 days between outbreaks and a transport time of around 5 days between Dakar and Barbados can be easily noted in the AOD diagram (Fig. 7, right). In order to highlight the strong correlation of these outbreaks with the propagation of AEWs, the wave troughs relevant for the presented case studies are indicated in Fig. 7.

### 4.1 Dust plume at the west African coast

On 12 June 2013 the *Falcon* performed a research flight at the west coast of Africa, departing from Cabo Verde at 08:52 UTC and landing in Dakar at 12:08 UTC. The model winds at 700 hPa are presented, together with the AOD, in Fig. 6a. Wind speeds around 15 to 25 $\mathrm{m\,s}^{-1}$ can be observed between 10 and 15° N, which is compatible with the presence of the AEJ. The inverted V-shape disturbance in the AEJ flow in the Dakar region, suggests the passage of an AEW during the observation period. The observation of the change in the meridional wind flow direction at pressure levels between 850 and 700 hPa is a typical way to detect AEWs, with the wave trough defined as the point of zero meridional wind (change from northerly to southerly flow) (e.g., Reed et al., 1977). According to this definition, the wave trough can be recognized at 17° W during the observation period (AEW 1; Fig. 7). This wave, sampled during the flight on 12 June 2013, propagated further to the west at an approximate speed of 8° ($\sim 900$ km) per day, reaching Barbados on 17 June 2013. Several other waves can be also observed in the presented period. All wave cases propagate westward with a similar speed, which gives a mean travel time of around 5 days between the African west coast and Barbados. This result is consistent with observations and previous studies on the AEW behavior (Zipser et al., 2009).

The AOD for the Dakar region presented in Fig. 6a shows a dust-loaded air mass on the leading edge of the AEW and a region of less dust load behind the trough. Satellite images (not shown), indicate the presence of strong convective activity behind the trough, which is a typical feature of the AEWs (Fink et al., 2003; Cifelli et al., 2010). The propagation of the dust outbreak as it leaves the west African coast can be observed in Fig. 7 (right). According to the model results, this outbreak was the largest one (highest AOD) during the SALTRACE observation period. The modeled passage of the AEW seen in Fig. 6a is coincident with a reduction in the amount of exported dust behind the trough (AEW 1). This

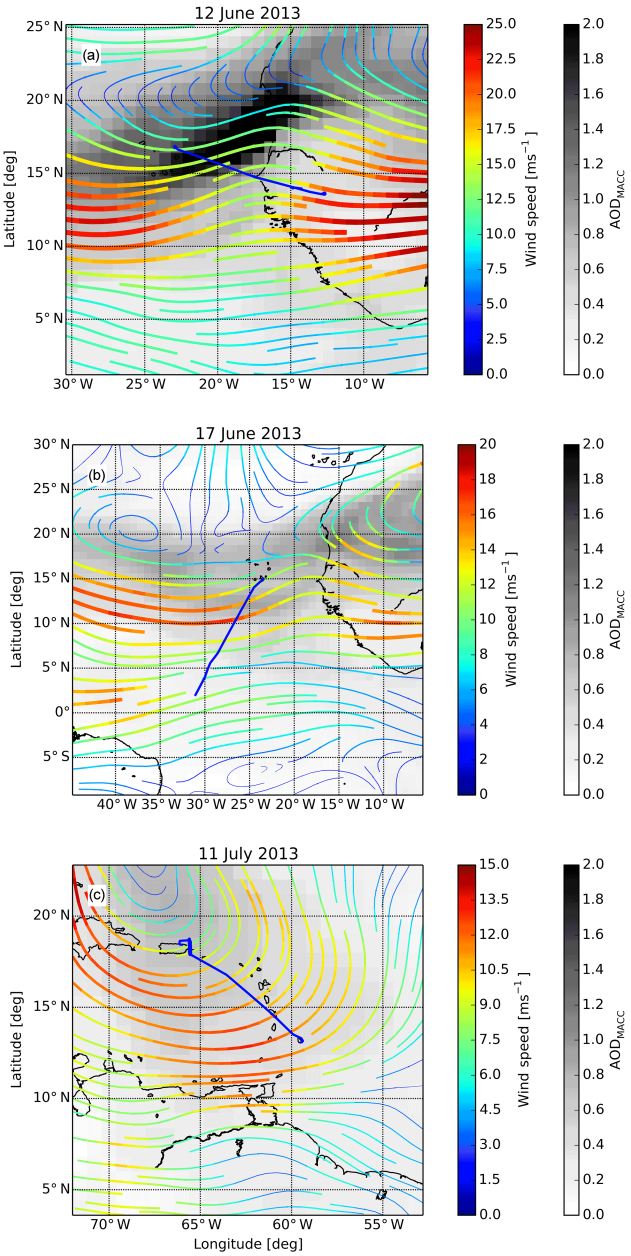


**Figure 6.** Horizontal winds at 700 hPa and AOD derived from the MACC model for the regions corresponding to the three cases: **(a)** 12 June 2013 09:00 UTC, flight between Sal and Dakar; **(b)** 17 June 2013 15:00 UTC: flight between Cabo Verde and South America; **(c)** 11 July 2013 18:00 UTC: flight between Barbados and Puerto Rico. The sections of the flight tracks shown in Figs. 8, 9 and 11 (blue, solid), wind streamlines (in m s$^{-1}$) and AOD (grey color scale) are shown.

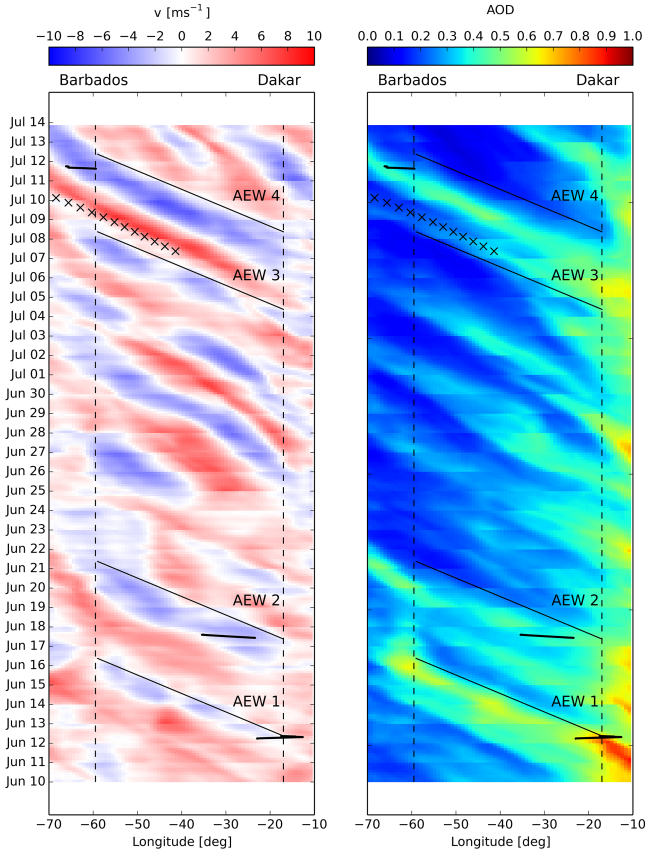


**Figure 7.** MACC model meridional wind (left) and AOD (right) presented in form of a Hovmöller diagram averaged for latitudes between 0 and 30° N and 700 hPa pressure level. The flights corresponding to each case (black, thick, solid), the longitude of Dakar and Barbados (black, dashed), relevant AEWs troughs (black, solid) and the position of the tropical storm Chantal (black, crosses) are indicated.

could be the result of the enhanced wet deposition associated with the convective cell activity (Desboeufs et al., 2010).

The DWL measurements corresponding to the selected case study are presented in Fig. 8. The extinction coefficient profiles derived from the DWL measurements presented in Fig. 8a are in qualitative agreement with the distribution simulated by the model (Fig. 8b), with an elevated dust plume between 1 and 6 km riding on top of the marine boundary layer as it leaves the African continent (17° W). These results are compatible with the BERTHA ground-based measurements carried out in Cabo Verde during the SAMUM-2b campaign (Tesche et al., 2011) in summer 2008, where a 0.5–1.0 km deep maritime boundary layer topped by a 4–5 km deep mineral dust layer was typically observed. As has been noted in the previous section, the model underestimates the extinction of the marine boundary layer and overestimates the extinction of the SAL. The average SAL extinction retrieved from the DWL for altitudes between 1 and 6 km and longitudes between 16.17 and 15° W is 0.11 km$^{-1}$, while the corresponding MACC average extinction is 0.4 km$^{-1}$. This difference is much larger than the systematic error of ±20 % estimated for the DWL backscatter retrievals. Although in this case the compared values are extinction coefficients and not backscatter coefficients, the lidar ratios used in the DWL

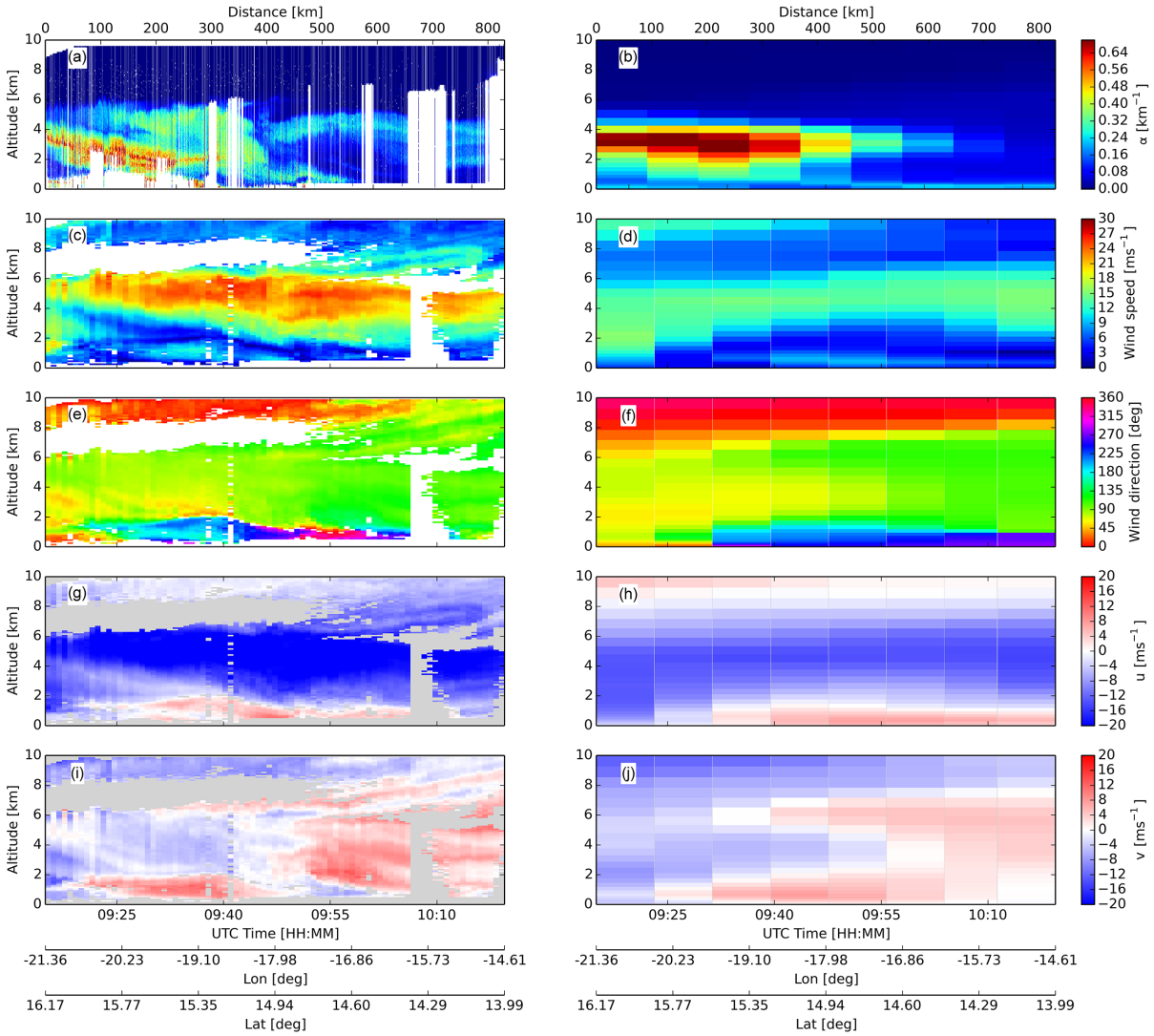


**Figure 8.** DWL measurements (left column) and MACC model (right column) along the measurement track for the flight on 12 June 2013. Panels **(a, b)** show the extinction coefficient; **(c, d)** the horizontal wind speed; **(e, f)** the horizontal wind direction; **(g, h)** the zonal wind component; **(i, j)** the meridional wind component. Regions where no atmospheric signal is available (e.g., below clouds, low laser energy, low aerosol load) are colored white in panels **(a)**, **(c)**, **(e)** and grey in panels **(g)**, **(i)**.

retrieval (55 sr for the SAL, 35 sr for the marine-dust mixed layer and 30 sr for the marine boundary layer) are in agreement with those found in the literature and small local variations cannot explain the large difference observed in this case study.

The enhanced cloud coverage associated with the previously mentioned convective system can be seen starting at 09:35 UTC (behind the wave trough) as white regions in the DWL extinction plot (Fig. 8a). These clouds, visible at altitudes between 6 and 8 km, completely blocked the DWL laser, which in turn led to missing data below them (white regions). An associated decrease in the aerosol load in this clouds region can also be noted in the DWL retrievals starting at 09:47 UTC. Since the MACC model extinction product does not include clouds, the enhanced cloud coverage cannot be seen in Fig. 8b.

The horizontal wind profiles retrieved by the DWL and simulated by MACC are presented as speed–direction and $u$–$v$ components in Fig. 8c–j. The presence of the AEJ can be recognized on both: the DWL speed measurements (Fig. 8c) and the corresponding MACC speed profiles (Fig. 8d) for altitudes between 3 and 6 km. The magnitude of the jet is, nevertheless, strongly underestimated by the model by almost 10 m s$^{-1}$, which is above the mean difference of 5 m s$^{-1}$ observed in the previous section for the mean of all flights in the AEJ region. The underestimation of the AEJ impacts not only in the amount of transported Saharan dust but also in the propagation and development of AEWs (Leroux and

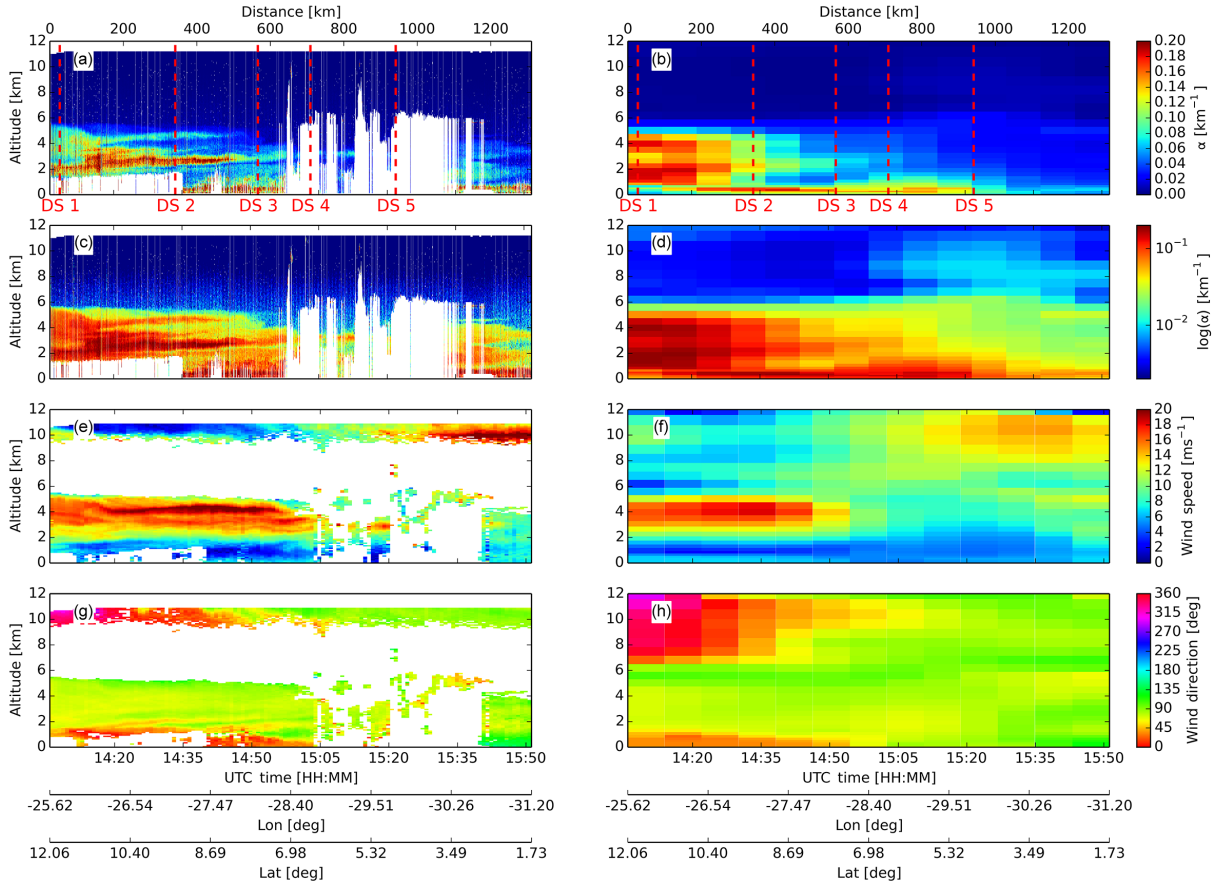


**Figure 9.** DWL measurements (left column) and MACC model (right column) along the measurement track for the flight on 17 June 2013. Panels **(a, b)** show the extinction coefficient; **(c, d)** the extinction coefficient plotted in logarithmic scale; **(e, f)** the horizontal wind speed; **(g, h)** the horizontal wind direction. The white color indicates regions were no atmospheric signal is available (e.g., below clouds, low laser energy, low aerosol load). The dropsondes' launch time (dashed, red) is indicated in **(a)** and **(b)**.

Hall, 2009). Below 2 km, a land–sea breeze system located over Dakar (−15° N, 18° W) can be recognized in the DWL and MACC wind speed–direction profiles. The passages of the AEWs are easier to recognize when the wind vector is presented as $u$ and $v$ components. The $u$ component of the measured (Fig. 8g) and simulated (Fig. 8h) wind profiles is dominated by the AEJ, while the $v$ component captures the wave trough observed in Figs. 7 and 8. Both the position of the trough and the amplitude of the wind meridional component are well reproduced by the model. A strong coincidence between the dust plume border and trough is also visible in both cases.

### 4.2 Dust long-range transport across the Atlantic

The second case corresponds to a flight between Cabo Verde and South America performed on 17 June 2017 between 13:24 and 17:21 UTC. This flight gives the opportunity to study the interface between the SAL and the ITCZ, as well as the AEJ, the tropical easterly jet (TEJ) (Chen and Loon, 1987) and the ability of the model to reproduce them. The synoptic situation, presented in Figs. 6b and 9, shows a dust plume laterally bound by an AEW trough located at 15° W (AEW 2, Fig. 7) and an AEW crest located at 40° W and south bound by the ITCZ, located between 3 and 8° N. In the DWL measurements, the ITCZ can be recognized by the presence of strong convective activity and the associated development of convective clouds at 6 km (white areas) and between 2 and 7° N.

The DWL and MACC extinction and horizontal wind profiles are presented in Fig. 9. The MACC model is able to reproduce the main characteristics of the aerosol vertical distribution. North of the ITCZ, a dust plume with its upper bound at 6 km is visible by both the model and the DWL. In the case of the DWL measurements, the SAL is lower bound by a characteristic wedge-shaped marine boundary layer topped by low-level clouds, while in the case of the MACC model, the lower bound seems to be lower and constant as a function of the latitude. The model and dropsonde temperature and water vapor mixing ratio vertical profiles presented in Fig. 10 show a generally good agreement, although a consistent un-

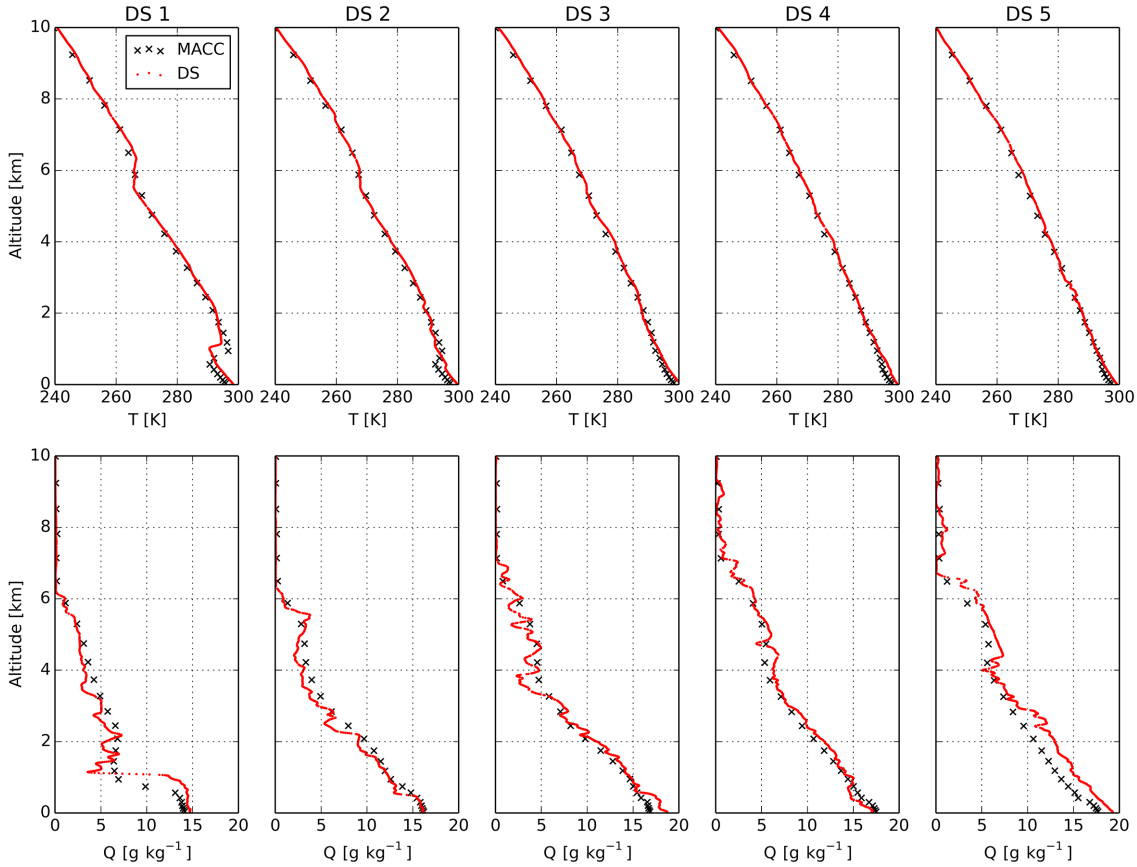


**Figure 10.** Temperature (upper row) and water vapor mixing ratio (lower row) measured by the dropsondes launched during the flight on 17 June 2013 (dots, red) and the corresponding MACC model values (crosses, black).

derestimation of the model temperature of around 2° K below 1 km can be observed. In the case of the first dropsonde (DS 1), the temperature and mixing ratio profiles are compatible with the differences observed by the DWL, with the model showing an ABL top inversion approximately 500 m below the measured one. Although in the case of the DWL the coverage in the ITCZ is limited by the presence of clouds, the dust load south of it is clearly reduced by the effect of wet deposition on both the DWL and the MACC model simulation. As in the previous section, the model indicates the presence of aerosols above the SAL, especially in the ITCZ region, which is not captured by the lidar. Since the extinction coefficients shown by the model are quite low, an additional set of extinction plots in logarithmic scale were added to highlight this feature (Fig. 7c and d). The average extinction coefficient shown in Fig. 7d for an altitude of 9.2 km range from 0.003 km$^{-1}$ between 14:35 and 14:50 UTC to 0.01 km$^{-1}$ between 15:05 and 15:35 UTC. Because the DWL relies on the atmospheric aerosols for the retrieval of wind measurements, such change in the aerosol load should result in a change in the wind retrieval coverage. Nevertheless, this is not observed in Fig. 7e and g, where the wind retrieval coverage is limited to a band of approximately 2 km below the *Falcon*, independently of the geographical location. While the extinction coefficients shown by MACC above the SAL are normally below 0.01 km$^{-1}$, its detection by the DWL, especially close to the *Falcon*, would be expected in the case of a real feature. The aerosols shown by the model in the upper troposphere are likely to be an artifact introduced by the model in order to compensate the lack of extinction in the ABL and hence balance the assimilated AOD from MODIS.

The horizontal wind speed profiles are presented in Fig. 7e and f for the DWL and the MACC model, respectively. The AEJ, visible in the DWL measurements on the north of the ITCZ for altitudes 2 km and almost 7 km can also be seen in the model, although slightly displaced to the north and with a lower mean speed. Below 1.5 km, northerly and southerly trade winds are visible in the model and DWL profiles. A third feature, located to the south of the ITCZ and at around 10 km is the TEJ. While the position of the TEJ is well captured by the model, the DWL measurements suggest a model underestimation of the wind speed of around 5 m s$^{-1}$.

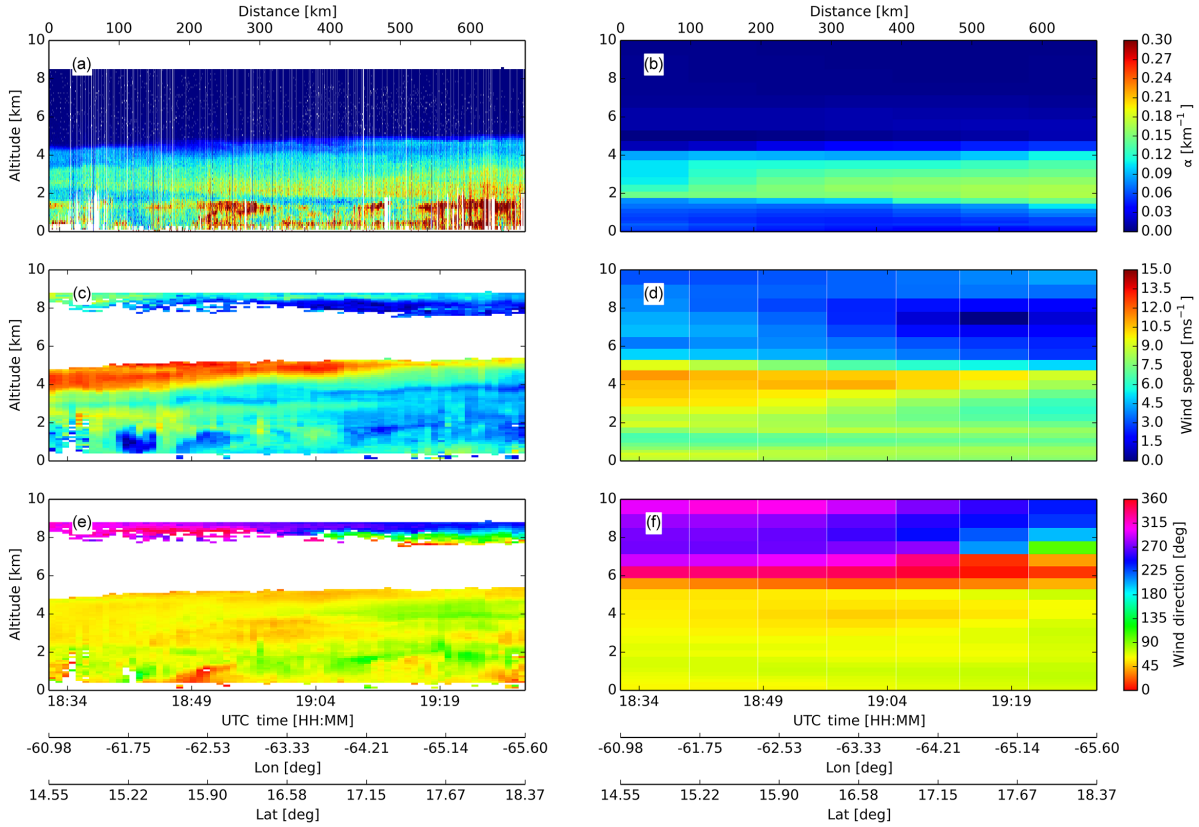


**Figure 11.** Same as Fig. 8, but for the flight on 11 July 2013. Zonal and meridional wind components are omitted.

### 4.3 Dust plume in the Caribbean region

The synoptic situation presented in Figs. 6c and 7 shows a dust-loaded air mass reaching Barbados on 11 July 2013. This Saharan dust outbreak was the first to reach Barbados after the passage of the tropical storm Chantal over the Barbados region, between 8 and 9 July 2013. According to the results from the MACC model, this outbreak left the African continent 5 days before, on 6 July 2013, together with an AEW. In contrast to the 12 June and 17 June cases, the dust moved behind the AEW (AEW 3; Fig. 7) trough in this case and almost no dust was visible in front of the trough. This change is likely to be due to the influence of the tropical storm Chantal and the associated wet deposition which can be clearly seen in Fig. 7 as a decrease in the AOD. On 11 July 2013, two research flights were performed. This case study focuses on the second flight, which departed from Barbados at 18:04 UTC and landed in Puerto Rico at 21:05 UTC. The DWL extinction and horizontal wind measurements are presented, together with the MACC model, in Fig. 10. A comparison between the DWL retrievals for the first flight on 11 July 2013 and the corresponding ground-based POLIS measurements is presented as part of the DWL calibration validation in Chouza et al. (2015).

As in the previous cases, the modeled SAL shape and extinction is in relatively good agreement with the DWL measurements, suggesting an adequate treatment of the Saharan dust long-range transport and deposition processes by the model. Both measurements and models show a dust plume with a descending upper bound and a rising lower bound as it moves westwards together with higher extinction coefficients in its lower half. The model results corresponding to the measurements conducted close after the takeoff from Barbados shows an aerosol plume extending from approximately 1.7 km up to 5 km bound by two temperature inversions (not shown). This is compatible with the radiosounding and POLIS ground-based lidar measurements presented in Groß et al. (2015), where the lidar measurements conducted on 11 July 2013 (23:00–24:00 UTC), 5 h after takeoff, show the SAL between 1.5 and 4.8 km. In the same way as the model, the sounding temperature profiles exhibit inversions at its lower and upper bounds. In coincidence with previous measurements, the ABL extinction is strongly underestimated by the model and a thin aerosol layer above the SAL is modeled, but not seen by the DWL.

As can be seen in Fig. 6c, the general circulation in the region is dominated by the Bermuda high pressure system, which leads to an anti-cyclonic flow over the Caribbean

(Fig. 6c). The modeled winds are in relatively good agreement with the measurements. The high wind speeds found between 4 and 5 km are underestimated by the model by approximately $3\,m\,s^{-1}$, while its wedge shape and direction are well reproduced. The influence on the lee side of Dominica and the Guadeloupe islands can be seen in the DWL retrievals for latitudes between 15 and 16° N. These islands, with surfaces of 750 and $1600\,km^2$ and elevations of up to 1447 and 1467 m, respectively, introduce relatively large disturbances in the low-level flow. This effect, characterized by a relatively sudden decrease in the wind speed and a change in the direction for altitudes below 1.5 km cannot be captured by the MACC model due to its relatively coarse grid of 80 km.

## 5 Summary and conclusions

Aerosol global models are of key importance not only for environmental and climate change studies but also as air quality monitoring tools. The evaluation of the model capabilities by mean of comparisons with observations is of great importance for improvement of the models. In this study, the ability of the MACC model to reproduce the Saharan dust long-range transport across the Atlantic Ocean was investigated by means of a comparison with DWL, CALIOP and dropsonde observations conducted during SALTRACE. For the first time a DWL was used to characterize the Saharan dust transport and its associated features.

First, the horizontal wind vector retrievals by the DLR airborne DWL during SALTRACE were evaluated with a comparison with collocated dropsonde measurements. The comparison shows a very good agreement, with a DWL–dropsonde mean difference of $0.08\,m\,s^{-1}$ and a standard deviation of $0.92\,m\,s^{-1}$ for the wind speed. For the case of the wind direction, the mean difference was 0.5° and the standard deviation 10°. These estimated accuracies are in agreement with previous studies (e.g., Weissmann et al., 2005).

The second part of this work focused on the evaluation of the MACC model using the wind and aerosol backscatter measurements from the DWL in combination with CALIOP extinction profiles and dropsondes. Two evaluation regions were defined: one close to the Saharan dust source on the west coast of Africa and a second one in the Caribbean region. Although the wind comparison shows a generally good agreement in both regions, a systematic underestimation of the AEJ wind speed was observed in the region close to west Africa. Since the AEJ is one of the main Saharan dust advection mechanisms, its underestimation would lead to a wrong estimation of the amount of dust being transported. Additionally, since the AEJ and the associated vertical and horizontal wind shear serve as an energy source for the AEWs, the correct modeling of jet speed and position is crucial to correctly model the AEWs propagation and evolution. As indicated by Tompkins et al. (2005), a change in the aerosol radiative effect climatology can alter the AEJ speed. Thus, the observed underestimation in the AEJ wind speed could be partially due to the lack of radiative coupling between winds and aerosols in this MACC operational analysis run in 2013. Follow-up studies could explore this coupling of the aerosol and wind fields in a manner similar to Rémy et al. (2015), specifically for the SAL. Such a study would allow, in combination with the results presented in this work, to estimate the importance of an interactive radiative coupling to correctly simulate the AEJ intensity, the Saharan dust vertical distribution and its long-range transport.

Based on CALIOP extinction profiles, the model average aerosol vertical distribution was evaluated in both regions. Although a generally good agreement was observed in the position and geometry of the SAL, a strong systematic underestimation of the marine boundary layer aerosol content was observed in both regions. Since the MACC model assimilates MODIS AOD measurements, the total model AOD is generally in good agreement with CALIOP measurements. A slight overestimation of aerosol in the upper troposphere was observed in the model, which is likely to be an artifact introduced by the model to compensate the lack of aerosol in the marine boundary layer and thus match the assimilated MODIS AOD. An additional confirmation of this explanation could be investigated in future studies by means of a comparison between the model and in situ aerosol measurements.

The good agreement between the modeled and measured AOD observed in this study serves as an indication of the potential of satellite data assimilation in global aerosol models. Currently, studies are being conducted in order to assimilate CALIOP attenuated backscatter vertical profiles in order to constrain the modeled aerosol vertical distribution. In a similar way, previous studies showed an improvement of modeled winds after the assimilation of airborne Doppler wind lidar measurements (Weissmann et al., 2007). Future satellite missions like Aeolus (ESA, 2008) and EarthCARE (Illingworth et al., 2014) will provide a whole new set of wind and aerosol vertical profile measurements which are expected to lead to a significant improvement in weather prediction and global climate models, especially in regions where observations are sparse.

In addition to the average wind and extinction comparison in both regions, three case studies were presented. These cases, which correspond to the initial, middle and final phase of the Saharan dust long-range transport process, allowed us to investigate the characteristic features of the Saharan dust transport and the ability of the model to reproduce them. The DWL measurements carried out close to the west African coast show a SAL extending from 1 km up to 6 km and the AEJ at altitudes between 3 and 6 km, with speeds of up to $25\,m\,s^{-1}$. Additionally, the passing of an AEW and the associated convective activity allowed us to investigate its effect on the dust distribution and transport pattern. As the dust is transported west over the Atlantic Ocean, the top of the SAL sinks, while its bottom rises. This typical SAL feature

was confirmed by the DWL retrievals corresponding to the second and third case studies. The measurements conducted over the Atlantic Ocean, corresponding to the second case study, showed a strong decrease in the dust load in the ITCZ as well as a rise in the lower edge of the SAL for low latitudes. The wind measurements carried out over the Atlantic revealed the presence of the AEJ north of the ITCZ, with speeds between 15 and 20 $m\,s^{-1}$ and altitudes between 2 and 5 km. As the dust plume reached the Caribbean, approximately 5 days after leaving Africa, the top of the SAL was slightly below 5 km and its bottom at 2 km.

Although in all cases we found a good qualitative agreement between the measurements and the model, an underestimation of almost 10 $m\,s^{-1}$ in the AEJ speed was observed in the first case study. This is approximately 2 times the observed difference between the mean dropsonde measurements and the model. As expected, due to the relatively coarse resolution of the model, some island-induced mesoscale (< 100 km) disturbances in the winds where observed by the DWL but not reproduced by the model. The analysis of the extinction coefficient profiles shows similar results to those based on CALIOP and MACC spatio-temporal averages. The modeled extinction values in the boundary layer corresponding to the three case studies were far below the measured ones by the DWL, while above the SAL a thin aerosol layer was observed in the model but not in the DWL retrievals.

## 6 Data availability

Data used in this manuscript can be provided upon request by e-mail to Dr. Oliver Reitebuch (oliver.reitebuch@dlr.de).

*Acknowledgements.* This work was funded by the Helmholtz Association under grant number VH-NG-606 (Helmholtz-Hochschul-Nachwuchsforschergruppe AerCARE). The SALTRACE campaign was mainly funded by the Helmholtz Association, DLR, LMU and TROPOS. CALIOP/CALIPSO data were obtained from the NASA Langley Research Center Atmospheric Science Data Center. The SALTRACE flights on Cabo Verde were funded through the DLR-internal project VolcATS (Volcanic ash impact on the Air Transport System). The first author thanks the German Academic Exchange Service (DAAD) for the financial support.

The article processing charges for this open-access publication were covered by a Research Centre of the Helmholtz Association.

Edited by: U. Wandinger
Reviewed by: two anonymous referees

## References

Amiridis, V., Wandinger, U., Marinou, E., Giannakaki, E., Tsekeri, A., Basart, S., Kazadzis, S., Gkikas, A., Taylor, M., Baldasano, J., and Ansmann, A.: Optimizing CALIPSO Saharan dust retrievals, Atmos. Chem. Phys., 13, 12089–12106, doi:10.5194/acp-13-12089-2013, 2013.

Ansmann, A., Petzold, A., Kandler, K., Tegen, I., Wendisch, M., Müller, D., Weinzierl, B., Müller, T., and Heintzenberg, J.: Saharan Mineral Dust Experiments SAMUM-1 and SAMUM-2: What have we learned?, Tellus B, 63, 403–429, 2011.

Benedetti, A., Morcrette, J.-J., Boucher, O., Dethof, A., Engelen, R. J., Fisher, M., Flentje, H., Huneeus, N., Jones, L., Kaiser, J. W., Kinne, S., Mangold, A., Razinger, M., Simmons, A. J., Suttie, M., and the GEMS-AER team: Aerosol analysis and forecast in the European Centre for Medium-Range Weather Forecasts Integrated Forecast System: 2. Data assimilation, J. Geophys. Res., 114, D13205, doi:10.1029/2008JD011115, 2009.

Bou Karam, D., Flamant, C., Knippertz, P., Reitebuch, O., Pelon, J., Chong, M., and Dabas, A.: Dust emissions over the Sahel associated with the West African monsoon intertropical discontinuity region: A representative case-study, Q. J. Roy. Meteor. Soc., 134, 621–634, 2008.

Boucher, O., Pham, M., and Venkataraman, C.: Simulation of the Atmospheric Sulfur Cycle in the LMD GCM: Model Description, Model Evaluation, and Global and European Budgets, Inst. Pierre-Simon Laplace, Paris, France, Note 23, available at: www.ipsl.jussieu.fr/poles/Modelisation/NotesSciences.htm (last access: 22 October 2014), 26 pp., 2002.

Busen, R.: Dropsondes and radiosondes for atmospheric measurements, in: Atmospheric Physics, edited by: Schumann, U., Springer, Berlin Heidelberg, 317–330, 2012.

Chen, T. and van Loon, H.: Interannual Variation of the Tropical Easterly Jet, Mon. Weather Rev., 115, 1739–1759, 1987.

Chouza, F., Reitebuch, O., Groß, S., Rahm, S., Freudenthaler, V., Toledano, C., and Weinzierl, B.: Retrieval of aerosol backscatter and extinction from airborne coherent Doppler wind lidar measurements, Atmos. Meas. Tech., 8, 2909–2926, doi:10.5194/amt-8-2909-2015, 2015.

Chouza, F., Reitebuch, O., Jähn, M., Rahm, S., and Weinzierl, B.: Vertical wind retrieved by airborne lidar and analysis of island induced gravity waves in combination with numerical models and in situ particle measurements, Atmos. Chem. Phys., 16, 4675–4692, doi:10.5194/acp-16-4675-2016, 2016.

Cifelli, R., Lang, T., Rutledge, S. A., Guy, N., Zipser, E. J., Zawislak, J., and Holzworth, R.: Characteristics of an African Easterly Wave Observed during NAMMA, J. Atmos. Sci., 67, 3–25, 2010.

Cuevas, E., Camino, C., Benedetti, A., Basart, S., Terradellas, E., Baldasano, J. M., Morcrette, J. J., Marticorena, B., Goloub, P., Mortier, A., Berjón, A., Hernández, Y., Gil-Ojeda, M., and Schulz, M.: The MACC-II 2007–2008 reanalysis: atmospheric dust evaluation and characterization over northern Africa and the Middle East, Atmos. Chem. Phys., 15, 3991–4024, doi:10.5194/acp-15-3991-2015, 2015.

Desboeufs, K., Journet, E., Rajot, J.-L., Chevaillier, S., Triquet, S., Formenti, P., and Zakou, A.: Chemistry of rain events in West Africa: evidence of dust and biogenic influence in convective systems, Atmos. Chem. Phys., 10, 9283–9293, doi:10.5194/acp-10-9283-2010, 2010.

Dunion, J. P. and Velden, C. S.: The impact of the Saharan air layer on Atlantic tropical cyclone activity, Bull. Am. Meteorol. Soc., 85, 353–365, 2004.

Eck, T. F., Holben, B. N., Reid, J. S., Dubovik, O., Smirnov, A., O'Neill, N. T., and Slutsker, I.: Wavelength dependence of the optical depth of biomass burning, urban, and desert dust aerosols, J. Geophys. Res., 104, 31333–31349, 1999.

ESA, ADM-Aeolus Science Report: http://esamultimedia.esa.int/docs/SP-1311_ADM-Aeolus_FINAL_low-res.pdf (last access: 28 April 2016), 2008.

Evan, A. T., Dunion, J., Foley, J. A., Heidinger, A. K., and Velden, C. S.: New evidence for a relationship between Atlantic tropical cyclone activity and African dust outbreaks, Geophys. Res. Lett., 33, L19813, doi:10.1029/2006GL026408, 2006.

Fink, A. H. and Reiner, A.: Spatio-temporal Variability of the Relation between African Easterly Waves and West African Squall Lines in 1998 and 1999, J. Geophys. Res., 108, 4332, doi:10.1029/2002JD002816, 2003.

Ginoux, P., Chin, M., Tegen, I., Prospero, J. M., Holben, B. N., Dubovik, O., and Lin, S.-J.: Sources and distributions of dust aerosols simulated with the GOCART model, J. Geophys. Res., 106, 20255–20273, 2001.

Gläser, G., Wernli, H., Kerkweg, A., and Teubler, F.: The transatlantic dust transport from North Africa to the Americas-Its characteristics and source regions, J. Geophys. Res. Atmos., 120, 11231–11252, 2015.

Groß, S., Tesche, M., Freudenthaler, V., Toledano, C., Wiegner, M., Ansmann, A., Althausen, D., and Seefeldner, M.: Characterization of Saharan dust, marine aerosols and mixtures of biomass burning aerosols and dust by means of multi-wavelength depolarization- and Raman-measurements during SAMUM-2, Tellus B, 63, 706–724, 2011.

Groß, S., Freudenthaler, V., Schepanski, K., Toledano, C., Schäfler, A., Ansmann, A., and Weinzierl, B.: Optical properties of long-range transported Saharan dust over Barbados as measured by dual-wavelength depolarization Raman lidar measurements, Atmos. Chem. Phys., 15, 11067–11080, doi:10.5194/acp-15-11067-2015, 2015.

Groß, S., Gasteiger, J., Freudenthaler, V., Müller, T., Sauer, D., Toledano, C., and Ansmann, A.: Saharan dust contribution to the Caribbean summertime boundary layer – A lidar study during SALTRACE, Atmos. Chem. Phys. Discuss., doi:10.5194/acp-2016-246, in review, 2016.

Guelle, W., Schulz, M., Balkanski, Y., and Dentener, F.: Influence of the source formulation on modeling the atmospheric global distribution of the sea salt aerosol, J. Geophys. Res., 106, 27509–27524, 2001.

Haarig, M., Althausen, D., Ansmann, A., Klepel, A., Baars, H., Engelmann, R., Groß, S., and Freudenthaler, V.: Measurement of the Linear Depolarization Ratio of Aged Dust at Three Wavelengths (355, 532 and 1064 nm) Simultaneously over Barbados, Proceeding of 27th International Laser Radar Conference, New York, doi:10.1051/epjconf/201611918009, 2015.

Heintzenberg, J.: The SAMUM-1 experiment over southern morocco: overview and introduction, Tellus B, 61, 2–11, 2009.

Henderson, S. W., Suni, P. J. M., Hale, C. P., Hannon, S. M., Magee, J. R., Bruns, D. L., and Yuen, E. H.: Coherent laser radar at 2 µm using solid-state lasers, IEEE T. Geosci. Remote, 31, 4–15, 1993.

Hollingsworth, A., Engelen, R. J., Textor, C., Benedetti, A., Boucher, O., Chevallier, F., Dethof, A., Elbern, H., Eskes, H., Flemming, J., Granier, C., Kaiser, J. W., Morcrette, J.-J., Rayner, R., Peuch, V.-H., Rouil, L., Schultz, M. G., Simmons, A. J., and The GEMS Consortium: Toward a monitoring and forecasting system for atmospheric composition: the GEMS project, B. Am. Meteorol. Soc., 89, 1147–1164, 2008.

Huneeus, N., Schulz, M., Balkanski, Y., Griesfeller, J., Prospero, J., Kinne, S., Bauer, S., Boucher, O., Chin, M., Dentener, F., Diehl, T., Easter, R., Fillmore, D., Ghan, S., Ginoux, P., Grini, A., Horowitz, L., Koch, D., Krol, M. C., Landing, W., Liu, X., Mahowald, N., Miller, R., Morcrette, J.-J., Myhre, G., Penner, J., Perlwitz, J., Stier, P., Takemura, T., and Zender, C. S.: Global dust model intercomparison in AeroCom phase I, Atmos. Chem. Phys., 11, 7781–7816, doi:10.5194/acp-11-7781-2011, 2011.

Illingworth, A. J., Barker, H. W., Beljaars, A., Ceccaldi, M., Chepfer, H., Cole, J., Delanoë, J., Domenech, C., Donovan, D. P., Fukuda, S., Hirakata, M., Hogan, R. J., Huenerbein, A., Kollias, P., Kubota, T., Nakajima, T., Nakajima, T. Y., Nishizawa, T., Ohno, Y., Okamoto, H., Oki, R., Sato, K., Satoh, M., Shephard, M., Wandinger, U., Wehr, 395 T., and van Zadelhoff, G.-J.: The EarthCARE satellite: The next step forward in global measurements of clouds, aerosols, precipitation and radiation, B. Am. Meteorol. Soc., 96, 1311–1332, 2014.

Inness, A., Baier, F., Benedetti, A., Bouarar, I., Chabrillat, S., Clark, H., Clerbaux, C., Coheur, P., Engelen, R. J., Errera, Q., Flemming, J., George, M., Granier, C., Hadji-Lazaro, J., Huijnen, V., Hurtmans, D., Jones, L., Kaiser, J. W., Kapsomenakis, J., Lefever, K., Leitão, J., Razinger, M., Richter, A., Schultz, M. G., Simmons, A. J., Suttie, M., Stein, O., Thépaut, J.-N., Thouret, V., Vrekoussis, M., Zerefos, C., and the MACC team: The MACC reanalysis: an 8 yr data set of atmospheric composition, Atmos. Chem. Phys., 13, 4073–4109, doi:10.5194/acp-13-4073-2013, 2013.

Kanitz, T., Engelmann, R., Heinold, B., Baars, H., Skupin, A., and Ansmann, A.: Tracking the Saharan Air Layer with shipborne lidar across the tropical Atlantic, Geophys. Res. Lett., 41, 1044–1050, 2014.

Karyampudi, V., Palm, S., Reagen, J., Fang, H., Grant, W., Hoff, R., Moulin, C., Pierce, H., Torres, O., Browell, E., and Melfi, S.: Validation of the Saharan dust plume conceptual model using Lidar, Meteosat, and ECMWF Data, B. Am. Meteorol. Soc., 80, 1045–1075, 1999.

Kim, D., Chin, M., Yu, H., Diehl, T., Tan, Q., Kahn, R. a., Tsigaridis, K., Bauer, S. E., Takemura, T., Pozzoli, L., Bellouin, N., Schulz, M., Peyridieu, S., Chédin, A., and Koffi, B.: Sources, sinks, and transatlantic transport of North African dust aerosol: A multimodel analysis and comparison with remote sensing data, J. Geophys. Res. Atmos., 119, 6259–6277, 2014.

Kim, M.-H., Kim, S.-W., Yoon, S.-C., and Omar, A. H.: Comparison of aerosol optical depth between CALIOP and MODIS-Aqua for CALIOP aerosol subtypes over the ocean, J. Geophys. Res. Atmos., 118, 13241–13252, 2013.

Kinne, S., Lohmann, U., Feichter, J., Schulz, M., Timmreck, C., Ghan, S., Easter, R., Chin, M., Ginoux, P., Takemura, T., Tegen, I., Koch, D., Herzog, M., Penner, J., Pitari, G., Holben, B., Eck, T., Smirnov, A., Dubovik, O., Slutsker, I., Tanre, D., Torres, O., Mishchenko, M., Geogdzhayev, I., Chu, D. A., and Kaufman, Y.: Monthly averages of aerosol properties: A global compari-

son among models, satellite data, and AERONET ground data, J. Geophys. Res. A., 108, 4634, doi:10.1029/2001JD001253, 2003.

Köpp, F., Rahm, S., and Smalikho, I.: Characterization of Aircraft Wake Vortices by 2-µm Pulsed Doppler Lidar, J. Atmos. Oceanic Tech., 21, 194–206, 2004.

Kristensen, T. B., Müller, T., Kandler, K., Benker, N., Hartmann, M., Prospero, J. M., Wiedensohler, A., and Stratmann, F.: Properties of cloud condensation nuclei (CCN) in the trade wind marine boundary layer of the western North Atlantic, Atmos. Chem. Phys., 16, 2675–2688, doi:10.5194/acp-16-2675-2016, 2016.

Lau, K. M. and Kim, K. M.: Cooling of the atlantic by saharan dust, Geophys. Res. Lett., 34, L23811, doi:10.1029/2007gl031538, 2007.

Leroux, S. and Hall, N. M. J.: On the Relationship between African Easterly Waves and the African Easterly Jet, J. Atmos. Sci., 66, 8, 2303–2316, 2009.

Mangold, A., De Backer, H., De Paepe, B., Dewitte, S., Chiapello, I., Derimian, Y., Kacenelenbogen, M., Leon, J.-F., Huneeus, N., Schulz, M., Ceburnis, D., O'Dowd, C. D., Flentje, H., Kinne, S., Benedetti, A., Morcrette, J. J., and Boucher, O.: Aerosol analysis and forecast in the ECMWF Integrated Forecast System, Part IV: Evaluation by means of case studies, J. Geophys. Res, 116, D03302, doi:10.1029/2010JD014864, 2011.

Messager, C., Parker, D. J., Reitebuch, O., Agusti-Panareda, A., Taylor, C. M., and Cuesta, J.: Structure and dynamics of the Saharan atmospheric boundary layer during the West African monsoon onset: observations and analyses from the research flights of 14 and 17 July 2006, Q. J. Roy. Meteor. Soc., 136, 107–124, 2010.

Morcrette, J.-J., Beljaars, A., Benedetti, A., Jones, L., and Boucher, O.: Sea salt and dust aerosols in the ECMWF IFS model, Geophys. Res. Lett., 35, L24813, doi:10.1029/2008GL036041, 2008.

Morcrette, J.-J., Boucher, O., Jones, L., Salmond, D., Bechtold, P., Beljaars, A., Benedetti, A., Bonet, A., Kaiser, J. W., Razinger, M., Schulz, M., Serrar, S., Simmons, A. J., Sofiev, M., Suttie, M., Tompkins, A. M., and Untch, A.: Aerosol analysis and forecast in the European centre for medium-range weather forecasts integrated forecast system: forward modeling, J. Geophys. Res., 114, D06206, doi:10.1029/2008JD011235, 2009.

Morcrette. J.-J., Benedetti, A., Jones, L., Kaiser, J. W., Razinger, M., and Suttie, M.: Prognostic aerosols in the ECMWF IFS: MACC vs. GEMS aerosols ECMWF Technical Memo, December 2011, available at: http://www.ecmwf.int/sites/default/files/elibrary/2011/11277-prognostic-aerosols-ecmwf-ifs-macc-vs-gems-aerosols.pdf, 2011.

Prospero, J. M.: Long-term measurements of the transport of African mineral dust to the southeastern United States: Implications for regional air quality, J. Geophys. Res.-Atmos., 104, 15917–15927, 1999.

Prospero, J. M. and Carlson, T. N.: Vertical and areal distribution of Saharan dust over the western Equatorial North Atlantic Ocean, J. Geophys. Res., 77, 5255–5265, 1972.

Reddy, M. S., Boucher, O., Bellouin, N., Schulz, M., Balkanski, Y., Dufresne, J.-L., and Pham, M.: Estimates of global multi-component aerosol optical depth and direct radiative perturbation in the Laboratoire de Météorologie Dynamique general circulation model, J. Geophys. Res., 110, D10S16, doi:10.1029/2004JD004757, 2005.

Reed, R. J., Norquist, D. C., and Recker, E. E.: The Structure and Properties of African Wave Disturbances as Observed During Phase III of GATE, Mon. Weather Rev., 105, 317–333, 1977.

Reitebuch, O.: Wind Lidar for Atmospheric Research, in: Atmospheric Physics, edited by: Schumann, U., Springer, Berlin Heidelberg, 487–507, 2012.

Rémy, S., Benedetti, A., Bozzo, A.. Haiden, T.. Jones, L., Razinger, M., Flemming, J., Engelen, R. J., Peuch, V. N., and Thépaut, J.-N.: Feedbacks of dust and boundary layer meteorology during a dust storm in the eastern Mediterranean, Atmos. Chem. Phys., 15, 12909–12933, doi:10.5194/acp-15-12909-2015, 2015.

Rogers, R. R., Vaughan, M. A., Hostetler, C. A., Burton, S. P., Ferrare, R. A., Young, S. A., Hair, J. W., Obland, M. D., Harper, D. B., Cook, A. L., and Winker, D. M.: Looking through the haze: evaluating the CALIPSO level 2 aerosol optical depth using airborne high spectral resolution lidar data, Atmos. Meas. Tech., 7, 4317–4340, doi:10.5194/amt-7-4317-2014, 2014.

Schepanski, K., Tegen, I., and Macke, A.: Saharan dust transport and deposition towards the tropical northern Atlantic, Atmos. Chem. Phys., 9, 1173–1189, doi:10.5194/acp-9-1173-2009, 2009.

Schulz, M., de Leeuw, G., and Balkanski, Y.: Sea-salt aerosol source functions and emissions, in: Emission of Atmospheric Trace Compounds, edited by: Granier, C., Artaxo, P., and Reeves, C. E., Kluwer Acad., Norwell, Mass., 333–354, 2004.

Schulz, M., Prospero, J., Baker, A., Dentener, F., Ickes, L., Liss, P., Mahowald, N., Nickovic, S., Garcia-Pando, C., Rodriguez, S., Sarin, M., Tegen, I., and Duce, R.: Atmospheric Transport and Deposition of Mineral Dust to the Ocean: Implications for Research Needs, Environ. Sci. Technol., 46, 10390–10404, 2012.

Smalikho, I.: Techniques of wind vector estimation from data measured with a scanning coherent Doppler Lidar, J. Atmos. Oceanic Tech., 20, 276–291, 2003.

Tesche, M., Groß, S., Ansmann, A., Müller, D., Althausen, D., Freudenthaler, V., and Esselborn, M.: Profiling of Saharan dust and biomass-burning smoke with multiwavelength polarization Raman lidar at Cape Verde, Tellus B, 63, 649–676, 2011.

Tesche, M., Wandinger, U., Ansmann, A., Althausen, D., Müller, D., and Omar, A. H.: Ground–based validation of CALIPSO observations of dust and smoke in the Cape Verde region, J. Geophys. Res., 118, 2889–2902, 2013.

Tompkins, A. M.: A Revised Cloud Scheme to Reduce the Sensitivity to Vertical Resolution, Tech. Memo. 0599, Res. Dep., Eur. Cent. for Medium-Range Weather Forecasts, Reading, UK, 25 pp., 2005a.

Tompkins, A. M., Cardinali, C., Morcrette, J. J., and Rodwell, M.: Influence of aerosol climatology on forecasts of the African Easterly Jet, Geophys. Res. Lett., 32, L10801, doi:10.1029/2004gl022189, 2005b.

Vaisala Dropsonde RD93 data-sheet: http://www.inemet.com/pdf/sondeo/dropsonde.pdf (last access: 10 April 2016), 2009.

Wandinger, U., Tesche, M., Seifert, P., Ansmann, A., Müller, D., and Althausen, D.: Size matters: Influence of multiple–scattering on CALIPSO light–extinction profiling in desert dust, Geophys. Res. Lett., 37, L10801, doi:10.1029/2010GL042815, 2010.

Weinzierl, B., Petzold, A., Esselborn, M.,Wirth, M., Rasp, K., Kandler, K., Schutz, L., Kopke, P., and Fiebig, M.: Airborne measurements of dust layer properties, particle size distribution and

mixing state of Saharan dust during SAMUM 2006, Tellus B, 61, 96–117, 2009.

Weinzierl, B., Sauer, D., Esselborn, M., Petzold, A., Veira, A., Rose, M., Mund, S., Wirth, M., Ansmann, A., Tesche, M., Groß, S., and Freudenthaler, V.: Microphysical and optical properties of dust and tropical biomass burning aerosol layers in the Cape Verde region-an overview of the airborne in situ and lidar measurements during SAMUM-2, Tellus B, 63, 589–618, 2011.

Weinzierl, B., Sauer, D., Minikin, A., Reitebuch, O., Dahlkotter, F., Mayer, B., Emde, C., Tegen, I., Gasteiger, J., Petzold, A., Veira, A., Kueppers, U., and Schumann, U.: On the visibility of airborne volcanic ash and mineral dust from the pilot's perspective in flight, Phys. Chem. Earth, 45/46, 87–102, 2012.

Weinzierl, B., Ansmann, A., Prospero, J. M., Althausen, D., Benker, N., Chouza, F., Dollner, M., Farrell, D., Fomba, K. W., Freudenthaler, V., Gasteiger, J., Groß, S., Haarig, M., Heinold, B., Kandler, K., Kristensen, T. B., Mayol-Bracero, O. L., Müller, T., Reitebuch, O., Sauer, D., Schäfler, A., Schepanski, K., Tegen, I., Toledano, C., and Walser, A.: The Saharan Aerosol Long-range TRansport and Aerosol-Cloud-Interaction Experiment (SALTRACE): overview and selected highlights, B. Am. Meteorol. Soc., in review, 2016.

Weissmann, M. and Cardinali, C.: Impact of airborne Doppler lidar observations on ECMWF forecasts, Q. J. R. Meteorol. Soc., 133, 107–116, 2007.

Weissmann, M., Busen, R., Dörnbrack, A., Rahm, S., and Reitebuch, O.: Targeted Observations with an Airborne Wind Lidar, J. Atmos. Oceanic Technol., 22, 1706–1719, 2005.

Winker, D. M., Vaughan, M. A., Omar, A. Hu, Y., Powell, K. A., Liu, Z., Hunt, W. H., and Young, S. A.: Overview of the CALIPSO Mission and CALIOP Data Processing Algorithms, J. Atmos. Oceanic Tech., 26, 2310–2323, 2009.

Yu, H., Chin, M., Yuan, T., Bian, H., Remer, L. A., Prospero, J. M., Omar, A., Winker, D., Yang, Y., Zhang, Y., Zhang, Z., and Zhao, C.: The fertilizing role of African dust in the Amazon rainforest: A first multiyear assessment based on data from Cloud-Aerosol Lidar and Infrared Pathfinder Satellite Observations, Geophys. Res. Lett., 42, 1984–1991, 2015.

Zipser, E. J., Twohy, C. H., Tsay, S. C., Thornhill, K. L., Tanelli, S., Ross, R., Krishnamurti, T. N., Ji, Q., Jenkins, G., Ismail, S., Hsu, N. C., Hood, R., Heymsfield, G. M., Heymsfield, A., Halverson, J., Goodman, H. M., Ferrare, R., Dunion, J. P., Douglas, M., Cifelli, R., Chen, G., Browell, E. V., and Anderson, B.: The saharan air layer and the fate of african easterly waves, B. Am. Meteorol. Soc., 90, 1137–1156, 2009.

Atmos. Chem. Phys., 16, 651–674, 2016
www.atmos-chem-phys.net/16/651/2016/
doi:10.5194/acp-16-651-2016


Atmospheric Chemistry and Physics Open Access EGU

# Investigations of boundary layer structure, cloud characteristics and vertical mixing of aerosols at Barbados with large eddy simulations

**M. Jähn[1], D. Muñoz-Esparza[2], F. Chouza[3], O. Reitebuch[3], O. Knoth[1], M. Haarig[1], and A. Ansmann[1]**

[1]Leibniz Institute for Tropospheric Research, Permoserstraße 15, 04318 Leipzig, Germany
[2]Earth and Environmental Sciences Division (EES-16), Los Alamos National Laboratory, P.O. Box 1663, Los Alamos, New Mexico 87545, USA
[3]Deutsches Zentrum für Luft- und Raumfahrt (DLR), Institute of Atmospheric Physics, Münchner Straße 20, 82234 Oberpfaffenhofen-Wessling, Germany

*Correspondence to:* M. Jähn (jaehn@tropos.de)

Received: 31 July 2015 – Published in Atmos. Chem. Phys. Discuss.: 24 August 2015
Revised: 10 December 2015 – Accepted: 14 December 2015 – Published: 21 January 2016

**Abstract.** Large eddy simulations (LESs) are performed for the area of the Caribbean island Barbados to investigate island effects on boundary layer modification, cloud generation and vertical mixing of aerosols. Due to the presence of a topographically structured island surface in the domain center, the model setup has to be designed with open lateral boundaries. In order to generate inflow turbulence consistent with the upstream marine boundary layer forcing, we use the cell perturbation method based on finite amplitude potential temperature perturbations. In this work, this method is for the first time tested and validated for moist boundary layer simulations with open lateral boundary conditions. Observational data obtained from the SALTRACE field campaign is used for both model initialization and a comparison with Doppler wind and Raman lidar data. Several numerical sensitivity tests are carried out to demonstrate the problems related to "gray zone modeling" when using coarser spatial grid spacings beyond the inertial subrange of three-dimensional turbulence or when the turbulent marine boundary layer flow is replaced by laminar winds. Especially cloud properties in the downwind area west of Barbados are markedly affected in these kinds of simulations. Results of an additional simulation with a strong trade-wind inversion reveal its effect on cloud layer depth and location. Saharan dust layers that reach Barbados via long-range transport over the North Atlantic are included as passive tracers in the model. Effects of layer thinning, subsidence and turbulent downward transport near the layer bottom at $z \approx 1800$ m become apparent. The exact position of these layers and strength of downward mixing is found to be mainly controlled atmospheric stability (especially inversion strength) and wind shear. Comparisons of LES model output with wind lidar data show similarities in the downwind vertical wind structure. Additionally, the model results accurately reproduce the development of the daytime convective boundary layer measured by the Raman lidar.

## 1 Introduction

A series of ground-based and airborne remote sensing measurements took place at and around Barbados during the SALTRACE (Saharan Aerosol Long-range Transport and Aerosol-Cloud-Interaction Experiment) 2013 summer campaign. Since Barbados is the easternmost island in the Caribbean and steady easterly trade winds are present, it is not affected by other surrounding islands. For that reason, Barbados is suitable for island effect studies both from the measurement and the modeling point of view. First of all, mineral dust emitted from the Saharan region is transported for more than 4000 km over the Atlantic Ocean with almost no anthropogenic influence. Dust layers arriving at Barbados can be detected with respect to layer height and thickness as well as aerosol composition. Secondly, cloud studies are possible due to persistent trade-wind circulation at the eastern Caribbean. For example, extensive investigations on shallow cumulus cloud properties and their response to different ambient cloud condensation nuclei (CCN) num-

ber concentrations took place during the CARRIBA (Cloud, Aerosol, Radiation and tuRbulence in the trade wInd regime over BArbados) project in 2010/2011 (Siebert et al., 2013). Within CARRIBA, airborne in situ measurements were conducted east of Barbados. The field site of the Max Planck Institute for Meteorology (MPI-M), Hamburg, Germany, with ground-based instruments is located at the east coast as well. The choice of these locations ensures that the island itself has very little to no influence on the measurements and thus marine boundary layer properties can be accurately investigated. During SALTRACE, the TROPOS (Leibniz Institute for Tropospheric Research, Leipzig) and LMU (Ludwig-Maximilians-Universität Munich) field sites were located at the area of the local Caribbean Institute for Meteorology and Hydrology (CIMH) near the west coast of Barbados (see Fig. 1), whereas the DLR (Deutsches Zentrum für Luft- und Raumfahrt) research aircraft Falcon was stationed at the international airport of Barbados. Regarding the measurement field site, incoming air masses at these sites are already influenced by the island due to surface roughness change, different energy fluxes and topographical features. Whereas the first two properties primarily influence the atmospheric boundary layer (ABL), gravity waves caused by the latter also propagate within the free troposphere.

There are several works regarding the understanding of airflow and thermodynamic quantities around Barbados. A first detailed observational study using pilot balloon measurements was done by DeSouza (1972) and further interpreted by Garstang et al. (1975). DeSouza's calculated vertical wind velocity fields showed a daytime divergence and nighttime convergence over the island. Mahrer and Pielke (1976) did a series of two- and three-dimensional numerical studies and found that DeSouza's calculations only hold for a flat island, because he neglected significant effects of terrain slope in his divergence calculations. Heat island effects on vertical mixing of aerosols at Cape Verde islands were studied by Engelmann et al. (2011) using aircraft lidar measurements and idealized large eddy simulations (LESs) with flat island surfaces. They found indications that the differential heating and the orographic impact control downward mixing of African aerosols, which results in a complex vertical layering over the Cape Verde region. Taking the topographical structures into account, Mahrer and Pielke (1976) pointed out some main characteristics, e.g., diurnal changes in the vertical wind velocity fields downwind (i.e., west coast of Barbados) with sinking motions over the center and western part of the island and an upwind cell off the west coast. Considering numerical sensitivity studies by Savijärvi and Matthews (2004, SM04 hereafter), the general conclusion was that these forced rising and sinking motions and their consecutive effects can only be explained if island orography is included in the numerical models. In their 2-D study, SM04 added a 200 m high central mountain to a 20 km wide island and showed that sea-breeze circulations are enhanced by upslope winds during the day. These topographically forced components will dominate if the large-scale mean wind is in the order of magnitude of at least $10\,\mathrm{m\,s^{-1}}$, which is the case for Barbados. Smith et al. (1997) assigned different island structures to different mountain wake types. Since the highest elevation of Barbados (Mt. Hillaby, with a height of 340 m a.s.l.) does not exceed the critical height for wave breaking, no wind wake can develop. However, a long trail of cumulus clouds extending westwards can evolve during the afternoon hours (cumulus cloud street). Kirshbaum and Fairman (2015) found that surface fluxes control the downwind circulation strength and the trade inversion controls precipitation and thus the disruption of cloud trails. Other influence factors like terrain height, wind speed and their interactions have multiple impacts on flow regimes, turbulence, cloud trail lengths etc. Another study on island effects with similar topographical heights compared to Barbados was done by Minda et al. (2010). They investigated the evolution of the convective boundary layer (CBL) above Okinawa Island, Japan. It was found that for a flat island simulation, the warmed land already induces a distinct roll cloud that is in agreement with the observations. However, the inclusion of island terrain leads to reinforced moisture uplifts, which in turn induce strong convection that can penetrate into the free atmosphere. Idealized numerical studies were conducted by Kirshbaum and Grant (2012) to investigate the impact of mesoscale ascent (with an island height of 500 m) on cumulus convection. There, a particularly important process with regard to the mean horizontal cloud size has been found. The broader the clouds are, the lower is the fractional entrainment rate in these clouds, which in the end leads to an increase in precipitation rates downstream. A key result from another combined theoretical and numerical study by Kirshbaum and Wang (2014) was that nonlinear interactions between mechanical and thermal flow over taller mountains were significant and thus lead to a strengthening of the lee-side convergence band.

There are also many studies where the focus lies on the orographic influence of tall islands (e.g., Hawaii Island or Dominica with mountain heights above 1 km) on the leeward flow and precipitation patterns. Esteban and Chen (2008) state that for a strong trade-wind flow, the daily rainfall totals at the windward side of the island of Hawaii show a nocturnal maximum due to the convergence of katabatic flow, whereas for weak trades ($\leq 5\,\mathrm{m\,s^{-1}}$) the rainfall amounts have their maximum in the late afternoon due to anabatic winds. In a work by Smith et al. (2009), orographic precipitation for the Caribbean island Dominica was studied. There, the conditionally unstable trade-wind layer together with terrain-forced lifting leads to convective triggering over the windward slope. The reduced instability on the lee side destroys convective clouds and creates a rainless area. A complementary study with airborne observations and cloud-resolving modeling for the same island was performed by Minder et al. (2013). The comparison showed that the dynamical structures are very well reproduced but that it was difficult to

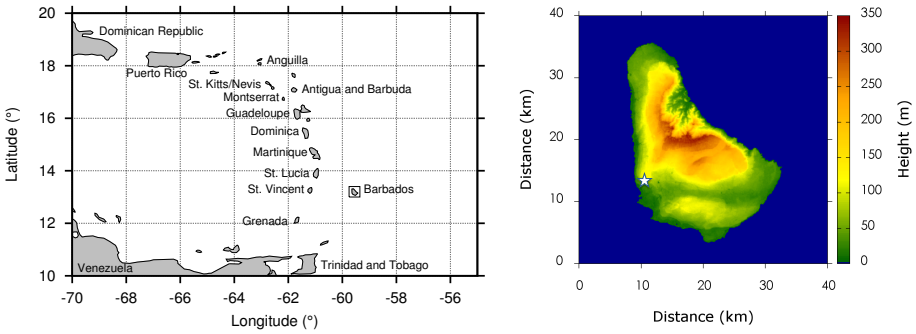


**Figure 1.** Left panel: part of the Caribbean including the Lesser Antilles. Right panel: topographical map of Barbados. The topographical data are obtained from the Consortium for Spatial Information (CGIAR-CSI) Shuttle Radar Topography Mission (SRTM) data set at 200 m resolution. The white star denotes the location of the CIMH, which is close to the measurement field site.

reproduce the observed rainfall using the model. Overall, mesoscale flow controls convection and rainfall over Dominica. At lower wind speeds, the circulations seem to be more thermally driven by solar heating.

The main objective of this work is to study local island effects on the modification of the boundary layer structure, microphysical properties and downwind vertical mixing of aerosols for selected days during the first SALTRACE field campaign. Regarding aerosols, especially Saharan dust, it is known from several studies that notable amounts of mineral dust reach Barbados via long-range transport over the North Atlantic, e.g., from first observations at the end of the 1960s (Prospero et al., 1970; Prospero and Carlson, 1970) or from back-trajectory calculations by Ellis and Merrill (1995).

Within this work, the following questions are addressed:

- How does the model setup have to be chosen to get an as realistic as possible representation of an island–ocean system in the trade-wind regime through the example of Barbados?
- How do turbulent inflow characteristics and grid spacing affect the simulation results?
- Can the daytime convective island boundary layer explain downward mixing of low-altitude Saharan dust layers?
- Are the simulation results comparable with lidar measurements over and in the lee of the island?

This paper is structured as follows. Section 2 deals with the general model setup. There, the numerical method, model physics, computational domain, boundary conditions, initial data and forcings are described. To generate a turbulent marine boundary layer, a novel method based on potential temperature perturbations is adopted, verified and applied to our numerical model and particular setup. Results for two case studies in June 2013 and two sensitivity tests are presented and discussed in Sect. 3. In Sect. 4, the simulation results are compared with stationary and airborne lidar data. Section 5 provides a summary and concluding remarks.

## 2 Model setup

All LESs are performed with the latest version of the non-hydrostatic, fully compressible All Scale Atmospheric Model (ASAM). An extensive model description is presented in Jähn et al. (2015), both covering numerical discretization methods and physical parameterizations. A special feature of ASAM is the usage of so-called cut cells for the orography. There, a grid box is cut by the intersection of the orographical structure. This method can handle steep terrain gradients and prevents discretization errors compared to traditional methods like terrain-following coordinates, also conserving the original shape of the topography to a high degree. The dynamical core solves the flux-form tendency equations for mass, momentum, energy (in terms of density potential temperature) and other scalars. The most important physical parameterizations include a Smagorinsky subgrid-scale model and a two-moment cloud microphysics scheme. Further details on the model are described in Appendix A.

In the next subsections, the computational domain, boundary conditions (BC), data initialization and forcings for the cases of study are described, followed by a novel method to generate inflow turbulence.

### 2.1 Domain and boundary conditions

To simulate atmospheric flow for the island–ocean system, the size of the model domain has to have appropriate values dependent on the island size. The main criterion in this case is that a marine boundary layer has to develop at least several kilometers before it interferes with the island area. Also, the downwind area should approximately be twice of the island width so that resulting structures induced by the island can be properly represented. Since Barbados is a 24 km wide (west–east) and 34 km long (south–north) island, a model domain with a spatial extent of 102.4 km $\times$ 102.4 km is chosen. The island is located at the domain center. The model top is set to 5 km altitude. Because of the required domain size and for computational reasons, the horizontal grid spacing is set

to $\Delta x = \Delta y = 200$ m. Such a resolution can be considered a "coarse" LES; however, it is sufficient to resolve some portion of inertial range scales, as will be shown later on through spectral analysis.

Due to the presence of the island area, non-cyclic lateral boundary conditions have to be used. Within the finite volumes/differences discretization strategy adopted herein, a "zero-gradient" boundary condition is applied to all scalars and velocity components at each lateral boundary (north, east, south, west). This means that the boundary-perpendicular flux for these quantities is set to zero, which leads to a simple radiation condition near the outlets with minimal wave reflection. A pressure correction for sound waves is applied to each actual normal velocity component and not to the initial wind profile, which also suppresses artificial wave reflection near the inflow boundary. This setup ensures stability for the whole simulation time and works appropriately with the turbulence generation method, as shown at the end of this section.

For the top boundary, a free-slip condition is applied, i.e., the gradient of the tangential velocity component is zero. In order to prevent gravity wave reflection, an additional relaxation term is applied on the right-hand side of the momentum equations:

$$\Phi^{n+1} = \ldots - \Delta t \cdot \rho K(d)(\Phi^n(d) - \Phi^0)\,, \tag{1}$$

with a damping function depending on the distance to the top boundary $d$:

$$K(d) = \begin{cases} d_f \sin^2\left(\frac{\pi}{2}\frac{d_w - d}{d_w}\right) & d < d_w\,, \\ 0 & d \geq d_w\,. \end{cases} \tag{2}$$

This damping layer is applied above $d_w = 4$ km model height (20 vertical layers) with a damping parameter $d_f = 1 \times 10^{-3}$.

Surface boundary conditions are represented by a momentum flux parameterization based on the Monin–Obukhov similarity theory (Monin and Obukhov, 1954):

$$\tau_{zx} = -\rho C_\mathrm{m} |\boldsymbol{v}_h| u\,, \tag{3}$$
$$\tau_{zy} = -\rho C_\mathrm{m} |\boldsymbol{v}_h| v\,. \tag{4}$$

$C_\mathrm{m}$ is the drag coefficient for momentum, which is defined as follows:

$$C_\mathrm{m} = \frac{k^2}{\Psi_\mathrm{M}^2}\,, \tag{5}$$

with

$$\Psi_\mathrm{M} = \ln\left(\frac{z + z_0}{z_0}\right) - \phi_\mathrm{m}\left(\frac{z}{L}\right)\,, \tag{6}$$

and $\phi_\mathrm{m}$ representing the integrated similarity function. $L$ stands for the Obukhov length and $k$ is the von Kármán constant.

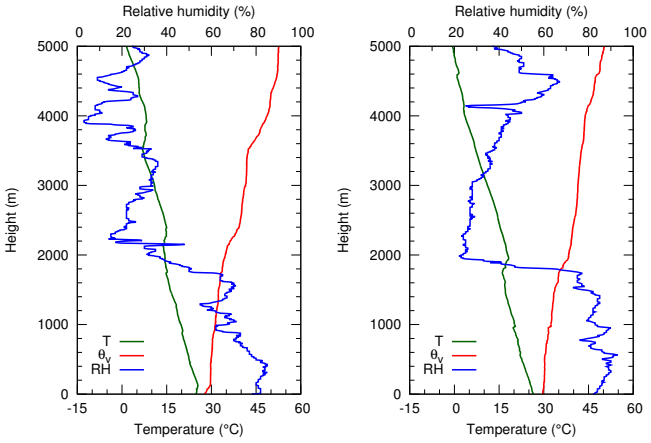


**Figure 2.** Nighttime radiosonde soundings on 22 June 2013 (left) and 27 June 2013 (right).

The topographic data are obtained from the Consortium for Spatial Information (CGIAR-CSI) Shuttle Radar Topography Mission (SRTM) data set (http://srtm.csi.cgiar.org) at 200 m resolution. A simple smoothing algorithm is applied to guarantee a proper grid pre-processing. In the smoothed data set, the maximum elevation is lowered by about 15 m compared to the raw topography data, which is an acceptable level.

Table 1 summarizes the model configuration for the Barbados LESs performed in Sect. 3.

### 2.2 Initial data

The two cases examined (22 and 27 June 2013) mainly differ in their atmospheric state and geostrophic forcing. Measured nighttime radiosonde profiles of temperature and humidity are directly used for model initialization (Fig. 2), which reduces the complexity of the simulations due to the absence of horizontal inhomogeneities and a time-varying background state. There are two reasons behind the choice of using single profiles instead of averaging multiple profiles. Firstly, a single initial profile is better for comparing the LES results with lidar data (cf. Sect. 4), which are obtained for a few selected cases during SALTRACE. Secondly, trade-wind inversions are only poorly represented when the soundings are averaged over many cases. This becomes apparent when considering the sharply defined inversion at the 27 June case, which is shown later on. Air density and pressure profiles are obtained by vertical integration with respect to hydrostatic equilibrium. Some simplifications are assumed for the geostrophic forcing. The wind direction is purely east (i.e., $d = 90°$ and $v_g = 0$), which is also for simplicity and to make it easier to define upwind and downwind regimes later on. The vertical wind profiles are expressed as piecewise linear functions for both cases. For the 22 June case, the initial wind at first linearly decreases above $z = 1600$ m altitude and then increases

**Table 1.** LES model configuration for the simulations performed in Sect. 3.

| Model parameter | Value/description |
|---|---|
| Domain | $102.4 \times 102.4 \times 5\,\mathrm{km}^3$ |
| Grid cells | $512 \times 512 \times 100$ |
| Time step | 4 s |
| Horizontal grid spacing | 200 m |
| Vertical grid spacing | 50 m |
| Start time (LT) | 02:00 |
| End time (LT) | 22:00 |
| Topography data | SRTM, 200 m resolution |
| Turbulence scheme | Standard Smagorinsky SGS model |
| Cloud microphysics | Two-moment scheme (no ice phase) by Seifert and Beheng (2006) |
| Wind direction | East (90°) |
| Lateral BC | Open radiative |
| Surface BC | Monin–Obukhov |
| Top BC | Free slip |
| Damping layer | For $z \geq 4.0$ km |

again above $z = 3000$ m:

$$u_{i,1}(z) = \tag{7}$$
$$\begin{cases} -10.0\,\mathrm{m\,s^{-1}}\,\frac{\log(z/z_0)}{\log(700\,\mathrm{m}/z_0)}\,, & z \leq 0.7\,\mathrm{km} \\ -10.0\,\mathrm{m\,s^{-1}}\,, & z \leq 1.6\,\mathrm{km} \\ -10.0\,\mathrm{m\,s^{-1}} + 4.29 \times 10^{-3}\,\mathrm{s^{-1}} & \\ \quad \cdot(z - 3000\,\mathrm{m})\,, & 1.6\,\mathrm{km} < z \leq 3.0\,\mathrm{km} \\ -4.0\,\mathrm{m\,s^{-1}} - 2.0 \times 10^{-3}\,\mathrm{s^{-1}} & \\ \quad \cdot(z - 5000\,\mathrm{m})\,, & 3.0\,\mathrm{km} < z \leq 5.0\,\mathrm{km}, \end{cases}$$

with a roughness length $z_0 = 0.01$ m. A change in wind direction to southwest is observed within the layer where the wind speed decreases. However, this is not captured by the LES due to the simplifications and assumptions mentioned above. Therefore, the effect of wind directional shear might be underestimated in the model for this case. The change in wind direction (±15°) is rather small at other altitudes, so the LES input profile can be considered a good approximation. For the 27 June case, the initial wind linearly decreases above $z = 3000$ m altitude:

$$u_{i,2}(z) = \tag{8}$$
$$\begin{cases} -11.5\,\mathrm{m\,s^{-1}}\,\frac{\log(z/z_0)}{\log(700\,\mathrm{m}/z_0)}\,, & z \leq 0.7\,\mathrm{km} \\ -11.5\,\mathrm{m\,s^{-1}}\,, & z \leq 3\,\mathrm{km} \\ -11.5\,\mathrm{m\,s^{-1}} + 5.25 \times 10^{-3}\,\mathrm{s^{-1}} & \\ \quad \cdot(z - 3000\,\mathrm{m})\,, & z > 3\,\mathrm{km}. \end{cases}$$

In this profile there is no distinct change in wind direction. Figure 3 visualizes the measured (green lines) and parameterized (red lines) velocity profiles for both cases. The LES background wind profiles are parameterized to closely match the soundings. Within the boundary layer, the LES profile should be near the nighttime measurements (dark-green line) because this is mainly a representation of the marine boundary layer. For the free troposphere, the LES profile should roughly be a mean of all three soundings, since no large-scale advection term is applied on the wind components during the simulation time.

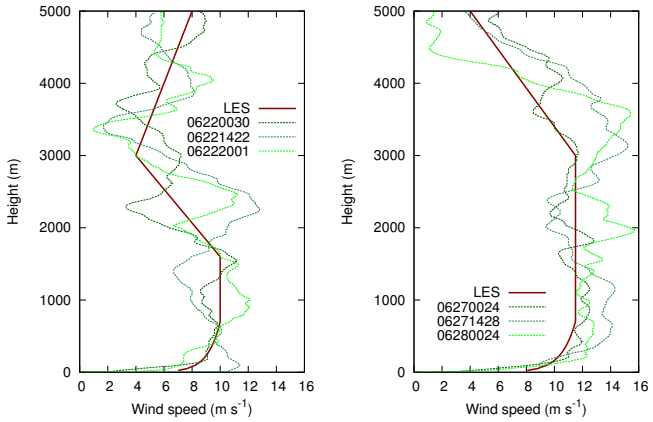


**Figure 3.** Parameterized (LES) and measured wind profiles from radiosondes on 22 June 2013 (left) and 27 June 2013 (right). Names indicate date and time in UTC.

Table 2 shows a comparison of the two simulated cases with respect to mean flow properties, trade inversion strength, moisture load (all derived from radiosonde profiles), CCN concentrations (obtained by ground-based measurements at Ragged Point station) and the location of the Saharan dust layer (estimated from BERTHA lidar measurements at CIMH). The differences in the geostrophic forcing are already discussed. Regarding the atmospheric stability, there is a much stronger trade inversion for the 27 June case with a local virtual potential temperature gradient of $14\,\mathrm{K\,km^{-1}}$. As mentioned in the introduction, the trade inversion controls the amount of precipitation and the lifetime of cloud streets. Furthermore, there is a 18 % stronger moisture load for the 27 June case, where a faster cloud development is expected. Due to the vertical and temporal variability in the

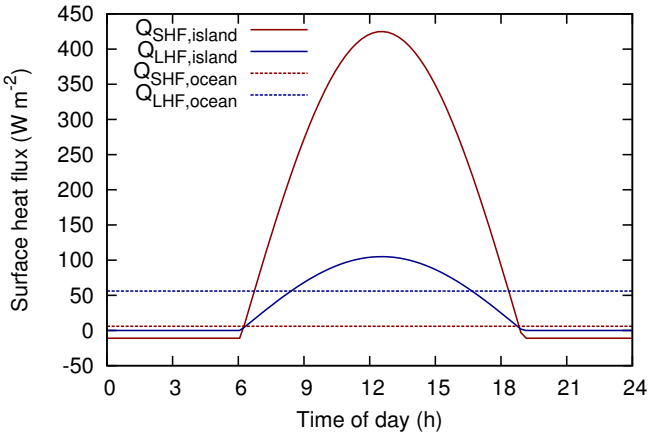


**Figure 4.** Parameterized diurnal variation in sensible (SHF) and latent heat fluxes (LHF) over island and ocean areas.

CCN number concentrations, a mean value of 300 $\mathrm{cm}^{-3}$ has been chosen for both cases, which is a typical magnitude for days with a moderate dust load, where aerosol optical depths between 0.2 and 0.4 are observed.

### 2.3 Forcings

Surface sensible and latent heat fluxes over the island and the ocean are obtained by separate 1-D simulations with full model physics. The parameterizations there include the radiation scheme (Fu and Liou, 1993) as well as land-use and soil models. The soil class "loam" was chosen to represent the average island soil type. Hydraulic and thermal parameters of this soil type can be found in Doms et al. (2011) and Jähn et al. (2015). For land surface parameterization, "shrubland" appears to be a good compromise between coastal beach areas and forest in the island interior. The roughness length of this land type is $z_{\mathrm{R,island}} = 0.2$ m, whereas the ocean roughness length is set to $z_{\mathrm{R,ocean}} = 0.01$ m. The usage of direct (compared to interactive) fluxes reduces computational costs for the LES runs and makes it easier to potentially reproduce these simulations by other models, especially due to a large number of existing radiation and land-use models. Figure 4 shows the diurnal variation in sensible and latent heat fluxes over the island area. The maximum sensible heat flux over the island is $Q_{\mathrm{SHF_{max},island}} = 425\,\mathrm{W\,m^{-2}}$ and the corresponding maximum latent heat flux is $Q_{\mathrm{LHF_{max},island}} = 105\,\mathrm{W\,m^{-2}}$. Surface heat fluxes over the ocean are constant during the whole simulation time with $Q_{\mathrm{SHF,ocean}} = 6\,\mathrm{W\,m^{-2}}$ and $Q_{\mathrm{LHF,ocean}} = 56\,\mathrm{W\,m^{-2}}$. Sunrise is at 05:36 LT and sunset is at 18:29 LT, whereby the fluxes are shifted by 30 min to represent the delay due the fact that the soil has to be heated first before energy exchange with the lower atmosphere can take place.

Later on, reference simulations with periodic boundary conditions are performed to obtain information of marine boundary layer characteristics. For these simulations, large-scale forcings from the BOMEX LES study of trade-wind cumulus convection (Siebesma et al., 2003) are applied. They include a piecewise linear subsidence velocity profile with an absolute peak value of $-560\,\mathrm{m\,day^{-1}}$, radiative cooling of $-2\,\mathrm{K\,day^{-1}}$ and large-scale advection of dry air into the lower boundary layer of $-1\,\mathrm{g\,kg^{-1}\,day^{-1}}$:

$$w_{\mathrm{sub}} = \begin{cases} -4.33\times10^{-6}\,\mathrm{s^{-1}}\,z\,, & z \le 1500\ \mathrm{m} \\ -0.0065 + 1.08\times10^{-5}\,\mathrm{s^{-1}} & \\ \quad \cdot(z - 1500\ \mathrm{m})\,, & 1500\ \mathrm{m} < z \le 2100\ \mathrm{m} \\ 0.0\,, & z > 2100\ \mathrm{m} \end{cases}, \tag{9}$$

$$\frac{\mathrm{d}\theta}{\mathrm{d}t} = \begin{cases} -2.315\times10^{-5}\,\mathrm{K\,s^{-1}}\,, & z \le 1500\ \mathrm{m} \\ -2.315\times10^{-5}\,\mathrm{K\,s^{-1}} & \\ \quad +2.315\times10^{-8}\,\mathrm{K\,s^{-1}\,m^{-1}} & \\ \quad \cdot(z - 1500\ \mathrm{m})\,, & 1500\ \mathrm{m} < z \le 2500\ \mathrm{m} \\ 0.0\,, & z > 2500\ \mathrm{m} \end{cases}, \tag{10}$$

$$\frac{\mathrm{d}q_v}{\mathrm{d}t} = \begin{cases} -1.2\times10^{-8}\,\mathrm{s^{-1}}\,, & z \le 300\,\mathrm{m} \\ -1.2\times10^{-8}\,\mathrm{s^{-1}} & \\ \quad +6\times10^{-11}\,\mathrm{s^{-1}\,m^{-1}} & \\ \quad \cdot(z - 300\ \mathrm{m})\,, & 300\ \mathrm{m} < z \le 500\ \mathrm{m} \\ 0.0\,, & z > 500\ \mathrm{m} \end{cases} \tag{11}$$

### 2.4 Turbulence generation – the cell perturbation method

The LES modeling technique has the advantage of allowing explicit resolution of turbulent production and part of the inertial range scales, and is today the most accurate and computationally feasible modeling approach in the context of high Reynolds number flows. LES results are strongly dependent on boundary conditions, therefore requiring specification of realistic inflow turbulence characteristics that propagate through the domain into the area of interest. In order to ensure that the incoming boundary layer characteristics at Barbados correspond to fully developed turbulence consistent with the imposed marine boundary layer forcing, we use the cell perturbation method recently proposed by Muñoz-Esparza et al. (2014). The cell perturbation method uses a novel stochastic approach based upon finite amplitude perturbations of the potential temperature field applied within a region near the inflow boundaries of the LES domain. This method has demonstrated superior performance when compared to a state-of-the-art synthetic turbulence generator and is computationally inexpensive (Muñoz-Esparza et al., 2015).

Previous studies where the cell perturbation method was developed and validated dealt with transitions from smooth mesoscale flow to nested LES (Muñoz-Esparza et al., 2014, 2015). In these idealized cases, boundary conditions at the LES domain boundaries were imposed from the mesoscale model instantaneous solution (Dirichlet boundary conditions), in which moisture effects were not considered. Herein, we further extend the application of the cell perturbation

method to turbulence inflow generation for cloud modeling including terrain effects. As explained in earlier sections, zero-gradient open radiative lateral boundary conditions need to be used in order to minimize wave reflections at the boundaries that do develop in fully compressible codes like the ASAM LES model when the domain includes terrain features. In order to test the best configuration for the cell perturbation method in this particular context, we perform a series of calculations where only the upstream region of the Barbados island is considered (i.e., incoming marine boundary layer). The reduced subset of the domain consists of a 51.2 km× 51.2 km area in the horizontal, with the same vertical extent and large-scale forcing described in Sect. 2.3 for the 22 June 2013 case study. To represent the marine boundary layer conditions that are going to be imposed through the entire simulation period, constant sensible and latent heat fluxes of $Q_{\mathrm{SHF,ocean}} = 6\ \mathrm{W\,m^{-2}}$ and $Q_{\mathrm{LHF,ocean}} = 56\ \mathrm{W\,m^{-2}}$ are used (see Fig. 4).

We explore the sensitivity of the generated turbulence by the cell perturbation method to the optimum perturbation Eckert number, $Ec = U_{\mathrm{g}}^2/c_{\mathrm{p}}\widetilde{\theta}_{\mathrm{pm}} = 0.2$, where $\widetilde{\theta}_{\mathrm{pm}}$ is the maximum potential temperature perturbation, and the perturbations are random and uniformly distributed in the interval $\left[-\widetilde{\theta}_{\mathrm{pm}}, +\widetilde{\theta}_{\mathrm{pm}}\right]$. Three square cells adjacent to the east boundary are used, which were found to provide the fastest transition to a fully developed turbulent state (Muñoz-Esparza et al., 2015). The cell size is set to $4 \times 4$ grid points to ensure that the cell wavelength falls within the inertial range of three-dimensional turbulence. The perturbation timescale, $t_{\mathrm{p}}$, was obtained from $\Gamma = t_{\mathrm{p}} U_1 (4\mathrm{d}x)^{-1} = 1$ (Muñoz-Esparza et al., 2015), with $U_1$ being the horizontal wind speed in the first vertical layer, resulting in a frequency to seed instantaneous perturbations of $t_{\mathrm{p}} = 145$ s. Figure 5 shows instantaneous contours of vertical velocity at $z = z_i/2 = 375$ m for different perturbation Eckert numbers, $Ec = 0.2$, 0.33 and 0.4, and for the periodic reference run. The cell perturbation method for the three $Ec$ numbers considerably accelerates the formation of three-dimensional turbulent structures that agree with the ones obtained in the reference simulation using periodic lateral boundary conditions. As the perturbation Eckert number increases (maximum perturbation amplitude decreases), the strength of the vertical velocities induced by the temperature perturbations is progressively reduced, and the onset of forcing-consistent turbulence seems to qualitatively occur at earlier distances from the inflow boundary.

In order to have a better understanding of the turbulence initiation and development processes, the energy spectrum evolution in the streamwise direction for the three velocity components is presented in Fig. 6. The cell perturbation method causes a rapid development of the upper-wavenumber portion of the energy spectrum for the $u$ and $v$ components. The larger scales (lower wavenumbers) require longer distances to be established due to large buoyant plumes having to emerge from the surface and populate across the entire extent of the boundary layer. This flow development pattern is consistent with the findings from Muñoz-Esparza et al. (2014) for convective conditions. In contrast, the energy spectrum for the vertical velocity reveals a rapid growth of turbulent energy that reaches levels 10 times greater than the periodic quasi-equilibrium solution (dashed black line) and that progressively dissipates as the flow transitions through the domain. We attribute this behavior to the cell size, $4\mathrm{d}x$, which for the resolution employed in this study may fall in the vicinity of the limit of the inertial range. Smaller cell sizes were not considered due to the energy dissipation at high wavenumbers present in finite differences/volumes discretizations. There, an interaction with fully resolved scales and triggering of an accelerated transition to a developed turbulence state would not have taken place. In addition, the use of zero-gradient lateral boundary conditions helps to maintain the signature of the perturbations more than in the case of Dirichlet boundary conditions, hence contributing to strengthen the periodically seeded perturbations. By increasing the perturbation Eckert number from 0.2 to 0.4 (first row vs. third row in Fig. 6), the energy overestimation is damped, and results after a fetch of 40 km for $Ec = 0.4$ are in close agreement with the periodic simulation used as a reference and have reached quasi-equilibrium converged statistics. The $Ec = 0.2$ case results in an energy deficit at wavenumbers close to the integral length scale, and also at the highest wavenumbers for the $w$ component. When the cell perturbation method is not used (NOCP panels, bottom row in Fig. 6), dramatic energy deficits are found, together with an unrealistic spiky energy distribution in which the expected energy production and cascade processes are not present.

Finally, we examine the vertical distribution of relevant boundary layer quantities at a downstream distance of 40 km from the east boundary (i.e., $x = 11.2$ km). Vertical profiles (Fig. 7) show the best agreement with the periodic simulation for the $Ec = 0.4$ and 0.33 cases, in particular for the turbulent kinetic energy levels and boundary layer structure. Momentum flux profiles exhibit slightly larger values in the first 250 m, due to the differences in the horizontal wind speed distribution near the surface. However, the boundary layer structure is similar, with the differences being related to distinct quasi-equilibrium solutions for the periodic and the open boundary condition simulations. Similar conclusions are found for the sensible and latent heat fluxes. The cell perturbation method was originally developed and tested in the context of dry boundary layers (Muñoz-Esparza et al., 2014, 2015). It is worth emphasizing that we have herein demonstrated for the first time, as can be seen from the latent heat flux profile, that the cell perturbation method has the ability to develop turbulent moisture features that are in agreement with the imposed forcing. The $Ec = 0.2$ case fails to produce a boundary layer structure that is similar to the reference periodic case, with excessive mixing attributed to an enhanced effect of the perturbations for the reasons mentioned above. Also, the NOCP case does not provide

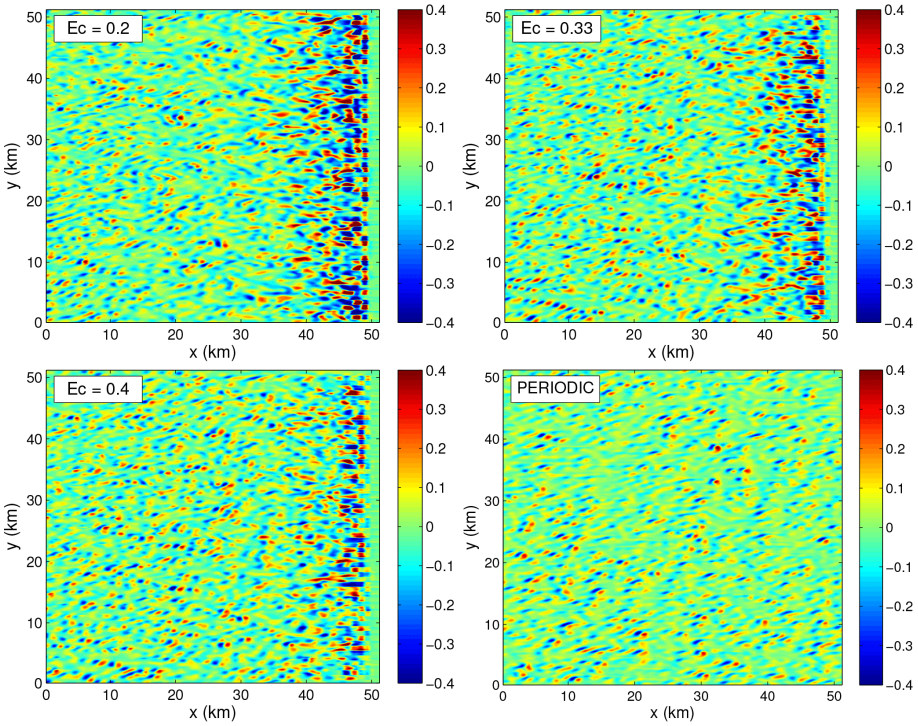


**Figure 5.** Instantaneous contours of vertical velocity at $z = z_i/2 = 375$ m for different perturbation Eckert numbers, $Ec = 0.2, 0.33, 0.4$, and the periodic case.

realistic turbulent boundary layer features corresponding to a strongly underdeveloped turbulent state. Therefore, we select the $Ec = 0.4$ setup as the inflow to be used for the island simulations presented in the remainder of the paper since it produces the most rapid development and stabilization of forcing-consistent turbulence. For the island cases, we use a domain with horizontal extent of 102.4 km × 102.4 km, which leaves sufficient fetch for the marine boundary layer to develop prior to the start of interaction with the topography of Barbados and its local stability effects.

## 3 Results

To investigate the effects of the Barbados island area on boundary layer properties, cloud generation and vertical mixing of aerosols, we define two subdomains that are considered to be representative of the upwind and downwind area, respectively. Figure 8 shows the position of these two subdomains. They both cover a base area of 10 km × 20 km and are used for averaging of vertical profiles and time series of the relevant quantities. The upwind domain east of Barbados (representing the marine boundary layer) is approximately 15 km away from the eastern boundary to avoid contamination from the inflow boundaries where turbulence has to be generated first. Looking into the model data, it becomes apparent that the flow has to pass at least half of the island area (≈ 12 km) before a well-mixed convective layer can fully develop. For that reason, the downwind subdomain is located between 35 km $< x <$ 45 km and thus covers the west coast island area and the marine offshore area in equal parts. The following analysis mainly consists of comparisons between these two regimes to investigate island effects on various parameters.

### 3.1 Overview of simulations performed

Besides the two mentioned case studies, two additional sensitivity studies are part of the island effect analysis. Here, the 22 June 2013 case serves as a reference case (REF). For the first sensitivity case (NOCP), the cell perturbation method is disabled so that the upwind flow is strongly underdeveloped. With this setup, the effect of having a realistic turbulent boundary layer around the island rather than idealized constant winds is investigated. In the next sensitivity case (DX400), the grid resolution is halved from 200 to 400 m horizontally and from 50 to 100 m vertically to point out the deficiencies in the use of coarser resolution without appropriate resolved turbulence and gray zone modeling (Wyngaard, 2004) for particular aspects of interest in boundary layers and cloud modeling. In this simulation, the cell perturbation method is also put off since the usage of a turbulent inflow in coarse resolution studies has not been utilized before and, moreover, appears to be questionable because the inertial subrange of the turbulence spectrum is not resolved anymore. The simulation ensemble is completed by the 27

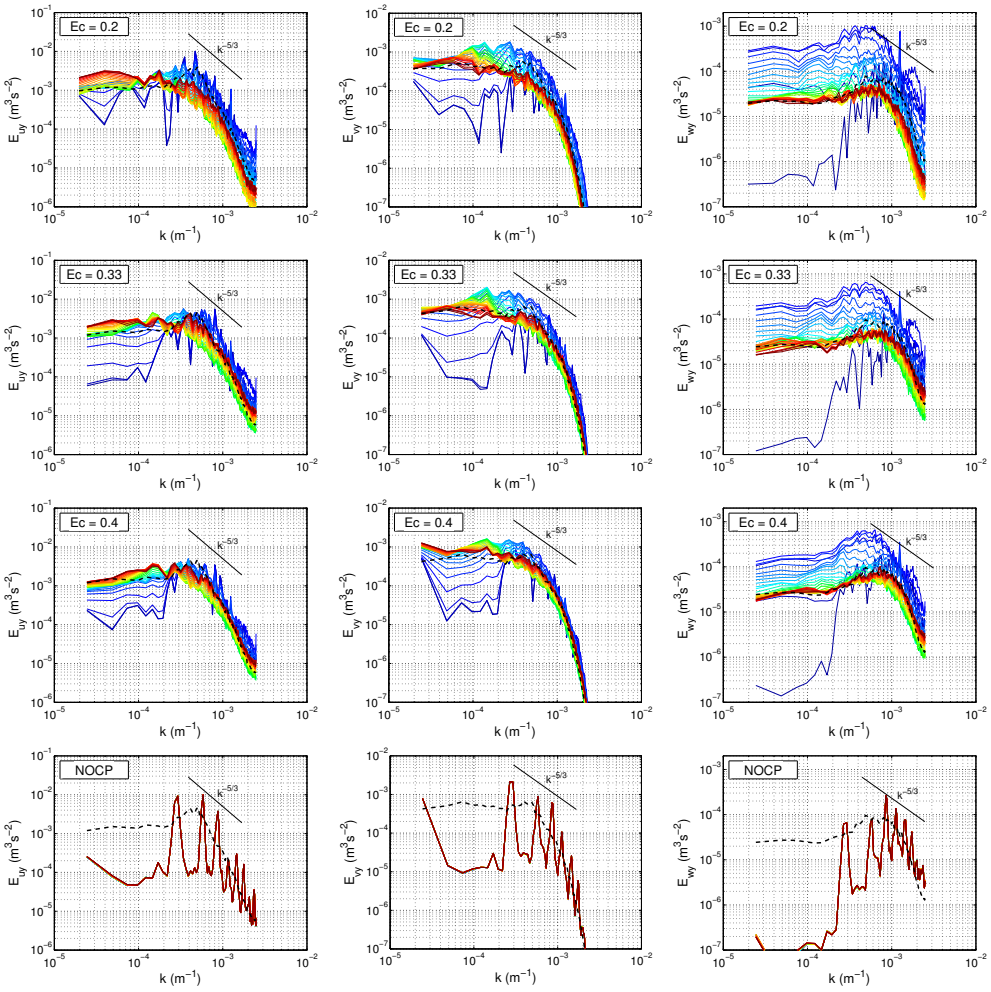


**Figure 6.** Spatial evolution of time-averaged energy spectra of $u$ (left), $v$ (middle) and $w$ component (right) in the $y$ direction at $z/z_i = 0.5$ for three perturbation Eckert numbers and the NOCP case. Color lines indicate distance from the east lateral boundary in steps of 0.8 km, 51.2 : −0.8 : 1.6 km, from blue to red. The dashed black line corresponds to the reference spectrum from the periodic computation, additionally averaged in the streamwise direction.

June 2013 case, mainly characterized by its strong trade-wind inversion (INV) and stronger background trade winds compared to the REF case. Table 3 summarizes the settings for all simulations that deviate from the standard configuration in Tables 1 and 2.

### 3.2 Boundary layer and cloud characteristics

To get a qualitative impression of the local situation simulated by the LES model, Fig. 9 shows a three-dimensional snapshot of the temperature and humidity field as well as cumulus clouds with up- and downdrafts visualized by isosurface fields at 12:00 LT for the reference case. The daytime convection is clearly visible by multiple updraft cells distributed over the whole island area, which subsequently leads to the development of non-precipitating shallow cumulus clouds. Advection of heated air from the central and southern part of the island towards the west can be seen in the surface temperature field (which is meant as temperature of the lowest model layer in this context), whereas the cooler marine flow narrows the thermal wake toward the meridional center of the domain up to 40 km downwind. This effect is connected with an island-induced change in wind speed and direction. The change in the humidity profile can be observed in the vertical cut plane at the western model boundary. A large amount of moisture is transported vertically upwards in the central region where also occasional cumulus clouds are present. A few tens of kilometers away in the $y$ direction, dryer air from heights of 500–1000 m is mixed downward.

For further insight into flow dynamics, especially for the downwind region, Fig. 10 provides the vertical wind field at $z \approx z_i/2$ for all four considered cases. Looking at the REF and INV case, several turbulent updraft bands with lengths

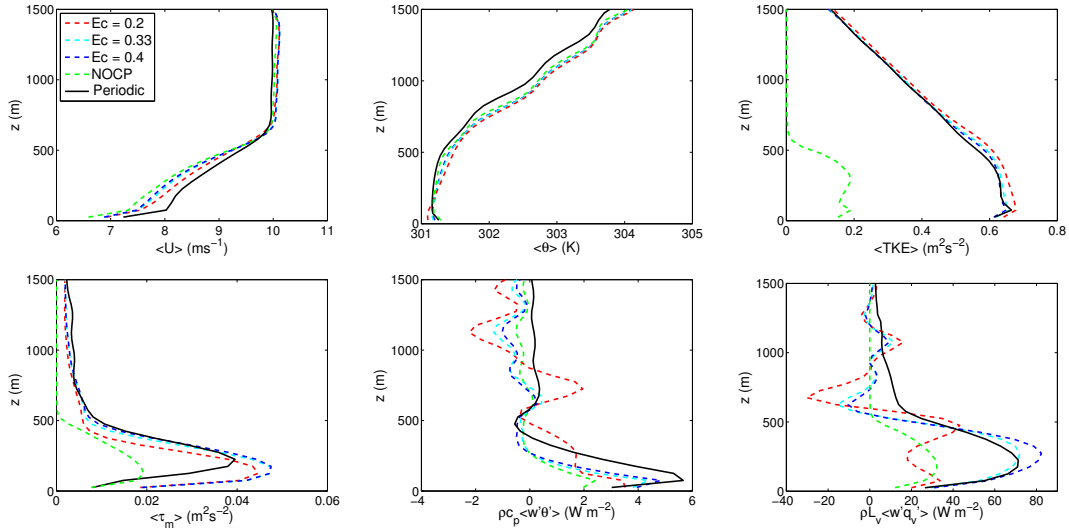


**Figure 7.** Vertical profiles of horizontal wind speed $\langle U \rangle$ (top left panel), potential temperature $\langle \theta \rangle$ (top middle), turbulent kinetic energy $\langle \mathrm{TKE} \rangle$ (top right), momentum flux $\langle \tau_\mathrm{m} \rangle$ (bottom left), sensible heat flux $\rho_0 c_\mathrm{pd} \langle w'\theta' \rangle$ (bottom middle) and latent heat flux $\rho_0 L_0 \langle w' q_\mathrm{v}' \rangle$ (bottom right) at a downstream distance of 40 km from the east boundary for different *Ec* numbers and the NOCP case (averaged along the $y$ direction and in time). The solid black line corresponds to the reference profile from the periodic computation, additionally averaged in the streamwise direction. The profiles are valid for the 22 June 2013 case.

**Table 2.** Parameter values of the cases to be examined: 22 June and 27 June 2013.

| Parameter | Unit | 22 June 2013 | 27 June 2013 |
|---|---|---|---|
| Maximum geostrophic wind $\lvert u_\mathrm{g} \rvert$ | $\mathrm{m\,s^{-1}}$ | 10.0 | 11.5 |
| Top altitude of trade-wind inversion $z_{\mathrm{inv,\,t}}$ | m | 2200 | 2000 |
| Bottom altitude of trade-wind inversion $z_{\mathrm{inv,\,b}}$ | m | 1600 | 1800 |
| Inversion strength $\mathrm{d}\theta_\mathrm{v}/\mathrm{d}z$ | $\mathrm{K\,km^{-1}}$ | 5.67 | 13.89 |
| Surface pressure $p_0$ | hPa | 1014.2 | 1013.9 |
| Integrated water vapor content up to $z = 2\,\mathrm{km}$ | $\mathrm{kg\,m\,kg^{-1}}$ | 22.14 | 26.16 |
| CCN concentration at 1 % supersaturation $N_{\mathrm{CCN,1\,\%}}$ | $\mathrm{cm^{-3}}$ | 300 | 300 |
| Top altitude of Saharan dust layer | m | 2800 | 2900 |
| Bottom altitude of Saharan dust layer | m | 1800 | 1700 |

of about 10 km in the zonal direction and vertical velocities up to $2.5\,\mathrm{m\,s^{-1}}$ develop all over the island area. However, one main band at $y \approx 52$ km remains persistent, even at higher altitudes. This updraft band is a result of the dynamic and thermal instability over the island, forming quasi two-dimensional horizontal vortex rolls with their axes aligned in the downwind direction (e.g. Etling and Brown, 1993). Toward the evening, as the surface sensible heat flux is not positive anymore and convection fades away, the band decouples from the island and vanishes (not shown). Turbulent updraft cells within the marine boundary layer with vertical velocities between 0.5 and $1\,\mathrm{m\,s^{-1}}$ are also visible since a turbulent inflow is generated with the cell perturbation method described in Sect. 2.5. In the INV case, these updrafts are a bit weaker, which is most likely due to the stronger mean horizontal wind speed. Wave-like structures in the upwind vertical velocity field are observed in the NOCP case. There, the flow remains laminar in this region, and since no perturbation is applied but surface fluxes are present, these artificial convergence lines are forming. Note that this effect is not seen in the REF and INV case. This underscores the importance of having an explicit inflow turbulence generation when working on LES scales. Just by visibly comparing the "coarse" simulation DX400 with the other cases, it becomes apparent that there is a lot of structure loss in the vertical wind field. All up- and downdraft bands – even the main updraft band downwind – are almost perfectly aligned in the $x$ direction. This shows the importance of using a grid spacing that resolves the inertial subrange of the velocity spectrum (cf. Bryan et al., 2003). Note that with coarser grid spacings the orographical structures of the island are also less represented.

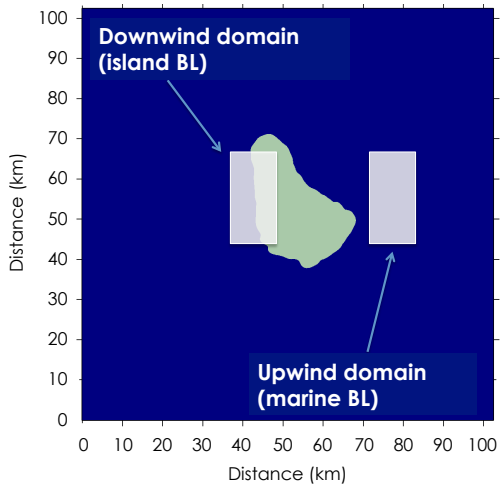


**Figure 8.** Definitions of subdomains for spatial averaging to cover different boundary layer characteristics: upwind marine regime east of Barbados (right) and downwind island regime over the west coast area (left).

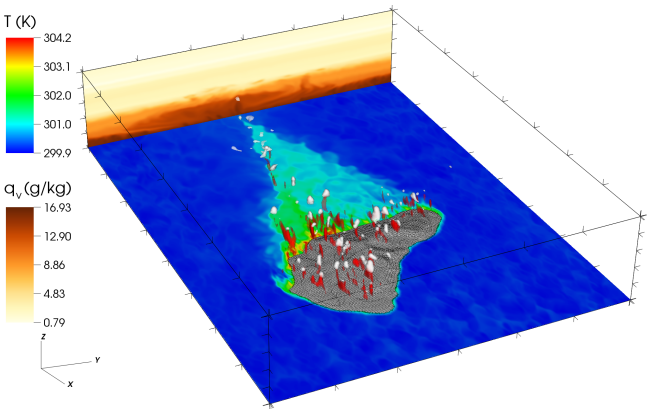


**Figure 9.** Perspective view of surface temperature and specific humidity field at the western boundary for the REF case. Clouds are visualized by 0.1 g kg$^{-1}$ isosurface in white coloring. Red coloring depicts an isosurface of 2 m s$^{-1}$ updrafts. Snapshot taken at 12:00 LT. A model area of 80 km × 60 km × 5 km is shown.

Figure 11 shows the surface wind fields and liquid water path for all simulated cases at 14:00 LT. In all these cases, the island convection affects both the strength (up to 4 m s$^{-1}$ stronger wind speeds compared to marine surface winds) and direction (±30°) of the wind in the downwind area of Barbados, thus leading to strong surface convergence and subsequently forming the updraft band as seen in Fig. 10 at $y = 52$ km. Despite having this elongated band, very little cloud formation is observed in this area for the REF, NOCP and INV cases, which is also the case for other times of the day (not shown). This means that no continuous cloud street is modeled on 22 and 27 June 2013, respectively. While cloud streets occur on around 60 % of undisturbed days, there are several effects that suppress cloud street generation (Kirshbaum and Fairman, 2015). In the REF (and NOCP) case, the relatively low moisture load (RH = 80 % near the surface, decreasing below 60 % at $z \approx 1300$ m) and a weak trade-wind inversion leads to a suppression of the development of a cloud trail. Both moisture and stratification are increased in the INV case but the stronger mean trade winds (almost 12 m s$^{-1}$) are the suppressing factor here (Kirshbaum and Fairman, 2015). Due to the absence of a turbulent inflow velocity field, the cumulus clouds over the island are horizontally aligned to the mean wind direction in the NOCP case. In the REF and INV cases, more realistic scattered cumulus cloud fields over the island area and downwind are modeled. Besides the distinct cloud bands, the DX400 case shows further very notable differences in the cloud field. First of all, clouds are broader because of the coarser grid spacing. In addition to that, a continuous cloud street is modeled, which can be considered an artifact since such a cloud band is not seen in either other simulations or satellite observations. Furthermore, the downwind horizontal velocity field is slightly stronger compared to the other cases. We attribute this behavior to the lack of resolved small scales that cannot extract energy from the large eddies and therefore grow and become more coherent. This effect is also observed to a lesser extent for the NOCP case.

**Table 3.** Parameter choices for the sensitivity simulations performed.

| Simulation name | Date | $\Delta x$, $\Delta y$ (m) | $\Delta z$ (m) | Turbulent inflow |
|---|---|---|---|---|
| REF | 22 Jun 2013 | 200 | 50 | yes |
| NOCP | 22 Jun 2013 | 200 | 50 | no |
| DX400 | 22 Jun 2013 | 400 | 100 | no |
| INV | 27 Jun 2013 | 200 | 50 | yes |

In the following, the diurnal development of the convective island boundary layer is investigated. Figure 12 shows time series of boundary layer and cloud properties for the downwind region around the west coast of Barbados. Further mean quantities of boundary layer and cloud characteristics are diagnosed and summarized in Table 4. The REF and the INV case have some properties in common. They both show a strong increase in cloud cover in the downwind region between 07:00 and 08:00 LT up to a maximum value of about 16 %. The boundary layer height $z_i$ displays a diurnal variation, growing up to $z = 1350$ m around 13:00 LT in the REF case. For the INV simulation, $z_i$ is approximately 100–150 m shallower. This parameter is calculated via the bulk Richardson criterion, where the boundary layer height is defined as the height where the bulk Richardson number $Ri_\mathrm{b}$ exceeds a value of 0.25, with

$$Ri_\mathrm{b} = \frac{g}{\theta_{\mathrm{v}0}} \frac{\theta_\mathrm{v} - \theta_{\mathrm{v}0}}{u^2 + v^2} z\,, \tag{12}$$

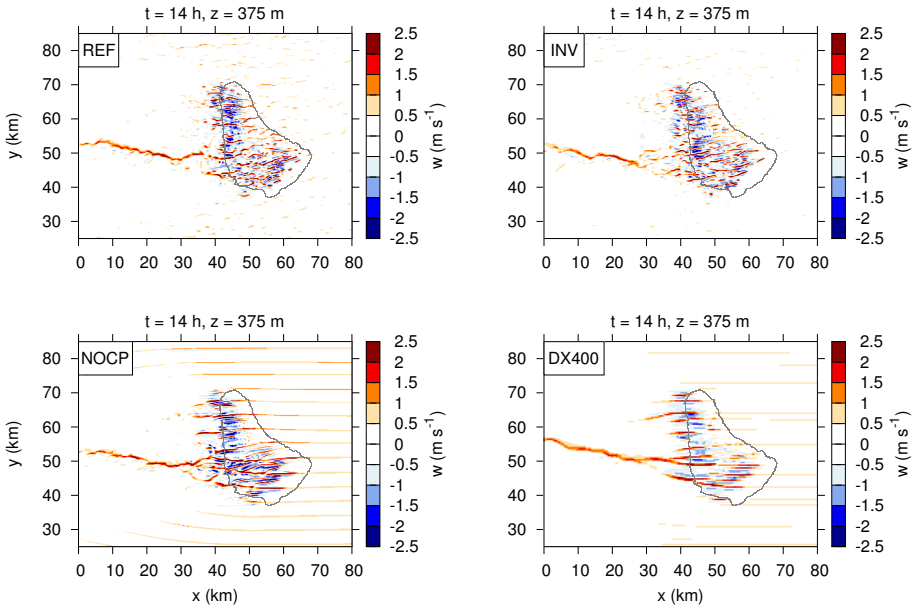


**Figure 10.** Vertical wind at $z = 375$ m a.s.l. at 14:00 LT for the four simulation cases (see Table 3).

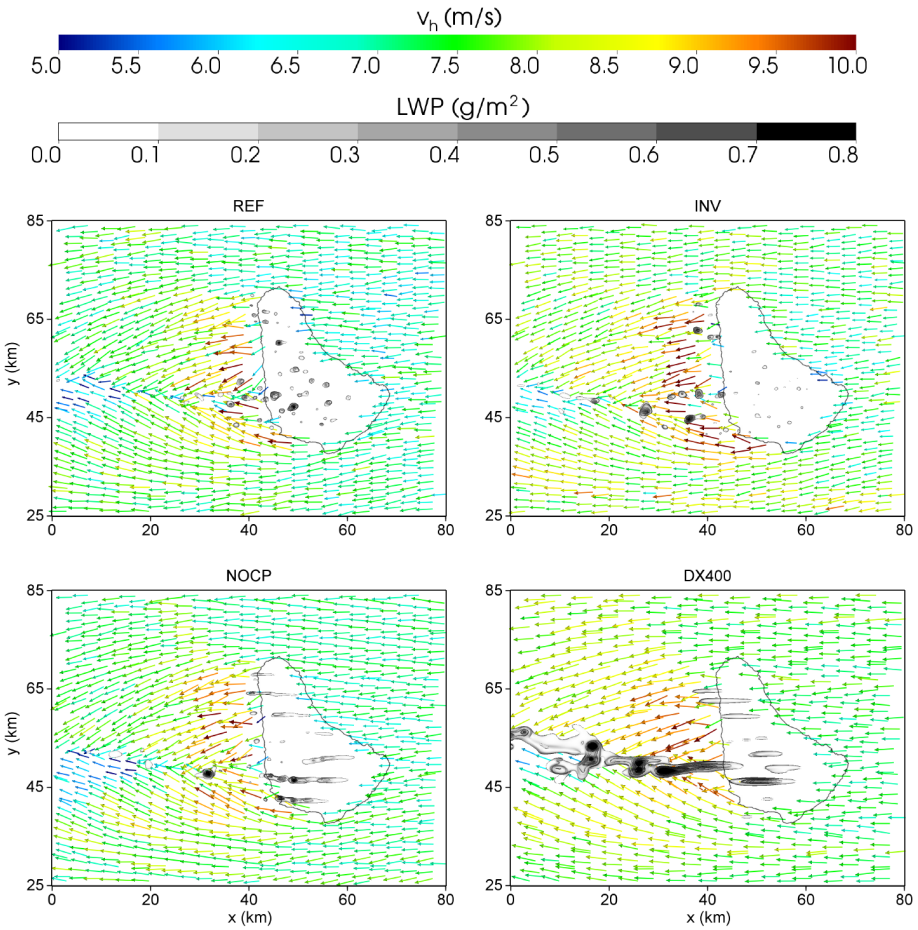


**Figure 11.** Horizontal cut planes ($xy$) of surface wind vectors and contours of liquid water path for all four simulation cases (see Table 3).

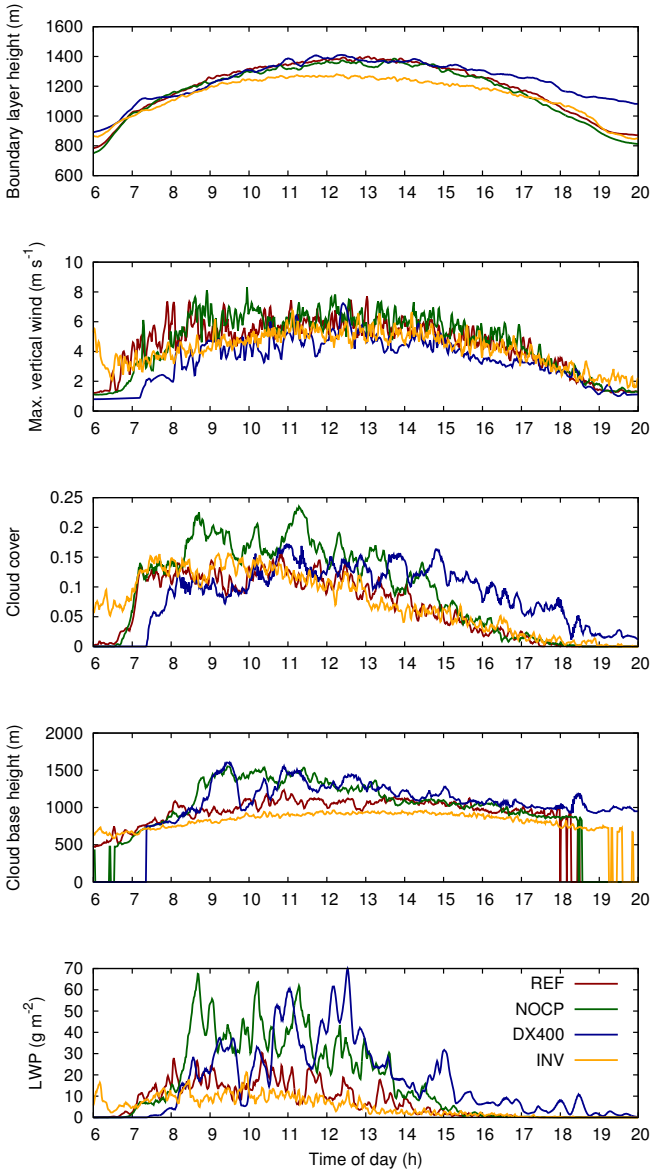


**Figure 12.** Time series of boundary layer height, maximum vertical velocity, cloud cover, cloud base height and liquid water path for the downwind domain. Spatial averaging as indicated in Fig. 8.

where $\theta_{v0}$ is the virtual potential temperature at the surface. Being relatively similar in boundary layer characteristics and cloud cover, there is a clear distinction between REF and INV with regard to cloud microphysical properties. Due to higher cloud base height in the REF case, the cumulus clouds tend to grow deeper, which is seen in the mean liquid water path (LWP) values as well as in the cloud base and top heights (see Table 4). The cloud cover, however, is fairly comparable for these two cases. Peak updraft values also show a diurnal variation, starting from approximately $w_{max} = 1\,\mathrm{m\,s^{-1}}$ (which is equivalent to the upwind area value) up to $w_{max} = 7\,\mathrm{m\,s^{-1}}$ around noon. The DX400 case has overall weaker peak updrafts; however, this does not mean that there is less vertical transport of energy, moisture, momentum etc. Due to the coarser grid spacing in every spatial direction there is a higher net upward transport.

To further investigate daytime-dependent vertical mixing and layering, Fig. 13 shows hourly averaged vertical profiles boundary layer and cloud parameters for the downwind domain compared to the daily upwind average. Comparing again the REF and INV cases, daytime-dependent differences in the density potential temperature and specific humidity profiles can be noticed (not shown). Lower levels at $z < 700$ m are warmer and dryer compared to the marine background. The vertical turbulent transport is evidenced by the profiles of sensible and latent heat fluxes. The sensible heat flux is linearly decreasing within the mixing layer up to heights between 700 m $< z <$ 900 m, depending on the time of day. The maximum latent heat fluxes occur between 600 m $< z <$ 800 m. Above that layer, the cloud water content reaches its maximum, which is connected to latent heat release and thus to an increase in the sensible heat flux and a decrease in the latent heat flux. In the INV case, the trade inversion around $z \approx 2000$ m inhibits further cloud development above this height, whereas in the REF simulation there is also a notable amount of cloud water above 2000 m. The presence of wind shear above 1500 m height leads to a secondary maximum of TKE around $z = 2000$ m, which is not the case in the shearless INV simulation.

In the NOCP case, i.e., without a turbulent inflow, persistent updraft bands form over the island area, which is consistent with the modeled cloud field from Fig. 11. The inflow characteristics have little effect on boundary layer properties like TKE, vertical velocity variance (not shown), sensible and latent heat flux (cf. Fig. 13). However, the values for the NOCP case tend to be a bit higher than in REF, especially between 500 and 700 m. One reason for this could be that the upwind marine boundary layer already vertically transported some amount of energy, which is missing in the NOCP case. More remarkable differences are noticeable with regard to cloud development. The LWC around $z \approx 1000$ m during noon is nearly doubled for the NOCP case. There is also a particularly pronounced secondary maximum of LWC around $z \approx 2100$ m in the same order of magnitude. With the average over the whole daytime period taken, the mean LWP is more than doubled in the NOCP case compared to the REF case, which is in agreement with higher LWC values and also higher cloud cover ($\approx +3$ %).

More undesired effects become apparent when using a coarser spatial resolution as in the DX400 case, which is most noticeable in the averaged vertical profiles. First of all, there is less variability in the potential temperature and specific humidity fields for altitudes $z > 1000$ m, which can be explained by the lack of turbulent vertical transport within the boundary layer (this effect can be seen in the vertical profile of TKE in Fig. 13 and in the profile of the vertical velocity variance). The LWC, however, has maximum val-

**Table 4.** Diagnostics the four sensitivity simulations (see Table 3), including cloud cover, cloud base height $z_{cb}$, cloud top height $z_{ct}$, boundary layer height $z_i$, water vapor path (WVP), liquid water path (LWP), and maximum updraft values $w_{max}$. All quantities are spatially averaged for the downwind area and temporally averaged between 06:00 and 18:00 LT.

| Case | Cloud cover (%) | $z_{cb}$ (m) | $z_{ct}$ (m) | $z_i$ (m) | WVP ($kg\,m\,kg^{-1}$) | LWP ($g\,m^{-2}$) | $w_{max}$ ($m\,s^{-1}$) |
|---|---|---|---|---|---|---|---|
| REF | 7.8 | 967 | 1167 | 1240 | 27.6 | 8.5 | 5.0 |
| NOCP | 11.0 | 1066 | 1269 | 1222 | 27.7 | 18.8 | 5.2 |
| DX400 | 9.7 | 1029 | 1237 | 1262 | 29.3 | 19.0 | 3.7 |
| INV | 8.6 | 846 | 1024 | 1174 | 33.2 | 5.9 | 4.5 |

ues of $0.028\,g\,m^{-3}$ around $z \approx 2000$ m, which is a factor of 2 higher compared to the REF case. This is accompanied by strong latent heat fluxes in these layers. Cloud growth is also more inhibited at finer resolutions due to explicit entrainment of dryer environmental air (e.g. Bryan et al., 2003). Having a distinct and quite symmetric diurnal variation in boundary layer and cloud properties in the other cases, the evening transition in the DX400 case is poorly represented, where still a notable number of clouds exist and a deeper boundary layer is modeled around 20:00 LT.

### 3.3 Vertical mixing of aerosols

After the long-range transport of Saharan dust into the Caribbean region, these dust layers arrive at Barbados with mean base heights of about 1.5–2 km a.s.l. Due to a possible interaction with the convective island boundary layer, vertical mixing of aerosols is investigated in this subsection. As already shown in Sect. 2, these aerosol layers are represented by passive tracers in the model. They are initialized with a relative concentration of 1 within the layer where the aerosol is detected and 0 otherwise. This approach has already been used for heat island effect studies in Engelmann et al. (2011). These relative concentrations can be related to mass concentrations of Saharan dust, e.g., $180\,\mu g\,m^{-3}$. This mass concentration and the Saharan dust layer heights are estimated from ground-based multi-wavelength aerosol lidar measurements and provide a rough idea of the magnitude of these quantities. Especially the particle depolarization ratio indicates that the pure dust layer begins at around 1.5 km altitude. A detailed analysis of dust layers during the campaign can be found in Groß et al. (2015). Figure 14 displays height–distance profiles of the boundary layer tracer $\phi_{BLT}$ and the Saharan dust tracer $\phi_{SDT}$ near the west coast of Barbados. In both cases, the turbulent character over the island section is visible as a vertical distribution of the passive tracer within the higher boundary layer and the corresponding decrease in tracer concentration. It is more pronounced for the southern part of the island, which is due to the broader land area width (20 km in the south compared to 10 km in the north). It also indicates the wind shear at the island boundaries (e.g., at $y = 43$ km), which causes the advection of air masses from $z > 700$ m into the boundary layer. This effect is more pronounced further west (not shown). In the REF case, the mean boundary layer height around noon was calculated to be $z_i \approx 1400$ m. The passive tracer analysis additionally shows some local overshoots at heights over 2 km a.s.l. The Saharan dust tracers do have a different vertical structure. For the REF simulation, the tracer is thinned out, with maximum concentrations between $1.9\,km < z < 2.4$ km, whereas in the INV case it is between $1.7\,km < z < 2.5$ km. There are also no overshoots visible beyond $z = 1.7$ km. The stronger turbulent mixing in the REF case can be explained by the presence of wind shear around $z \approx 1.5$ km height, whereas in the INV case the strong trade-wind inversion suppresses further development of turbulence in higher altitudes. The logarithmic scale indicates the tracer diffusion, which shows that about 1 % of the maximum concentration is present at altitudes between 1.3 and 1.5 km (depending on the case) and locally down to 1.0 km altitude due to the island effect.

Although there are already some indications of downward aerosol transport, a better quantification of these effects is still needed to achieve a better understanding of the processes behind it. For that reason, mean vertical profiles are calculated in the same manner as the boundary layer and cloud analysis. Figure 15 shows vertical profiles of tracer-related quantities for the REF and the INV case. The tracer profile is being deformed by vertical transport processes, which can be originated by larger-scale or turbulent processes. To distinguish between those two, the total vertical tracer flux $\langle w\phi_{SDT}\rangle$ and the turbulent vertical tracer flux $\langle w'\phi'_{SDT}\rangle$ are computed. According to the model data, there is already a persistent downward movement east of Barbados between $1.5\,km < z < 3.0$ km, which corresponds to a subsidence velocity of $w = -407\,m\,day^{-1}$ for the REF case and $w = -345\,m\,day^{-1}$ for the INV case. There is a total relative downward flux for the downwind area in the REF case at 1.2 km height, with a maximum magnitude of $\langle w\phi_{SDT}\rangle = -0.03\,m\,s^{-1}$. The height of this local extremum depends on the time of day, with higher altitudes in the morning and around noon and lower altitudes toward the evening. A net positive upward flux is always present above $z = 2$ km, becoming zero at $z = 3$ km. About one-third to one-half of the total downward flux is caused by turbulent mixing, having its local maxima at $z = 1.8$ km, which is the lower bound of the

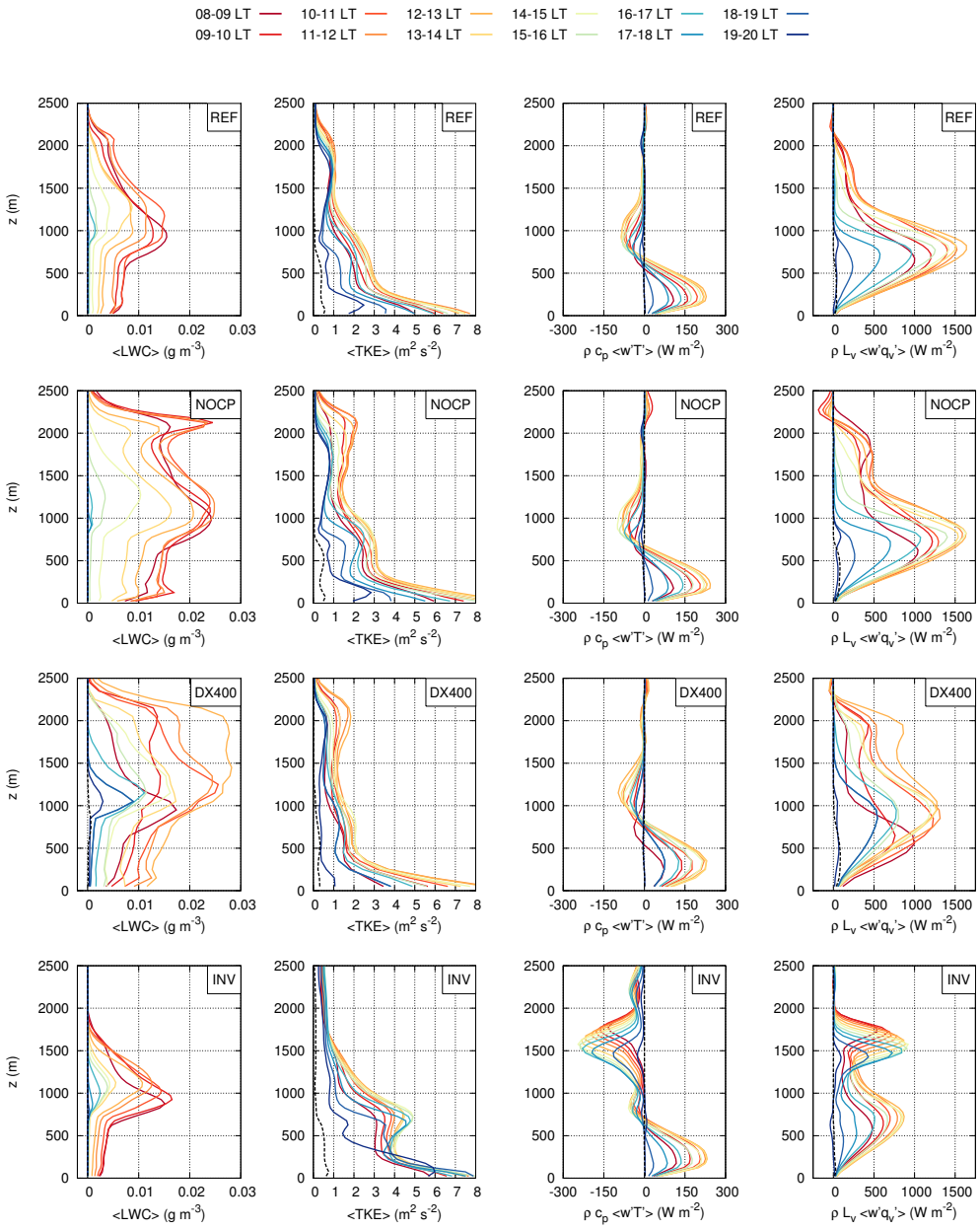


**Figure 13.** Vertical profiles of liquid water content ⟨LWC⟩, resolved turbulent kinetic energy ⟨TKE⟩, sensible and latent heat flux $\rho_0 c_{\mathrm{pd}} \langle w' T' \rangle$ and $\rho_0 L_0 \langle w' q_{\mathrm{v}}' \rangle$ for all four considered cases (REF, NOCP, DX400 and INV from top to bottom). Spatial averaging as indicated in Fig. 8. Black dashed lines represent the marine upwind area and are temporally averaged between 08:00 and 20:00 LT. Colored solid lines represent for hourly averages during different times of the day for the downwind area.

Saharan dust layer. The daytime turbulent downward mixing is about 5 times stronger in the INV case but is shifted approximately 400 m toward the surface compared to REF. Due to the tracer subsidence, the layer also reaches these altitudes of maximum turbulent downward mixing, which would not be the case if the dust layer remained at its initial height of 1.7 km. The downwind total tracer flux, however, is positive (upwards) for all altitudes and is almost 1 order of magnitude stronger compared to REF. Since the mean wind speed only slightly differs between the two cases and surface fluxes are the same, it can be concluded that atmospheric stability (especially inversion strength) and the presence of wind shear in the sub-inversion layer have a major impact on altitude and strength of layers with preferably upward or downward mixing properties. The model data suggest that the net effect, i.e., effects from both mean transport and turbulent mixing, is downward transport around the dust layer base for the downwind region in REF and a net upward transport in INV.

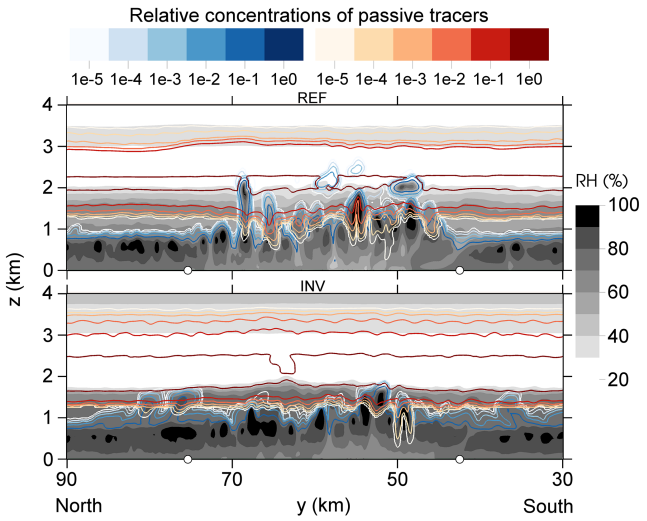


**Figure 14.** Meridional cut planes ($y$–$z$ profiles, 3 km off the west coast of Barbados) of the relative passive tracer concentrations and relative humidity for the REF (top panel) and the INV case (bottom panel). Red/orange contour coloring represents the Saharan dust tracer concentration $\phi_{\mathrm{SDT}}$ and blue contour coloring represents the boundary layer tracer concentration $\phi_{\mathrm{BLT}}$ on a logarithmic scale. White circles denote the location of the northern and southern island edges. The snapshots are taken at 12:00 LT.

## 4 Comparison with lidar data

### 4.1 Doppler wind lidar: velocity fields

In order to qualitatively evaluate the results obtained by the LES model, a comparison with the measurements performed by an airborne Doppler wind lidar (DWL) is presented in this section. Vertical and horizontal wind speed measurements from a flight on 20 June 2013 are compared to the simulation results of the 27 June 2013 case. A simulation with initial data at 20 June 2013 could not have been performed because no nighttime radiosonde data were available on this particular day. Although the measurements and the simulation correspond to different days, the comparison of the radiosonde profiles used for the LES initialization launched on 27 June and the dropsonde measurements obtained during the measurement flight on 20 June show a good agreement in the altitude of the trade inversion, relative humidity levels and temperature profile (Fig. 16). Especially the measured horizontal wind speed profile from the dropsondes matches better to the 27 June than the 22 June simulation case.

The airborne DWL used for this comparison was deployed onboard the DLR Falcon 20 research aircraft during the SALTRACE campaign. The system, based on an instrument developed by Lockheed Martin Coherent Technologies and enhanced by DLR to provide airborne measurement capabilities, can be operated in either nadir-pointing mode or scanning mode (Reitebuch, 2012; Chouza et al., 2015). The nadir-pointing mode allows the retrieval of vertical wind speeds with a vertical resolution of 100 m and a horizontal resolution of approximately 200 m with a random error lower than 0.15 m s$^{-1}$ and a systematic error lower than 0.05 m s$^{-1}$. Note that these resolutions are almost identical to the grid spacings used in the LES. The overflight took place between 10:36 and 10:44 LT at a flight altitude of 2900 m.

Figure 17 shows the flight track corresponding to the overflight (plane 2 in the figure) together with the LES results of the vertical wind speed for the 27 June case at 10:30 LT. For this overflight, vertical wind measurements on the lee side and over the island are available.

A comparison between the measured and the simulated vertical wind speed profiles is displayed in Fig. 18, where some main structures can be recognized in both profiles. Strong vertical winds associated with convective activity over Barbados can be observed in both the simulation and the measurements. In the case of the measurements, the presence of convective clouds limits the lidar coverage over the island (between 47 and 63 km on the $x$ axis). For the measurements performed on the lee side of Barbados and for altitudes above 1 km a series of waves with a wavelength of approximately 10 km and an amplitude of 2 m s$^{-1}$ can be recognized. A similar feature can be seen in the LES data, but with a slightly weaker amplitude.

To get a better idea of the horizontal distribution of these waves at a certain level, Fig. 19 shows the vertical wind speed at the trade-wind inversion height for different times during the day. It seems that the strength of daytime convective activity plays a minor role since the overall pattern looks very similar in all three snapshots, with the exception of minimally stronger fluctuations toward the afternoon hours. A marked wave structure in the lee of the island is visible, which is the result of trapped gravity waves due to the strong inversion. Again, a similar wavelength amplitude of about 10 km can be seen and stronger amplitudes (comparable to the DWL measurements) originating from the northern part of Barbados are also visible.

Figure 20 shows a comparison between the mean and the variance of the measured and simulated vertical wind speed on the lee side (between 0 and 35 km on the $x$ axis) of Barbados. The mean vertical wind profiles of the measurements (black line) show a reasonable agreement with the LES results regarding the overall structure (e.g., cut planes 1, 2 and 5, which are located at the southern and northern edge of Barbados, covering a similar spatial area as in the flight route). The mean vertical velocity below 1 km height indicates a downdraft region on the lee side of Barbados. This can be explained by the daytime circulation pattern in the lee of Barbados since the updraft band located between the center and southern part of the island causes downdrafts at its lateral flanks. Planes 3 and 4 reflect this behavior with positive vertical velocities below 1 km height. The variance of the vertical wind field shows an overall increase with altitude both for measurement and model results. However, the strength of these fluctuations is increased in the measurement

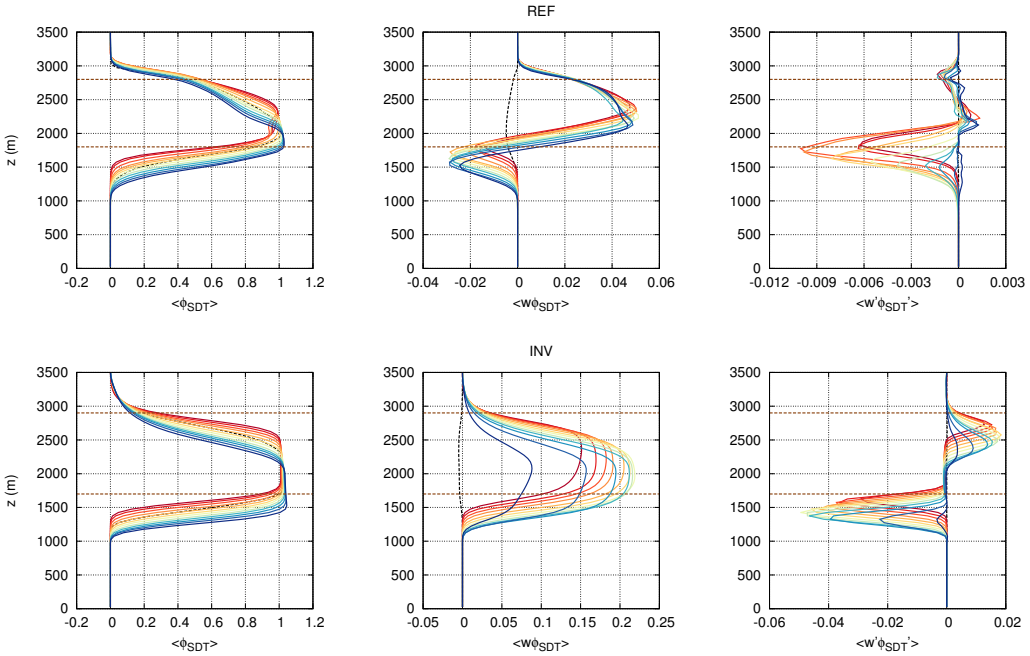


**Figure 15.** Vertical profiles of the passive Saharan dust tracer $\langle\phi_{\mathrm{SDT}}\rangle$ (left panel), the total vertical tracer flux $\langle w\phi_{\mathrm{SDT}}\rangle$ (middle panel) and the resolved turbulent tracer flux $\langle w'\phi'_{\mathrm{SDT}}\rangle$ (right panel) for the REF case (top row) and the INV case (bottom row). Solid line colors and spatial as well as temporal averaging as in Fig. 13. The horizontal brown dashed line represents the initial location of the Saharan dust tracer between 1800 m $\leq z \leq$ 2800 m for REV and between 1700 m $\leq z \leq$ 2900 m for INV.

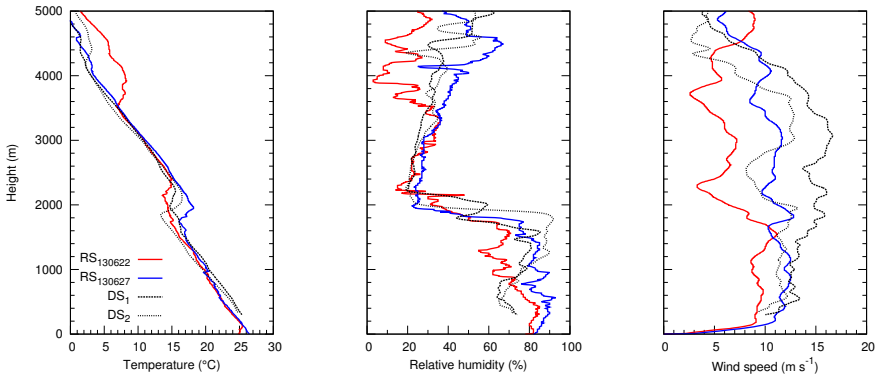


**Figure 16.** Comparison of measured temperature (left panel), relative humidity (middle panel) and wind speed (right panel) obtained from the nighttime radiosonde launches (solid lines) on 22 June (red curve) and 27 June (blue curve) and two dropsonde profiles during the wind lidar measurements at 20 June onboard the Falcon aircraft. $\mathrm{DS}_1$ (dashed lines) was launched 100 km to the west of Barbados at 12:46:59 UTC and $\mathrm{DS}_2$ (dotted lines) was launched 200 km to the east of Barbados at 13:22:51 UTC.

data, which could result from differences in the forcing, e.g., stronger surface fluxes than the prescribed ones in the LES model.

### 4.2 Multi-wavelength Raman lidar: convective boundary layer structure

A stationary lidar system deployed at the CIMH during the SALTRACE campaign was the polarizing Raman lidar BERTHA (Backscatter, Extinction, lidar Ratio, Temperature, Humidity profiling Apparatus; Tesche et al., 2011). Continuous measurements were performed on 22 June 2013 from 09:49 to 17:23 LT and after sunset (around 18:30 LT) from 19:32 to 22:30 LT.

The range-corrected signal for the 532 nm cross polarized channel is shown in the top panel of Fig. 21. The vertical resolution is 7.5 m and the time resolution varies from 3 to 15 s. The mean wind speed (< 3 km altitude) was approximately 10 m s$^{-1}$, which results in a horizontal resolution of 30 to 150 m. A first strong dust layer in a very dry environment (20–30 % RH) was detected between 1.8 and 2.8 km, topped

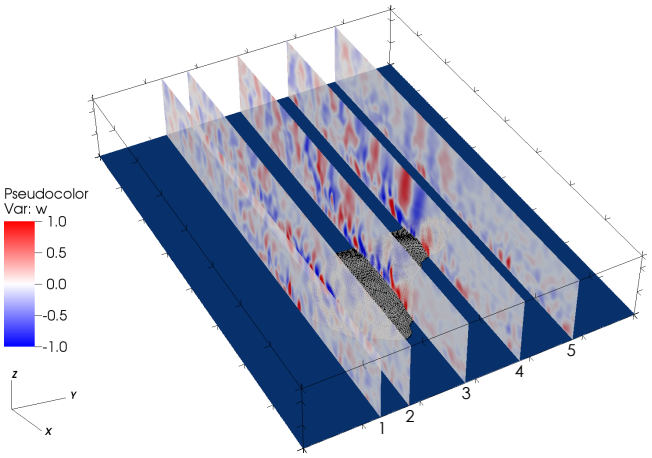


**Figure 17.** Locations of the five considered vertical planes for the comparison between the LES results and the DWL measurements within a domain of 60 km ($y$) and 80 km ($x$) up to an altitude of 2.5 km ($z$). The vertical wind (in m s$^{-1}$) along the planes is indicated in red (updrafts) and blue (downdrafts). Plane 2 is similar to the Falcon flight track. Planes 1 and 5 have no intersection with the island area, which is visualized by surface cut cells of the computational grid. Ocean area is in blue.

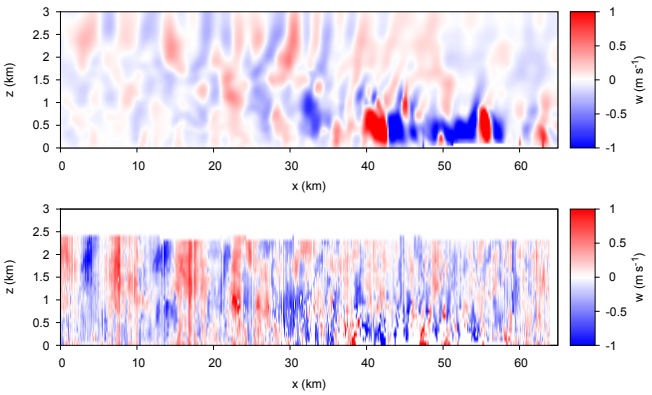


**Figure 18.** LES model output of zonal height–distance profiles of vertical wind speed component (upper panel) at 10:30 LT. DWL vertical wind speed component (lower panel) between 10:36 and 10:44 LT. Location indicated in Fig. 17. Island area is between 47 km $< x <$ 63 km.

by a second, weaker dust layer between 2.8 and 3.7 km which was more humid (40–50 % RH). Temperature inversions set the limits of the total dust layer or Saharan Air Layer. The lidar signal shows clouds all over the day around 1 km height and close to 1800 m. On average, 20 clouds per hour cross the lidar beam with an increasing number in the afternoon, leading to a cloud cover (in this context defined on a temporal scale) of roughly 50 %. At nighttime only a single cloud was detected within 3 h of measurement, which confirms the convective character of the daytime clouds at the investigated day over the west coast of Barbados. The bottom panel in Fig. 21 shows the LES model output of the corresponding height–time profile of relative humidity for this day and the same location. The diurnal variation in convective vertical moisture transport is clearly pronounced. Clouds (white/red coloring) develop at the same altitudes as in the BERTHA lidar measurements. Even higher and deeper clouds up to the top of the trade inversion at $z = 2$ km are resolved. Higher cloud activity can be noticed in the measurements, whereas the LES model results show fewer clouds toward the late afternoon. This effect can be attributed to the relatively low ocean latent heat flux from the marine boundary layer forcing, which tends to dry out the lower troposphere over a longer period of time (i.e., toward the afternoon and evening hours). Additionally, there is a notable increase in moisture during the afternoon (see the 16:01 LT radiosonde launch compared to the other ones) within the first 800 m of the lower troposphere. Because of the fact that no additional large-scale forcing (in this case, advection of moist air) is applied during the simulation time, this effect expectedly cannot be captured by the LES.

Further comparisons regarding the cloud base height are conducted, revealing an even better agreement between the BERTHA lidar measurements and the model results. Figure 22 shows the temporal evolution of the cloud base height derived from the REF case LES output and the cloud base height derived from BERTHA lidar measurements during 22 June 2013. The cloud base was detected from the lidar signal with an accuracy of ±50 m. The algorithm sets the cloud base if the 52.5 m vertically smoothed 532 nm total signal increases by a factor of 2 within 50 m. To get an overview of the day, the temporal resolution was set to 30 s. This procedure reproduces the temporal cloud evolution in Fig. 22. The spread gives an idea about the cloud thickness due to the fact that if a cloud overpasses the lidar beam, it is very likely that cloud water near the cloud top is detected at the beginning and/or at the end of the overpass. However, in some cases, it indicates some single clouds that start at an altitude of 1600 m. At noon, the cloud base gets higher and the clouds are generally thinner, which can be seen the in range of variation in the lidar data, which is very low at this period of time. Overall, there is less variability in the LES data due to the spatial averaging over the downwind region.

## 5 Conclusions

We have presented a numerical study for investigating island-induced effects on boundary layer structure, cloud generation and vertical mixing of aerosol layers at the easternmost Caribbean island of Barbados. The simulations were performed with the model ASAM on large eddy scale, where the horizontal resolution of $\Delta x = \Delta y = 200$ m is adequate to still resolve the lower wavenumber end of the inertial subrange of the turbulence spectrum.

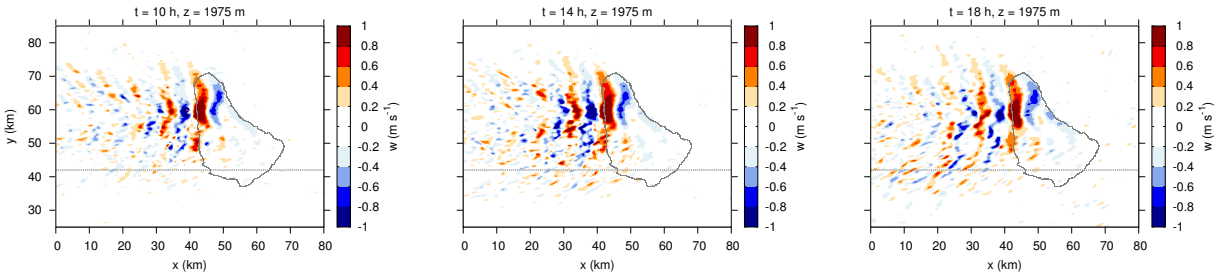


**Figure 19.** LES model output of vertical wind fields around the trade-wind inversion height at $z = 1975$ m at 10:00, 14:00 and 18:00 LT on 27 June 2013. The gray dashed line indicates the Falcon flight track (similar to cut plane 2 in Fig. 17).

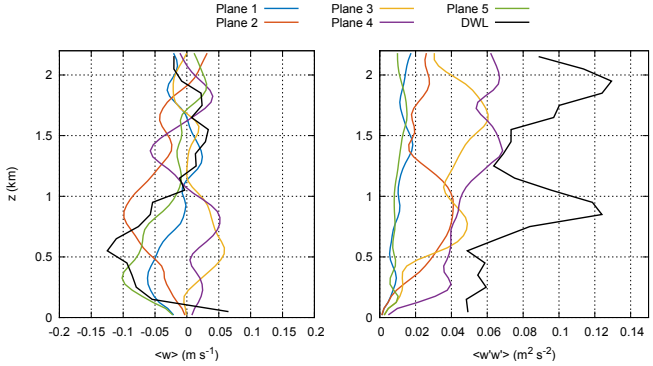


**Figure 20.** Comparison between the mean (left panel) and the variance (right panel) of the measured (black line) and simulated (colored lines) vertical wind fields at the lee side of Barbados at 10:30 LT. The wind profiles are horizontally averaged in the $x$ direction along the five different cut planes indicated in Fig. 17.

In order to generate inflow turbulence consistent with the upstream marine boundary layer forcing, the cell perturbation method based on finite amplitude perturbations was used. This method has been successfully adapted to moist boundary layer simulations with open lateral boundary conditions. Spectral analysis and examinations of vertical profiles of boundary layer quantities were used to determine the optimal Eckert number for the simulations. It was found that a value of $Ec = 0.4$ is most suitable for the island simulations, guaranteeing rapid development of turbulence that is very close to results from periodic BC simulations. This perturbation Eckert number differs from the optimum $Ec = 0.2$ derived for neutral stability (Muñoz-Esparza et al., 2015). These weaker-amplitude temperature perturbations appear to be due to a combination of the use of open boundary conditions and near production range grid resolution.

After the model was set up, several simulations were performed to analyze island effects. The atmospheric state is described by a horizontally homogeneous profile obtained via nighttime radiosonde launches. On the one hand, the used profile cannot be seen as a representative state, which could have been achieved by averaging multiple profiles. On the other hand, these quasi-idealized simulations enabled the possibility to compare the LES output data with DWL measurements. Large-scale forcings are not applied during the simulation time, i.e., a time-invariant background state is used, which makes it easier to analyze daytime changes in boundary layer and cloud characteristics as a result of convective island activity. The radiosonde profile from 22 June 2013 served as a reference case for a crucial sensitivity study, which revealed the following:

- Disadvantages of neglecting a turbulent inflow and modeling within the “terra incognita” or “gray zone” become apparent (Wyngaard, 2004). If the turbulent inflow generation is turned off, i.e., no marine boundary layer develops, cloud properties are drastically changed over and in the lee of the island. There, cloud cover, liquid water path and cloud base height have significantly higher values compared to the reference case. Also, the cloud morphology is different, having horizontally aligned cloud bands instead of scattered cumulus clouds.

- Using a generally coarser horizontal grid spacing of $\Delta x = \Delta y = 400$ m shows the same issues regarding cloud properties. Additionally, boundary layer turbulence is not well resolved but vertical energy transport is enhanced overall, which leads to the formation of a cloud street along the updraft band past Barbados. This has not been seen in the other cases and can thus be considered an artificial effect.

- For the two considered cases (22 and 27 June 2013), analysis of the daytime convective boundary layer shows generally similar vertical profiles for both, although slight differences were detected due to wind shear effects in particular. Also, for the case with the strong trade inversion, the boundary layer grew approximately 150 m deeper. Significant differences were again visible in cloud properties. In the latter case, the trade inversion inhibited cloud growth beyond 1800 m altitude, whereas local overshoots through the weaker inversion occurred in the 22 June case.

Vertical mixing of aerosols, in our case Saharan dust layers, has been qualitatively and quantitatively analyzed by in-

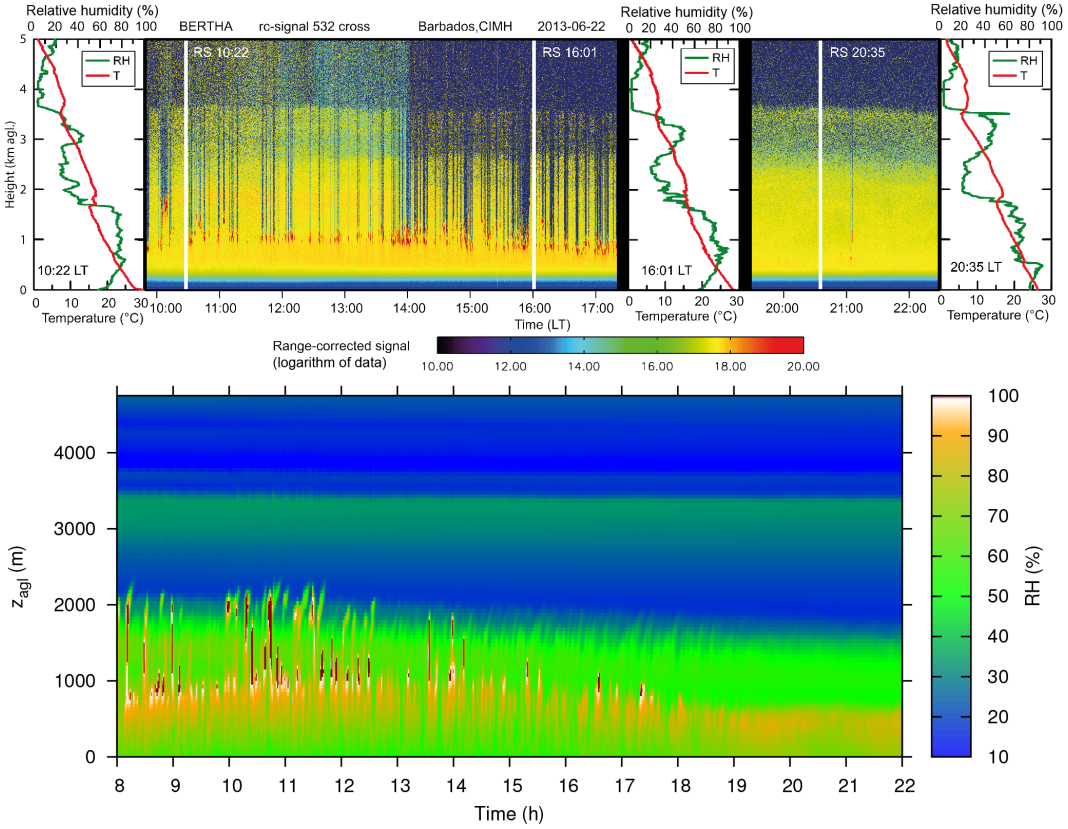


**Figure 21.** Top panel: BERTHA lidar measurements at CIMH and three radiosonde profiles of 22 June 2013. The range-corrected signal of the 532 nm cross-polarized channel is shown. The aerosol layer (in yellow) reaches up to 3.7 km. The signal peaks (in red) are liquid clouds through which the lidar beam cannot penetrate, resulting in the lack of signal above the cloud. At 14:04 LT the temporal resolution was changed from 15 s to 3 s. Bottom panel: LES model results of relative humidity at the CIMH grid point for the REF case, corresponding to 22 June 2013.

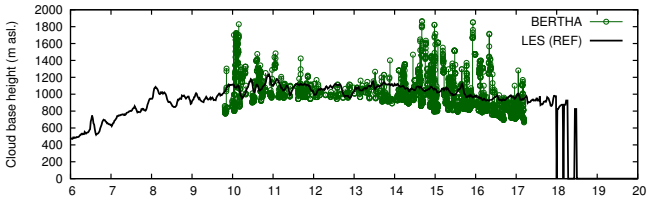


**Figure 22.** Temporal evolution of the spatially averaged cloud base height from the LES REF case (black line) and cloud base height derived from BERTHA lidar measurements (green circles) during 22 June 2013 at the west coast near the CIMH.

cluding passive tracers in the LES model. They are initialized at the same heights as they are seen in lidar data during the considered days. The model data suggested that a continuous subsidence velocity within these layers was present, which led to a mean sinking of 400 m toward the surface. Layers of turbulent downward mixing have also been detected between 1200 and 1700 m altitude. It can be concluded that if the dust layer reaches this height range, turbulent downward mixing of aerosol takes place, which is separated from large-scale subsidence effects. The exact position of these layers and the strength of downward turbulent mixing and transport are mainly controlled by atmospheric stability and wind shear. It became apparent that for the INV case the net direction of vertical transport is upwards for heights around the Saharan dust layer base. A larger number of simulation cases would provide further insight into this effect and the influence of trade inversion strength.

Qualitative comparisons with DWL measurements were carried out to validate the LES model results. A lot of similarities were found despite comparing different days, which, however, were very similar in terms of atmospheric stability, mean wind and temperature profile. First of all, large-scale changes in dynamics occur, which expectedly cannot be directly captured by the model. Furthermore, the vertical wind field shows a similar structure for both measurements and LES, highlighting the convective activity over the island and trapped gravity waves around the strong trade inversion. The amplitude of these waves was a bit higher in the measurements, which is also seen in the vertical wind variance profile. Taking these comparison results into account and con-

necting them to the boundary layer and tracer analysis, it is possible that turbulent (downward) mixing of aerosol layers could be even more enhanced than the LES model results suggest.

From the stationary Raman lidar BERTHA, which was deployed near the west coast of Barbados, cloud base heights and thickness were estimated and compared with the LES data. With these two techniques combined, a consistent picture of the diurnal convective activity and cloud generation over the island was gained for the most part.

Possible future model development could focus on the direct and indirect aerosol effect as well as shadowing effects. This would lead to a better understanding of the effects of dust particles in connection with low-level clouds on their radiative feedback, e.g., as shown in Ge et al. (2014).

Furthermore, finer horizontal grid spacings than 200 m would be desirable to either confirm the robustness of the obtained results or reveal additional effects of finer resolved turbulent structures. This would lead to a better simulation of stably stratified areas, e.g., at the trade inversion. Also, it can be expected that, with a higher effective model grid resolution, the computed velocity variances would be closer to the measurement results of the Doppler lidar system. However, this requires a great deal of computational effort, especially when performing sensitivity tests with a larger number of simulations.

As a general conclusion of this work, the simulations performed provided a detailed image of downwind boundary layer structure, cloud and vertical mixing processes, which agree well with lidar measurements. The model data can also help to better interpret the ground-based observations gained during the SALTRACE campaign at the Barbados west coast (CIMH field site).

## Appendix A: Numerical setup and model physics

ASAM numerically solves the fully compressible flux-form Euler equations:

$$\frac{\partial \rho}{\partial t} + \nabla \cdot (\rho \boldsymbol{v}) = 0\,, \tag{A1}$$

$$\frac{\partial (\rho \boldsymbol{v})}{\partial t} + \nabla \cdot (\rho \boldsymbol{v}\boldsymbol{v}) = - \nabla \cdot \boldsymbol{\tau} - \nabla p - \rho \boldsymbol{g} - 2\boldsymbol{\Omega} \times (\rho \boldsymbol{v})\,, \tag{A2}$$

$$\frac{\partial (\rho \phi)}{\partial t} + \nabla \cdot (\rho \boldsymbol{v} \phi) = -\nabla \cdot \boldsymbol{q}_\phi + S_\phi\,. \tag{A3}$$

Here, $\rho$ is the total air density, $\boldsymbol{v} = (u, v, w)^{\mathrm{T}}$ is the three-dimensional velocity vector, $p$ is the air pressure, $\boldsymbol{g}$ is the gravitational acceleration, $\boldsymbol{\Omega}$ is the angular velocity vector of the Earth, $\phi$ is a scalar quantity (representing energy and microphysical variables) and $S_\phi$ is the sum of its corresponding source terms. The subgrid scale (SGS) terms are $\boldsymbol{\tau}$ for momentum and $\boldsymbol{q}_\phi$ for a given scalar. The energy equation in the form of Eq. (A3) is represented by the density potential temperature $\theta_\rho$ (Emanuel, 1994):

$$\theta_\rho = \theta \left( 1 + q_\mathrm{v} \left[ \frac{R_\mathrm{v}}{R_\mathrm{d}} - 1 \right] - q_\mathrm{c} \right). \tag{A4}$$

Hence, the air pressure can be diagnosed via the equation of state

$$p = \rho R_\mathrm{d} \theta_\rho \left( \frac{p}{p_0} \right)^{\kappa_\mathrm{m}}, \tag{A5}$$

where $\theta = T(p_0/p)^{\kappa_\mathrm{m}}$ is the potential temperature, $q_\mathrm{v} = \rho_\mathrm{v}/\rho$ is the mass ratio of water vapor in the air (specific humidity), $q_\mathrm{c} = \rho_\mathrm{c}/\rho$ is the mass ratio of cloud water in the air, $p_0$ is a reference pressure and $\kappa_\mathrm{m} = (q_\mathrm{d} R_\mathrm{d} + q_\mathrm{v} R_\mathrm{v})/(q_\mathrm{d} c_\mathrm{pd} + q_\mathrm{v} c_\mathrm{pv} + [q_\mathrm{c} + q_\mathrm{r}] c_\mathrm{pl})$ is the Poisson constant for the air mixture (dry air, water vapor, cloud water, rain water) with $q_\mathrm{d} = \rho_\mathrm{d}/\rho$. $R_\mathrm{d}$ and $R_\mathrm{v}$ are the gas constants for dry air and water vapor, respectively. The Coriolis parameter $f = 2\omega \sin\varphi = 3.3 \times 10^{-5}\,\mathrm{s}^{-1}$ is calculated from a latitude value of $\varphi = 13.18°$, with $\omega$ being the angular velocity of the Earth.

To parameterize the SGS stress terms in Eqs. (A2) and (A3), a standard Smagorinsky model is used to represent the influence of the eddies smaller than the grid size into the resolved flow structures. The SGS stress terms are $\tau_{ij} = \overline{u_i u_j} - \overline{u}_i \overline{u}_j$ for momentum and $q_{ij} = \overline{u_i q_j} - \overline{u}_i \overline{q}_j$ for potential temperature. The effect of subgrid-scale motion on the resolved large scales $\tau_{ij}$ is represented by

$$\tau_{ij} = -2\nu_\mathrm{t} \overline{S}_{ij}\,, \tag{A6}$$

where $\overline{S}_{ij} = \frac{1}{2}\left( \frac{\partial \overline{u}_i}{\partial x_j} + \frac{\partial \overline{u}_j}{\partial x_i} \right)$ is the strain rate tensor and $\nu_\mathrm{t}$ the turbulent eddy viscosity. By taking stratification effects into account, the eddy viscosity is determined by

$$\nu_\mathrm{t} = (C_\mathrm{s} \overline{\Delta})^2 \max\left[ 0, \left( |\overline{\mathbf{S}}|^2 \left( 1 - \frac{Ri}{Pr} \right) \right) \right]^{1/2}, \tag{A7}$$

where $Ri$ is the Richardson number and $Pr$ is the turbulent Prandtl number (Lilly, 1962; Smagorinsky, 1963). The Richardson number is defined as

$$Ri = \frac{\frac{g}{\theta_\rho} \frac{\partial \theta_\rho}{\partial z}}{|\overline{\mathbf{S}}|^2}\,, \tag{A8}$$

where $\overline{\Delta}$ is a length scale based on the grid spacing and $C_\mathrm{s} = 0.2$ is the Smagorinsky coefficient as estimated by Lilly (1967), and using the Einstein summation notation for standardization:

$$|\overline{\mathbf{S}}| = \sqrt{2 \overline{S}_{ij} \overline{S}_{ij}}\,. \tag{A9}$$

By using the cut cell approach, tiny and/or anisotropic cells might occur in the vicinity of topographical structures. Thus, the length scale has to be a function of all local grid spacings in orthogonal direction and prescribed correction functions (cf. Scotti et al., 1993; Jähn et al., 2015).

The cloud microphysics parameterization is based on the two-moment scheme Seifert and Beheng (2006) with adjustments applied from Horn (2012) and without ice phase. In this scheme, mass and number density of the hydrometeor classes' cloud droplets and raindrops are represented. A total of seven microphysical processes are included: condensation/evaporation, CCN activation to cloud droplets at supersaturated conditions, autoconversion, self-collection of cloud droplets and raindrops, accretion and evaporation of rain. The aerosol activation process is prescribed by a power law function based on grid space supersaturation $s$:

$$N_\mathrm{CCN}(S) = N_\mathrm{CCN,1\,\%} s^\kappa, \tag{A10}$$

with the hygroscopicity parameter $\kappa = 0.462$. By having CCN number concentration measurements available for different supersaturations, an extrapolated value of the CCN number concentration at 1 % supersaturation can be determined. It is assumed that all CCN are activated at a critical supersaturation value of $s_\mathrm{max} = 1.1$ %.

*Acknowledgements.* The first author was internally funded by TROPOS. The authors thank Bernd Heinold and the two reviewers for their constructive comments. Satellite data were downloaded from NOAA's web archive (ftp://ftp.nnvl.noaa.gov/GOES/). The basemap was provided by the Earth Observatory Team – NASA (http://earthobservatory.nasa.gov). High-resolution topography data were provided by the CGIAR-CSI SRTM data set (http://srtm.csi.cgiar.org). Numerical simulations were performed at the HPC cluster of and at the Jülich Supercomputing Centre (JSC). We would also like to thank Thomas Bjerring Kristensen from TROPOS for provision of CCN data. The SALTRACE campaign was mainly funded by the Helmholtz Association, DLR, LMU and TROPOS.

Edited by: J. Schwarz

## References

Bryan, G. H., Wyngaard, J. C., and Fritsch, J. M.: Resolution requirements for the simulation of deep moist convection, Mon. Weather Rev., 131, 2394–2416, doi:10.1175/1520-0493(2003)131<2394:RRFTSO>2.0.CO;2, 2003.

Chouza, F., Reitebuch, O., Groß, S., Rahm, S., Freudenthaler, V., Toledano, C., and Weinzierl, B.: Retrieval of aerosol backscatter and extinction from airborne coherent Doppler wind lidar measurements, Atmos. Meas. Tech., 8, 2909–2926, doi:10.5194/amt-8-2909-2015, 2015.

DeSouza, R. L.: A study of atmospheric flow over a tropical island, PhD Thesis, Dep. of Meteorol., Florida State University, Tallahassee, 1972.

Doms, G., Förstner, J., Heise, E., Herzog, H.-J., Mironov, D., Raschendorfer, M., Reinhardt, T., Ritter, B., Schrodin, R., Schulz, J.-P., and Vogel, G.: A Description of the Nonhydrostatic Regional COSMO Model, Deutscher Wetterdienst, 2011.

Ellis, W. G. and Merrill, J. T.: Trajectories for Saharan dust transported to Barbados using Stoke's Law to describe gravitational settling, J. Appl. Meteorol., 34, 1716–1726, 1995.

Emanuel, K. A.: Atmospheric Convection, Oxford University Press, 1994.

Engelmann, R., Ansmann, A., Horn, S., Seifert, P., Althausen, D., Tesche, M., Esselborn, M., Fruntke, J., Lieke, K., Freudenthaler, V., and Gross, S.: Doppler lidar studies of heat island effects on vertical mixing of aerosols during SAMUM-2, Tellus, 63B, 448–458, 2011.

Esteban, M. A. and Chen, Y.-L.: The impact of trade wind strength on precipitation over the windward side of the island of Hawaii, Mon. Weather Rev., 136, 913–928, 2008.

Etling, D. and Brown, R.: Roll vortices in the planetary boundary layer: a review, Bound.-Lay. Meteorol., 65, 215–248, doi:10.1007/BF00705527, 1993.

Fu, Q. and Liou, K. N.: Parameterization of the radiative properties of cirrus clouds, J. Atmos. Sci., 50, 2008–2025, doi:10.1175/1520-0469(1993)050<2008:POTRPO>2.0.CO;2, 1993.

Garstang, M., Tyson, P. D., and Emmitt, G. D.: The structure of heat islands, Rev. Geophys. Space Ge., 13, 139–165, 1975.

Ge, C., Wang, J., and Reid, J. S.: Mesoscale modeling of smoke transport over the Southeast Asian Maritime Continent: coupling of smoke direct radiative effect below and above the low-level clouds, Atmos. Chem. Phys., 14, 159–174, doi:10.5194/acp-14-159-2014, 2014.

Groß, S., Freudenthaler, V., Schepanski, K., Toledano, C., Schäfler, A., Ansmann, A., and Weinzierl, B.: Optical properties of long-range transported Saharan dust over Barbados as measured by dual-wavelength depolarization Raman lidar measurements, Atmos. Chem. Phys., 15, 11067–11080, doi:10.5194/acp-15-11067-2015, 2015.

Horn, S.: ASAMgpu V1.0 – a moist fully compressible atmospheric model using graphics processing units (GPUs), Geosci. Model Dev., 5, 345–353, doi:10.5194/gmd-5-345-2012, 2012.

Jähn, M., Knoth, O., König, M., and Vogelsberg, U.: ASAM v2.7: a compressible atmospheric model with a Cartesian cut cell approach, Geosci. Model Dev., 8, 317–340, doi:10.5194/gmd-8-317-2015, 2015.

Kirshbaum, D. J. and Fairman, J. G.: Cloud trails past the Lesser Antilles, Mon. Weather Rev., 143, 995–1017, doi:10.1175/MWR-D-14-00254.1, 2015.

Kirshbaum, D. J. and Grant, A. L. M.: Invigoration of cumulus cloud fields by mesoscale ascent, Q. J. Roy. Meteor. Soc., 138, 2136–2150, doi:10.1002/qj.1954, 2012.

Kirshbaum, D. J. and Wang, C.-C.: Boundary layer updrafts driven by airflow over heated terrain, J. Atmos. Sci., 71, 1425–1442, doi:10.1175/JAS-D-13-0287.1, 2014.

Lilly, D. K.: On the numerical simulation of buoyant convection, Tellus, 14, 148–172, doi:10.1111/j.2153-3490.1962.tb00128.x, 1962.

Lilly, D. K.: The representation of small scale turbulence in numerical simulation experiments, IBM Scientific Computing Symposium on Environmental Sciences, 195–210, 1967.

Mahrer, Y. and Pielke, R. A.: Numierical simulation of the airflow over Barbados, Mon. Weather Rev., 104, 1392–1402, 1976.

Minda, H., Furuzawa, F. A., Satoh, S., and Nakamura, K.: Convective boundary layer above a subtropical island observed by C-band radar and interpretation using a cloud resolving model, J. Meteorol. Soc. Jpn., 88, 285–312, 2010.

Minder, J. R., Smith, R. B., and Nugent, A. D.: The dynamics of ascent-forced orographic convection in the tropics: results from Dominica, J. Atmos. Sci., 70, 4067–4088, 2013.

Monin, A. S. and Obukhov, A. M.: Basic turbulence mixing laws in the atmospheric surface layer, Tr. Inst. Teor. Geofiz. Akad. SSSR, 24, 163–187, 1954.

Muñoz-Esparza, D., Kosović, B., Mirocha, J., and van Beeck, J.: Bridging the transition from mesoscale to microscale turbulence in numerical weather prediction models, Bound.-Lay. Meteorol., 153, 409–440, doi:10.1007/s10546-014-9956-9, 2014.

Muñoz-Esparza, D., Kosović, B., van Beeck, J., and Mirocha, J.: A stochastic perturbation method to generate inflow turbulence in large-eddy simulation models: application to neutrally stratified atmospheric boundary layers, Phys. Fluids, 27, 035102, doi:10.1063/1.4913572, 2015.

Prospero, J. and Carlson, T.: Radon-222 in the North Atlantic trade winds: Its relationship to dust transport from Africa, Science, 167, 974–977, 1970.

Prospero, J., Bonatti, E., Schubert, C., and Carlson, T.: Dust in the Caribbean atmosphere traced to an African dust storm, Earth Plan. Sci. Lett., 9, 287–293, 1970.

Reitebuch, O.: Wind lidar for atmospheric research, in: Atmospheric Physics – Background, Methods, Trends, Springer Series on Research Topics in Aerospace, Springer, Berlin/Heidelberg, 487–507, 2012.

Savijärvi, H. and Matthews, S.: Flow over Small Heat Islands: a numerical sensitivity study, J. Atmos. Sci., 61, 859–868, 2004.

Scotti, A., Meneveau, C., and Lilly, D. K.: Generalized Smagorinsky model for anisotropic grids, Phys. Fluids A, 5, 2306–2308, 1993.

Seifert, A. and Beheng, K. D.: A two-moment cloud microphysics parameterization for mixed-phase clouds, Meteorol. Atmos. Phys., 92, 45–66, 2006.

Siebert, H., Beals, M., Bethke, J., Bierwirth, E., Conrath, T., Dieckmann, K., Ditas, F., Ehrlich, A., Farrell, D., Hartmann, S., Izaguirre, M. A., Katzwinkel, J., Nuijens, L., Roberts, G., Schäfer, M., Shaw, R. A., Schmeissner, T., Serikov, I., Stevens, B., Stratmann, F., Wehner, B., Wendisch, M., Werner, F., and Wex, H.: The fine-scale structure of the trade wind cumuli over Barbados – an introduction to the CARRIBA project, Atmos. Chem. Phys., 13, 10061–10077, doi:10.5194/acp-13-10061-2013, 2013.

Siebesma, A. P., Bretherton, C. S., Brown, A., Chlond, A., Cuxart, J., Duynkerke, P. G., Jiang, H., Khairoutdinov, M., Lewellen, D., Moeng, C.-H., Sanchez, E., Stevens, B., and Stevens, D. E.: A large eddy simulation intercomparison study of shallow cumulus convection, J. Atmos. Sci., 60, 1201–1219, doi:10.1175/1520-0469(2003)60<1201:ALESIS>2.0.CO;2, 2003.

Smagorinsky, J.: General circulation experiments with the primitive equations, Mon. Weather Rev., 164, 91–99, 1963.

Smith, R. B., Gleason, A. C., and Gluhosky, P. A.: The Wake of St. Vincent, J. Atmos. Sci., 54, 606–623, 1997.

Smith, R. B., Schafer, P., Kirshbaum, D. J., and Regina, E.: Orographic precipitation in the tropics: experiments in Dominica, J. Atmos. Sci., 66, 1698–1716, 2009.

Tesche, M., Groß, S., Ansmann, A., Müller, D., Althausen, D., Freudenthaler, V and Esselborn, M: Profiling of Saharan dust and biomass burning smoke with multiwavelength polarization Raman lidar at Cape Verde, Tellus, 63B, 649–676, 2011.

Wyngaard, J. C.: Toward numerical modeling in the "Terra Incognita", J. Atmos. Sci., 61, 1816–1826, doi:10.1175/1520-0469(2004)061<1816:TNMITT>2.0.CO;2, 2004.

# Appendix C

# Acronyms

**AEJ** African Easterly Jet

**AeroCom** Aerosol Comparison between Observations and Models

**AERONET** Aerosol Robotic Network

**AEW** African easterly wave

**AMMA** African Monsoon Multidisciplinary Analyses

**AOD** atmospheric optical depth

**AR5** fifth Intergovernmental Panel on Climate Change (IPCC) assesment report

**ASAM** All-Scale Atmospheric Model

**BERTHA** backscatter extinction lidar-ratio temperature humidity profiling apparatus

**BOMEX** Barbados Oceanographic and Meteorological Experiment

**CALIOP** Cloud-Aerosol Lidar with Orthogonal Polarization

**CALIPSO** Cloud-Aerosol Lidar and Infrared Pathfinder Satellite Observations

**CCN** cloud condensation nuclei

**CFD** computational fluid dynamics

**CIMH** Caribbean Institute of Meteorology and Hydrology

**CPC** condensation particle counter

**CW** continuous-wave

**DLR** Deutsches Zentrum für Luft- und Raumfahrt

**DNS** Direct Numerical Simulation

**DOD** dust optical depth

**DWL** Doppler wind lidar

**ECMWF** European Centre for Medium-Range Weather Forecasts

**ERF** effective radiative forcing

**GATE** Global Atmospheric Research Program Atlantic Tropical Experiment

**GMES** Global Monitoring for Environment and Security

**GPU** Graphical Processing Unit

**IPCC** Intergovernmental Panel on Climate Change

**ITCZ** Intertropical Convergence Zone

**LES** Large Eddy Simulations

**LITE** Lidar In-space Technology Experiment

**MACC** Monitoring Atmospheric Composition and Climate

**MODIS** Moderate Resolution Imaging Spectroradiometer

**POLIS** Portable Lidar System

**SAL** Saharan Air Layer

**SALTRACE** Saharan Aerosol Long-range Transport and Aerosol-Cloud-Interaction Experiment

**SAMUM-1** first Saharan Mineral Dust Experiment

**SAMUM-2** second Saharan Mineral Dust Experiment

**TROPOS** Leibniz Institute for Tropospheric Research

**WIND** Wind Infrared Doppler Lidar

# Bibliography


Ansmann, A., Petzold, A., Kandler, K., Tegen, I., Wendisch, M., Müller, D., Weinzierl, B., Müller, T., and Heintzenberg, J.: Saharan Mineral Dust Experiments SAMUM-1 and SAMUM-2: what have we learned?, Tellus B, 63, 403–429, URL http://www.tellusb.net/index.php/tellusb/article/view/16236, 2011.

Baker, A. R., Kelly, S. D., Biswas, K. F., Witt, M., and Jickells, T. D.: Atmospheric deposition of nutrients to the Atlantic Ocean, Geophysical Research Letters, 30, doi:10.1029/2003GL018518, URL http://dx.doi.org/10.1029/2003GL018518, 2296, 2003.

Benedetti, A., Morcrette, J.-J., Boucher, O., Dethof, A., Engelen, R. J., Fisher, M., Flentje, H., Huneeus, N., Jones, L., Kaiser, J. W., Kinne, S., Mangold, A., Razinger, M., Simmons, A. J., and Suttie, M.: Aerosol analysis and forecast in the European Centre for Medium-Range Weather Forecasts Integrated Forecast System: 2. Data assimilation, Journal of Geophysical Research: Atmospheres, 114, doi:10.1029/2008JD011115, URL http://dx.doi.org/10.1029/2008JD011115, d13205, 2009.

Benedetti-Michelangeli, G., Congeduti, F., and Fiocco, G.: Measurement of Aerosol Motion and Wind Velocity in the Lower Troposphere by Doppler Optical Radar, Journal of the Atmospheric Sciences, 29, 906–910, doi:10.1175/1520-0469(1972)029⟨0906:MOAMAW⟩2.0.CO;2, 1972.

Burpee, R. W.: The Origin and Structure of Easterly Waves in the Lower Troposphere of North Africa, Journal of the Atmospheric Sciences, 29, 77–90, doi:10.1175/1520-0469(1972)029⟨0077:TOASOE⟩2.0.CO;2, URL http://dx.doi.org/10.1175/1520-0469(1972)029<0077:TOASOE>2.0.CO;2, 1972.

Carlson, T. N. and Caverly, R. S.: Radiative characteristics of Saharan dust at solar wavelengths, Journal of Geophysical Research, 82, 3141–3152, doi:10.1029/JC082i021p03141, URL http://dx.doi.org/10.1029/JC082i021p03141, 1977.

Carlson, T. N. and Prospero, J. M.: The Large-Scale Movement of Saharan Air Outbreaks over the Northern Equatorial Atlantic, Journal of Applied Meteorology, 11, 283–297, doi:10.1175/1520-0450(1972)011⟨0283:TLSMOS⟩2.0.CO;2, URL http://dx.doi.org/10.1175/1520-0450(1972)011<0283:TLSMOS>2.0.CO;2, 1972.

Chane Ming, F., Vignelles, D., Jegou, F., Berthet, G., Renard, J.-B., Gheusi, F., and Kuleshov, Y.: Gravity-wave effects on tracer gases and stratospheric aerosol concentrations during the 2013 ChArMEx campaign, Atmospheric Chemistry and Physics, 16, 8023–8042, doi:10.5194/acp-16-8023-2016, URL http://www.atmos-chem-phys.net/16/8023/2016/, 2016.

Chouza, F., Reitebuch, O., Groß, S., Rahm, S., Freudenthaler, V., Toledano, C., and Weinzierl, B.: Retrieval of aerosol backscatter and extinction from airborne coherent Doppler wind lidar measurements, Atmospheric Measurement Techniques, 8, 2909–2926, doi:10.5194/amt-8-2909-2015, URL http://www.atmos-meas-tech.net/8/2909/2015/, 2015.

Chouza, F., Reitebuch, O., Jähn, M., Rahm, S., and Weinzierl, B.: Vertical wind retrieved by airborne lidar and analysis of island induced gravity waves in combination with numerical models and in situ particle measurements, Atmospheric Chemistry and Physics, 16, 4675–4692, doi:10.5194/acp-16-4675-2016, URL http://www.atmos-chem-phys.net/16/4675/2016/, 2016a.

Chouza, F., Reitebuch, O., Benedetti, A., and Weinzierl, B.: Saharan dust long-range transport across the Atlantic studied by an airborne Doppler lidar and the MACC model, Atmospheric Chemistry and Physics, 16, 11 581–11 600, doi:10.5194/acp-16-11581-2016, URL http://www.atmos-chem-phys.net/16/11581/2016/, 2016b.

Cook, K. H.: Generation of the African Easterly Jet and Its Role in Determining West African Precipitation, Journal of Climate, 12, 1165–1184, doi:10.1175/1520-0442(1999)012⟨1165:GOTAEJ⟩2.0.CO;2, URL http://dx.doi.org/10.1175/1520-0442(1999)012<1165:GOTAEJ>2.0.CO;2, 1999.

Cuevas, E., Camino, C., Benedetti, A., Basart, S., Terradellas, E., Baldasano, J. M., Morcrette, J. J., Marticorena, B., Goloub, P., Mortier, A., Berjón, A., Hernández, Y., Gil-Ojeda, M., and Schulz, M.: The MACC-II 2007-2008 reanalysis: atmospheric dust evaluation and characterization over northern Africa and the Middle East, Atmospheric Chemistry and Physics, 15, 3991–4024, doi:10.5194/acp-15-3991-2015, URL http://www.atmos-chem-phys.net/15/3991/2015/, 2015.

Darwin, C. R.: An account of the fine dust which often falls on vessels in the Atlantic ocean, Quarterly Journal of the Geological Society of London, 2, 26 – 30, 1846.

Delany, A., Delany, A. C., Parkin, D., Griffin, J., Goldberg, E., and Reimann, B.: Airborne dust collected at Barbados, Geochimica et Cosmochimica Acta, 31, 885 – 909, doi:http://dx.doi.org/10.1016/S0016-7037(67)80037-1, URL http://www.sciencedirect.com/science/article/pii/S0016703767800371, 1967.

Denjean, C., Cassola, F., Mazzino, A., Triquet, S., Chevaillier, S., Grand, N., Bourrianne, T., Momboisse, G., Sellegri, K., Schwarzenbock, A., Freney, E., Mallet, M., and Formenti, P.: Size distribution and optical properties of mineral dust aerosols transported

in the western Mediterranean, Atmospheric Chemistry and Physics, 16, 1081–1104, doi:10.5194/acp-16-1081-2016, URL http://www.atmos-chem-phys.net/16/1081/2016/, 2016.

Engelmann, R., Ansmann, A., Horn, S., Seifert, P., Althausen, D., Tesche, M., Esselborn, M., Fruntke, J., Lieke, K., Freudenthaler, V., and Groß, S.: Doppler lidar studies of heat island effects on vertical mixing of aerosols during SAMUM-2, Tellus B, 63, URL http://www.tellusb.net/index.php/tellusb/article/view/16239, 2011.

Evan, A. T., Dunion, J., Foley, J. A., Heidinger, A. K., and Velden, C. S.: New evidence for a relationship between Atlantic tropical cyclone activity and African dust outbreaks, Geophysical Research Letters, 33, doi:10.1029/2006GL026408, URL http://dx.doi.org/10.1029/2006GL026408, l19813, 2006.

Fiocco, G. and Smullin, L. D.: Detection of Scattering Layers in the Upper Atmosphere (60-140 km) by Optical Radar, Nature, 199, 1275–1276, doi:10.1038/1991275a0, 1963.

Freudenthaler, V., Seefeldner, M., Groß, S., and Wandinger, U.: Accuracy of linear depolarisation ratios in clean air ranges measured with POLIS-6 at 355 and 532 nm, in: Proceedings of the 27th Interntaional Laser Radar Conference, New York City, 2015.

Gasteiger, J., Groß, S., Weinzierl, B., Sauer, D., and Freudenthaler, V.: Particle settling and convective mixing in the Saharan Air Layer as seen from an integrated model, lidar, and in-situ perspective, Atmospheric Chemistry and Physics Discussions, 2016, 1–23, doi:10.5194/acp-2016-480, URL http://www.atmos-chem-phys-discuss.net/acp-2016-480/, 2016.

Griffin, D. W.: Atmospheric Movement of Microorganisms in Clouds of Desert Dust and Implications for Human Health, Clinical Microbiology Reviews, 20, 459–77, doi:10.1128/CMR.00039-06, URL http://dx.doi.org/10.1128/CMR.00039-06, 2007.

Groß, S., Freudenthaler, V., Schepanski, K., Toledano, C., Schäfler, A., Ansmann, A., and Weinzierl, B.: Optical properties of long-range transported Saharan dust over Barbados as measured by dual-wavelength depolarization Raman lidar measurements, Atmospheric Chemistry and Physics, 15, 11 067–11 080, doi:10.5194/acp-15-11067-2015, URL http://www.atmos-chem-phys.net/15/11067/2015/, 2015.

Haarig, M., Althausen, D., Ansmann, A., Klepel, A., Baars, H., Engelmann, R., Groß, S., and Freudenthaler, V.: Measurement of the linear depolarization ratio of aged dust at three wavelengths (355, 532 and 1064 nm) simultaneously over Barbados, in: Proceedings of the 27th Interntaional Laser Radar Conference, S8b.04, New York City, 2015.

Heintzenberg, J.: The SAMUM-1 experiment over Southern Morocco: overview and introduction, Tellus B, 61, 2–11, doi:10.1111/j.1600-0889.2008.00403.x, URL http://dx.doi.org/10.1111/j.1600-0889.2008.00403.x, 2009.

Hendricks, J., Righi, M., and Aquila, V.: Atmospheric Physics, chap. Global Atmospheric Aerosol Modeling, pp. 561–576, Springer, Berlin Heidelberg, 2012.

Hosseinpour, F. and Wilcox, E. M.: Aerosol interactions with African/Atlantic climate dynamics, Environmental Research Letters, 9, 075 004, URL http://stacks.iop.org/1748-9326/9/i=7/a=075004, 2014.

Huffaker, R. M.: Laser Doppler Detection Systems for Gas Velocity Measurement, Appl. Opt., 9, 1026–1039, doi:10.1364/AO.9.001026, URL http://ao.osa.org/abstract.cfm?URI=ao-9-5-1026, 1970.

Huneeus, N., Schulz, M., Balkanski, Y., Griesfeller, J., Prospero, J., Kinne, S., Bauer, S., Boucher, O., Chin, M., Dentener, F., Diehl, T., Easter, R., Fillmore, D., Ghan, S., Ginoux, P., Grini, A., Horowitz, L., Koch, D., Krol, M. C., Landing, W., Liu, X., Mahowald, N., Miller, R., Morcrette, J.-J., Myhre, G., Penner, J., Perlwitz, J., Stier, P., Takemura, T., and Zender, C. S.: Global dust model intercomparison in AeroCom phase I, Atmospheric Chemistry and Physics, 11, 7781–7816, doi:10.5194/acp-11-7781-2011, URL http://www.atmos-chem-phys.net/11/7781/2011/, 2011.

Huneeus, N., Basart, S., Fiedler, S., Morcrette, J.-J., Benedetti, A., Mulcahy, J., Terradellas, E., Pérez García-Pando, C., Pejanovic, G., Nickovic, S., Arsenovic, P., Schulz, M., Cuevas, E., Baldasano, J. M., Pey, J., Remy, S., and Cvetkovic, B.: Forecasting the northern African dust outbreak towards Europe in April 2011: a model intercomparison, Atmospheric Chemistry and Physics, 16, 4967–4986, doi:10.5194/acp-16-4967-2016, URL http://www.atmos-chem-phys.net/16/4967/2016/, 2016.

IPCC: Climate Change 2013: The Physical Science Basis. Contribution of Working Group I to the Fifth Assessment Report of the Intergovernmental Panel on Climate Change, Cambridge University Press, Cambridge, United Kingdom and New York, NY, USA, doi:10.1017/CBO9781107415324, URL www.climatechange2013.org, 2013.

Jähn, M., Knoth, O., König, M., and Vogelsberg, U.: ASAM v2.7: a compressible atmospheric model with a Cartesian cut cell approach, Geoscientific Model Development, 8, 317–340, doi:10.5194/gmd-8-317-2015, URL http://www.geosci-model-dev.net/8/317/2015/, 2015.

Jähn, M., Muñoz Esparza, D., Chouza, F., Reitebuch, O., Knoth, O., Haarig, M., and Ansmann, A.: Investigations of boundary layer structure, cloud characteristics and vertical mixing of aerosols at Barbados with large eddy simulations, Atmospheric Chemistry and Physics, 16, 651–674, doi:10.5194/acp-16-651-2016, URL http://www.atmos-chem-phys.net/16/651/2016/, 2016.

Janiga, M. A. and Thorncroft, C. D.: The Influence of African Easterly Waves on Convection over Tropical Africa and the East Atlantic, Monthly Weather Review, 144, 171–192, doi:10.1175/MWR-D-14-00419.1, 2016.

Jickells, T. D., An, Z. S., Andersen, K. K., Baker, A. R., Bergametti, G., Brooks, N., Cao, J. J., Boyd, P. W., Duce, R. A., Hunter, K. A., Kawahata, H., Kubilay, N., laRoche, J., Liss, P. S., Mahowald, N., Prospero, J. M., Ridgwell, A. J., Tegen, I., and Torres, R.: Global Iron Connections Between Desert Dust, Ocean Biogeochemistry, and Climate, Science, 308, 67–71, doi:10.1126/science.1105959, URL http://science.sciencemag.org/content/308/5718/67, 2005.

Jones, C., Mahowald, N., and Luo, C.: The Role of Easterly Waves on African Desert Dust Transport, Journal of Climate, 16, 3617–3628, doi:10.1175/1520-0442(2003)016⟨3617:TROEWO⟩2.0.CO;2, 2003.

Jones, C., Mahowald, N., and Luo, C.: Observational evidence of African desert dust intensification of easterly waves, Geophysical Research Letters, 31, doi:10.1029/2004GL020107, URL http://dx.doi.org/10.1029/2004GL020107, l17208, 2004.

Junge, C. E.: Recent Investigations in Air Chemistry, Tellus, 8, 127–139, doi:10.1111/j.2153-3490.1956.tb01205.x, URL http://dx.doi.org/10.1111/j.2153-3490.1956.tb01205.x, 1956.

Jury, M. R. and Santiago, M. J.: Composite analysis of dust impacts on African easterly waves in the Moderate Resolution Imaging Spectrometer era, Journal of Geophysical Research: Atmospheres, 115, doi:10.1029/2009JD013612, URL http://dx.doi.org/10.1029/2009JD013612, d16213, 2010.

Kanitz, T., Engelmann, R., Heinold, B., Baars, H., Skupin, A., and Ansmann, A.: Tracking the Saharan Air Layer with shipborne lidar across the tropical Atlantic, Geophysical Research Letters, 41, 1044–1050, doi:10.1002/2013GL058780, URL http://dx.doi.org/10.1002/2013GL058780, 2014.

Karyampudi, V. M.: A detailed synoptic-scale study of the structure, dynamics, and radiative effects of the Saharan air layer over the eastern tropical Atlantic during GARP Atlantic Tropical Experiment, Master's thesis, The Pennsylvania State University, 1979.

Karyampudi, V. M. and Carlson, T. N.: Analysis and Numerical Simulations of the Saharan Air Layer and Its Effect on Easterly Wave Disturbances, Journal of the Atmospheric Sciences, 45, 3102–3136, doi:10.1175/1520-0469(1988)045⟨3102:AANSOT⟩2.0.CO;2, URL http://dx.doi.org/10.1175/1520-0469(1988)045<3102:AANSOT>2.0.CO;2, 1988.

Karyampudi, V. M., Palm, S. P., Reagen, J. A., Fang, H., Grant, W. B., Hoff, R. M., Moulin, C., Pierce, H. F., Torres, O., Browell, E. V., and Melfi, S. H.: Validation of the Saharan Dust Plume Conceptual Model Using Lidar, Meteosat, and ECMWF Data, Bulletin of the American Meteorological Society, 80, 1045–1075, doi:10.1175/1520-0477(1999)080⟨1045:VOTSDP⟩2.0.CO;2, URL http://dx.doi.org/10.1175/1520-0477(1999)080<1045:VOTSDP>2.0.CO;2, 1999.

Kim, D., Chin, M., Yu, H., Diehl, T., Tan, Q., Kahn, R. A., Tsigaridis, K., Bauer, S. E., Takemura, T., Pozzoli, L., Bellouin, N., Schulz, M., Peyridieu, S., Chdin, A., and Koffi, B.: Sources, sinks, and transatlantic transport of North African dust aerosol: A multimodel analysis and comparison with remote sensing data, Journal of Geophysical Research: Atmospheres, 119, 6259–6277, doi:10.1002/2013JD021099, URL http://dx.doi.org/10.1002/2013JD021099, 2013JD021099, 2014.

Knippertz, P. and Stuut, J.-B. W.: Mineral Dust: A Key Player in the Earth System, chap. Introduction, pp. 1–14, Springer Netherlands, Dordrecht, doi:10.1007/978-94-017-8978-3_1, URL http://dx.doi.org/10.1007/978-94-017-8978-3_1, 2014.

Knippertz, P. and Todd, M. C.: The central west Saharan dust hot spot and its relation to African easterly waves and extratropical disturbances, Journal of Geophysical Research: Atmospheres, 115, doi:10.1029/2009JD012819, URL http://dx.doi.org/10.1029/2009JD012819, d12117, 2010.

Köpp, F., Schwiesow, R. L., and Werner, C.: Remote Measurements of Boundary-Layer Wind Profiles Using a CW Doppler Lidar, Journal of Climate and Applied Meteorology, 23, 148–154, doi:10.1175/1520-0450(1984)023⟨0148:RMOBLW⟩2.0.CO;2, 1984.

Köpp, F., Rahm, S., and Smalikho, I.: Characterization of Aircraft Wake Vortices by 2-m Pulsed Doppler Lidar, Journal of Atmospheric and Oceanic Technology, 21, 194–206, doi:10.1175/1520-0426(2004)021⟨0194:COAWVB⟩2.0.CO;2, URL http://dx.doi.org/10.1175/1520-0426(2004)021<0194:COAWVB>2.0.CO;2, 2004.

Kulmala, M., Asmi, A., Lappalainen, H. K., Baltensperger, U., Brenguier, J.-L., Facchini, M. C., Hansson, H.-C., Hov, Ø., O'Dowd, C. D., Pöschl, U., Wiedensohler, A., Boers, R., Boucher, O., de Leeuw, G., Denier van der Gon, H. A. C., Feichter, J., Krejci, R., Laj, P., Lihavainen, H., Lohmann, U., McFiggans, G., Mentel, T., Pilinis, C., Riipinen, I., Schulz, M., Stohl, A., Swietlicki, E., Vignati, E., Alves, C., Amann, M., Ammann, M., Arabas, S., Artaxo, P., Baars, H., Beddows, D. C. S., Bergström, R., Beukes, J. P., Bilde, M., Burkhart, J. F., Canonaco, F., Clegg, S. L., Coe, H., Crumeyrolle, S., D'Anna, B., Decesari, S., Gilardoni, S., Fischer, M., Fjaeraa, A. M., Fountoukis, C., George, C., Gomes, L., Halloran, P., Hamburger, T., Harrison, R. M., Herrmann, H., Hoffmann, T., Hoose, C., Hu, M., Hyvärinen, A., Hõrrak, U., Iinuma, Y., Iversen, T., Josipovic, M., Kanakidou, M., Kiendler-Scharr, A., Kirkevåg, A., Kiss, G., Klimont, Z., Kolmonen, P., Komppula, M., Kristjánsson, J.-E., Laakso, L., Laaksonen, A., Labonnote, L., Lanz, V. A., Lehtinen, K. E. J., Rizzo, L. V., Makkonen, R., Manninen, H. E., McMeeking, G., Merikanto, J., Minikin, A., Mirme, S., Morgan, W. T., Nemitz, E., O'Donnell, D., Panwar, T. S., Pawlowska, H., Petzold, A., Pienaar, J. J., Pio, C., Plass-Duelmer, C., Prévôt, A. S. H., Pryor, S., Reddington, C. L., Roberts, G., Rosenfeld, D., Schwarz, J., Seland, Ø., Sellegri, K., Shen, X. J., Shiraiwa, M., Siebert, H., Sierau, B., Simpson, D., Sun, J. Y., Topping, D., Tunved, P.,

Vaattovaara, P., Vakkari, V., Veefkind, J. P., Visschedijk, A., Vuollekoski, H., Vuolo, R., Wehner, B., Wildt, J., Woodward, S., Worsnop, D. R., van Zadelhoff, G.-J., Zardini, A. A., Zhang, K., van Zyl, P. G., Kerminen, V.-M., S Carslaw, K., and Pandis, S. N.: General overview: European Integrated project on Aerosol Cloud Climate and Air Quality interactions (EUCAARI) - integrating aerosol research from nano to global scales, Atmospheric Chemistry and Physics, 11, 13 061–13 143, doi:10.5194/acp-11-13061-2011, URL http://www.atmos-chem-phys.net/11/13061/2011/, 2011.

Lau, K. M. and Kim, K. M.: Cooling of the Atlantic by Saharan dust, Geophysical Research Letters, 34, doi:10.1029/2007GL031538, URL http://dx.doi.org/10.1029/2007GL031538, l23811, 2007.

Longueville, F., Ozer, P., Doumbia, S., and Henry, S.: Desert dust impacts on human health: an alarming worldwide reality and a need for studies in West Africa, International Journal of Biometeorology, 57, 1–19, doi:10.1007/s00484-012-0541-y, URL http://dx.doi.org/10.1007/s00484-012-0541-y, 2012.

MACC-III: Final report, Tech. rep., MACC-III consortium, URL https://atmosphere.copernicus.eu/sites/default/files/repository/MACCIII_FinalReport.pdf, 2016.

Mahowald, N. M., Zender, C. S., Luo, C., Savoie, D., Torres, O., and del Corral, J.: Understanding the 30-year Barbados desert dust record, Journal of Geophysical Research: Atmospheres, 107, AAC 7–1–AAC 7–16, doi:10.1029/2002JD002097, URL http://dx.doi.org/10.1029/2002JD002097, 4561, 2002.

Mahowald, N. M., Rivera, G. D. R., and Luo, C.: Comment on "Relative importance of climate and land use in determining present and future global soil dust emission" by I. Tegen et al., Geophysical Research Letters, 31, doi:10.1029/2004GL021272, URL http://dx.doi.org/10.1029/2004GL021272, l24105, 2004.

Mahowald, N. M., Baker, A. R., Bergametti, G., Brooks, N., Duce, R. A., Jickells, T. D., Kubilay, N., Prospero, J. M., and Tegen, I.: Atmospheric global dust cycle and iron inputs to the ocean, Global Biogeochemical Cycles, 19, doi:10.1029/2004GB002402, URL http://dx.doi.org/10.1029/2004GB002402, gB4025, 2005.

Mangold, A., De Backer, H., De Paepe, B., Dewitte, S., Chiapello, I., Derimian, Y., Kacenelenbogen, M., Lon, J.-F., Huneeus, N., Schulz, M., Ceburnis, D., O'Dowd, C., Flentje, H., Kinne, S., Benedetti, A., Morcrette, J.-J., and Boucher, O.: Aerosol analysis and forecast in the European Centre for Medium-Range Weather Forecasts Integrated Forecast System: 3. Evaluation by means of case studies, Journal of Geophysical Research: Atmospheres, 116, doi:10.1029/2010JD014864, URL http://dx.doi.org/10.1029/2010JD014864, d03302, 2011.

Maring, H., Savoie, D. L., Izaguirre, M. A., Custals, L., and Reid, J. S.: Mineral dust aerosol size distribution change during atmospheric transport, Journal of Geophysical

Research: Atmospheres, 108, doi:10.1029/2002JD002536, URL http://dx.doi.org/10.1029/2002JD002536, 8592, 2003.

Mayor, S. D., Dérian, P., Mauzey, C. F., Spuler, S. M., Ponsardin, P., Pruitt, J., Ramsey, D., and Higdon, N. S.: Comparison of an analog direct detection and a micropulse aerosol lidar at 1.5-$\mu$m wavelength for wind field observationswith first results over the ocean, Journal of Applied Remote Sensing, 10, 016 031–016 031, 2016.

Messager, C., Parker, D. J., Reitebuch, O., Agusti-Panareda, A., Taylor, C. M., and Cuesta, J.: Structure and dynamics of the Saharan atmospheric boundary layer during the West African monsoon onset: observations and analyses from the research flights of 14 and 17 July 2006, Quarterly Journal of the Royal Meteorological Society, 136, 107–124, doi:10.1002/qj.469, URL http://dx.doi.org/10.1002/qj.469, 2010.

Morcrette, J.-J., Boucher, O., Jones, L., Salmond, D., Bechtold, P., Beljaars, A., Benedetti, A., Bonet, A., Kaiser, J. W., Razinger, M., Schulz, M., Serrar, S., Simmons, A. J., Sofiev, M., Suttie, M., Tompkins, A. M., and Untch, A.: Aerosol analysis and forecast in the European Centre for Medium-Range Weather Forecasts Integrated Forecast System: Forward modeling, Journal of Geophysical Research: Atmospheres, 114, doi:10.1029/2008JD011235, URL http://dx.doi.org/10.1029/2008JD011235, d06206, 2009.

Nalli, N. R., Clemente-Colón, P., Morris, V., Joseph, E., Szczodrak, M., Minnett, P. J., Shannahoff, J., Goldberg, M. D., Barnet, C., Wolf, W. W., et al.: Profile observations of the Saharan air layer during AEROSE 2004, Geophysical research letters, 32, 2005.

Prospero, J. M.: Atmospheric dust studies on Barbados, Bulletin of the American Meteorological Society, 49, 645, 1968.

Prospero, J. M. and Carlson, T. N.: Saharan air outbreaks over the tropical North Atlantic, pp. 677–691, 1981.

Prospero, J. M., Ginoux, P., Torres, O., Nicholson, S. E., and Gill, T. E.: Environmental characterization of global sources of atmospheric soil dust identified with the NIMBUS 7 Total Ozone Mapping Spectrometer (TOMS) absorbing aerosol product, Reviews of Geophysics, 40, 2–1–2–31, doi:10.1029/2000RG000095, URL http://dx.doi.org/10.1029/2000RG000095, 1002, 2002.

Prospero, J. M., Landing, W. M., and Schulz, M.: African dust deposition to Florida: Temporal and spatial variability and comparisons to models, Journal of Geophysical Research: Atmospheres, 115, doi:10.1029/2009JD012773, URL http://dx.doi.org/10.1029/2009JD012773, d13304, 2010.

Prospero, J. M., Collard, F.-X., Molini, J., and Jeannot, A.: Characterizing the annual cycle of African dust transport to the Caribbean Basin and South America and its

impact on the environment and air quality, Global Biogeochemical Cycles, 28, 757–773, doi:10.1002/2013GB004802, URL http://dx.doi.org/10.1002/2013GB004802, 2013GB004802, 2014.

Rahm, S.: Measurement of a wind field with an airborne continuous-wave Doppler lidar, Opt. Lett., 20, 216–218, doi:10.1364/OL.20.000216, URL http://ol.osa.org/abstract.cfm?URI=ol-20-2-216, 1995.

Reitebuch, O., Werner, C., Leike, I., Delville, P., Flamant, P. H., Cress, A., and Engelbart, D.: Experimental Validation of Wind Profiling Performed by the Airborne 10-m Heterodyne Doppler Lidar WIND, Journal of Atmospheric and Oceanic Technology, 18, 1331–1344, doi:10.1175/1520-0426(2001)018⟨1331:EVOWPP⟩2.0.CO;2, 2001.

Schepanski, K., Tegen, I., Todd, M. C., Heinold, B., Bönisch, G., Laurent, B., and Macke, A.: Meteorological processes forcing Saharan dust emission inferred from MSG-SEVIRI observations of subdaily dust source activation and numerical models, Journal of Geophysical Research: Atmospheres, 114, doi:10.1029/2008JD010325, URL http://dx.doi.org/10.1029/2008JD010325, d10201, 2009.

Schulz, M., Prospero, J. M., Baker, A. R., Dentener, F., Ickes, L., Liss, P. S., Mahowald, N. M., Nickovic, S., García-Pando, C. P., Rodríguez, S., et al.: Atmospheric transport and deposition of mineral dust to the ocean: implications for research needs, Environmental science & technology, 46, 10 390–10 404, 2012.

Schumann, U., Weinzierl, B., Reitebuch, O., Schlager, H., Minikin, A., Forster, C., Baumann, R., Sailer, T., Graf, K., Mannstein, H., Voigt, C., Rahm, S., Simmet, R., Scheibe, M., Lichtenstern, M., Stock, P., Rüba, H., Schäuble, D., Tafferner, A., Rautenhaus, M., Gerz, T., Ziereis, H., Krautstrunk, M., Mallaun, C., Gayet, J.-F., Lieke, K., Kandler, K., Ebert, M., Weinbruch, S., Stohl, A., Gasteiger, J., Groß, S., Freudenthaler, V., Wiegner, M., Ansmann, A., Tesche, M., Olafsson, H., and Sturm, K.: Airborne observations of the Eyjafjalla volcano ash cloud over Europe during air space closure in April and May 2010, Atmospheric Chemistry and Physics, 11, 2245–2279, doi:10.5194/acp-11-2245-2011, URL http://www.atmos-chem-phys.net/11/2245/2011/, 2011.

Seinfeld, J. and Pandis, S.: Atmospheric chemistry and physics: from air pollution to climate change, Wiley, 1998.

Tegen, I. and Fung, I.: Contribution to the atmospheric mineral aerosol load from land surface modification, Journal of Geophysical Research: Atmospheres, 100, 18 707–18 726, doi:10.1029/95JD02051, URL http://dx.doi.org/10.1029/95JD02051, 1995.

Tegen, I., Hollrig, P., Chin, M., Fung, I., Jacob, D., and Penner, J.: Contribution of different aerosol species to the global aerosol extinction optical thickness: Estimates from model results, Journal of Geophysical Research: Atmospheres, 102, 23 895–23 915, doi:10.1029/97JD01864, URL http://dx.doi.org/10.1029/97JD01864, 1997.

Tegen, I., Werner, M., Harrison, S. P., and Kohfeld, K. E.: Relative importance of climate and land use in determining present and future global soil dust emission, Geophysical Research Letters, 31, doi:10.1029/2003GL019216, URL http://dx.doi.org/10.1029/2003GL019216, l05105, 2004.

Textor, C., Schulz, M., Guibert, S., Kinne, S., Balkanski, Y., Bauer, S., Berntsen, T., Berglen, T., Boucher, O., Chin, M., Dentener, F., Diehl, T., Easter, R., Feichter, H., Fillmore, D., Ghan, S., Ginoux, P., Gong, S., Grini, A., Hendricks, J., Horowitz, L., Huang, P., Isaksen, I., Iversen, I., Kloster, S., Koch, D., Kirkevåg, A., Kristjansson, J. E., Krol, M., Lauer, A., Lamarque, J. F., Liu, X., Montanaro, V., Myhre, G., Penner, J., Pitari, G., Reddy, S., Seland, Ø., Stier, P., Takemura, T., and Tie, X.: Analysis and quantification of the diversities of aerosol life cycles within AeroCom, Atmospheric Chemistry and Physics, 6, 1777–1813, doi:10.5194/acp-6-1777-2006, URL http://www.atmos-chem-phys.net/6/1777/2006/, 2006.

Thorncroft, C. and Hodges, K.: African Easterly Wave Variability and Its Relationship to Atlantic Tropical Cyclone Activity, Journal of Climate, 14, 1166–1179, doi:10.1175/1520-0442(2001)014⟨1166:AEWVAI⟩2.0.CO;2, 2001.

Tsamalis, C., Chédin, A., Pelon, J., and Capelle, V.: The seasonal vertical distribution of the Saharan Air Layer and its modulation by the wind, Atmospheric Chemistry and Physics, 13, 11 235–11 257, doi:10.5194/acp-13-11235-2013, URL http://www.atmos-chem-phys.net/13/11235/2013/, 2013.

Vincent, R. A. and Reid, I. M.: HF Doppler Measurements of Mesospheric Gravity Wave Momentum Fluxes, Journal of the Atmospheric Sciences, 40, 1321–1333, doi:10.1175/1520-0469(1983)040⟨1321:HDMOMG⟩2.0.CO;2, URL http://dx.doi.org/10.1175/1520-0469(1983)040<1321:HDMOMG>2.0.CO;2,, 1983.

Weinzierl, B., Sauer, D., Minikin, A., Reitebuch, O., Dahlktter, F., Mayer, B., Emde, C., Tegen, I., Gasteiger, J., Petzold, A., Veira, A., Kueppers, U., and Schumann, U.: On the visibility of airborne volcanic ash and mineral dust from the pilots perspective in flight, Physics and Chemistry of the Earth, 4546, 87 – 102, doi:http://dx.doi.org/10.1016/j.pce.2012.04.003, URL http://www.sciencedirect.com/science/article/pii/S1474706512000496, 2012.

Weinzierl, B., Ansmann, A., Prospero, J. M., Althausen, D., Benker, N., Chouza, F., Dollner, M., Farrell, D., Fomba, W. K., Freudenthaler, V., Gasteiger, J., Groß, S., Haarig, M., Heinold, B., Kandler, K., Kristensen, T. B., Mayol-Bracero, O. L., Müller, T., Reitebuch, O., Sauer, D., Schäfler, A., Schepanski, K., Spanu, A., Tegen, I., Toledano, C., and Walser, A.: The Saharan Aerosol Long-range Transport and Aerosol-Cloud-Interaction Experiment (SALTRACE): overview and selected highlights, Bulletin of the American Meteorological Society, -, –, doi:10.1175/BAMS-D-15-00142.1, URL http://dx.doi.org/10.1175/BAMS-D-15-00142.1, in press.

Werner, C. H., Flamant, P. H., Reitebuch, O., Köpp, F., Streicher, J., Rahm, S., Nagel, E., Klier, M., Herrmann, H., Loth, C., Delville, P., Drobinski, P., Romand, B., Boitel, C., Oh, D., Lopez, M., Meissonnier, M., Bruneau, D., and Dabas, A. M.: Wind infrared Doppler lidar instrument, Optical Engineering, 40, doi:10.1117/1.1335530, 2001.

Wu, M.-L. C., Reale, O., Schubert, S. D., Suarez, M. J., and Thorncroft, C. D.: African Easterly Jet: Barotropic Instability, Waves, and Cyclogenesis, Journal of Climate, 25, 1489–1510, doi:10.1175/2011JCLI4241.1, URL http://dx.doi.org/10.1175/2011JCLI4241.1, 2012.

Yu, H., Chin, M., Yuan, T., Bian, H., Remer, L. A., Prospero, J. M., Omar, A., Winker, D., Yang, Y., Zhang, Y., Zhang, Z., and Zhao, C.: The fertilizing role of African dust in the Amazon rainforest: A first multiyear assessment based on data from Cloud-Aerosol Lidar and Infrared Pathfinder Satellite Observations, Geophysical Research Letters, 42, 1984–1991, doi:10.1002/2015GL063040, URL http://dx.doi.org/10.1002/2015GL063040, 2015GL063040, 2015.

Zhang, H., McFarquhar, G. M., Cotton, W. R., and Deng, Y.: Direct and indirect impacts of Saharan dust acting as cloud condensation nuclei on tropical cyclone eyewall development, Geophysical Research Letters, 36, doi:10.1029/2009GL037276, URL http://dx.doi.org/10.1029/2009GL037276, l06802, 2009.

# Acknowledgments

At this point, I would like to thank to all those who contributed to the success of this work.

First and foremost, I wish to thank Dr. Reitebuch for his guidance during this last three years. His knowledge, continuous support and readiness for discussion made my time as PhD student an immensely rewarding experience. Furthermore, I am very grateful to my supervisor Prof. Dr. Weinzierl for giving me the opportunity to work as part of her group. Her insightful comments and suggestions were an invaluable help while working on this thesis. I thank also my co-supervisor Prof. Dr. Rapp for his valuable support and recommendations.

I would also like to give a big thanks to all my colleagues of the Institut für Physik der Atmosphäre in general and the lidar group in particular, who provide me with an excellent and stimulating working atmosphere. A special thanks goes to Dr. Rahm and Dr. Witschas for the fruitful discussions on the lidar retrieval techniques presented in this thesis.

The work on this thesis was supported by the Deutscher Akademischer Austauschdienst. Their economical and organizational support made my move to Germany really easy and enjoyable.

Further thanks are due to my Argentinian colleagues at the División Lidar for introducing me to the world of lidars.

Finalmente, quiero agradecer a todos aquellos que de una u otra forma hicieron de mi quien soy. A mis amigos y compañeros. A mi hermano Martín. A mis padres, Mariano y Margarita. A mi querida Deborah. Este trabajo pertenece a todos ustedes también.